



MAX-PLANCK-GESELLSCHAFT

TECHNISCHE UNIVERSITÄT MÜNCHEN
MAX-PLANCK-INSTITUT FÜR QUANTENOPTIK

Topological Phases of Matter with Subsystem Symmetries

David T. Stephen

Vollständiger Abdruck der von der Fakultät für Physik
der Technischen Universität München
zur Erlangung des akademischen Grades eines
Doktors der Naturwissenschaften (Dr. rer. nat.)
genehmigten Dissertation.

Vorsitzender: Prof. Jonathan J. Finley, Ph.D.

Prüfer der Dissertation: 1. Prof. Dr. Norbert Schuch
2. Prof. Dr. Frank Pollmann

Die Dissertation wurde am 21.06.2021 bei der Technischen Universität München
eingereicht und durch die Fakultät für Physik am 20.07.2021 angenommen.

Abstract

Quantum many-body systems display exotic emergent behaviour due to the presence of quantum entanglement. Two fields where entanglement plays an essential role are quantum phases of matter and quantum computation. This thesis sits at the intersection of these two fields, and studies topological phases of matter with subsystem symmetries and their application to quantum computation. Subsystem symmetries are a type of symmetry that act on rigid lower-dimensional subsystems of the entire system, including lines, planes, or fractals. These symmetries have recently found importance in the context of condensed matter physics, thanks to their relation to fracton topological order, and in quantum information, thanks to their relation to measurement-based quantum computation (MBQC). This thesis starts in the latter context, where we give a systematic method to construct symmetry-protected topological phases of matter protected by subsystem symmetries (SSPT phases). Our construction uses the language of quantum cellular automata, which also naturally describes the use of the constructed phases as resources for universal MBQC, thereby providing a unified understanding of the relation between SSPT phases and MBQC. Having understood the computational properties of SSPT phases, we move on to studying their physical properties. We examine corrections to the entanglement area law in SSPT phases of matter and show that, contrary to prior belief, these corrections are uniform throughout an SSPT phase and can therefore be used to characterize them in manner similar to the topological entanglement entropy for topological phases. We use this result as the basis of a numerical algorithm for detecting SSPT order in ground states, which we use to discover an extended phase of matter surrounding the 2D cluster state. In the final chapter, we study how subsystem symmetries can enrich topological phases of matter. We construct a 3D model in which planar subsystem symmetries fractionalize on loop-like topological excitations, resulting in an extensive symmetry-protected degeneracy of the excitations and an increased value of the topological entanglement entropy. We then gauge the subsystem symmetries to obtain a number of related models, including models of fracton topological order, which showcase more of the possible types of subsystem symmetry enrichment that can occur in 3D. Overall, the results of this thesis give a first step towards our understanding of novel topological phases of matter with subsystem symmetries, and exemplify the symbiotic relationship between the fields of quantum phases of matter and quantum computation.

Zusammenfassung

Quanten-Vielteilchensysteme zeigen aufgrund von Quantenverschränkung exotisches emergentes Verhalten. Zwei Bereiche, in denen Verschränkung eine wesentliche Rolle spielt, sind Quantenphasen der Materie und Quanteninformatik. Diese Dissertation befasst sich mit dem Schnittpunkt dieser beiden Felder und untersucht topologische Phasen der Materie mit Subsystemsymmetrien und deren Anwendung zur Quanteninformationsverarbeitung. Subsystemsymmetrien sind eine Art von Symmetrie, die auf rigide, niederdimensionale Subsysteme des Gesamtsystems wirken, einschließlich Linien, Ebenen oder Fraktale. Diese Symmetrien haben in letzter Zeit Bedeutung im Kontext der Physik der kondensierten Materie gefunden, dank ihrer Beziehung zur fraktalen topologischen Ordnung, und in der Quanteninformatik, dank ihrer Beziehung zur messungsbasierten Quantenberechnung (MBQC). Diese Arbeit setzt im letzteren Kontext an, wo wir eine systematische Methode zur Konstruktion von symmetriegeschützten topologischen Phasen der Materie angeben, die durch Subsystemsymmetrien geschützt sind (SSPT-Phasen). Unsere Konstruktion verwendet die Sprache der zellulären Quantenautomaten, die auch auf natürliche Weise die Verwendung der konstruierten Phasen als Ressourcen für universelle MBQC beschreibt und so ein einheitliches Verständnis der Beziehung zwischen SSPT-Phasen und MBQC ermöglicht. Nachdem wir die rechnerischen Eigenschaften von SSPT-Phasen verstanden haben, gehen wir dazu über, ihre physikalischen Eigenschaften zu untersuchen. Wir untersuchen Korrekturen des Verschränkungsflächengesetzes in SSPT-Phasen der Materie und zeigen, dass diese Korrekturen, entgegen der bisherigen Annahme, in einer SSPT-Phase einheitlich sind und daher zu ihrer Charakterisierung in ähnlicher Weise wie die topologische Verschränkungsentropie für topologische Phasen benutzt werden können. Wir verwenden dieses Ergebnis als Grundlage eines numerischen Algorithmus zum Aufspüren von SSPT-Ordnung in Grundzuständen, mit dem wir eine ausgedehnte Phase der Materie entdecken, die den 2D-Clusterzustand umgibt. Im letzten Kapitel untersuchen wir, wie Subsystemsymmetrien topologische Phasen der Materie bereichern können. Wir konstruieren ein 3D-Modell, in dem planare Subsystemsymmetrien zu schleifenartige topologische Anregungen fraktionieren, was zu einer ausgedehnten symmetriebeschützten Entartung der Anregungen und einem erhöhten Wert der topologischen Verschränkungsentropie führt. Wir eichen dann die Subsystem-Symmetrien, um eine Reihe verwandter Modelle zu erhalten, einschließlich Modelle mit fraktionaler topologischer Ordnung, die weitere Arten von Subsystemsymmetrieanreicherung zeigen, welche in 3D auftreten können. Insgesamt stellen die Ergebnisse dieser Dissertation einen ersten Schritt zum Verständnis neuartiger topologischer Phasen der Materie mit Subsystemsymmetrien dar und veranschaulichen die symbiotische Beziehung zwischen Quantenphasen der Materie und Quanteninformatik.

Acknowledgements

This thesis would have never been possible without the support of the many people who I've met during these four years. First and foremost, I would like to thank my advisor Norbert Schuch, without whom this adventure would have never begun. I am extremely grateful for him giving me the freedom to take my research in any direction I wanted, and for always being available for interesting, helpful, and fun discussions. I am also grateful to Ignacio Cirac for his kind advice and for his role in cultivating a fantastic group atmosphere, and to the staff at MPQ who helped me in so many ways and saved me many hours of bureaucratic headache.

I was able to reach the end of this journey thanks to the many friends that supported me along the way. I would like to particularly thank Henrik Dreyer for introducing me to many of these friends and for the fun times hanging out and jamming, as well as Caroline de Groot, Albert Gasull Celades, Lorenzo Festa, and Dominic Wild for the many nights spent cooking and playing games at home, among other adventures. I also greatly enjoyed the company of other friends including Julian Roos, Nicola Pancotti, Ruben Verresen, Johannes Knörzer, Daniel Malz, Daniel Robaina, Jiří Guth Jarkovský, Patrick Emonts, Giacomo Giudice, Christoph Sünderhauf, Mohsin Iqbal, and Vitaly Wirthl. Also, I thank my roommates Sambit Mitra and Ritika Dagar for a fun and relaxing home environment.

I am indebted to my many international collaborators for their scientific insight and friendship, including Robert Raussendorf, Hendrik Poulsen Nautrup, Juani Bermejo-Vega, Jens Eisert, Dominic Williamson, José Garre-Rubio, and Arpit Dua. I thank Robert Raussendorf in particular for his continued support and assistance even throughout my PhD. I also acknowledge support from the Natural Sciences and Engineering Research Council of Canada (NSERC) for funding a large part of my PhD.

Finally, I am most grateful to my parents and my brother, whose many lessons have helped me through all aspects of life, and to Annie Park for her warmth and support that helped me feel the comfort of home that I cherish so deeply.

Contents

1	Introduction	1
2	Background to quantum phases of matter, tensor networks, and quantum computation	7
2.1	Gapped quantum systems	7
2.1.1	Definition of gapped phases of quantum matter	9
2.2	Symmetry-protected topological order	12
2.2.1	Group cohomology and the Else-Nayak procedure	12
2.2.2	Example of SPT order in 1D	15
2.2.3	Example of SPT order in 2D	17
2.3	Intrinsic topological order	21
2.3.1	Example of topological order in 2D	22
2.3.2	Example of topological order in 3D	24
2.3.3	Topological entanglement entropy	25
2.3.4	Gauging as a duality map between phases	27
2.4	Symmetry-enriched topological order	30
2.4.1	Examples of SET order in 2D	31
2.5	Tensor networks	37
2.5.1	Tensor network fundamentals	37
2.5.2	Symmetries and the classification of phases in tensor networks	44
2.5.3	Tensor network numerics	50
2.6	Measurement-based quantum computation with SPT phases	52
2.6.1	MBQC in tensor networks	53
2.6.2	Computational phases of matter in 1D	55
2.6.3	Higher dimensions and implications	56
2.7	Subsystem symmetries	58
2.7.1	The cluster state and SSPT order	58
2.7.2	Tensor network representation	61
2.7.3	The cluster phase	62
2.7.4	Quasi-1D SPT order	64
2.7.5	Universal MBQC in the cluster phase	65
2.7.6	Gauging subsystem symmetries and fracton topological order	67
3	Universal subsystem symmetry protected topological phases from quantum cellular automata	69
3.1	Quantum cellular automata	72

3.2	Defining PEPS from QCA	74
3.2.1	Stabilizer representations of fixed-point PEPS	77
3.2.2	Simple CQCA	79
3.3	SPT order with L -cycle symmetries	81
3.4	Relation to SSPT order	85
3.4.1	From quasi-1D to 2D	85
3.4.2	Line-like symmetries protect glider CQCA	86
3.5	Computational power of the QCA phases	88
3.5.1	Period of the CQCA	89
3.5.2	Determining gate set	91
3.5.3	Proving computational universality	92
3.5.4	Periodic, entangling CQCA as universal resources for MBQC	95
3.6	Discussion & Conclusions	96
4	Detecting subsystem symmetry-protected topological order via entanglement entropy	99
4.1	Cluster phase and corrections to the area law	100
4.2	Analytical argument for uniformity of the SPEE	104
4.2.1	Tensor network description of the cluster phase	104
4.2.2	Constraining the SPEE in the cluster phase	105
4.3	Numerical detection of SSPT order	109
4.3.1	Description of the algorithm	109
4.3.2	Stability of the cluster phase	110
4.3.3	Beyond the cluster phase — Time reversal symmetry	112
4.3.4	Remarks on the numerical method	116
4.4	3D cluster states	117
4.5	Discussions & Conclusions	119
5	Subsystem symmetry-enriched topological order in three dimensions	123
5.1	SPT order with global and subsystem symmetries	126
5.1.1	Boundary of the SSPT	129
5.2	Subsystem symmetry enriched topological order	132
5.2.1	Excitations and symmetry enrichment	133
5.2.2	Topological entanglement entropy	135
5.2.3	Calculation of topological entanglement entropy	138
5.3	Gauging the subsystem symmetries	142
5.3.1	Symmetry defects and gauging	142
5.3.2	Gauging only subsystem symmetries: Fracton order	144
5.3.3	Gauging global and subsystem symmetries: Panoptic order	147
5.4	Discussion & Conclusions	148
6	Conclusions	151

Chapter 1

Introduction

The complexity that arises from the interactions of many quantum particles, the “quantum many-body problem”, represents the frontier of modern physics. Various systems coming from nearly every field of physics, including black holes, complex molecules, and solid-state materials, are made up of a large number of particles that interact according to the laws of quantum mechanics to generate exotic emergent phenomena. The root cause of complexity in quantum mechanical systems is entanglement, which describes the fundamental inability to understand the state of a many-particle system in terms of states of the individual particles. In fact, sometimes a single particle contains no information at all about the state of the system. Instead, information is distributed non-locally between all particles, and this is reflected by the fact that the number of possible states that a system can take grows exponentially quickly with the number of particles. This fact makes it impossible to write down a generic state of even a modest (~ 50) number of particles, and trying to tame the quantum many-body problem in light of this can seem like a fruitless endeavour.

Luckily, it turns out that entanglement in realistic systems comes in small doses, and it has a particular structure that allows it to be described in an efficient way when viewed from the right perspective. This perspective comes from the field of quantum information, whose underlying goal is to describe, quantify, and utilize entanglement [1]. Tools coming from quantum information such as quantum circuits and tensor networks allow us to form representations of quantum systems that distribute entanglement between particles in an incremental manner, providing a natural extension of traditional mean-field approaches which try to solve a problem as best as possible without introducing entanglement [2, 3]. Such representations allow us to not only express many-body quantum states in a compact form, but also to directly analyze their entanglement structure which, as we will see, is key to understanding emergent many-body phenomena. The recent prominence of techniques inspired by quantum information across all disciplines of physics speaks to the essential role that is played by entanglement.

Two areas of research that are deeply rooted in the physics of entangled many-body systems are quantum computation and quantum phases of matter [1, 2]. In quantum computation, entanglement is viewed as a resource, and the ability to prepare and measure entangled many-body states allows the design of computa-

tional algorithms that solve important problems like factoring exponentially faster than the best known classical algorithms. Entanglement is a key ingredient in such algorithms, as non-entangled or even weakly-entangled systems can be efficiently simulated by a classical computer, precluding any potential computational advantage given by the quantum resources [4]. Entanglement also plays an essential role in the classification of quantum phases of matter [5]. As opposed to conventional phases of matter that are characterized by symmetry and local order parameters, quantum phases of matter exhibiting topological order are characterized by ground states that have complex patterns of long-range entanglement. The classification of the different possible phases of matter then becomes the classification of patterns of entanglement. Emergent quasi-particles called anyons that arise from this entanglement have properties that can be strikingly different from the basic constituents of the system, such as an electric charge that is a fraction of the elementary charge, or exchange statistics that are neither fermionic nor bosonic.

The fields of quantum computation and quantum phases of matter both began to mature at the start of the century and have been evolving alongside each other since then, such that they are now deeply intertwined. This is due in large part to the fact that quantum phases of matter find practical application in the storage and processing of quantum information [6–9]. Perhaps the most familiar example is the idea of topological quantum computation, which leverages the anyons of two-dimensional (2D) topologically ordered systems to perform error-resilient quantum computation. A complementing approach uses Majorana fermions located at the edges of topologically ordered one-dimensional (1D) chains [10]. In the paradigm of measurement-based quantum computation (MBQC) [11], which is driven solely by single-body measurements of an entangled many-body state, the type of entanglement suitable for computation turns out to be the same type that is found in states exhibiting symmetry-protected topological (SPT) order [12–27] – an insight that is particularly relevant to this thesis. Indeed, every time a new type of quantum order is discovered, it is not long before its uses for quantum computation are being investigated.

Intriguingly, the intertwinement of the two fields also goes in the opposite direction, where new models of topological order are designed from scratch to have specific computational properties [6, 18, 23, 28–31]. This leads to a very interesting relationship between theory and experiment: Rather than designing a toy model to capture the essential physics of a real-life material, the toy model is the starting point, and the task then is to find or engineer a physical system which can realize its computational properties in the laboratory. This pattern began early on with Kitaev’s toric code model [6], which is one of the simplest and most important models of topological order. This model was designed for the robust storage of quantum information, and it has since been realized on small scales in quantum simulators based on nuclear magnetic resonance [32, 33], photons [34, 35], and superconducting arrays [36, 37]. Many other in-depth characterizations of quantum phases of matter have been spurred by the desire to understand their computational properties [7, 9, 15, 38–49] and, as we will discuss shortly, extreme cases of this synergy have even led to the definition of new quantum phases of matter that are tailor-made for specific computational tasks [12, 23, 26, 30]. Without the continual

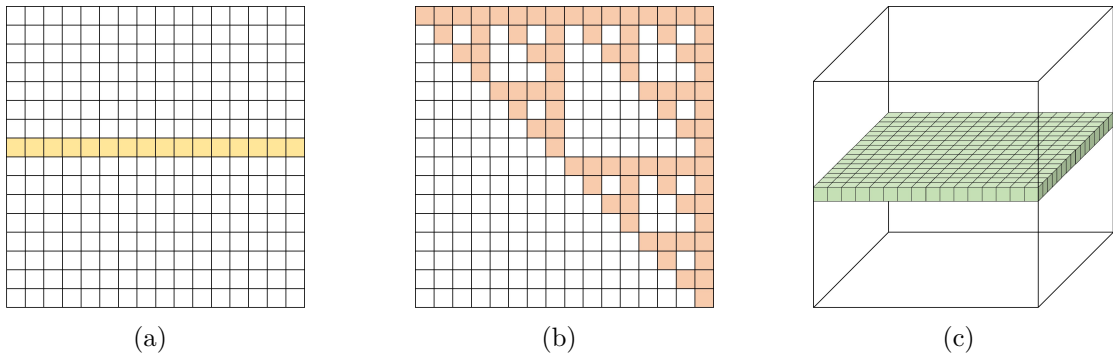


Figure 1.1: Examples of (a) line, (b) fractal, and (c) plane subsystem symmetries. The symmetry operators act non-trivially only on the shaded parts of the system.

motivation and inspiration coming from quantum computation, the landscape of quantum phases of matter would undoubtedly look very different today.

The central theme of this thesis is the notion of subsystem symmetries. These are symmetries which act non-trivially only on rigid lower-dimensional subsystems of the entire system, such as lines, planes, or even fractals, as pictured in Fig. 1.1. As such, they lie in between the more conventional global symmetries, which act on the entire system, and gauge symmetries, which act only in a small region around one particle. These symmetries may seem somewhat arbitrary and unphysical, but they have recently arisen in two separate contexts, both of which were born out of considerations for quantum computation.

The first context in which subsystem symmetries arose was that of fracton topological order (or simply “fracton order”) [50]. This is a new notion of topological order that came out of the search for a robust quantum memory. The first¹ example of fracton order was Haah’s cubic code model [30]. In this model, anyons appear at the corner of extended operators with fractal geometry, such that a single anyon cannot move without incurring an energy penalty. These mobility constraints, which are the defining property of fracton order, can be viewed as conservation laws, *i.e.* symmetries, along rigid subsystems, which establishes the connection to subsystem symmetries. The energy landscape created by the mobility constraints makes the cubic code an attractive candidate for a quantum memory, since there is a macroscopic energy barrier between different ground states [44], so information can be robustly stored in the ground state subspace even at finite temperature [45]. Since the discovery of the cubic code, many more examples of fracton order have been discovered [52–58], attracting a significant amount of attention both for their potential uses in quantum computation and for their novel physical properties that challenge existing beliefs about what kinds of topological order are possible.

The second context in which subsystem symmetries arose, and the context which is most relevant to this thesis, is subsystem symmetry protected topological

¹Technically, Chamon’s model [51] was the first model of fracton order, but it wasn’t until Haah’s code that the importance and novelty of these models was appreciated and the field of research truly began.

(SSPT) order [26, 59]. This is a type of topological order that exists only in the presence of subsystem symmetries, generalizing the usual SPT order which is protected by global symmetries [60]. The prototypical example of a state with SSPT order is the 2D cluster state [11], which was originally introduced as a resource state for universal MBQC. The notion of SSPT order came from the desire to extend the computational power of the 2D cluster state to an entire phase of matter. While conventional SPT order was sufficient to achieve this in 1D systems [19], moving to 2D systems required the identification of line-like subsystem symmetries of the 2D cluster state [12, 16] and the subsequent definition of SSPT order [26]. Interest in SSPT order also arose simultaneously and independently in the condensed matter physics community, thanks to its unique properties beyond that of conventional SPT order [59], and research since then has been equally driven by both communities.

These two examples show that topological phases of matter with subsystem symmetries exemplify the idea that quantum computation and quantum phases of matter are two fields that cannot, and should not, be disentangled. The aim of this thesis is to follow this tenet by launching an in-depth exploration of the relationship between subsystem symmetries, topological order, and quantum computation.

The rest of this thesis is organized as follows. In Chapter 2, we will review the relevant background material about phases of matter, tensor networks, and quantum computation that is needed for the subsequent chapters. The chapter ends by describing the 2D cluster state, which is the main character of this thesis, and showcasing its relation to SSPT order and MBQC. This discussion forms the starting point for the main results of this thesis. In Chapter 3, we will present a unified formalism for understanding SSPT phases and their relation to MBQC via the language of quantum cellular automata. In Chapter 4, we will turn towards the physical properties of SSPT phases, and show how they can be characterized and also detected numerically by entanglement entropy. In Chapter 5, we will discuss how subsystem symmetries can also be used to enrich topological order in 3D using a concrete model that exhibits fractionalization of subsystem symmetries. Finally, in Chapter 6 we will give conclusions and discuss open questions raised by this thesis.

Publications

A number of manuscripts were published during this PhD, some of which are contained in a modified form in this thesis with permission from the American Physical Society ©2019. The included passages from these publications were written entirely by myself. What follows is a summary of the publications, their role in this thesis, and a brief description of my contributions to those which are included in this thesis:

Publications included in this thesis

- Computationally Universal Phase of Quantum Matter. Robert Raussendorf, Cihan Okay, Dong-Sheng Wang, **David T. Stephen***, and Hendrik Poulsen Nautrup*. Phys. Rev. Lett. 122, 090501 (2019). [26]

**These authors contributed equally to this manuscript.*

This publication was initiated before the beginning of the PhD work and finished over the course of the first year. While the key results of this work were proven by R. Raussendorf, I played an important role in the early development of the project as well as the refinement, interpretation, and presentation of the results. Aspects of this publication appear in Section 2.7 of Chapter 2 as background material.

- Subsystem symmetries, quantum cellular automata, and computational phases of quantum matter. **David T. Stephen**, Hendrik Poulsen Nautrup, Juani Bermejo-Vega, Jens Eisert, and Robert Raussendorf. Quantum 3, 142 (2019). [61]

This project was led by myself, and I am responsible for the key constructions and proofs. The other authors played various roles, with the initial idea being conceived with the help of H. Poulsen Nautrup and R. Raussendorf. H. Poulsen Nautrup also made significant contributions to the stabilizer construction, the proof of Theorem 2, and the discussion of periodic QCA. This publication appears in Chapter 3 with some modifications.

- Detecting subsystem symmetry protected topological order via entanglement entropy. **David T. Stephen**, Henrik Dreyer, Mohsin Iqbal, and Norbert Schuch. Phys. Rev. B 100, 115112 (2019). [62]

This project was initiated and led by myself, and I am responsible for providing the direction for the project. All other authors contributed to all aspects of the paper. In particular, N. Schuch contributed particularly to the analytical proof of uniformity of the SPEE, H. Dreyer performed the numerical calculations behind Fig. 4.2 and developed the argument based on perturbation theory, and M. Iqbal performed the numerical simulations behind Figs. 4.5, 4.6. This publication appears in Chapter 4 with some modifications.

- Subsystem symmetry enriched topological order in three dimensions. **David T. Stephen**, José Garre-Rubio, Arpit Dua, and Dominic J. Williamson. Phys. Rev. Research 2, 033331 (2020). [63]

This project was initiated and led by myself, and I am responsible for most of the constructions and calculations. All other authors contributed to various aspects, and D. J. Williamson in particular had a significant contribution to the discussion on gauging subsystem symmetries. This publication appears in Chapter 5 with some modifications.

Publications not included in this thesis

- Inaccessible entanglement in symmetry protected topological phases. Caroline de Groot, **David T. Stephen**, Andras Molnar, and Norbert Schuch. Journal of Physics A: Mathematical and Theoretical 53, 335302 (2020). [64]
- String order parameters for symmetry fractionalization in an enriched toric code. José Garre-Rubio, Mohsin Iqbal, and **David T. Stephen**. Phys. Rev. B **103**, 125104 (2021). [65]

Chapter 2

Background to quantum phases of matter, tensor networks, and quantum computation

This chapter contains an introduction to the core concepts that will be used throughout the remainder of the thesis. Starting with the definition of gapped systems and gapped phases of matter (Section 2.1), we will introduce and give examples of symmetry-protected topological order (Section 2.2), intrinsic topological order (Section 2.3), and symmetry-enriched topological order (Section 2.4). Then, in Section 2.5, we will introduce the notation of tensor networks, which is used extensively in Chapters 3 and 4, and discuss some basic concepts surrounding them as well as their application to phases of matter. Section 2.6 will then introduce measurement-based quantum computation and its relation to symmetry-protected topological order. Finally, we will introduce the notion of subsystem symmetries and the cluster phase in Section 2.7, which will directly lead into Chapter 3.

2.1 Gapped quantum systems

The physical systems studied in this thesis are gapped quantum spin lattices. Here, by spin lattice, we refer to a Hilbert space \mathcal{H} composed of a tensor product of N smaller d -dimensional Hilbert spaces \mathbb{C}^d which represent “spins”¹, such that $\mathcal{H} = \bigotimes_{i=1}^N \mathbb{C}^d$. We consider local Hamiltonians acting on these lattices, which are Hamiltonians of the form $H = \sum_{i=1}^N h_i$ where each term h_i acts only on a small number r of spins around site i , where r is independent of N . When we say that a system is gapped, we imagine a sequence of local Hamiltonians on increasing system sizes, such that there is a gap between the ground state manifold and the first excited state which remains finite in the thermodynamic limit [66]. The dimension of \mathcal{H} grows exponentially with the number N of spins. This is the basic cause for the complexity of describing such systems, as the amount of space needed to even write down a state quickly becomes practically infeasible.

¹Since we are often inspired by quantum information, we may also call these systems qubits (for $d = 2$) or qudits (for general d).

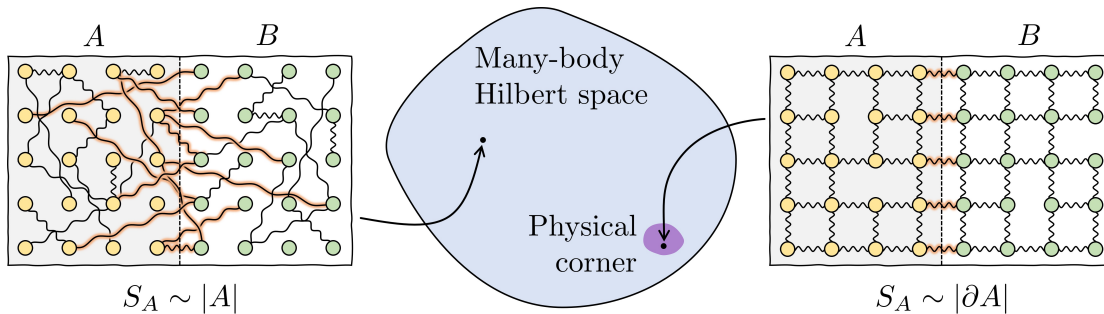


Figure 2.1: The physical corner of the many-body Hilbert space. The left and right images are representative states of the quantum spin lattices where entanglement between particles is represented schematically by a wavy bond. Each lattice is divided into subsystems A and B by the dashed line. The number of entangled bonds that cross this line roughly determines the entanglement S_A between A and B .

Gapped spin lattices are unique among quantum many-body systems in that they live only in a tiny fraction of the exponentially large Hilbert space, the “physical corner”. This is to be naturally expected, given that a local Hamiltonian has only Nd^{2r} parameters compared to the d^{2N} of a generic Hamiltonian. The physical corner can be characterized in terms of entanglement, which is quantified by the entanglement entropy. Suppose we divide our lattice into two subregions A and B . We can define the entanglement entropy associated to this bipartition as,

$$S_A = -\text{Tr } \rho_A \ln \rho_A, \quad (2.1)$$

where $\rho_A = \text{Tr}_B |\psi\rangle\langle\psi|$ is the reduced density matrix corresponding to subsystem A . For a generic state in the Hilbert space, S_A will grow as the size of A , $S_A \sim |A|$, since every spin in A will have some entanglement with the subsystem B [67]. For ground states of gapped local Hamiltonians, on the other hand, the entropy will typically follow an *area law*, $S(\rho_A) \sim |\partial A|$, where $|\partial A|$ is the size of the boundary between A and B [68]. The area law reflects the fact that gapped local Hamiltonians have exponentially decaying correlations [69], so entanglement between A and B is mostly concentrated near the boundary between them. The physical corner of Hilbert space is occupied by those states which obey entanglement area laws, which in turn correspond to the ground states of local gapped Hamiltonians. The above discussion is summarized in Fig. 2.1.

The studies in this thesis are facilitated by the use of exactly solvable Hamiltonians. These are Hamiltonians whose local terms all commute with each other, such that all eigenvectors and eigenvalues can be obtained exactly. For such models, one can talk rather interchangeably about a Hamiltonian and its ground states. In fact, many important properties of a model such as the braiding statistics and fusion rules of topological excitations [70–72] as well as the existence of gapless edge modes [73, 74] can be determined by ground state entanglement alone. Exactly solvable Hamiltonians are usually very far from what one would find in a physically realistic system, even after several layers of simplifying approximations. Despite this, these models are still capable of capturing the essential features of more

realistic models. This is because these models can be seen as the output of certain renormalization-group (RG) transformations which wash out microscopic details of the system, leaving behind only the essential long-wavelength physics [75, 76]. This perspective is particularly useful in the context of phases of matter, where different points in a phase of matter are expected to flow towards exactly solvable RG fixed-points that represent each phase [77]. We will see in this chapter and the next that generic points in certain phases of matter can be viewed as “expansions” about the fixed-points in a manner that can be made very precise [15, 26].

2.1.1 Definition of gapped phases of quantum matter

We now move on to a formal definition of gapped phases of quantum matter. As opposed to the more familiar phases of matter whose transitions are driven by changes in temperature, quantum phases of matter are defined for systems at zero temperature, and phase transitions are driven by the change of some system parameter such as the strength of a magnetic field. For gapped systems, the low-temperature physics is dominated by the ground states and low-energy excited states, such that these states are sufficient to understand the nature of the quantum order in a state. For gapless systems this is not possible, so the story is much more complicated, although some interesting progress has been made recently [78–81].

We define phases of matter in terms of phase transitions, such that two systems are said to be in the same phase if they can be adiabatically connected without encountering a phase transition. A phase transition in a gapped system is accompanied by the divergence of some physical quantity such as correlation length, which occurs when the Hamiltonian gap is closed [82]. Therefore, we can define gapped phases of matter in the following way:

Definition 1 (Gapped phases of matter). *Two gapped, local Hamiltonians H , H' are in the same gapped phase of matter if there exists a continuous path of gapped, local Hamiltonians H_γ with $\gamma \in [0, 1]$ such that $H_0 = H$ and $H_1 = H'$.*

That is, we say that two gapped systems are in the same phase if they can be continuously connected without closing the gap. The trivial phase is defined to be the phase that contains product states. This definition is useful and intuitive, but it doesn’t tell us much about the structure that is shared between systems belonging to the same phase. To remedy this, we can formulate an equivalent definition in terms of the entanglement of ground state wave functions.

The central concept that connects the two definitions is quasi-adiabatic continuation [83]. Given a gapped path $H(\gamma)$ connecting two Hamiltonians, one can consider the unitary time evolution $U = \mathcal{T}[e^{-i \int_0^1 d\gamma \tilde{H}(\gamma)}]$, where \mathcal{T} is the time-ordering operator and $\tilde{H}(\gamma)$ is a slightly modified path of quasi-local Hamiltonians that can be obtained from $H(\gamma)$ [82]. If the path is uniformly gapped, one can be sure that the ground states will not be mapped to excited states via this evolution, such that this gives a unitary mapping between the ground state subspaces at $\gamma = 0$ and $\gamma = 1$. The use of the modified path $\tilde{H}(\gamma)$ ensures that the evolution can be done in a time that is independent of system size. This guarantees that U preserves locality, in that it maps local operators to local operators, and therefore

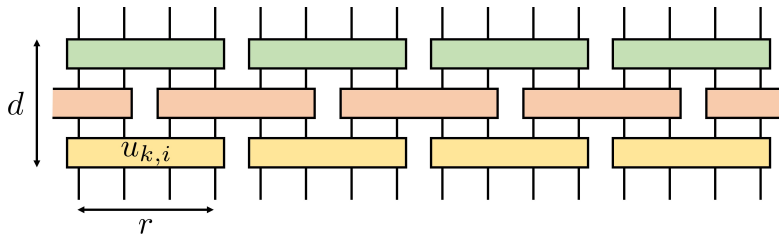


Figure 2.2: A finite depth quantum circuit of depth 3 and range 4.

cannot modify any global properties of the state. Finally, one can Trotterize the time evolution operator to express it as a sequence of unitary gates, such that it has the appearance of a *finite depth quantum circuit*, defined as follows:

Definition 2 (Finite depth quantum circuit). *A finite depth quantum circuit (FDQC) of depth d and range r is a unitary of the form*

$$U = \prod_{k=1}^d \left(\prod_i u_{k,i} \right) \quad (2.2)$$

where, for each k , $u_{k,i}$ are local operators with range r and non-overlapping support, see Fig. 2.2.

From the above, we see that any path of gapped Hamiltonians can be translated into a FDQC connecting them. Conversely, any FDQC can be translated into a path of gapped Hamiltonians by simply “inverting” the Trotter expansion to extract the local Hamiltonian terms that generate each gate in the FDQC [82]. Therefore, the following definition is equivalent to Definition 1:

Definition 3 (Gapped phases of matter via FDQCs). *Two gapped ground states $|\psi\rangle$ and $|\psi'\rangle$ are in the same gapped phase if they are related by a FDQC U_c , i.e., $|\psi'\rangle = U_c|\psi\rangle$.*

This definition shows that gapped phases of matter are distinguished by differing patterns of long-range entanglement, defined as entanglement that cannot be generated by a FDQC. Throughout this thesis, we will adopt the definition in terms of FDQC, since it gives better insight into the entanglement structure of phases, and it better suited to our techniques, which are often inspired by quantum information and computation.

We can refine the classification of phases by introducing symmetry. We consider on-site symmetries, which are symmetries that act as a tensor product over the degrees of freedom,

$$U(g) = \bigotimes_{i=1}^N u_i(g), \quad (2.3)$$

where each $u_i(g)$ is a unitary linear representation of a symmetry group G . Here, a linear representation is one that respects the group multiplication, i.e. $u_i(g)u_i(h) = u_i(gh)$. One often considers global on-site symmetries, where the symmetry acts in the same way on every site, i.e. $u_i(g) = u(g)$ for all i . In this thesis, we will

also consider cases beyond this, such as subsystem symmetries, where $U(g)$ has non-trivial support only on lower-dimensional subsystems of the whole system, and the related L -cycle symmetries, where $U(g)$ is translationally invariant only up to an enlarged unit cell.

For systems equipped with such a symmetry, we can define phases of matter in the following way:

Definition 4 (Gapped phases of matter via FDQCs with symmetry). *Two gapped ground states $|\psi\rangle$ and $|\psi'\rangle$ with a global, on-site symmetry $U(g)$ for $g \in G$ are in the same gapped phase with symmetry if they are related by a FDQC U_c , i.e., $|\psi'\rangle = U_c|\psi\rangle$, and additionally each gate $u_{k,i}$ in U_c satisfies $[u_{k,i}, U(g)] = 0$.*

Note that it is important to enforce that each gate in the FDQC commutes with the symmetry, and it is not enough to only require the whole circuit to be symmetric. In the Hamiltonian language, adding symmetry amounts to enforcing that the interpolating Hamiltonian respects the symmetry along the entire path.

In the absence of symmetry breaking, we can broadly split the gapped phases into three classes: symmetry-protected topological order, intrinsic topological order, and symmetry-enriched topological order. We now will give a brief introduction to each of the three classes in turn.

2.2 Symmetry-protected topological order

The simplest of the three classes is symmetry-protected topological order. States with SPT order are defined as states which are in the trivial phase without symmetries, but a non-trivial phase with symmetries [60]. That is, they can be prepared from a product state with a FDQC, but not by one with symmetric gates. For this reason, they can be loosely thought of as the most trivial of all non-trivial orders. In fact, the ‘T’ in SPT is sometime taken to stand for ‘trivial’.

SPT phases are said to be trivial in the bulk since, in the absence of a boundary, there is a unique gapped ground state and no bulk topological excitations. This follows straightforwardly from the fact that they can be prepared by acting with a FDQC on an initial product state. The non-trivial properties of SPT order manifest most evidently on the boundary. In general, when a boundary is introduced into a system with an on-site symmetry, it becomes necessary to decorate that symmetry with some additional action localised near the boundary in order to leave the state invariant. The essence of SPT order comes from the fact that, while the bulk symmetry action can be written as a tensor product on-site linear representations, the boundary action cannot be [84]. As a consequence of this “boundary anomaly”, one finds that an SPT ordered Hamiltonian with boundary cannot have a unique gapped ground state, and must instead either spontaneously break the symmetry, become gapless, or possess boundary topological order. The differences between eigenstates lying within the bulk energy gap are exponentially localised near the boundary, so an SPT ordered system is said to carry non-trivial edge modes.

In the next sections, we will show how to precisely characterize and classify the boundary anomalies of SPT phases in terms of group cohomology, and then provide simple examples in 1D and 2D.

2.2.1 Group cohomology and the Else-Nayak procedure

Symmetry-protected topological phases can be partially classified using the language of group cohomology [60]. In this language, one deals with cohomology classes $[\omega]$ which are elements of the k -th cohomology groups $H^k(G, U(1))$. Given a symmetry group G , bosonic SPT phases in d dimensions can be labelled by the elements of $H^{d+1}(G, U(1))$. In 4D and higher (or 3D if anti-unitary symmetries are considered [85]), there are also SPT phases that are beyond the cohomology classification [86], and we will discuss the physical reason later.

In Ref. [84], the authors showed how to understand the cohomology class associated to a ground state in terms of the anomalous boundary symmetry, and they described an explicit procedure that can be used to extract it. This procedure, which we call the Else-Nayak procedure, gives important physical intuition about SPT phases, and is a practical tool that we will use throughout the thesis.

To begin, we introduce a boundary to our system. This can be done by choosing some subregion M of the system and removing all Hamiltonian terms that are not completely contained in M , resulting in a truncated system with boundary ∂M . In general, this will result in new eigenstates appearing below the bulk gap which are the edge excitations. The bulk symmetry representation $U_M(g) = \otimes_{i \in M} u_i(g)$ can

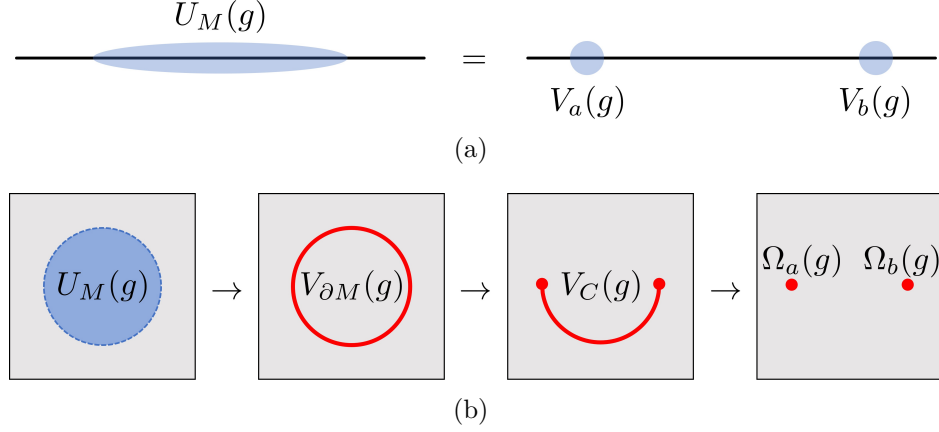


Figure 2.3: (a) The Else-Nayak procedure in a 1D system. (b) The Else-Nayak procedure in a 2D system.

be projected onto the low energy subspace to obtain an effective edge representation of the symmetry $V_{\partial M}(g)$ which acts only along the boundary. While $U_M(g)$ is a product of single-site linear representations, $V_{\partial M}(g)$ is not in general. We call $V_{\partial M}(g)$ a *domain wall operator*. To continue, we will explain the procedure in 1D and 2D, and the extension to higher dimensions will become evident.

For a 1D system, M corresponds to a line segment, and ∂M is the two endpoints of this segment, which we label as a and b . Then, assuming that M is large compared to the correlation length of the system, we can write $V_{\partial M}(g) = V_a(g) \otimes V_b(g)$ where $V_a(g)$ ($V_b(g)$) acts only in a region near a (b), see Fig. 2.3(a). Since $V_{\partial M}(g)$ acts the same as $U_M(g)$, it must be a linear representation. But $V_a(g)$ only needs to be a representation up to a phase, *i.e.* a projective representation. Indeed, if we have $V_a(g)V_a(h) = \omega(g, h)V_a(gh)$ for some phase factors $\omega(g, h)$, then $V_{\partial M}(g)$ is still a representation as long as $V_b(g)$ carries the opposite phase factors.

From the associativity of $V_a(g)$, it is straightforward to show that $\omega(g, h)$ satisfies the following *cocycle condition*,

$$\omega(g, h)\omega(gh, k) = \omega(h, k)\omega(g, hk). \quad (2.4)$$

Functions that take two elements of a group and return a phase factor satisfying this equation are called *2-cocycles*. We are free to re-phase $V_a(g) \mapsto \beta(g)V_a(g)$ (as long as $V_b(g)$ is given the opposite phase), which means our cocycle is only defined up to the relation,

$$\omega(g, h) \sim \beta(g)\beta(h)\beta^{-1}(gh)\omega(g, h). \quad (2.5)$$

The equivalence classes of 2-cocycles modulo the *coboundary* transformation of Eq. 2.5 are called *2-cohomology classes* and, under point-wise multiplication, they form a finite abelian group called the second cohomology group, denoted $H^2(G, U(1))$. Given a cocycle ω , we denote the cohomology class it belongs to by $[\omega] \in H^2(G, U(1))$.

In this case, we see that the cohomology group classifies inequivalent projective representations, corresponding to the different ways the symmetry can act on the

boundary of the region M . Since the different classes form a discrete group, one can imagine that it is impossible to smoothly interpolate between two classes, meaning that two systems with different cohomology classes must be in different SPT phases. This argument can be formalized by proving that a smooth change in a state can only result in modifying the cocycle by a coboundary transformation, and therefore cannot change the cohomology class [87].

The key physical property of 1D SPT phases, the existence of robust zero-energy edge states, can be understood from these results. Namely, if the low-energy subspace corresponding to boundary excitations has to transform as a non-trivial projective representation, it must have a degeneracy greater than one, since a 1D system cannot transform projectively. In general, we can say that the size of the edge mode in an SPT phase labelled by a group G and cohomology class $[\omega]$ is equal to the minimum dimension of an irreducible representation of G belonging to the class $[\omega]$. In Section 2.5.2, we will define a certain class of SPT phases where this dimension can be easily calculated.

Having understood that the second cohomology group classifies 1D SPT phases, let's see how the third cohomology group can classify 2D SPT phases. In this case, M is a finite patch of the 2D system, so ∂M is a 1D line and $V_{\partial M}(g)$ acts as some 1D operator, see Fig. 2.3(b). In general, the domain wall operator $V_{\partial M}(g)$ is not a tensor product of local operators. Now, we restrict this operator to a line segment C corresponding to half of ∂M , which is the step analogous to restricting to $V_a(g)$ in 1D. We define $V_C(g)$ to be the truncation of $V_{\partial M}(g)$ to C . This truncation can easily be done if, *e.g.* $V_M(g)$ has a representation as a quantum circuit, in which case we simply remove all gates not completely contained in C . The truncation is in general only defined up to some unitary operators acting on the endpoints of C . Thus, $V_C(g)$ only needs to form a representation up to such operators, *i.e.*,

$$V_C(g)V_C(h) = \Omega(g, h)V_C(gh), \quad (2.6)$$

where $\Omega(g, h) = \Omega_a(g, h) \otimes \Omega_b(g, h)$, and $\Omega_{a/b}$ are operators localised near the two endpoints of C , see Fig. 2.3(b).

Now, using the associativity of $V_C(g)$, we can derive the following constraint on Ω .

$$\Omega(g, h)\Omega(gh, k) = V_C(g)\Omega(h, k)V_C^{-1}(g)\Omega(g, hk), \quad (2.7)$$

which is the non-abelian equivalent of Eq. 2.4. As in the 1D case, $\Omega_a(g)$ only needs to satisfy Eq. 2.7 up to a phase factor ω ,

$$\Omega_a(g, h)\Omega_a(gh, k) = \omega(g, h, k)V_C(g)\Omega_a(h, k)V_C^{-1}(g)\Omega_a(g, hk). \quad (2.8)$$

By reducing various products of $\Omega_a(g, h)$ in different ways, one can again derive a cocycle constraint for ω (see Ref. [84] for details),

$$\omega(gh, k, l)\omega(g, h, kl) = \omega(g, h, k)\omega(g, hk, l)\omega(h, k, l). \quad (2.9)$$

Functions satisfying this equation are called *3-cocycles*. Finally, since Ω_a is only defined up to phase factors, we again find that the 3-cocycles are defined only up to the following relation,

$$\omega(g, h, k) \sim \beta(g, h)\beta(gh, k)\beta^{-1}(h, k)\beta^{-1}(g, hk)\omega(g, h, k). \quad (2.10)$$

As before, the 3-cocycles modulo this relation are called 3-cohomology classes, and belong to the third cohomology group $H^3(G, U(1))$. In Ref. [84], the authors give an argument that the 3-cohomology class cannot change under smooth deformations of a state, so that the different classes again index the different SPT phases in 2D. In this case, the non-trivial 3-cocycle captures the fact that $V_{\partial M}(g)$ is not a product of on-site operators. The physical manifestation of such a non-local boundary symmetry is that the boundary cannot have a uniquely gapped ground state, and must instead be gapless or spontaneously break the symmetry and therefore be degenerate [74].

We can now imagine how to proceed to higher dimensions. Starting with the on-site symmetry, one restricts to a finite region to extract the equivalent symmetry action on the boundary. One then further restricts that equivalent action to a region with boundary, and so on, until the boundaries become points, at which point the accumulated phase factor can be extracted. In d dimensions, this phase factor will be a $d + 1$ -cocycle, belonging to some equivalence class in the cohomology group $H^{d+1}(G, U(1))$. An essential part of this procedure is that one needs a way to truncate the boundary symmetry actions. This is easy if, for example, the boundary symmetry can be represented by a quantum circuit. If this is not possible, one cannot finish the procedure to extract a cocycle, and this gives a possible physical intuition for the SPT phases which are beyond the cohomological classification. Indeed, in Ref. [86], the authors constructed a beyond-cohomology SPT model in 4D, and they showed that the boundary symmetry action cannot be represented as a quantum circuit.

2.2.2 Example of SPT order in 1D

Having understood the cohomological classification of SPT order, let us consider some explicit examples. To start, we will look at the simplest example of SPT order, the 1D cluster state [88]. To emphasize the SPT nature of the state, we define it on a periodic chain of N qubits via a FDQC as follows:

$$|\mathcal{C}\rangle = \left(\prod_{i=1}^N CZ_{i,i+1} \right) |+\cdots+\rangle, \quad (2.11)$$

where the qubits are all initialized in the state $|+\rangle = \frac{1}{\sqrt{2}}(|0\rangle + |1\rangle)$, and CZ is a two-body unitary gate defined by $CZ_{ij} = |0\rangle\langle 0|_i \otimes \mathbb{1}_j + |1\rangle\langle 1|_i \otimes Z_j = \text{diag}(1, 1, 1, -1)$, and Z is the Pauli- Z operator (similarly, X and Y will represent the other Pauli operators throughout this thesis). To obtain a Hamiltonian for which the cluster state is the unique ground state, we can start with the paramagnetic Hamiltonian $H = -\sum_{i=1}^N X_i$, for which $|+\cdots+\rangle$ is the unique ground state, and then conjugate this Hamiltonian by the circuit $\prod_{i=1}^N CZ_{i,i+1}$ to obtain,

$$H_C = -\sum_{i=1}^N Z_{i-1} X_i Z_{i+1}, \quad (2.12)$$

where we used the relation $CZ_{ij} X_i CZ_{ij} = X_i Z_j$. We see that the cluster state satisfies the relations $Z_{i-1} X_i Z_{i+1} |\mathcal{C}\rangle = |\mathcal{C}\rangle$ for all i . Furthermore, the cluster state

is the unique state that satisfies these relations, so it is a *stabilizer state*, which is a state that can be uniquely specified as the +1 eigenstate of a set of Pauli operators [89]. In this language, the operators $S_i := Z_{i-1}X_iZ_{i+1}$ are called *stabilizers*.

When N is even, it is easy to see that this Hamiltonian commutes with a $\mathbb{Z}_2 \times \mathbb{Z}_2$ symmetry group generated by $X_{\text{odd}} = \prod_{i=1}^{N/2} X_{2i-1}$ and $X_{\text{even}} = \prod_{i=1}^{N/2} X_{2i}$. Since $|\mathcal{C}\rangle$ is the unique ground state, it must also be symmetric, which can be confirmed directly using the circuit representation. If we label elements of $\mathbb{Z}_2 \times \mathbb{Z}_2$ by bit pairs (g_1, g_2) for $g_i = 0, 1$, we can write the symmetry representation as $U(g_1, g_2) = X_{\text{even}}^{g_1} X_{\text{odd}}^{g_2}$. While the FDQC as a whole commutes with these symmetries, the individual CZ gates do not, which is a consequence of the non-trivial SPT order that we now demonstrate by using the Else-Nayak procedure to extract the 2-cocycle.

Let M be a finite section of the 1D chain, corresponding to sites $1, \dots, L$ for an even number $L < N$. The truncated Hamiltonian acting on the system with boundary is then,

$$H_{\mathcal{C},M} = - \sum_{i=2}^{L-1} Z_{i-1}X_iZ_{i+1}. \quad (2.13)$$

Because we have removed the stabilizers associated to the sites $i = 1$ and $i = L$, the ground space of $H_{\mathcal{C},M}$ is four-fold degenerate. To determine the action of the symmetry in this degenerate ground state subspace, we use the method described in Refs. [90, 91]. We first characterize this ground space by an effective algebra of Pauli operators $\bar{X}_1, \bar{Z}_1, \bar{X}_L, \bar{Z}_L$ which commute with the bulk Hamiltonian terms and therefore preserve the ground space. If we define the truncated circuit $U_{CZ,M} = \prod_{i=1}^{L-1} CZ_{i,i+1}$, we can observe that the bulk Hamiltonian terms can be written as $Z_{i-1}X_iZ_{i+1} = U_{CZ,M}X_iU_{CZ,M}^\dagger$ for $i = 2, \dots, L-1$, such that the following are suitable choices of boundary Pauli operators,

$$\begin{aligned} \bar{X}_1 &= U_{CZ,M}X_1U_{CZ,M}^\dagger = X_1Z_2, & \bar{Z}_1 &= U_{CZ,M}Z_1U_{CZ,M}^\dagger = Z_1, \\ \bar{X}_L &= U_{CZ,M}X_LU_{CZ,M}^\dagger = Z_{L-1}X_L, & \bar{Z}_L &= U_{CZ,M}Z_LU_{CZ,M}^\dagger = Z_L. \end{aligned} \quad (2.14)$$

Using these, we can determine how the symmetry acts on this degenerate boundary space. Defining $U_M(g_1, g_2) = \prod_{i=1}^{L/2} X_{2i}^{g_1} X_{2i-1}^{g_2}$, we find that the left ($i = 1$) edge transforms as,

$$U_M(g_1, g_2)\bar{X}_1U_M(g_1, g_2) = (-1)^{g_1}\bar{X}_1, \quad U_M(g_1, g_2)\bar{Z}_1U_M(g_1, g_2) = (-1)^{g_2}\bar{Z}_1. \quad (2.15)$$

This shows that $U_M(g_1, g_2) \sim \bar{Z}^{g_1}\bar{X}^{g_2}$ when acting on the left edge, so we write $V_a(g_1, g_2) = \bar{Z}^{g_1}\bar{X}^{g_2}$. Similarly, for the right edge, we can find $V_b(g_1, g_2) = \bar{X}^{g_1}\bar{Z}^{g_2}$. Then, we can focus on the left edge to obtain the 2-cocycle characterizing the projective representation,

$$\begin{aligned} \omega(g_1, g_2; h_1, h_2) &= V_a(g_1, g_2)V_a(h_1, h_2)V_a^{-1}(g_1 \oplus h_1, g_2 \oplus h_2) \\ &= (-1)^{g_2h_1}, \end{aligned} \quad (2.16)$$

where \oplus denotes mod-2 addition. This cocycle belongs to a non-trivial cohomology class, meaning that it cannot be expressed in the form $\omega(g_1, g_2; h_1, h_2) =$

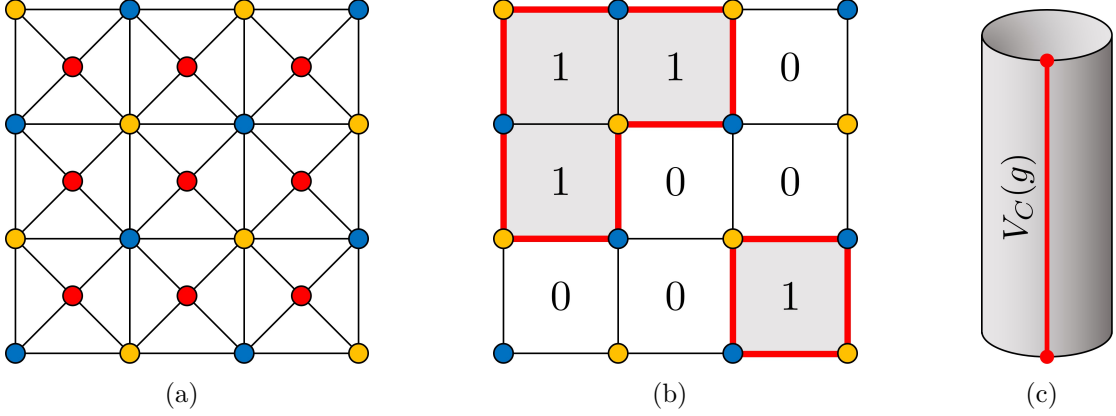


Figure 2.4: (a) The Union-Jack lattice. Red qubits live on the faces of the square lattice, while blue and yellow qubits alternate on the vertices. (b) The decorated domain wall structure of $|UJ\rangle$. Displayed is one element of the superposition over the states of the face qubits, with CZ unitaries applied on the domain walls, marked in red. (c) A cylinder with a g -flux inserted. Treated as a quasi-1D system in the vertical direction, this system carries a 1D SPT order characterized by the slant product $\chi_g(h, k)$.

$\beta(g_1, g_2)\beta(h_1, h_2)\beta(g_1 \oplus h_1, g_2 \oplus h_2)$. One can check this by calculating the commutation relations,

$$\begin{aligned} \frac{\omega(g_1, g_2; h_1, h_2)}{\omega(h_1, h_2; g_1, g_2)} &= V_a(g_1, g_2)V_a(h_1, h_2)V_a^{-1}(g_1, g_2)V_a^{-1}(h_1, h_2) \\ &= (-1)^{g_2 h_1 \oplus g_1 h_2}. \end{aligned} \quad (2.17)$$

which would be trivial if ω belonged to the trivial class. Therefore, we see that the 1D cluster state has non-trivial SPT order, as evidence by the anti-commutation of the boundary symmetry generators. Moreover, we see that there is no symmetric boundary Hamiltonian term we could add in terms of the operators \bar{X}_1, \bar{Z}_1 (since such a term must commute with both \bar{X} and \bar{Z} , and must therefore be proportional to the identity matrix). Therefore, the boundary degeneracy cannot be lifted without breaking the bulk symmetry.

2.2.3 Example of SPT order in 2D

We move on to an example of SPT order in 2D, which will be characterized by a non-trivial 3-cocycle. The state can be defined on any triangulation of 2D space, but we choose the Union-Jack lattice [22], which can be viewed as a square lattice with one qubit on each vertex and one on each face, as pictured in Fig. 2.4(a). This lattice contains a number of triangles $\langle ijk \rangle$ consisting of one face qubit and a neighbouring pair of vertices. The Union-Jack state can then be defined in a similar manner as the cluster state [22], namely,

$$|UJ\rangle = \left(\prod_{\langle ijk \rangle} CCZ_{ijk} \right) |+\cdots+\rangle, \quad (2.18)$$

where $CCZ_{ijk} = |0\rangle\langle 0|_i \otimes \mathbb{1}_{jk} + |1\rangle\langle 1|_i \otimes CZ_{jk} = \text{diag}(1, 1, 1, 1, 1, 1, 1, -1)$. The same model was defined on the triangular lattice in Ref. [91], and it is closely related to an earlier model proposed in Ref. [90]. We can again obtain a Hamiltonian for this model by conjugating the paramagnetic Hamiltonian $H = -\sum_i X_i$ by the circuit of CCZ gates to obtain,

$$H_{UJ} = -\sum_i X_i \prod_{\langle ijk \rangle} CZ_{jk}, \quad (2.19)$$

where the product is over all triangles containing qubit i , and we used the relation $CCZ_{ijk} X_i CCZ_{ijk}^\dagger = X_i CZ_{jk}$.

The Union-Jack lattice is three colourable, meaning we can assign one of three colours to each qubit such that no neighbouring qubits share a colour, as depicted in Fig. 2.4(a). We can then define the global symmetry operators X_R, X_B, X_Y which apply to X to all red, blue, and yellow vertices, respectively. One can readily verify that these commute with H_{UJ} and form a $G = \mathbb{Z}_2 \times \mathbb{Z}_2 \times \mathbb{Z}_2$ symmetry group, so we use the notation $U(g_1, g_2, g_3) = X_R^{g_1} X_B^{g_2} X_Y^{g_3}$ for $(g_1, g_2, g_3) \in G$.

To diagnose the SPT order of this model, we consider truncating to a lattice M whose boundary consists of alternating blue and yellow vertices, as in Fig. 2.4(a). By removing all Hamiltonian terms not completely contained in M , we obtain a truncated Hamiltonian with degeneracy 2^L where L is the length of the boundary. We can define the truncated circuit $U_{CCZ,M}$ that consists of CCZ gates applied to all triangles in M . Then, we again characterize this degenerate space in terms of effective Pauli operators \bar{X}_i, \bar{Z}_i for $i = 1, \dots, L$ defined as follows,

$$\begin{aligned} \bar{X}_i &= U_{CCZ,M} X_i U_{CCZ,M}^\dagger = X_i \prod_{\langle ijk \rangle} CZ_{jk}, \\ \bar{Z}_i &= U_{CCZ,M} Z_i U_{CCZ,M}^\dagger = Z_i, \end{aligned} \quad (2.20)$$

where the product over $\langle ijk \rangle$ in the definition of \bar{X}_i now runs over the triangles of the truncated lattice. Now we can calculate the effect of the bulk symmetry $U_M(g, h, k)$ on these boundary operators as follows,

$$\begin{aligned} U_M(g_1, g_2, g_3) \bar{X}_i U_M(g_1, g_2, g_3)^\dagger &= \bar{Z}_{i-1}^{g_1} \bar{X}_i \bar{Z}_{i+1}^{g_1}, \\ U_M(g_1, g_2, g_3) \bar{Z}_{2i} U_M(g_1, g_2, g_3)^\dagger &= (-1)^{g_2} \bar{Z}_{2i}, \\ U_M(g_1, g_2, g_3) \bar{Z}_{2i-1} U_M(g_1, g_2, g_3)^\dagger &= (-1)^{g_3} \bar{Z}_{2i-1}, \end{aligned} \quad (2.21)$$

where we taken even (odd) i to correspond to blue (yellow) boundary qubits. From these relations, we can conclude that $U_M(g_1, g_2, g_3)$ acts on the boundary as,

$$V_{\partial M}(g_1, g_2, g_3) = \left(\prod_{i=1}^L \bar{C}\bar{Z}_{i,i+1} \right)^{g_1} \left(\prod_{i=1}^L \bar{X}_{2i} \right)^{g_2} \left(\prod_{i=1}^L \bar{X}_{2i-1} \right)^{g_3}. \quad (2.22)$$

This boundary action is not a product of single-site operators, but rather it has the form of a quantum circuit due to the CZ gates, indicating the non-trivial SPT order of the model. We can now calculate the 3-cocycle which characterizes this non-local action. Let us introduce the condensed notation $\vec{g} = (g_1, g_2, g_3)$,

and consider a finite segment $C = [a, b]$ of ∂M where we take a and b to both be odd (*i.e.* yellow qubits) without loss of generality. Then, letting $V_C(\vec{g})$ be the truncation of $V_{\partial M}(\vec{g})$, where we remove all operators not completely contained in C , we can calculate Eq. 2.6,

$$\begin{aligned} V_C(\vec{g})V_C(\vec{h}) &= \Omega(\vec{g}, \vec{h})V_C(\vec{g})V_C(\vec{h}), \\ \text{where } \Omega(\vec{g}, \vec{h}) &= (Z_a Z_b)^{g_2 h_1}. \end{aligned} \quad (2.23)$$

Writing $\Omega_a(\vec{g}, \vec{h}) = (Z_a)^{g_2 h_1}$, Eq. 2.8 becomes,

$$\begin{aligned} \Omega_a(\vec{g}, \vec{h})\Omega_a(\vec{g} \oplus \vec{h}, \vec{k}) &= \omega(\vec{g}, \vec{h}, \vec{k})V_C(\vec{g})\Omega_a(\vec{h}, \vec{k})V_C^{-1}(\vec{g})\Omega_a(\vec{g}, \vec{h} \oplus \vec{k}), \\ \text{where } \omega(\vec{g}, \vec{h}, \vec{k}) &= (-1)^{g_3 h_2 k_1}. \end{aligned} \quad (2.24)$$

To confirm that this 3-cocycle corresponds to a non-trivial cohomology class, we use the slant product [92, 93], which can be defined for any group element g as,

$$\chi_g(h, k) := \frac{\omega(g, h, k)\omega(h, k, g)}{\omega(h, g, k)}. \quad (2.25)$$

When ω is a 3-cocycle, χ_g will be a 2-cocycle, belonging to some cohomology class in $H^2(G, U(1))$. The physical meaning of the slant product is the following. If we put our 2D system on a cylinder, we can thread a symmetry flux corresponding to a group element g through the cylinder. In practice, this can be done by inserting the truncated domain-wall operator $V_C(g)$ along the length of the cylinder, as shown in Fig. 2.4(c). The resulting system can carry a fractional symmetry charge on the boundaries. That is, if we consider our system to be a quasi-1D system along the length of the cylinder, it can belong to a non-trivial 1D SPT phase. The 2-cocycle which describes this 1D SPT phase is precisely the slant product χ_g .

If a 3-cocycle ω has a slant product χ_g that belongs to a non-trivial class in $H^2(G, U(1))$, then ω itself must belong to a non-trivial class in $H^3(G, U(1))$. In the present example, we can compute,

$$\chi_{(1,0,0)}(\vec{h}, \vec{k}) = (-1)^{h_3 k_2} \quad (2.26)$$

Since $\chi_{(1,0,0)}(\vec{h}, \vec{k}) \neq \chi_{(1,0,0)}(\vec{k}, \vec{h})$, it must belong to a non-trivial class in $H^2(G, U(1))$, so ω is also in a non-trivial class and therefore $|UJ\rangle$ has non-trivial SPT order.

As another diagnosis of the non-trivial SPT order of $|UJ\rangle$, let us consider what possible boundary Hamiltonian terms we could add in terms of the boundary operators \bar{X}_i, \bar{Z}_i . If we ask that the boundary Hamiltonian $\bar{H}_{\partial M}$ respects the bulk symmetry, we need it to commute with $V_{\partial M}(\vec{g})$ for all \vec{g} . The simplest family of Hamiltonians we can write down which respects the symmetries is,

$$\bar{H}_{\partial M} = -h \sum_i (\bar{X}_i + \bar{Z}_{i-1} \bar{X}_i \bar{Z}_{i+1}) - J \sum_i (\bar{Z}_{2i} \bar{Z}_{2i+2} + \bar{Z}_{2i-1} \bar{Z}_{2i+1}). \quad (2.27)$$

When $h = 0$, this Hamiltonian corresponds to two copies of the Ising model, which spontaneously break the symmetry and have degenerate ground states. When $J = 0$, the Hamiltonian is that of the 1D cluster state in an external field,

tuned to its gapless critical point [94]. Furthermore, for both $h, J \neq 0$, there is an extended gapless phase, which can be considered as being protected by the anomalous boundary symmetry [95]. We see that this simple example of a boundary Hamiltonian does not lead to a unique gapped ground state, and indeed it was shown in Ref. [74] that a system which respects an anomalous symmetry (one with a non-trivial 3-cocycle) cannot have a unique gapped ground state.

A final perspective on the SPT order of $|UJ\rangle$ comes from the decorated domain wall (DDW) perspective [96]. Namely, using the relation $CCZ_{ijk} = |0\rangle\langle 0|_i \otimes \mathbb{1}_{jk} + |1\rangle\langle 1|_i \otimes CZ_{jk}$, we observe that, for every face in the lattice, the effect of the CCZ operators acting on that face is to put CZ operators along the edges of the face if that face is in the state $|1\rangle$, and otherwise it does nothing. These CZ operators acting on the initial $|+\rangle$ states create 1D cluster states (Eq. 2.11). Therefore, $|UJ\rangle$ can be expressed as an equal-weight superposition over all configurations of the face qubits, where the domain walls between face qubits are decorated by 1D cluster states on the vertex qubits, as pictured in Fig. 2.4(b). One can deduce the presence of non-trivial boundary physics from this DDW picture [96].

2.3 Intrinsic topological order

In this section we consider intrinsic topological order, which is usually referred to simply as topological order. Here, we use the word intrinsic to indicate that the topological order does not rely on the presence of a symmetry, as would be the case for SPT order. That is, intrinsic topological phases are those that cannot be mapped to a product state via any FDQC, such that they are characterized by certain patterns of long-range entanglement.

The namesake feature of topological order is a ground state degeneracy that depends on the topology of the manifold that the system lives on [6]. While the ground state will be unique on a topologically trivial manifold such as a sphere, it will become degenerate on a manifold with holes such as a torus. Furthermore, in the case that the ground space is degenerate, the different ground states cannot be distinguished by any local operator, in contrast to, *e.g.*, an Ising model where the degenerate ground states are distinguished by local magnetization. The sensitivity to global topology and the locally indistinguishable ground states are indicators of the long-range nature of the entanglement in topologically ordered systems.

The most important feature of topological phases is the existence of topological excitations with anyonic statistics, or simply *anyons*. In 2D, anyons are point-like excitations which, when exchanged or braided around each other, can give phase factors different from bosonic or fermionic statistics, such as factors of i . These anyons can fuse together to annihilate each other or create new anyon types, and certain topological orders can have non-abelian anyons whose fusion rules depend on their braiding history [6, 7]. In 3D and higher, the topological excitations may no longer be point-like, and can instead be extended 1D objects, for example [97]. These 1D excitations can also be characterized by generalized 3-loop braiding processes [98]. In general, the set of topological excitations along with the information of how they braid and fuse with each other can completely classify the possible topological phases, and mathematical language that captures this algebraic theory of anyons is that of category theory [99].

Topological order has extremely promising applications for the storage and processing of quantum information [6–9]. This is primarily due to the way in which information can be stored non-locally in a topologically ordered system: if we store information in the degenerate ground space of a topological order, the local indistinguishability of the ground states ensures that the information cannot be destroyed by any local errors that appear due to effects such as thermal noise. Over time, these local errors may conspire to form a logical error that affects the encoded information, but this can be actively prevented by using techniques from quantum error correction [6]. One can further perform operations on the encoded information by adiabatically manipulating the topology of the lattice [9]. These operations are topological in the sense that they are insensitive to local details of their implementation, and hence they also enjoy a certain robustness against noise. Unfortunately, in many cases these operations are insufficient for universal computation [100], and they must be supplemented with additional techniques such as magic state distillation, all culminating in the field of fault-tolerant quantum computation [101]. Another approach to universal topological computation uses

non-abelian anyons, where one can encode logical information in the collective state of several spatially separated anyons [7]. This information is again robust to local noise sources, and furthermore their non-abelian nature allows one to perform logical operations by braiding, which is again a topological operation that is insensitive to local details.

2.3.1 Example of topological order in 2D

To demonstrate the basic features of topological order, we will look at the simple example of the 2D toric code [6]. The system lives on a square lattice with periodic boundary conditions (a torus), where qubits live on the edge of the lattice. The toric code is defined by the following Hamiltonian,

$$\begin{aligned}
 H_{TC} &= - \sum_i A_i - \sum_f B_f, \\
 A_i &= \prod_{e \ni i} Z_e, \\
 B_f &= \prod_{e \in f} X_e,
 \end{aligned} \tag{2.28}$$

where $e \ni i$ denotes all edges incident on vertex i , and $e \in f$ denotes all edges around a face f , as depicted in Fig. 2.5(a). The Hamiltonian terms all mutually commute, so the ground space consists of states that are in the +1 eigenspace of each term. On an $L \times L$ torus, there are $2L^2$ qubits, but only $2L^2 - 2$ independent Hamiltonian terms, since we have the relations $\prod_i A_i = \mathbb{1}$ and $\prod_f B_f = \mathbb{1}$. Therefore, the ground space is $2^2 = 4$ -fold degenerate.

We can get an understanding of the long-range entanglement in the ground states by visualising them directly. Observe that the states in the +1 eigenspace of all A_i terms are those with an even number of qubits in the $|1\rangle$ state around each vertex, and the B_f terms transform between different states in this eigenspace. Therefore, the following is a ground state of H_{TC} ,

$$|TC\rangle = \frac{1}{\mathcal{N}} \sum_{\text{loops}} |\text{loop}\rangle, \tag{2.29}$$

where the sum is over all basis states $|\text{loop}\rangle$ which have an even number of edges in the state $|1\rangle$ around each vertex. If we visualize basis states by drawing a line on an edge if the qubit is in the state $|1\rangle$, then the sum in Eq. 2.29 is over all states where the lines form closed loops, see Fig. 2.5(c). Such a state is often called a “loop-soup”. To understand the degeneracy of the ground space on a torus, note that acting with the B_p terms can never create or destroy a single topologically non-trivial loop, *i.e.* a loop which wraps all the way around the torus. The four degenerate ground states are therefore distinguished by whether or not the states $|\text{loop}\rangle$ in Eq. 2.29 are chosen to contain these non-trivial loops. Since there are two non-trivial loops, each of which can be present or not, there are four ground states.

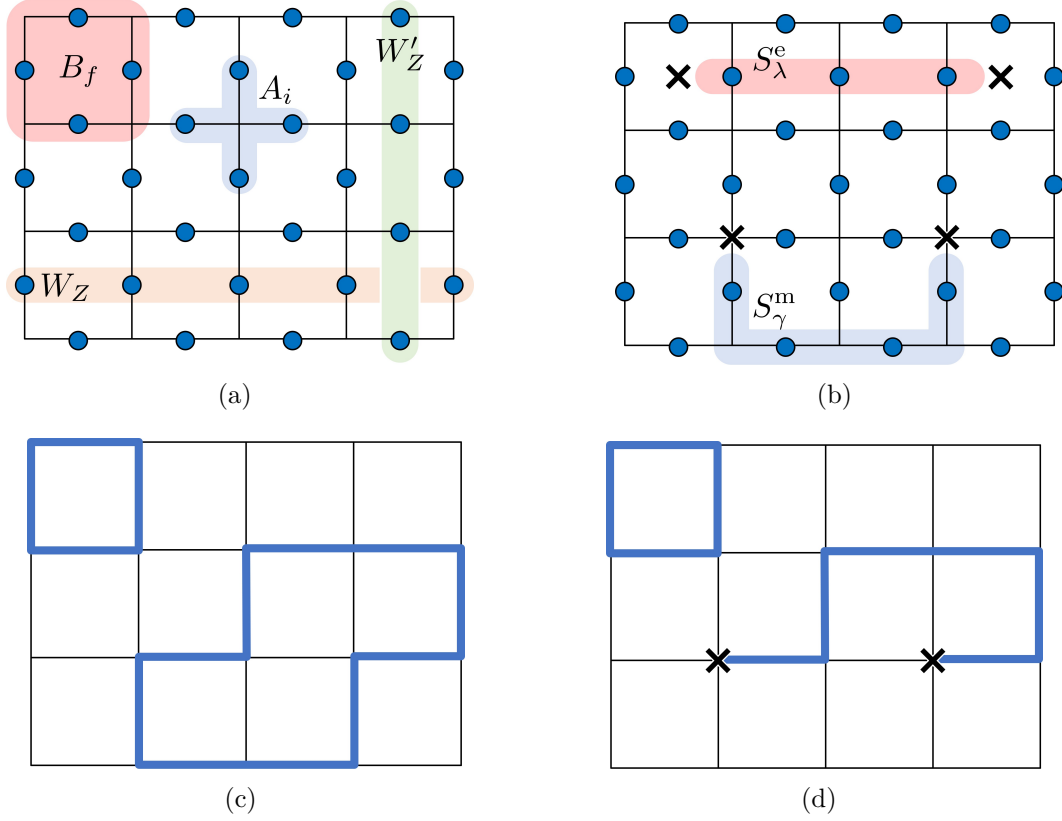


Figure 2.5: The toric code model. In all figures, the lattice has periodic boundary conditions with qubits on the edges being identified. (a) Terms in H_{TC} and Wilson loop operators. (b) String operators that create excitations at their endpoints, with crosses marking the locations of violated Hamiltonian terms. (c) The ground state $|TC\rangle$ is a superposition over all configurations where the edges in state $|1\rangle$, denoted by a thick line, form closed loops. One such configuration is shown. (d) Acting with S_γ^m from (b) on the configuration of (c) flips qubits to create a configuration with an open string, where excitations appear at the endpoints of the string.

These ground states can be distinguished by non-local Wilson operators defined as,

$$W_Z = \prod_{e \in C_1} Z_e, \quad (2.30)$$

$$W'_Z = \prod_{e \in C_2} Z_e, \quad (2.31)$$

where C_1 and C_2 are topologically non-trivial loops, as indicated in Fig. 2.5(a). Then, for example, $\langle W_Z \rangle = -1$ if there is a non-trivial loop in the vertical direction, and $+1$ otherwise. In summary, the ground states of H_{TC} can be visualized as equal-weight superpositions over closed-loop configurations, a loop-soup, and they are distinguished from each other by non-local operators which wrap around the entire system.

The excitations of the model, corresponding to states where a subset of Hamiltonian terms have eigenvalue -1 , are created at the endpoints of string operators,

see Fig. 2.5(b). The operator,

$$S_\lambda^e = \prod_{e \in \lambda} Z_e, \quad (2.32)$$

creates a pair of violations of the B_f terms, called *electric* (e) anyons, at the endpoints of a curve $\lambda \subset E$ on the dual lattice. Likewise, the operator

$$S_\gamma^m = \prod_{e \in \gamma} X_e. \quad (2.33)$$

produces a pair of violations of the A_i terms, called *magnetic* (m) anyons, at the endpoints of a curve $\gamma \subset E$ on the lattice. If one tries to braid an e-anyon around an m-anyon, one will inevitably have to move a Z operator past an X , which results in a sign of -1 . This shows that the e and m anyons have a mutual -1 braiding statistic.

The m-anyons have an intuitive representation in terms of the loop-soup picture. Namely, acting with S_γ^m on any closed-loop state $|\text{loop}\rangle$ results in a state where there are endpoints of open loops at the endpoints of γ . So, while the ground states are superpositions of closed loops, the endpoints of open loops coincide with m-anyons, see Fig. 2.5(d). This picture will be useful for an intuitive construction of enriching the toric code with symmetry in Section 2.4. The e-anyons appear as a sign structure in the superposition over loops (Eq. 2.29). Namely, in the presence of an e-anyon on a face f , a given loop configuration $|\text{loop}\rangle$ gains a relative factor of -1 if an odd number of loops encircle f .

2.3.2 Example of topological order in 3D

Here we will briefly introduce the 3D toric code as a simple example of topological order in 3D [97, 102]. The model lives on a 3D cubic lattice with qubits on the faces $f \in F$. The Hamiltonian is defined as follows,

$$\begin{aligned} H_{3DTC} &= - \sum_e A_e - \sum_c B_c, \\ A_e &= \prod_{f \ni e} Z_f, \\ B_c &= \prod_{f \in c} X_f, \end{aligned} \quad (2.34)$$

where $f \ni e$ denotes the four faces incident on the edge e , and $f \in c$ denotes the six faces around the cell c .

In the same way that the 2D toric code ground states can be viewed as equal-weight superpositions over closed-loop configurations (loop-soup), the ground states of the 3D toric code can be viewed as closed-membrane configurations (membrane-soup). Namely, if we represent states on our lattice by colouring a face if its associated qubit is in the state $|1\rangle$, then the ground state consists of configurations $|\text{mem.}\rangle$ where the coloured faces create closed 2D surfaces, or, membranes,

$$|TC_{3D}\rangle = \frac{1}{\mathcal{N}} \sum_{\text{mem.}} |\text{mem.}\rangle. \quad (2.35)$$

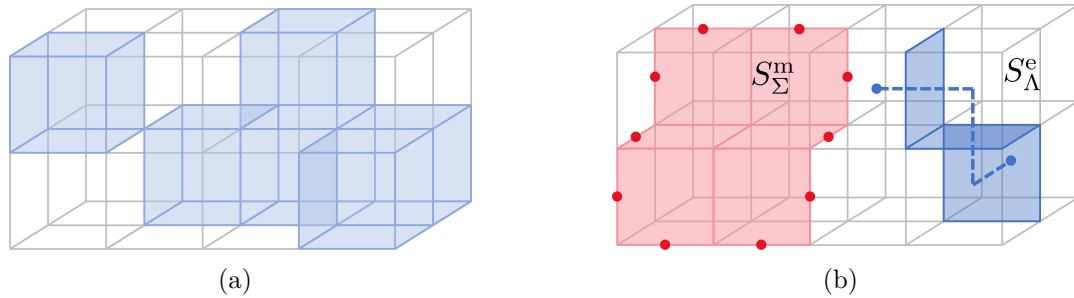


Figure 2.6: The 3D toric code model. (a) The membrane-soup picture of the ground state. One state $|\text{mem.}\rangle$ of the soup is pictured by colouring faces in the state $|1\rangle$. (b) The membrane and string operators that create excitations. The violated Hamiltonian terms are marked by circles.

This structure is depicted in Fig. 2.6(a). On topologically non-trivial manifolds like a 3-torus, there are degenerate ground states that can be obtained by including topologically non-trivial (non-contractible) membranes in the superposition.

The excitations in the model come in two types, see Fig. 2.6(b). Electric excitations corresponding to violations of B_c appear at the endpoints of string operators,

$$S_\Lambda^e = \prod_{f \in \Lambda} Z_f, \quad (2.36)$$

where Λ is a set of faces defined by a curve on the dual lattice. The most important distinction between the 2D and 3D toric codes is that magnetic excitations of the 3D toric code, corresponding to violations of A_e , are extended 1D objects rather than point-like particles. They appear at the boundaries of membrane operators,

$$S_\Sigma^m = \prod_{f \in \Sigma} X_f, \quad (2.37)$$

where Σ is some open membrane of faces. The electric and magnetic excitations have a mutual braiding statistic of -1 upon winding an electric excitation through the loop of a magnetic excitation. The picture of the excitations in terms of the membrane-soup picture is similar to that of the loop-soup: The magnetic excitations appear at the 1D boundaries of open membranes, and an electric excitation at cell c gives the different states $|\text{mem.}\rangle$ in the membrane-soup a -1 sign if an even number of membranes enclose c .

2.3.3 Topological entanglement entropy

One important notion in characterizing topological order is the topological entanglement entropy (TEE), which refers to a constant correction γ to the entanglement area law [103–105],

$$S(\rho_A) = \alpha|\partial A| - \gamma + \dots, \quad (2.38)$$

where the dots indicate terms that go to zero as the size of A is increased. The TEE reflects the presence of long range entanglement in the system, and shows that

there are some global constraints on the structure of ρ_A which are independent of system size. The TEE is an invariant of a topological phase, in that it is insensitive to small deformations of the region A and small changes in the quantum state. In fact, it has been shown that the TEE is equal to the total quantum dimension of topological order which, in the case of abelian topological order, simply counts the number of distinct anyons [72, 104, 105]. Furthermore, by calculating the TEE on a torus for the various degenerate ground states, one can even retrieve the anyon braiding statistics, which can give a nearly complete determination of the topological order [70]. This emphasizes the fact that the ground state entanglement encodes not only ground state properties, but also important information about the excitations.

To extract the TEE for a 2D system, one straightforward method is to calculate the entropy between two halves of a cylinder of radius L . Making fits of entropy vs L , the area law prefactor α will be the slope, and the TEE γ will be the y -intercept. This method has been used successfully in numerical calculations, especially since it is amenable to a quasi-1D approach [106]. However, it is also sensitive to finite-size effects, since the form Eq. 2.38 only holds for large A . It can be more insightful to rather extract the TEE in terms of a linear combination of entropies, in such a way that the area law contributions cancel exactly, leaving only the TEE behind [104, 105]. However, as we will discuss in Chapter 4, all of these prescriptions are vulnerable to “false positives” where the extracted value of the TEE does not match the expected value [107].

For stabilizer models like the toric code, there is a simple recipe to calculate entanglement entropy [103]. Recall that a stabilizer state $|\psi\rangle$ on N qubits can be uniquely described by a set of N stabilizers S_i which are products of Pauli operators (for models like the toric code with degenerate ground states, a unique ground state can be specified by adding non-local Wilson loops into the set of stabilizers). The stabilizers generate an abelian group $G = \langle S_i | i = 1, \dots, N \rangle$. Let us assume that the stabilizers are all independent, *i.e.* there are no non-trivial products of stabilizers that equal the identity. Then we have $|G| = 2^N$. We can express $|\psi\rangle$ in terms of the projector onto the +1 eigenspace of all stabilizers,

$$\rho = |\psi\rangle\langle\psi| = \prod_{i=1}^N \frac{1}{2}(\mathbb{1} + S_i) = \frac{1}{2^N} \sum_{g \in G} g. \quad (2.39)$$

Now consider an arbitrary bipartition of the system into subsystems A and B , and define the subgroup $G_A \subset G$ as the set of elements of G which act non-trivially only within A . Observe that, if we trace over subsystem B , every element of G that is not in G_A has trace 0 (since Pauli operators have trace 0). Then, we have,

$$\rho_A = \text{Tr}_B \rho = \frac{1}{2^{N_A}} \sum_{g \in G_A} g, \quad (2.40)$$

where N_A is the number of qubits in subsystem A . Now, we can calculate the Rényi α -entropy, defined as,

$$S_A^{(\alpha)} \equiv S^{(\alpha)}(\rho_A) = \frac{1}{1-\alpha} \log_2 \text{Tr}(\rho_A^\alpha), \quad (2.41)$$

where the Von Neumann entropy $S_A = -\text{Tr} \rho_A \ln \rho_A$ is recovered in the limit $\alpha \rightarrow 1$. Noting that,

$$\rho_A^\alpha = \frac{|G_A|^{\alpha-1}}{2^{N_A \cdot \alpha}} \sum_{g \in G_A} g, \quad (2.42)$$

and $\text{Tr} \sum_{g \in G_A} g = 2^{N_A}$, we have,

$$S_A^{(\alpha)} = N_A - \log_2 |G_A|. \quad (2.43)$$

This result is independent of α since the spectrum of ρ is flat for stabilizer states.

2.3.4 Gauging as a duality map between phases

Intrinsic topological order is closely related to the idea of gauge theories. In fact, the toric code model can be viewed as a \mathbb{Z}_2 lattice gauge theory. The concept of gauging—mapping a system with a global symmetry to one with a local symmetry—is ubiquitous in physics. In the context of gapped phases of matter, it plays an interesting role as a duality mapping between different types of topological order. The concept will be very important for Chapter 5 of this thesis, so we review it here.

Let us begin with a 2D transverse field Ising model describing qubits on the vertices of a square lattice,

$$H_{TFIM} = -J \sum_{\langle ij \rangle} Z_i Z_j - h \sum_i X_i. \quad (2.44)$$

This system has a \mathbb{Z}_2 global on-site symmetry $U = \otimes_i X_i$. In the limit $h \rightarrow 0$, the symmetry is spontaneously broken and the degenerate ground space of H_{TFIM} is spanned by the states $|00\dots 0\rangle$ and $|11\dots 1\rangle$, while the unique ground state in the limit $J \rightarrow 0$ is $|+\dots +\rangle$. These two regimes are separated by a symmetry-breaking phase transition.

To gauge the \mathbb{Z}_2 global symmetry, we first add new qubit “gauge” degrees of freedom to the links of the lattice. To couple them to the vertex degrees of freedom, we modify the Ising interaction according to the usual minimal coupling procedure,

$$Z_i Z_j \mapsto Z_i Z_{e_{ij}} Z_j, \quad (2.45)$$

where e_{ij} denotes the edge between vertices i and j . The modified Hamiltonian now commutes with a local gauge symmetry given by the operators,

$$G_i = X_i \prod_{\langle ij \rangle} X_{e_{ij}}. \quad (2.46)$$

To add some dynamics to the gauge fields, we can introduce a Hamiltonian term which commutes with the gauge symmetry, and with the existing Hamiltonian terms for simplicity. The smallest such operator can be found to be $\prod_{e \in f} Z_e$, where $e \in f$ denotes all edges around a face f . Altogether, we have the gauge-matter Hamiltonian,

$$H_{g-m} = -J \sum_{\langle ij \rangle} Z_i Z_{e_{ij}} Z_j - h \sum_i X_i - K \sum_f \prod_{e \in f} Z_e, \quad (2.47)$$

where $e \in f$ denotes all edges around a face f . This describes a Hamiltonian formulation of a \mathbb{Z}_2 lattice gauge theory [108].

Since G_i all commute with the Hamiltonian, we can enforce a gauge constraint of $G_i = 1$ which specifies the “physical” Hilbert space. Having enforced this constraint, we can replace $X_i \mapsto \prod_{\langle ij \rangle} X_{e_{ij}}$ in H_{g-m} , after which it is observed that H_{g-m} commutes with Z_i for all vertices i . We can again focus on the sector where $Z_i = 1$ for all i , which essentially freezes the vertex (matter) degrees of freedom to the $|0\rangle$ state. This results in a Hamiltonian acting only on the gauge degrees of freedom,

$$H_g = -J \sum_e Z_e - h \sum_i \prod_{e \ni i} X_e - K \sum_f \prod_{e \in f} Z_e, \quad (2.48)$$

where $e \ni i$ denotes all edges incident on vertex i . If we set $J = 0$, we recognize that H_g is identical to the toric code Hamiltonian (Eq. 2.28), up to a lattice shift that interchanges vertices and faces. On the other hand, if we turn on J , this introduces a confinement of fluxes (m-anyons) in the toric code via a tension that penalizes long loops, which drives it into a topologically trivial phase [109]. That is to say, the gauging procedure maps the paramagnetic phase of the transverse field Ising model to the topological toric code, while it maps the symmetry-breaking phase to a topologically trivial phase where m-anyons are confined.

The overall procedure, which takes a Hamiltonian defined on the matter (vertex) degrees of freedom to a new Hamiltonian on the gauge (edge) degrees of freedom can be summarized by the following mapping on the \mathbb{Z}_2 -symmetric Pauli algebra,

$$X_i \mapsto \prod_{e \ni i} X_e \quad Z_i Z_j \mapsto \prod_{e \in \gamma_{ij}} Z_e, \quad (2.49)$$

where γ_{ij} is a path connecting i and j . This path is only defined up to multiplication by the local operators $\prod_{e \in f} Z_e$, which are equal to 1 in the ground space of the gauged Hamiltonian. It is straightforward to generalize this procedure to arbitrary lattices and (finite) symmetry groups [93]. For example, performing this procedure for the 3D paramagnet on a cubic lattice results in the 3D toric code.

Another perspective on the gauging map can be given in terms of a duality transformation on states [91]. On a basis state $\otimes_i |a_i\rangle$ of the vertex qubits, the gauging map Γ produces a state of the edge qubits defined as,

$$\Gamma \left(\otimes_i |a_i\rangle \right) = \otimes_{\langle ij \rangle} |b_{e_{ij}}\rangle, \quad b_{e_{ij}} = a_i \oplus a_j, \quad (2.50)$$

where \oplus denotes mod-2 addition. In this way, the edge qubits are in the state $|1\rangle$ on the domain walls of the vertex qubits, and $|0\rangle$ otherwise, as depicted below for a single face of the lattice,

$$\begin{array}{ccc}
 \begin{array}{cc} a_i & a_j \\ \bullet & \bullet \\ | & | \\ \bullet & \bullet \\ a_l & a_k \end{array} & \mapsto & \begin{array}{ccc} & a_i \oplus a_j & \\ \bullet & & \bullet \\ | & & | \\ \bullet & & \bullet \\ a_k \oplus a_l & & a_j \oplus a_k \end{array}
 \end{array} \quad (2.51)$$

We can see from this that the states after gauging will all have local (gauge) symmetry $\prod_{e \in f} Z_e$ for all faces f , since this evaluates to $(-1)^{a_i+a_j+a_k+a_l+a_i+a_i} = 1$. The mapping is surjective on this gauge-symmetric subspace, while it is injective if we restrict the domain of Γ to the \mathbb{Z}_2 -symmetric subspace of states. Furthermore, the mapping preserves the inner product of states. That is, Γ defines an isometric duality map between the space of states with a global symmetry to the space of states with a gauge symmetry [91]. The corresponding action of Γ on \mathbb{Z}_2 -symmetric operators is exactly the one defined in Eq. 2.49.

The viewpoint of gauging as a duality map is very helpful. Since it is an isometry, it preserves the spectrum of Hamiltonians, such that a smooth, gapped path connecting two states before gauging, will translate to a smooth path after gauging. The mapping also preserves locality. Therefore, if two systems are in different gapped phases after gauging (subject to the gauge symmetry constraint), meaning there is no gapped path connecting them, they will also be in different phases after gauging (subject to the global symmetry constraint). This gives a method to identify the non-trivial order of a state via gauging [41, 90, 91].

Let us showcase this method with a few examples. As a simple case, applying the gauging map to the 1D transverse field Ising model simply interchanges the Ising and magnetic field terms, such that the gauging map is nothing more than the famous Kramers-Wannier duality that maps the paramagnetic phase to the ferromagnetic phase ². On the other hand, the 1D cluster state (Eq. 2.12) turns out to map onto itself after gauging (up to a local basis change) [110]. Since the ferromagnet is in a different phase than the cluster state (as they have different symmetry), we can confirm that the paramagnet is also in a different phase than the cluster state, *i.e.* the cluster state has non-trivial SPT order.

In higher dimensions, the situation becomes more interesting. Consider the Union-Jack SPT model (Eq. 2.19), and let us first focus on the diagonal \mathbb{Z}_2 subgroup of the symmetry group, corresponding to flipping every spin on the lattice. Gauging this subgroup results in the double-semion model defined on the square-octagon lattice (the dual of the Union-Jack lattice) [90]. This model is similar to the toric code, except it has anyons with semionic statistics, defined by a phase of i upon self-exchange. These semionic statistics show that the double-semion model is in a different topological phase from the toric code, so the 2D paramagnet, which we saw gauges to the toric code, is in a different symmetry-protected phase from the Union-Jack model. Going further, we can consider gauging the whole \mathbb{Z}_2^3 symmetry group of the Union-Jack model, which turns out to lead to a non-abelian topological order called the D_8 quantum double model, as we will discuss in the next section. There, we will also gauge other subgroups of \mathbb{Z}_2^3 to obtain models with symmetry-enriched topological order.

²In this case, the gauge symmetry turns out to be the same global symmetry, since there is only one “loop” in a 1D ring: the whole ring.

2.4 Symmetry-enriched topological order

When intrinsic topological order is additionally equipped with a symmetry, the phase classification can become refined. Two systems which are in the same intrinsic topological phase without symmetry may be in different phases when a symmetry is imposed, and we call these phases symmetry-enriched topological (SET) phases. These phases are characterized by a non-trivial action of the symmetry on the anyons of the topological order. An important concept in SET phases is that of symmetry defects. These are defined to appear at the endpoints of the open domain wall operators $V_C(g)$, as defined in Section 2.2.1 and Fig. 2.3(b), and they can be viewed as confined quasi-particles (confined because the domain wall operator connecting the defects has an energy cost). The effect of braiding a g -defect around an anyon has the same effect as applying the symmetry g to the anyon. The resulting theory containing both anyons and symmetry defects is described by the mathematical framework of G -enriched category theory, which gives a classification of SET order [111].

To understand the ways in which a global symmetry $U(g)$ can act non-trivially on the anyons, consider a topological state containing two separated anyonic excitations labelled by a and b , as shown in Fig. 2.7. Suppose that these two anyons can annihilate each other when brought together. First, it is possible that the action of the symmetry can send each of a and b to a different species of anyon. This permutation is not arbitrary, as the permuted anyons species must still be able to annihilate each other. Assuming for simplicity that permutation does not occur, the other possibility is known as symmetry fractionalization. For a gapped system with local interactions, it will be possible to reduce the effect of $U(g)$ to a tensor product of operators $V_a(g)$ and $V_b(g)$ localised near the anyons, as shown in Fig. 2.7. This is possible because, far from the anyons, the state looks locally like the ground state and is therefore symmetric. Now the situation is the same as what occurs in a 1D SPT order: the global symmetry can be reduced as $U(g) \sim V_a(g) \otimes V_b(g)$. Therefore, $V_a(g)$ can be a projective representation that carries non-trivial phase factors, so long as $V_b(g)$ carries the inverse factors.

In the context of SET phases, there turns out to be an additional restriction on the possible projective representations: the phase factors that appear in the representation $V_a(g)$ must be obtainable by braiding some anyon around a [111]. Because the non-trivial $U(1)$ phase factors can be labelled by anyons (which are necessarily abelian to get phase factors from braiding), the relevant cohomology group which classifies symmetry fractionalization is not $H^2(G, U(1))$, as it was for 1D SPT phases, but rather $H^2(G, \mathcal{A})$, where \mathcal{A} is the set of abelian anyons [111]. Because of this, certain symmetry groups G which do not support non-trivial 1D SPT phases can nonetheless lead to non-trivial symmetry fractionalization, with $G = \mathbb{Z}_2$ being a simple example [112]. When anyon permutation is present, the cohomology group has to be additionally supplemented with an action of the group G on the set \mathcal{A} [113].

Enriching a topological phase with symmetry can augment its usefulness for quantum computation. By treating the symmetry defects as part of the anyon content of the theory, one can expand the set of logical operators implementable by

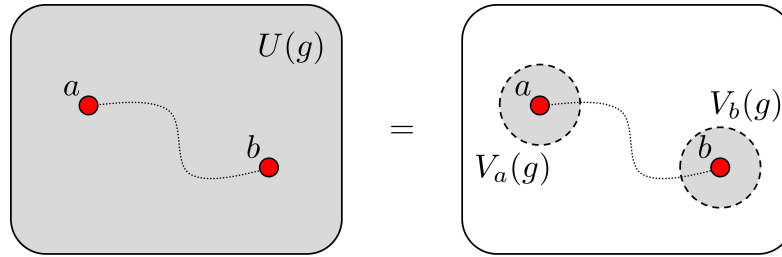


Figure 2.7: Illustration of the phenomenon of symmetry fractionalization. a and b denote two anyonic excitations. The action of the global symmetry $U(g)$ reduces to a product of actions $V_{a/b}(g)$ acting near the anyons.

braiding [9, 39, 43, 47]. An early example of this was shown in Ref. [39], where the author considered an anyon permuting symmetry of the toric code given by a lattice shift, and showed that the corresponding lattice defect acted like a non-abelian anyon. It has also been shown that models of SET order appearing on the boundary of certain 3D SPT ordered systems can be used as quantum memories that are self-correcting in the presence of certain bulk symmetries [42].

2.4.1 Examples of SET order in 2D

In this section we construct exactly solvable models of SET order in 2D. To do this, we will make use of the gauging procedure outlined in the previous section. Starting with the Union-Jack model introduced in Section 2.2.3, we will gauge different subgroups of the symmetry group to obtain different types of SET order. For this section, it is convenient to view the Union-Jack lattice as having qubits on the vertices and faces of a square lattice, where the red qubits in Fig. 2.4(a) live on the faces and the blue/yellow qubits alternate on the vertices.

Example with symmetry fractionalization

To obtain an SET model exhibiting symmetry fractionalization, we will gauge the \mathbb{Z}_2 subgroup of the symmetry of H_{UJ} corresponding to flipping red (face) qubits X_R . This will leave us with a residual $\mathbb{Z}_2 \times \mathbb{Z}_2$ subgroup which will fractionalize on the magnetic excitations. We note that this same model was derived in Ref. [114] from a different perspective.

First, let us derive the ground state wave function after gauging. Recall that $|UJ\rangle$ in Eq. 2.18 is defined by acting with a unitary circuit on a product state, so we can get the gauged ground state by applying the gauged version of the circuit to the gauged initial state. Note that the red qubits form a square lattice, so we can directly apply the gauging map to obtain a new lattice with the red qubits on the edges between the blue and yellow qubits. The gauged initial state consists of blue and yellow qubits still in the $|+\rangle$ state, with the red edge qubits now forming a toric code $|TC\rangle$. The gauged version of the unitary circuit consists of CCZ gates acting on every triplet of neighbouring blue and yellow qubits plus the red qubit between them. Applying this circuit to the gauged initial state, we get the SET ground state.

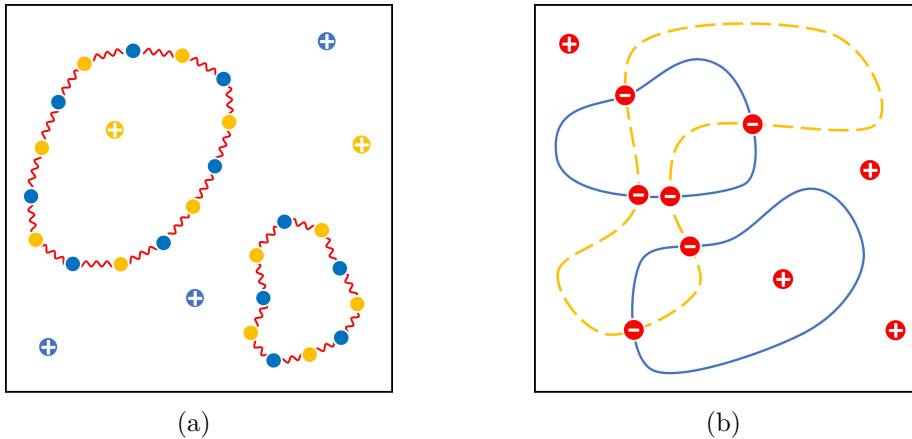


Figure 2.8: (a) The ground state of H_{SET} exhibiting symmetry fractionalization is an equal-weight superposition of loop configurations formed by the red qubits. The blue and yellow qubits are in $|+\rangle$ states away from the loops, and in 1D cluster states along the loops, indicated by the wavy red lines. (b) The ground state of H'_{SET} exhibiting an anyon permuting symmetry. The blue and yellow qubits independently form closed loops indicated by the solid and dashed lines, respectively. The red qubits are in the $|-\rangle$ state at the intersections of the blue and yellow loops, and otherwise in the $|+\rangle$ state.

To understand the structure of the resulting state, recall that the ground states of the toric code can be described as a loop soup, which is an equal weight superpositions of configurations in which the edge qubits in state $|1\rangle$ form closed loops, as depicted in Fig. 2.5(c). When we act on such a configuration with the gauged CCZ unitaries, we get a CZ between all pairs of vertices along loops, and no effect away from the loops³. The CZ 's along loops act on the initial $|+\rangle$ states of the blue and yellow vertices, creating segments of 1D cluster states. So the SET ground state can be viewed as an equal weight superposition of closed loop configurations where the loops are decorated with 1D cluster states, see Fig. 2.8(a). One can also see this structure by starting with the DDW structure of the Union-Jack model (Fig. 2.4(b)) and applying the gauging map, which directly maps states of the face qubits to closed-loop configurations on the domain walls.

In this picture, the residual $\mathbb{Z}_2 \times \mathbb{Z}_2$ symmetry is inherited from the same symmetry carried by the 1D cluster states. The decorated structure also allows us to understand the nature of the fractionalization. Recall that, in the toric code, magnetic excitations appear at the endpoints of open loops, see Fig. 2.5(d). Now, these endpoints coincide with the edges of 1D cluster states, which fractionalize the symmetry as discussed in Section 2.2.2. Therefore, the magnetic anyons carry the same fractionalization as the boundary of the 1D cluster state.

To see the fractionalization more explicitly, we will construct the gauged Hamiltonian and derive the action of the symmetry on the string operators. Following

³This follows from the fact that $CCZ|ijk\rangle = |i\rangle \otimes CZ^i|jk\rangle$.

the recipe outlined in Section 2.3.4 the gauged Hamiltonian is,

$$H_{SET} = - \sum_i A_i - \sum_f B_f - \sum_i C_i \frac{1 + A_i}{2}, \quad (2.52)$$

where,

$$\begin{aligned} A_i &= \prod_{e \ni i} Z_e, \\ B_f &= \prod_{e \in f} X_e C Z_{\partial e}, \\ C_i &= X_i \prod_{\langle ij \rangle} C Z_{j, e_{ij}}. \end{aligned} \quad (2.53)$$

Therein, $CZ_{\partial e}$ denotes the action of CZ on the two vertex qubits at the endpoints of edge e . The terms B_f (C_i) are the direct output of applying the gauging map the Hamiltonian terms in H_{UJ} associated to the red (blue/yellow) qubits, while A_i is the zero-flux term. We have additionally projected C_i onto the zero-flux subspace to ensure that H_{SET} commutes with the residual $\mathbb{Z}_2 \times \mathbb{Z}_2$ symmetry.

Now, consider the following string operator,

$$S_\Gamma = \prod_{e \in \Gamma} X_e C Z_{\partial e}, \quad (2.54)$$

where Γ is some open string of edges with terminal vertices i_1 and i_2 , which we assume to both be yellow without loss of generality. If we apply this operator to a ground state $|SET\rangle$, we get an excited state with e-anyons at i_1 and i_2 , corresponding to $A_i = -1$. Because $A_i = -1$ at these points, the projection $\left(\frac{1+A_i}{2}\right)$ annihilates the Hamiltonian terms involving $C_{i_{1/2}}$, so we can dress the endpoints of S_Γ with Z 's without changing the energy of the resulting excitations. This means we have four different string operators,

$$S_\Gamma(a, b) = S_\Gamma Z_{i_1}^a Z_{i_2}^b, \quad a, b = 0, 1, \quad (2.55)$$

such that each anyon carries a two-fold degeneracy. Furthermore, the $\mathbb{Z}_2 \times \mathbb{Z}_2$ symmetry acts projectively on each anyon. To see this, consider the subspace of degenerate states $|a, b\rangle := S_\Gamma(a, b)|SET\rangle$. We compute,

$$\begin{aligned} X_B |a, b\rangle &= |a \oplus 1, b \oplus 1\rangle, \\ X_Y |a, b\rangle &= (-1)^a (-1)^b |a, b\rangle. \end{aligned} \quad (2.56)$$

Therefore, $X_B \sim X \otimes X$ and $X_Y \sim Z \otimes Z$ in this subspace. Since X and Z anticommute, each anyon carries a projective representation of $\mathbb{Z}_2 \times \mathbb{Z}_2$, which demonstrates the fractionalization.

Example with anyon permuting symmetry

A very simple model of SET order with an anyon permuting symmetry can be obtained by taking two copies of the toric code and considering a \mathbb{Z}_2 symmetry that swaps the two layers, thereby exchanging the anyons between layers [115].

Even simpler, we can consider a single toric code, where lattice translation by a factor of $(\frac{1}{2}, \frac{1}{2})$, followed by global application of the unitary $H = \frac{X+Z}{\sqrt{2}}$ exchanges the electric and magnetic anyons [39]. Here, we will continue the above story and obtain a model with anyon permutation by gauging the $\mathbb{Z}_2 \times \mathbb{Z}_2$ symmetry of $H_{U,J}$ corresponding to X_B and X_Y . This will leave us with a \mathbb{Z}_2 symmetry which will permute the anyons in the resulting topological order. The resulting model is more complex, but it allows us to make a useful final statement about the commutation of gauging maps. It also has an advantage that the symmetries remain products of on-site X operators, so we don't need two-body SWAP operations or lattice translations.

We again begin by the finding gauged ground state. Notice that the blue and yellow vertices each form 45° -rotated square lattices whose edges intersect on the faces of the original lattice. Gauging each X_B and X_Y separately then results in a system with three qubits on each face of a square lattice: the original red qubit, and gauge qubits corresponding to the original blue and yellow sublattices. In the gauged initial state, the red qubits remain in the $|+\rangle$ state while the blue and yellow qubits independently form two toric codes on the rotated square lattices. The gauged unitary circuit applies CCZ to the three qubits on each face. The resulting gauged ground state can be viewed as two independent loop soups formed by the blue and yellow qubits. In any given configuration of loops, the red qubits are in the $|+\rangle$ state, except where the blue and yellow loops intersect, where the CCZ gate has the effect of applying a Z to the red qubit, flipping $|+\rangle$ to $|-\rangle$. This structure is pictured in Fig. 2.8(b).

How can we see the anyon permutation from this structure? Observe that, for every closed loop configuration, there is an even number of intersections between yellow and blue loops, so there will be an even number of red qubits in the $|-\rangle$ state, so X_R is a symmetry. Now suppose we act with X_R on a configuration containing an open yellow string with m -anyons at its endpoints. The symmetry action will give a loop configuration a factor of -1 if an odd number of blue loops encircle the endpoints of the yellow string, since that would mean there are an odd number of blue-yellow intersections and therefore an odd number of red qubits in the $|-\rangle$ state. As discussed in Section 2.3.1, this sign structure means there are blue e-anyons located at the endpoints of the yellow string. In other words, the symmetry X_R attaches a blue e-anyon to the yellow m -anyon. We can repeat the same analysis exchanging blue and yellow. Overall, if we let $m_{b/y}$ ($e_{b/y}$) denote the blue/yellow m -anyons (e-anyons), then the residual \mathbb{Z}_2 symmetry permutes anyons by attaching to every m -particle an e-particle of opposite colour, *i.e.* $m_{b/y} \leftrightarrow m_{b/y}e_{y/b}$.

Let us again derive the gauged Hamiltonian to capture the anyon permutation more explicitly. For convenience, we denote the subsets of all blue/yellow vertices by $V_{B/Y}$, and label the three qubits per face as $f_{r,b,y}$ with f_r labelling the ungauged red qubit. The gauged Hamiltonian reads,

$$H'_{SET} = - \sum_{v \in V_B} \left(A_v^y - B_v^b \frac{1 + A_v^y}{2} \right) - \sum_{v \in V_Y} \left(A_v^b - B_v^y \frac{1 + A_v^b}{2} \right) - \sum_{f \in F} C'_f, \quad (2.57)$$

where, if we let $F_v \subset F$ denote the four faces surrounding vertex v ,

$$\begin{aligned} A_v^{b/y} &= \prod_{f \in F_v} Z_{f_{b/y}}, \\ B_v^{b/y} &= \prod_{f \in F_v} X_{f_{b/y}} C Z_{f_r, f_{y/b}}, \\ C'_f &= X_{f_r} C Z_{f_b, f_y}. \end{aligned} \tag{2.58}$$

We have again projected certain terms onto the zero-flux subspace to ensure the Hamiltonian is symmetric.

To see the permutation, consider the following string operator,

$$Q_\Lambda = \prod_{f \in \Lambda} X_{f_y} C Z_{f_r, f_b}, \tag{2.59}$$

where Λ is a connected path of faces. If we apply this operator to a ground state $|\psi_g\rangle$ of H'_{SET} , we get an excited state with a pair of yellow m-anyons (corresponding to violations of A_v^y) located at the two blue vertices at the endpoints of the path. Now, if we apply the symmetry to this state, we find,

$$X_F Q_\Lambda |\psi_g\rangle = Q_\Lambda \left(\prod_{f \in \Lambda} Z_{f_b} \right) X_F |\psi_g\rangle = Q_\Lambda \prod_{f \in \Lambda} Z_{f_b} |\psi_g\rangle. \tag{2.60}$$

The string operator $\prod_{f \in \Lambda} Z_{f_b}$ acting on $|\psi_g\rangle$ create violations of B_v^b at the same yellow vertices, which correspond to blue e-anyons. Continuing in this way, we can reproduce all of the permutation actions claimed above in terms of the transformation properties of string operators.

Gauging all symmetries

For completeness, we can also consider gauging the whole $\mathbb{Z}_2 \times \mathbb{Z}_2 \times \mathbb{Z}_2$ symmetry group of H_{UJ} . While it is cumbersome to perform this calculation explicitly, we can use some general results to determine the resulting gauge theory. First, suppose we start from H_{SET} and gauge the fractionalized $\mathbb{Z}_2 \times \mathbb{Z}_2$ symmetry. In general, when a symmetry acts on the anyons as a higher-dimensional (projective) representation, gauging it results in non-abelian anyons [111]. The fractionalization pattern observed for H_{SET} corresponds precisely to that shown in Fig. 2(c) of Ref. [116], and it is shown therein that gauging the symmetry results in a model with D_8 topological order [105], where D_8 is the non-abelian symmetry group of a square.

Now, let us rather start from H'_{SET} and gauge the anyon-permuting symmetry. In Ref. [115], it was shown in general that gauging an anyon-permuting symmetry leads to non-abelian anyons. The symmetry considered in Ref. [115] was a layer swap of a bilayer toric code, which appears superficially different from the permutation observed for H'_{SET} . However, upon a relabelling of anyons that preserves the braiding and fusion rules, the two symmetries turn out to be the same. Therefore, the resulting gauge theory should be the same as the one found in Ref. [115], namely D_8 topological order.

As the two above cases show, we expect a non-abelian D_8 topological order after gauging all symmetries of H_{UJ} , regardless of the order in which the symmetries are gauged. This reinforces the intuition that the gauging operations for a pair of commuting symmetry subgroups should commute, which will be helpful for part of Chapter 5.

2.5 Tensor networks

By this point, we have seen in several examples the importance that ground state wavefunctions play in the classification and characterization of gapped phases of matter. Due to the exponentially growing Hilbert space of quantum many-body systems, it can quickly become impossible to write down these wavefunctions without the use of efficient representations. One such representation is the stabilizer formalism which we have used several times already. Another representation works directly in the physical corner of Hilbert space which, as discussed in Section 2.1, consists of states satisfying an entanglement area law. Such states are naturally captured using the language of tensor networks. This language plays an essential role in Chapters 3 and 4 of this thesis, so here we outline some of its basic concepts and techniques.

Let us first describe a brief history of tensor networks. While traces of tensor network methods date back to transfer matrix methods in statistical mechanics [117], a true appreciation of their power started with the Affleck-Kennedy-Lieb-Tasaki (AKLT) state [118]. This state was constructed to help understand the physics of the spin-1 antiferromagnetic Heisenberg chain⁴. The authors of Ref. [118] showed that, by slightly modifying the model, one can obtain a Hamiltonian whose ground state can be written down exactly in a very simple form that involves distributing a fixed amount of entanglement between neighbouring sites. Soon after this, the concept of finitely-correlated states was introduced to generalize the AKLT construction to a large class of Hamiltonians with provable spectral gaps [119]. These states eventually extended to the so-called matrix product states (MPS), which are simple 1D tensor networks. Concurrently, the density-matrix-renormalization-group (DMRG) algorithm for finding ground states of 1D Hamiltonians was introduced by White [120], and later it was understood that this algorithm was essentially just a variational method over the class of MPS [121]. Eventually, analogues of these constructions in 2D dimensions and higher, called projected-entangled pair states (PEPS), were introduced and found to also have impressive analytical and numerical power [122–124]. By now, tensor networks are a well-established tool for both numerical and analytical studies of quantum many-body systems and beyond [3, 125].

2.5.1 Tensor network fundamentals

Tensor networks are used to provide an efficient description of quantum states and operators, while also providing a useful graphical calculus. The description breaks the quantum wavefunction, which has exponentially many parameters, into a contraction of smaller tensors. Here, a tensor is simply a multidimensional array with a certain number of legs that index its entries. For example, a general wavefunction of N systems with dimension d can be described by a tensor c with

⁴The AKLT state also happens to be a prototypical example of SPT order, and lies in the same SPT phase as the 1D cluster state.

N indices as,

$$|\psi\rangle = \sum_{i_1, \dots, i_N=1}^d c_{i_1, i_2, \dots, i_N} |i_1, i_2, \dots, i_N\rangle. \quad (2.61)$$

Tensor networks describe the various ways in which the tensor c can be decomposed into a network of smaller tensors in order to reduce the number of free parameters.

Matrix product states

An important example of a tensor network decomposition is the matrix product state (MPS):

$$c_{i_1, i_2, \dots, i_N} = \sum_{\alpha_1, \dots, \alpha_N=1}^D A_{\alpha_1, \alpha_2}^{i_1} A_{\alpha_2, \alpha_3}^{i_2} \dots A_{\alpha_N, \alpha_1}^{i_N}. \quad (2.62)$$

Here, the defining object is the three-index tensor A with components $A_{\alpha, \beta}^i$. The index i is called the *physical index*, as it runs over the dimension of the on-site Hilbert space. The indices α, β which are summed over are called the *virtual indices*, and D is called the *bond dimension* of the tensor network. If we express the tensors in terms of matrices $A^i = \sum_{\alpha, \beta=1}^D A_{\alpha, \beta}^i |\alpha\rangle\langle\beta|$ acting in the *virtual space* of the MPS, then we can write,

$$c_{i_1, i_2, \dots, i_N} = \text{Tr} A^{i_1} A^{i_2} \dots A^{i_N}, \quad (2.63)$$

which makes the name ‘‘matrix product state’’ more evident. Here, and throughout most of this thesis, we consider translationally invariant MPS, where the tensor A does not depend on the site, and periodic boundary conditions, which lead to the trace in the above equation.

One can formally derive an MPS representation of an arbitrary state by a series of successive Schmidt decompositions, where the Schmidt rank across a given cut becomes the bond dimension across that cut [4]. For generic states, this will lead to an MPS whose bond dimension D grows exponentially with the system size N . However, states in the physical corner of Hilbert space, *i.e.* states satisfying an area law (even allowing logarithmic violations), can be well-approximated by MPS whose bond dimension grows at most polynomially in N [126, 127]. Intuitively, this is because, for states satisfying an area law, the Schmidt coefficients decay quickly enough to allow one to throw away all but polynomially many of them without significantly changing the quantum state. This truncation of the Schmidt coefficients then gives a corresponding reduction in the bond dimension. This result means that we can represent such states using only NdD^2 coefficients (where the factor of N appears in absence of translational invariance), which is an immense improvement over the 2^N coefficients required to write down c_{i_1, i_2, \dots, i_N} in general.

We can depict an MPS graphically in the following way. First, we depict the tensor A as a three-legged object,

$$A_{\alpha, \beta}^i = \alpha \text{---} \underset{A}{\bullet} \text{---} \beta \text{---} \overset{i}{\text{---}}. \quad (2.64)$$

Then, we use the rule that connecting the legs of two tensors corresponds to summing over the corresponding indices, such that we can represent the wavefunction of Eq. 2.62 as,

$$c_{i_1, i_2, \dots, i_N} = \left(\begin{array}{c} i_1 \\ | \\ \bullet \\ | \\ A \end{array} \text{---} \begin{array}{c} i_2 \\ | \\ \bullet \\ | \\ A \end{array} \text{---} \dots \text{---} \begin{array}{c} i_N \\ | \\ \bullet \\ | \\ A \end{array} \right), \quad (2.65)$$

where the bent legs at the two ends of the chain connect to each other, representing periodic boundary conditions. We will often draw the above diagram without labelling indices to represent the state $|\psi\rangle$. This graphical description is very useful, as it allows us to make compact descriptions of complex quantum states and make various calculations on them without having to deal with many indices explicitly.

Transfer matrix and correlations in MPS

We now define the transfer matrix, which is a central object used in MPS calculations. As an equation, the transfer matrix is defined as

$$T = \sum_{i=1}^d A^i \otimes \bar{A}^i, \quad (2.66)$$

where the bar denotes complex conjugation. As a diagram, we have,

$$T = \begin{array}{c} \bar{A} \\ \text{---} \\ \bullet \\ | \\ \bullet \\ \text{---} \\ A \end{array}. \quad (2.67)$$

The transfer matrix encodes many important properties of the MPS (in fact it specifies it completely up to a change of basis). For example, let us calculate the two-point correlation function,

$$\langle \psi | O_i O_j | \psi \rangle = \dots \begin{array}{c} \bar{A} \quad \bar{A} \quad \bar{A} \quad \dots \quad \bar{A} \quad \bar{A} \quad \bar{A} \\ \text{---} \\ \bullet \quad \bullet \quad \bullet \quad \dots \quad \bullet \quad \bullet \quad \bullet \\ | \quad | \quad | \quad \dots \quad | \quad | \quad | \\ \bullet \quad \bullet \quad \bullet \quad \dots \quad \bullet \quad \bullet \quad \bullet \\ | \quad | \quad | \quad \dots \quad | \quad | \quad | \\ A \quad A \quad A \quad \dots \quad A \quad A \quad A \end{array} \dots \quad (2.68)$$

Letting $\ell = |i - j| - 1$, we can write the above diagram as the following equation,

$$\langle \psi | O_i O_j | \psi \rangle = \text{Tr} \left(T(O) T^\ell T(O) T^{N-\ell-2} \right), \quad (2.69)$$

where we have defined,

$$T(O) = \begin{array}{c} \bar{A} \\ \text{---} \\ \bullet \\ | \\ \bullet \\ | \\ O \\ | \\ \bullet \\ \text{---} \\ A \end{array}. \quad (2.70)$$

We now employ an eigenvalue decomposition of T . While it is not Hermitian in general, we assume that it is nonetheless diagonalizable,

$$T = \sum_{i=1}^{D^2} \lambda_i |R_i\rangle\langle L_i|. \quad (2.71)$$

This decomposition has the property $\langle L_i | R_j \rangle = \delta_{i,j}$ and $|\lambda_1| \geq |\lambda_2| \geq \dots \geq |\lambda_{D^2}|$. Let us normalize T such that $\lambda_1 = 1$, and denote the corresponding eigenvectors as $|R_1\rangle \equiv |R\rangle$ and $|L_1\rangle \equiv |L\rangle$. For now, we assume that $|\lambda_i| < 1$ for all $i > 1$, such that T has a unique largest eigenvalue in magnitude. In this case, for large N , we can write $T^N = |R\rangle\langle L|$ with corrections that go to zero exponentially in N . Then, if $N \gg \ell \gg 1$, we can write,

$$\begin{aligned} \langle \psi | O_i O_j | \psi \rangle &= \text{Tr} \left(T(O) \left(|R\rangle\langle L| + \sum_{i=2}^{D^2} \lambda_i^\ell |R_i\rangle\langle L_i| \right) T(O) |R\rangle\langle L| \right) \\ &= \langle L | T(O) | R \rangle \langle L | T(O) | R \rangle + \sum_{i=2}^{D^2} \lambda_i^\ell \langle L | T(O) | R_i \rangle \langle L_i | T(O) | R \rangle. \end{aligned} \quad (2.72)$$

Now observe that $\langle L | T(O) | R \rangle = \langle \psi | O_i | \psi \rangle$, so we can identify the first term of the above as $\langle \psi | O_i | \psi \rangle \langle \psi | O_j | \psi \rangle$. If we subtract this part, we obtain the connected correlator,

$$\langle \psi | O_i O_j | \psi \rangle - \langle \psi | O_i | \psi \rangle \langle \psi | O_j | \psi \rangle = \mathcal{O}(\lambda_2^\ell) = \mathcal{O}(e^{-\ell/\xi}), \quad (2.73)$$

which decays to zero exponentially with correlation length $\xi = -1/\ln|\lambda_2|$. On the other hand, if $|\lambda_2| = 1$, we can generally find some local operator O which has long-range correlations, *i.e.* correlations that do not decay with distance. This is the case for a ferromagnetic ground state $|000\dots\rangle + |111\dots\rangle$ for which $\langle \psi | Z_i Z_j | \psi \rangle - \langle \psi | Z_i | \psi \rangle \langle \psi | Z_j | \psi \rangle = 1$ for all $i \neq j$.

Therefore, we see that, if the largest eigenvalue of T is unique in magnitude, the MPS has a finite correlation length $\xi = -1/\ln|\lambda_2|$ for all local operators, while a degenerate largest eigenvalue leads to long-range correlations. If the former case is satisfied, the MPS is said to be *normal* [3]. This is the generic case in the absence of symmetry breaking [128], and all MPS found in this thesis from this point on are assumed to be normal.

Sometimes, we will find it convenient to re-orient the legs of the transfer matrix and its fixed-points. Namely, we can equivalently write the transfer matrix as a quantum channel,

$$\mathcal{T}(\rho) = \sum_i A^i(\rho) A^{i\dagger}, \quad (2.74)$$

and its dual channel,

$$\mathcal{T}^\dagger(\rho) = \sum_i A^{i\dagger}(\rho) A^i. \quad (2.75)$$

The eigenvectors $|R\rangle$ and $\langle L|$ correspond to fixed-points σ_R and σ_L of \mathcal{T} and \mathcal{T}^\dagger , respectively.

Bulk-boundary correspondence and entanglement in MPS

Another key property of MPS is the bulk-boundary correspondence [129], which states that, if we divide the system into two connected subsystems A and B , the reduced density matrix $\rho_A = \text{Tr}_B |\psi\rangle\langle\psi|$ has the same spectrum as another matrix σ that can be viewed as living on the virtual indices on the boundary between A and B . To derive this correspondence, let us first write an MPS with open boundary conditions,

$$\begin{aligned}
 |\psi\rangle &= \sum_{i_1, \dots, i_N} A_L^{i_1} A^{i_2} \dots A^{i_{N-1}} A_R^{i_N} |i_1, i_2, \dots, i_N\rangle \\
 &= \begin{array}{c} \text{---} \\ | \\ \bullet \\ \text{---} \\ A_L \end{array} \text{---} \begin{array}{c} | \\ \bullet \\ \text{---} \\ A \end{array} \text{---} \begin{array}{c} | \\ \bullet \\ \text{---} \\ A \end{array} \dots \begin{array}{c} | \\ \bullet \\ \text{---} \\ A \end{array} \text{---} \begin{array}{c} | \\ \bullet \\ \text{---} \\ A \end{array} \text{---} \begin{array}{c} | \\ \bullet \\ \text{---} \\ A_R \end{array} , \quad (2.76)
 \end{aligned}$$

for some vectors (dual vectors) A_L^i (A_R^i). With this, we can depict ρ_A in the following way,

$$\rho_A = \begin{array}{c} \text{---} \\ | \\ \bullet \\ \text{---} \\ \dots \\ | \\ \bullet \\ \text{---} \\ A \end{array} \text{---} \begin{array}{c} | \\ \bullet \\ \text{---} \\ \dots \\ | \\ \bullet \\ \text{---} \\ A \end{array} \text{---} \begin{array}{c} | \\ \bullet \\ \text{---} \\ \dots \\ | \\ \bullet \\ \text{---} \\ A \end{array} \text{---} \begin{array}{c} | \\ \bullet \\ \text{---} \\ \dots \\ | \\ \bullet \\ \text{---} \\ B \end{array} \text{---} \begin{array}{c} | \\ \bullet \\ \text{---} \\ \dots \\ | \\ \bullet \\ \text{---} \\ B \end{array} \text{---} \begin{array}{c} | \\ \bullet \\ \text{---} \\ \dots \\ | \\ \bullet \\ \text{---} \\ B \end{array} , \quad (2.77)$$

where we have omitted the tensor labels to avoid confusion with the label for subsystem A . The part of the tensor network contained in subsystem B is nothing more than the transfer matrix applied many times to a boundary vector, which converges to the right fixed-point σ_R for $|B| \gg \xi$ giving,

$$\rho_A = \begin{array}{c} \text{---} \\ | \\ \bullet \\ \text{---} \\ \dots \\ | \\ \bullet \\ \text{---} \\ A \end{array} \text{---} \begin{array}{c} | \\ \bullet \\ \text{---} \\ \dots \\ | \\ \bullet \\ \text{---} \\ A \end{array} \text{---} \begin{array}{c} | \\ \bullet \\ \text{---} \\ \dots \\ | \\ \bullet \\ \text{---} \\ A \end{array} \text{---} \begin{array}{c} | \\ \bullet \\ \text{---} \\ \dots \\ | \\ \bullet \\ \text{---} \\ \sigma_R \end{array} . \quad (2.78)$$

For the part contained in subsystem A , we first express it in terms of a linear map \mathcal{L} from the virtual indices at the boundary of A and B to the physical indices,

$$\mathcal{L} = \begin{array}{c} \text{---} \\ | \\ \bullet \\ \text{---} \\ \dots \\ | \\ \bullet \\ \text{---} \\ A_L \end{array} \text{---} \begin{array}{c} | \\ \bullet \\ \text{---} \\ \dots \\ | \\ \bullet \\ \text{---} \\ A \end{array} \text{---} \begin{array}{c} | \\ \bullet \\ \text{---} \\ \dots \\ | \\ \bullet \\ \text{---} \\ A \end{array} \text{---} . \quad (2.79)$$

We can now apply the polar decomposition to \mathcal{L} to write $\mathcal{L} = \mathcal{V}\mathcal{P}$ where $\mathcal{P} = \sqrt{\mathcal{L}^\dagger \mathcal{L}}$ is a positive matrix and \mathcal{V} is an isometry from the virtual to physical legs, $\mathcal{V}^\dagger \mathcal{V} = \mathbb{1}_{D \times D}$. We can write $\mathcal{L}^\dagger \mathcal{L}$ graphically as,

$$\mathcal{L}^\dagger \mathcal{L} = \begin{array}{c} \text{---} \\ | \\ \bullet \\ \text{---} \\ \dots \\ | \\ \bullet \\ \text{---} \\ \sigma_L \end{array} \text{---} \begin{array}{c} | \\ \bullet \\ \text{---} \\ \dots \\ | \\ \bullet \\ \text{---} \\ \sigma_L \end{array} = \left[\begin{array}{c} \text{---} \\ | \\ \bullet \\ \text{---} \\ \dots \\ | \\ \bullet \\ \text{---} \\ \sigma_L \end{array} \right] , \quad (2.80)$$

which can be replaced with the left fixed-point σ_L as shown. Therefore, we can write $\mathcal{P} = \sqrt{\sigma_L}$. Putting everything together, we have

$$\rho_A = \begin{array}{c} \begin{array}{|c|} \hline \mathcal{V} \\ \hline \end{array} \\ \text{---} \\ \begin{array}{|c|} \hline \mathcal{V}^\dagger \\ \hline \end{array} \end{array} \begin{array}{c} \sqrt{\sigma_L} \\ \sqrt{\sigma_L^T} \end{array} \sigma_R = \mathcal{V}^\dagger \sqrt{\sigma_L^T} \sigma_R \sqrt{\sigma_L^T} \mathcal{V}. \quad (2.81)$$

Since \mathcal{V} is an isometry, this shows that ρ_A has the same spectrum as the operator $\sigma = \sqrt{\sigma_L^T} \sigma_R \sqrt{\sigma_L^T}$ that lives in the virtual space, up to padding with zeros. The most immediate conclusion of this is that the entanglement entropy $S(\rho_A)$ is equivalent to $S(\sigma)$, which is upper bounded by $\log D$, giving a clear derivation of the area law for MPS. More generally, the entanglement spectrum, defined as the spectrum of ρ_A , is contained in the spectrum of σ . The entanglement spectrum plays an important role in the understanding of gapped phases of matter [73, 130], and tensor networks provide an efficient way to obtain it and represent the information contained within it.

Example of an MPS: the 1D cluster state

To see an example of an MPS, let us derive the MPS representation of the 1D cluster state from its circuit representation (Eq. 2.11). Observe that the initial state $|+\cdots+\rangle$ is an equal weight superposition over all states in the $|0/1\rangle$ basis. The action of the circuit of CZ gates on these basis states is to give a factor of -1 for every pair of neighbouring 1's. That is, the cluster state can be equivalently written as,

$$|\mathcal{C}\rangle = \frac{1}{2^{N/2}} \sum_{i_1, \dots, i_N=0,1} (-1)^{\# \text{ of neighbouring 1's}} |i_1, \dots, i_N\rangle. \quad (2.82)$$

An MPS representation of this wavefunction can be obtained by defining the components of a tensor C_1 as,

$$\begin{aligned} C_1^0 &= |0\rangle\langle+|, \\ C_1^1 &= |1\rangle\langle-|. \end{aligned} \quad (2.83)$$

In this way, $\text{Tr } C_1^{i_1} \dots C_1^{i_N}$ evaluates to a sequence of inner products which equal -1 if two neighbours are in the $|1\rangle$ state and 1 otherwise (since only $\langle-|1\rangle = -1$). So the cluster state can be represented exactly as an MPS with bond dimension $D = 2$. We remark that the subscript “1” is used here to distinguish this tensor, which has one qubit per unit cell, from a later one which will have two qubits per unit cell.

When considering MPS as resources for measurement-based quantum computation, we will sometimes want to express the MPS tensor with respect to a different basis of the physical index. For this, we introduce notation $A[\phi] := \sum_i \langle\phi|i\rangle A^i$

which represents the contraction of the physical leg of A with the state $|\phi\rangle$. For example, the cluster state tensors can be written in the X -basis as

$$\begin{aligned} C_1[+] &:= \frac{1}{\sqrt{2}}(C_1^0 + C_1^1) = H, \\ C_1[-] &:= \frac{1}{\sqrt{2}}(C_1^0 - C_1^1) = HZ, \end{aligned} \tag{2.84}$$

where $H = \frac{X+Z}{\sqrt{2}}$ is the Hadamard matrix.

Projected entangled pair states

Tensor networks in higher dimensions are typically referred to as projected entangled pair states (PEPS). This name comes from the method of constructing tensor networks by distributing a maximally entangled pair of virtual particles between neighbouring sites and mapping these onto the physical degree of freedom by a projection matrix⁵. This picture is not so useful for our purposes, so we do not expand on it further, but we nonetheless will use conventional terminology of PEPS.

For a model with degrees of freedom on the vertices of a square lattice, we can start with a five-index tensor A ,

$$A_{\alpha\beta\gamma\delta}^i = \alpha \begin{array}{c} i \ \gamma \\ \diagdown \ \diagup \\ \bullet \\ \diagup \ \diagdown \\ \delta \end{array} \beta, \tag{2.85}$$

and use it to build a basic PEPS,

$$|\psi\rangle = \begin{array}{c} \dots \\ \dots \\ \dots \end{array} \begin{array}{c} \bullet \\ \bullet \\ \bullet \end{array} \begin{array}{c} \bullet \\ \bullet \\ \bullet \end{array} \begin{array}{c} \bullet \\ \bullet \\ \bullet \end{array} \begin{array}{c} \bullet \\ \bullet \\ \bullet \end{array} \begin{array}{c} \bullet \\ \bullet \\ \bullet \end{array} \begin{array}{c} \dots \\ \dots \\ \dots \end{array}, \tag{2.86}$$

which gives us our state $|\psi\rangle$ after applying appropriate open or closed boundary conditions. It would be very cumbersome to write down an equation for this wavefunction, as we could in the case of an MPS, but the power of the graphical representation ensures that this is rarely necessary.

Many of the concepts discussed above for MPS carry over to PEPS, but with some important modifications. In fact, throughout this thesis, we will largely deal with PEPS in a quasi-1D representation. By placing a PEPS on a cylinder or torus or circumference N , we can *block* a column of tensors and group legs to obtain an

⁵See Ref. [87] for an explanation and a demonstration of the equivalence to the normal picture.

[134] or string order [135], can be understood locally in terms of symmetries of the local tensors. Studying these symmetries leads to an extremely powerful approach to detect and even classify topological order [134, 136, 137], SPT order [87, 93, 130, 138–140], and others [141–144]. In particular, the procedure to extract cocycles characterizing SPT order can be made more rigorous and well-defined as compared to the Else-Nayak procedure. Here, we give a summary of these results in 1D and 2D.

Symmetries and SPT order in MPS

First, let us consider how global on-site symmetries are manifested in MPS. Suppose our tensor satisfies the following condition,

$$\begin{array}{c} u \\ | \\ \bullet \\ | \\ A \end{array} = V \begin{array}{c} | \\ \bullet \\ | \\ A \end{array} V^\dagger, \quad (2.91)$$

where V is a unitary matrix. In this notation, an operator drawn by an open leg of a tensor represents the operator acting on that leg, such that the condition can be written as an equation as $\sum_j u_{ij} A^j = V A^i V^\dagger$. Then, the state $|\psi\rangle$ has a global symmetry $u^{\otimes N}$ since the V and V^\dagger coming from neighbouring tensors cancel on the virtual bond between them. Graphically,

$$\begin{aligned} & \begin{array}{c} u \\ | \\ \bullet \\ | \\ A \end{array} \text{---} \begin{array}{c} u \\ | \\ \bullet \\ | \\ A \end{array} \text{---} \dots \text{---} \begin{array}{c} u \\ | \\ \bullet \\ | \\ A \end{array} \\ &= \begin{array}{c} | \\ \bullet \\ | \\ A \end{array} \text{---} V \begin{array}{c} | \\ \bullet \\ | \\ A \end{array} V^\dagger \text{---} V \begin{array}{c} | \\ \bullet \\ | \\ A \end{array} V^\dagger \text{---} \dots \text{---} V \begin{array}{c} | \\ \bullet \\ | \\ A \end{array} V^\dagger \\ &= \begin{array}{c} | \\ \bullet \\ | \\ A \end{array} \text{---} \begin{array}{c} | \\ \bullet \\ | \\ A \end{array} \text{---} \dots \text{---} \begin{array}{c} | \\ \bullet \\ | \\ A \end{array}. \end{aligned} \quad (2.92)$$

It turns out that this is the only way to encode a global symmetry into a normal MPS, subject to some technical conditions [145]. That is, if u is a global symmetry, we can always find a V such that Eq. 2.91 holds.

This observation leads to a classification of 1D SPT phases. If we have a symmetry group G with on-site representation $u(g)$, this corresponds to a virtual representation $V(g)$ acting on the virtual bond of the MPS as defined by Eq. 2.91. Because $V(g)$ always appears with its hermitian conjugate, it is only defined up to a phase factor. Therefore, we are in the same situation as in Section 2.2.1, where the endpoint operators $V_{a/b}(g)$ were also only defined up to a phase. In fact, $V(g)$ satisfies the same relations as $V_a(g)$, so it is a projective representation, $V(g)V(h) = \omega(g, h)V(gh)$, and the 2-cocycle ω corresponds to some cohomology class $[\omega]$ in $H^2(G, U(1))$. The virtual representation $V(g)$ therefore provides a more transparent and unique way to extract $[\omega]$, as compared to the somewhat vague procedure outlined in Section 2.2.1.

The advantage of the MPS formulation is that one can prove that $[\omega]$ can not be changed under symmetric, gap preserving deformations of the MPS tensor A

[87]. Therefore, we have a proof that states with different $[\omega]$ belong to distinct SPT phases, at least within the realm of MPS, which approximate gapped ground states well. To have a completely rigorous proof, one would additionally need to show that there is a symmetric gapped path between an arbitrary gapped ground state and its MPS approximation.

Constraints on MPS tensors in SPT phases

From the above procedure, we can extract a cohomology class $[\omega]$ from an MPS tensor A with on-site symmetry $u(g)$. It turns out that we can also do the reverse: given $[\omega]$ and $u(g)$, we can constrain the possible A that are consistent with the symmetry relation of Eq. 2.91. This result, along with its analogues for more complicated symmetries in 2D, is of central importance for this thesis.

The following is a reproduction of the proof in Ref. [15]. Consider a tensor A which satisfies the symmetry relation of Eq. 2.91, which we rewrite for a group G as,

$$\sum_j u(g)_{ij} A^j = V(g) A^i V(g)^\dagger. \quad (2.93)$$

To proceed, we make some restrictions on the symmetry and SPT phase. First, we restrict that G is a finite abelian group, which implies that we can choose the basis $\{|k\rangle\}$ of our physical on-site Hilbert space to diagonalize $u(g)$, such that $u(g)|k\rangle = \chi_k(g)|k\rangle$ for some 1D representations $\chi_k(g)$. For reasons that will become clear in the next section, we call this basis the *wire basis*. The second restriction is to SPT phases labelled by a cohomology class $[\omega]$ that is *maximally non-commutative*, meaning the subset $\{g \in G | \omega(g, h) = \omega(h, g) \forall h \in G\}$ contains only the identity element⁶. In terms of the virtual representation $V(g)$, this condition means that $V(g)V(h) = V(h)V(g)$ for all $h \in G$ if and only if $g = e$, hence the term maximally non-commutative. It is known that any $V(g)$ having a maximally non-commutative cocycle can be written as,

$$V(g) = \mathbb{1} \otimes \tilde{V}(g), \quad (2.94)$$

where $\tilde{V}(g)$ is an irreducible representation of dimension $\sqrt{|G|}$ [15]. This gives some insight into the boundary physics of MPS: in order for the boundary to transform under such a representation, it must support an edge mode of dimension at least $\sqrt{|G|}$.

In Ref. [15], the authors used Schur's Lemma to prove that any normal MPS tensor A transforming as in Eq. 2.93, subject to the above restrictions, can be put into the following form,

$$A[k] = B[k] \otimes C[k], \quad (2.95)$$

where $B[k]$ are arbitrary matrices and $C[k] = \tilde{V}(g_k)$ for a group element $g_k \in G$ that is determined by the equation,

$$\chi_k(g) \tilde{V}(g_k) = \tilde{V}(g) \tilde{V}(g_k) \tilde{V}(g)^\dagger. \quad (2.96)$$

⁶We observe that this condition is independent of the choice of cocycle ω representing the class $[\omega]$. A group G can support a maximally non-commutative cocycle only if it is of the form $G = H \times H$ for some group H [146].

According to Eq. 2.95, the virtual space decomposes into two subsystems. We call the subsystem where $B[k]$ ($C[k]$) acts the junk (logical) subsystem. Importantly, as one moves around in the SPT phase labelled by $[\omega]$, the matrices $B[k]$ change while $C[k]$ do not. This decomposition therefore provides a concrete way to see the entanglement that is uniform throughout an SPT phase, *i.e.* that which is conducted via the logical subsystem of the tensor network.

Importantly, Eq. 2.95 only holds in the wire basis. An equivalent basis-independent way of stating the result is as follows. Letting C be the tensor defined by the components $C[k] = \tilde{V}(g_k)$, we can write the tensor A as,

$$\begin{array}{c} | \\ \bullet \\ \text{---} \\ A \end{array} = \begin{array}{c} | \\ \bullet \\ \text{---} \\ B \\ \bullet \\ \text{---} \\ C \end{array} \quad \text{where} \quad \begin{array}{c} u(g) \\ | \\ \bullet \\ \text{---} \\ B \end{array} = \begin{array}{c} | \\ \bullet \\ \text{---} \\ B \\ | \\ u(g) \end{array}, \quad (2.97)$$

where B is a tensor describing some MPO. Note the condition that B commutes with the symmetry action is essential, since otherwise the statement holds trivially from the fact that every state in the same SPT phase as the cluster phase can be related to the cluster state by a FDQC (which can be represented as an MPO). The symmetry condition on B ensures that, upon contracting the physical leg with a state $|k\rangle$ in the $u(g)$ -basis, the result is Eq. 2.95.

This decomposition is central to our understanding of measurement-based quantum computation with SPT phases, as we will see in Section 2.6. It can also be used, for example, to find the hidden symmetry breaking structure present in SPT phases [147], to quantify the entanglement in SPT phases under symmetry-restricted operations [64], and to understand the sign structure in SPT phases [48]. A more general result which drops both restrictions of finite abelian G and maximally non-commutative $[\omega]$ was given in Ref. [148]. Therein, the authors show how to constrain the MPS tensor in terms of certain Clebsch-Gordon coefficients of the symmetry representations. However, this more general decomposition lacks some of the structure that allow results such as those mentioned above to be proven, especially the connection to quantum computation. In Ref. [149], it was shown that this structure can be recovered if the maximally non-commutative constraint is removed, while the finite abelian group constraint is preserved.

Example: SPT order in 1D cluster state

As an example of SPT order in MPS, we can re-examine SPT order of the 1D cluster state under the lens of MPS. Recall that the 1D cluster state has a $\mathbb{Z}_2 \times \mathbb{Z}_2$ symmetry generated by flipping all even or all odd spins. To fit this into the above framework where the symmetry acts in the same way on every site, we need to consider a two-qubit unit cell. If we consider the local X -basis for each qubit, we

can express the blocked tensor C_2 in terms of the components,

$$\begin{aligned}
 C_2[++] &:= C_1[+]C_1[+] = \mathbb{1}, \\
 C_2[+-] &:= C_1[+]C_1[-] = Z, \\
 C_2[-+] &:= C_1[-]C_1[+] = X, \\
 C_2[--] &:= C_1[-]C_1[-] = XZ,
 \end{aligned} \tag{2.98}$$

where the subscript “2” represents the two-qubit unit cell. Pictorially, we draw this blocking as,

$$\begin{array}{c} | \\ \bullet \\ \text{---} \\ C_1 \end{array} \begin{array}{c} | \\ \bullet \\ \text{---} \\ C_1 \end{array} = \begin{array}{c} \parallel \\ \bullet \\ \text{---} \\ C_2 \end{array} . \tag{2.99}$$

We can use Eq. 2.98 to find the operators $V(g)$ in Eq. 2.93. Writing $g = (g_1, g_2) \in \mathbb{Z}_2 \times \mathbb{Z}_2$ as in Section 2.2.2, we can work out that $V(g_1, g_2) = Z^{g_1} X^{g_2}$, in agreement with the calculations of Section 2.2.2. This representation satisfies our condition of maximal non-commutativity, and we can confirm that Eq. 2.95 holds, since the local X -basis is the wire basis in this case, and the matrices in Eq. 2.98 are indeed elements of $V(g)$. Other states in the same SPT phase as the cluster state can therefore be written in terms of MPS tensors of the form in Eq. 2.97 where $C = C_2$.

Symmetries and SPT order in PEPS

Gapped phases in 2D can also be understood in terms of symmetries of the local tensors in a PEPS, although our understanding is not nearly as complete or rigorous as in the 1D scenario. A simple way to encode a global symmetry into a PEPS is given by a straightforward extension of Eq. 2.91,

$$\begin{array}{c} u \\ \diagdown \\ \bullet \\ \diagup \end{array} \text{---} = V \begin{array}{c} W \\ \diagdown \\ \bullet \\ \diagup \\ W^\dagger \end{array} \text{---} V^\dagger . \tag{2.100}$$

For some unitary matrices V and W . As in the case of MPS, we can define a class of *normal PEPS* for which we can prove that Eq. 2.100 is the only way to represent a global symmetry of a PEPS [150]. However it turns out that the class of normal PEPS is much more restrictive than that of normal MPS. In particular, they cannot capture topological order or SPT order. The reason they cannot capture topological order is because every normal PEPS is provably the unique ground state of its parent Hamiltonian [134] and therefore cannot replicate the topological degeneracy. The reason they cannot capture SPT order is the following. We can extract a cocycle from the virtual representation $V(g)$ (or $W(g)$, which may or may not be the same). Suppose we then block our tensors into 2×2 unit cells. Then, the symmetry relation of the blocked tensor looks like,

$$\begin{array}{c} u \quad u \\ \diagdown \quad \diagdown \\ \bullet \quad \bullet \\ \diagup \quad \diagup \\ u \quad u \\ \diagdown \quad \diagdown \\ \bullet \quad \bullet \\ \diagup \quad \diagup \end{array} = V \begin{array}{c} W \quad W \\ \diagdown \quad \diagdown \\ \bullet \quad \bullet \\ \diagup \quad \diagup \\ W^\dagger \quad W^\dagger \end{array} V^\dagger . \tag{2.101}$$

Now, our virtual representation on the left edge has gone from $V(g)$ to $V(g) \otimes V(g)$. If $V(g)$ has cocycle ω , then $V(g) \otimes V(g)$ will have cocycle ω^2 , which will correspond to a different cohomology class. So we see that the cohomology class, and therefore the SPT phase, is not stable under blocking [134]. If we disallow blocking by enforcing translational invariance, then ω can have a well defined meaning. Such phases that are stable only with translational invariance are called weak SPT phases [60].

To capture genuine 2D SPT order, one needs to consider more general classes of PEPS. One proposal that has emerged is the class of MPO-injective PEPS [93]. These satisfy the following symmetry relation,

$$\begin{array}{c} u \\ | \\ \bullet \\ | \\ \text{---} \end{array} = \begin{array}{c} \text{---} \bullet \text{---} \\ / \quad \backslash \\ \bullet \quad \bullet \\ \backslash \quad / \\ \text{---} \bullet \text{---} \end{array}, \quad (2.102)$$

where the action in the virtual space is that of an MPO. Unlike Eq. 2.100, Eq. 2.102 is stable under blocking, since the relation on a blocked tensor gives,

$$\begin{array}{c} u \quad u \\ | \quad | \\ \bullet \quad \bullet \\ / \quad \backslash \\ u \quad u \\ | \quad | \\ \bullet \quad \bullet \\ \backslash \quad / \\ \text{---} \bullet \text{---} \end{array} = \begin{array}{c} \text{---} \bullet \text{---} \\ / \quad \backslash \\ \bullet \quad \bullet \\ \backslash \quad / \\ \text{---} \bullet \text{---} \end{array}. \quad (2.103)$$

So the same MPO appears in the virtual space of the blocked tensor. As long as the quantity we extract from the MPO is independent of its length, we can get an invariant that is stable under blocking. Given our understanding of 2D SPT phases, this invariant should be a 3-cocycle. The procedure to extract this cocycle was given in Ref. [74], and we will not demonstrate the procedure in full here. The key point is that, given an MPO representation $O(g)$, there is a special “zipper” tensor which fuses the product of MPOs $O(g)O(h)$ into a single MPO $O(gh)$. There are then two inequivalent ways to use the zipper tensors to fuse three different MPOs $O(g)$, $O(h)$, and $O(k)$, and these two ways differ by a phase factor $\omega(g, h, k)$; the 3-cocycle. This procedure is again similar to the Else-Nayak procedure: we first reduce the global symmetry in a patch to a 1D operator on the boundary (here, the MPO), and then we extract the cocycle from the boundary of that 1D operator (via the zipper tensor).

As in the 1D case, the tensor network approach lets us make more powerful statements. For example, an alternate construction called “semi-injective” PEPS [140] can also capture 2D SPT orders thanks to an entangled-plaquette structure that resembles the original CZX model proposed in Ref. [74]. Using semi-injective PEPS, more rigorous claims can be made regarding the well-definedness of the MPO representation and the 3-cocycle. As another example, one can prove that no normal MPS can be invariant under an MPO representation with non-trivial 3-cocycle [74]. This means that an invariant state must develop long range order (such that the MPS is not normal) or be critical (such that it cannot be represented as an MPS), putting the observations we made about the boundaries of 2D SPT phases in Section 2.2.3 on more rigorous footing.

Other phases of matter in PEPS

PEPS can also capture other phases of matter beyond SPT order [3]. For example, to capture intrinsic topological order, one can impose symmetries of the PEPS tensor that act purely on the virtual legs,

$$\begin{array}{c} \diagup \\ \bullet \\ \diagdown \end{array} = U_g \begin{array}{c} U_g \\ \diagup \\ \bullet \\ \diagdown \\ U_g^\dagger \end{array} U_g^\dagger, \quad (2.104)$$

where U_g is a representation of a finite group G [134]. PEPS with these symmetries can capture G -quantum double models, which are generalizations of the toric code model (for which $G = \mathbb{Z}_2$) [105] and simple symmetry-enriched models obtained via anyon condensation [151]. The same symmetry constraints where G is an infinite group can capture critical models [144]. Similarly, PEPS tensors with a virtual MPO symmetry can capture more complicated topological orders such as twisted quantum double models [152] and string-net models [153], as well as general symmetry-enriched topological models [142].

2.5.3 Tensor network numerics

Apart from their analytical applications, tensor networks are equally (or even more) powerful when applied to numerical calculations [124]. Since we will use tensor network-based numerical techniques in Chapter 4, we will briefly go over the basic ideas here. The core principles behind tensor network numerics are that (a) tensor networks provide a way to efficiently parametrize the physical corner of Hilbert space that contains ground states of gapped Hamiltonians, as discussed above, and (b) a tensor network representation allows efficient computation of expectation values by using transfer matrices and their fixed-points to condense the environment surrounding a local operator, as we have seen above for 1D systems. The bond dimension D , which limits the amount of entanglement in the system (with $D = 1$ corresponding to a mean-field theory ansatz), gives us systematic control over error in the approximations.

A large class of tensor network algorithms can be viewed as variational methods within the space of tensor network states. That is, one varies the basic tensor A defining an MPS or PEPS in order to minimize a quantity of interest such as energy. There are many ways to do this variation in 1D [124, 154, 155], with DMRG being a key early example. In 2D, this problem is more difficult, a primary reason being that 2D tensor networks cannot be efficiently contracted in general [156]. Luckily, one can use various transfer matrix methods [157, 158] or methods inspired by real-space renormalization [159, 160] to approximately contract the tensor network, with an error that is again controllable using the bond dimension. Using such methods, one can efficiently calculate expectation values of local operators, and even correlation functions. This in turn allows one to calculate energy gradients which can be used to optimize the variational ground state tensor [161, 162].

Another broad class of tensor network algorithms is time-evolving block decimation (TEBD) algorithms [4, 163] In 1D, these involve taking an initial MPS and

evolving it by acting with a quantum circuit or an MPO at each time step. The resulting state is still an MPS, but with an enlarged bond dimension. In order to keep the bond dimension from exploding over time, the crucial step is to truncate this MPS back to the original bond dimension in such a way that the state is changed as little as possible. Determining the optimal truncation is straightforward to perform in 1D using singular-value decompositions and the canonical form [4], but it is much harder to determine in 2D due to the lack of an equivalent of the canonical form, although many successful approaches have nonetheless been found [164–167]. These types of algorithms can capture time evolution (including imaginary time evolution which can be used to compute ground states) and can be used to find fixed-points of transfer matrices, which is a necessary step in some of the approximate 2D contraction schemes mentioned above.

Combining these two classes of algorithms gives a powerful suite of tools that can be used to understand many-body systems. Many of these algorithms can work directly in the thermodynamic limit, eliminating finite size effects and enabling the sharp detection of events like phase transitions. In some cases, they can even be used for critical systems that cannot be captured by a tensor network with finite bond dimension. This possibility is based on the observation that a finite bond dimension can be viewed as an effective length scale, and observing the scaling of observables with this length scale can be used to extract the universal quantities that characterize critical systems [168–170]. Also, by interpreting the space of tensor network states as a non-linear manifold, one can formulate tangent-space methods to access low-energy excited states in addition to the ground state [171].

Another reason that tensor networks are excellent numerical tools, particularly in the context of quantum phases of matter, is that they allow direct access to the entanglement degrees of freedom of a wavefunction via the virtual legs of the network. For example, we have seen that one can easily extract entanglement entropies and, more generally, the entire entanglement spectrum [129], which contains vital information about the quantum order of a ground state. This direct access to the entanglement is particularly useful in the context of topological phases, where one can construct excited states containing anyons using operators living on the virtual legs of the tensor network, which can then be used to construct order parameters for topological phase transitions [137].

2.6 Measurement-based quantum computation with SPT phases

As alluded to in the introduction, there is a deep connection between measurement-based quantum computation (MBQC) and SPT phases. MBQC is a model of quantum computation that is driven solely by single-body measurements on an initially entangled many-body *resource state* [11]. The initialization of the logical information, the unitary evolution, and the final readout are all performed using these single-body measurements. The fundamental questions of MBQC are therefore to find which resource states lead to universal computation, and then to understand how these states may be prepared in a laboratory setting. To this end, much research was done into finding resource states which appear as the unique ground state of physically realistic gapped Hamiltonians, allowing them to be prepared by cooling a system governed by such a Hamiltonian to low temperatures. Many of these examples, such as the 2D AKLT states, fall into the picture of valence-bond-states [172], whose use for MBQC can be clearly seen from the lens of quantum teleportation [122]. These ventures brought the study MBQC closer to condensed matter physics, and allowed us to characterize physical systems by their computational capability.

Remarkably, it turns out that in some cases this computational capability is not a property of a single ground state, but rather an entire gapped phase of matter. We call such phases of matter *computational phases of matter* [12–15, 17, 19, 20]. In this setting, physical phases of matter coincide with regions of uniform computational capability. This was first observed for classes of states containing 1D AKLT state, which allows universal MBQC on a single encoded qubit [173]. The 1D AKLT state can be viewed as an exactly solvable point in the 1D SPT phase protected by $SO(3)$ spin rotation, often referred to as the Haldane phase⁷. Ref. [13] studied a family of states in this phase described by a single parameter β known as the bilinear-biquadratic spin chain, and showed that the system could be used for MBQC even away from the AKLT point, so long as β was chosen such that the system remained in the Haldane phase. The author was able to formulate the MBQC protocol in terms of the properties of the Haldane phase, thereby establishing a relationship between MBQC and SPT order.

To see why SPT phases can be useful for MBQC, consider the following toy picture. From Section 2.2, we know that 1D SPT phases have robust edge modes. That is, if we consider an SPT ordered state on a half-infinite spin chain, there will be a edge mode degeneracy associated to the edge of the chain. For a simple $\mathbb{Z}_2 \times \mathbb{Z}_2$ chain like the cluster state, this means that the ground state will be two-fold degenerate, with the two ground states differing by some operator exponentially localised near the edge.

Suppose we encode a qubit state $|L\rangle$ in this edge mode. If we measure the spin closest to the boundary of the chain, the measured spin will be projected to a product state $|s\rangle$ depending on the measurement outcome. This spin is now

⁷It turns out that a finite subgroup $\mathbb{Z}_2 \times \mathbb{Z}_2 \subset SO(3)$ is sufficient to protect the SPT order, allowing us to fit this example into our later results that require abelian symmetries.

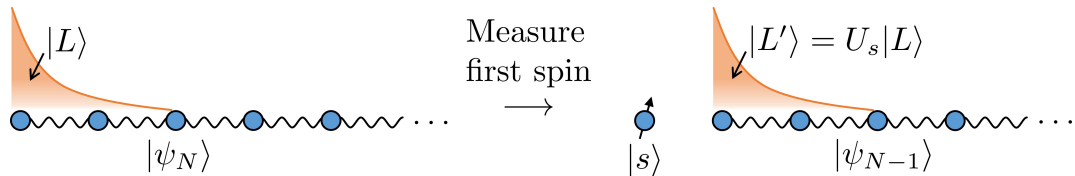


Figure 2.9: Toy picture of measurement-based quantum computation in SPT phases. The orange wedge represents the two-level edge mode that is localised near the edge. Measurement of the right-most spin induces unitary evolution of the edge mode.

disentangled from the rest of the chain, so we can ignore it from now on. What remains is a chain that is one spin shorter, and this new chain will also have an edge mode that will in general be in a new state $|L'\rangle$. The key insight is that, if we choose our measurement basis correctly, the new state $|L'\rangle$ will be related to the original one via a unitary that depends on the measurement outcome s , $|L'\rangle = U_s |L\rangle$. In other words, measurement of the physical spins translates into unitary evolution of the encoded qubit on the edge [13]. Since the edge modes are robust within an SPT phase, one may hope that this notion of computation is robust as well. This is indeed the case for a fairly general class of 1D SPT phases, as we will see shortly.

2.6.1 MBQC in tensor networks

The above picture can be made precise using matrix product states [122, 174]. Specifically, consider an MPS with open boundary conditions, which we can write in the following form,

$$\begin{aligned}
 |\psi\rangle &= \sum_{i_1, \dots, i_N} \langle L | A^{i_1} A^{i_2} \dots A^{i_{N-1}} A^{i_N} | R \rangle | i_1, i_2, \dots, i_N \rangle \\
 &= \langle L | \text{---} \underset{A}{\bullet} \text{---} \underset{A}{\bullet} \text{---} \dots \text{---} \underset{A}{\bullet} \text{---} \underset{A}{\bullet} \text{---} | R \rangle, \tag{2.105}
 \end{aligned}$$

for some boundary vectors $\langle L |$ and $| R \rangle$. Now suppose we encode a logical qudit in $|L\rangle$. If we measure the first spin (corresponding to index i_1) and obtain a measurement outcome corresponding to an eigenstate $|s\rangle$ of the measured observable, then the state of the unmeasured spins is

$$|\psi'\rangle = \sum_{i_2, \dots, i_N} \langle L' | A^{i_2} \dots A^{i_{N-1}} A^{i_N} | R \rangle | i_2, i_3, \dots, i_N \rangle, \tag{2.106}$$

where the new boundary vector is,

$$|L'\rangle = A[s]^\dagger |L\rangle, \tag{2.107}$$

and we recall the notation $A[\phi] := \sum_i \langle \phi | i \rangle A^i$. Pictorially, this is,

$$\begin{aligned}
 |\psi'\rangle &= \langle L | \begin{array}{c} \text{---} \bullet \text{---} \bullet \text{---} \dots \text{---} \bullet \text{---} \bullet \text{---} \\ | \quad | \quad | \quad | \\ A \quad A \quad \dots \quad A \quad A \end{array} | R \rangle \\
 &= \langle L | \begin{array}{c} \text{---} \bullet \text{---} \bullet \text{---} \bullet \text{---} \\ | \quad | \quad | \\ A[s] \quad A \quad A \end{array} | R \rangle. \tag{2.108}
 \end{aligned}$$

If $A[s]$ is a unitary, we will have induced unitary evolution of the virtual space by measurement of the physical space. Of course, $A[s]$ depends on the measurement outcome s , which we cannot control, and this is a fundamental issue that can be solved particularly nicely in the context of SPT phases.

Let us consider a specific example of the above process using the 1D cluster state as a resource. Recall that the cluster state can be described by an MPS with a two-qubit unit cell defined by the matrices $A[ab] = X^a Z^b$ where $a, b = 0 (1)$ represents the state $|+\rangle (|-\rangle)$ (See Eq. 2.98). Then, measuring two qubits in the X -basis results in an outcome-dependent Pauli operator in the virtual space. The outcome-dependent operator is called a byproduct operator, and it can be dealt with using the symmetry relation of the MPS tensor. Observe that these Pauli byproduct operators are elements of the projective representation $V(g)$ for some $g \in \mathbb{Z}_2 \times \mathbb{Z}_2$. Then, we can propagate this operator to the other end of the chain using the symmetry relation in Eq. 2.91,

$$\begin{aligned}
 \langle L | \begin{array}{c} \text{---} \bullet \text{---} \bullet \text{---} \bullet \text{---} \dots \\ | \quad | \quad | \\ A \quad A \quad A \end{array} V(g) \\
 = \langle L | \begin{array}{c} \text{---} \bullet \text{---} \bullet \text{---} \bullet \text{---} \dots \\ | \quad | \quad | \\ A \quad A \quad A \end{array} \begin{array}{c} u(g) \quad u(g) \quad u(g) \\ | \quad | \quad | \end{array} \dots. \tag{2.109}
 \end{aligned}$$

In this way, this process of *byproduct propagation* pushes the byproduct operator to the end of the chain, where it will eventually affect the decoding of the logical state. The practical meaning of this is that all future measurement bases must be altered according to the symmetry operators $u(g)$. This is a symmetry-based perspective on the conventional formulation of MBQC, where measurement bases are modified according to past measurement outcomes.

Using byproduct propagation, we can use the 1D cluster state as a “quantum wire”, where measurements in the X -basis deterministically shuttle the state $|L\rangle$ along the chain. In other words, we can do the identity gate with perfect fidelity. This is why we called the X -basis the wire basis in Section 2.5.2. We can perform non-trivial gates by rotating the measurement basis away from the wire basis. Define a rotated basis spanned by the states,

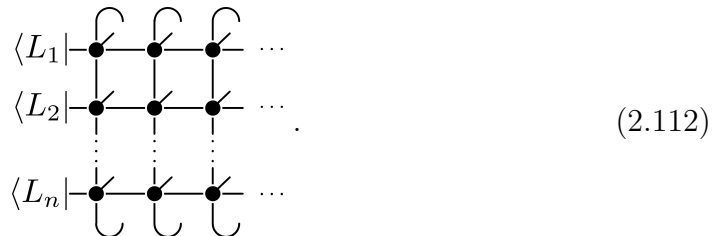
$$\begin{aligned}
 |\theta_+\rangle &= \cos(\theta)|+\rangle - i \sin(\theta)|-\rangle, \\
 |\theta_-\rangle &= -i \sin(\theta)|+\rangle + \cos(\theta)|-\rangle. \tag{2.110}
 \end{aligned}$$

If we measure the first qubit in the unit cell in the rotated basis, and the second in the wire basis, we get,

$$\begin{aligned} A[\theta_+b] &= \cos(\theta)A[+b] + i \sin(\theta)A[-b] = (\cos(\theta)\mathbb{1} + i \sin(\theta)X) Z^b = e^{i\theta X} Z^b, \\ A[\theta_-b] &= i \sin(\theta)A[+b] + \cos(\theta)A[-b] = (i \sin(\theta)\mathbb{1} + \cos(\theta)X) Z^b = e^{i\theta X} X Z^b. \end{aligned} \quad (2.111)$$

Putting these together, we find $A[\theta_a b] = e^{i\theta X} X^a Z^b$, so the measurement results in a rotation by θ about the X -axis of the encoded qubit, up to Pauli byproducts. Similarly, measuring the first qubit in the wire basis and the second qubit in the rotated basis gives a rotation about the Z -axis. These two types of rotations generate all unitary evolutions of a single qubit, so we can achieve universal quantum computation *on a single qubit* when using a 1D cluster state as a resource.

We can also capture MBQC with 2D resource states using PEPS. Namely, if we put a PEPS on a cylinder of circumference n (or fix the boundaries otherwise), we can encode n states on the boundary,



Measuring the first column of spins, for example, would result in an MPO acting on the encoded states. We will explore this further in the Section 2.7.

2.6.2 Computational phases of matter in 1D

The universality of the 1D cluster state persists throughout the entire $\mathbb{Z}_2 \times \mathbb{Z}_2$ SPT phase in which it resides, and this is in fact true for all SPT phases with maximally non-commutative cocycles (as defined in Section 2.5.2). The key reason why this is possible is Eq. 2.95. Suppose we encode our logical state $|\psi\rangle$ only in the logical subsystem of Eq. 2.95, writing $|L\rangle = |J\rangle \otimes |\psi\rangle$ for some arbitrary vector $|J\rangle$ in the junk subspace. Then, measuring in the wire basis evolves the virtual state as,

$$|L'\rangle = A[k]|L\rangle = B[k]|J\rangle \otimes C[k]|\psi\rangle, \quad (2.113)$$

so the junk and logical subsystems remain unentangled. Since $C[k] = \tilde{V}(g_k)$, and the virtual symmetry representation acts only on the logical subspace (Eq. 2.94), we can also do byproduct propagation as before. Therefore, we recover the quantum wire property in the logical subspace. The junk subspace evolves in an uncontrollable and *a priori* unknown manner, but this is not a problem yet, since the encoded qubit stays in the logical subspace.

The difficulty comes when we try to do non-trivial gates on the encoded qubit. Suppose we measure in a rotated basis and obtain some measurement outcome which is a superposition of states in the wire basis, $\alpha|k\rangle + \beta|k'\rangle$. The evolution of the virtual space induced by this measurement is,

$$|L'\rangle = \alpha \left(B[k]|J\rangle \otimes C[k]|\psi\rangle \right) + \beta \left(B[k']|J\rangle \otimes C[k']|\psi\rangle \right), \quad (2.114)$$

such that the junk and logical subsystems are now entangled. Since we might not have any knowledge of the matrices $B[k]$, this makes it difficult to keep track of the encoded state $|\psi\rangle$, and to perform byproduct propagation. An early solution to this problem came from Ref. [17], where the authors used a “computational renormalization” scheme (inspired by an earlier work [14]), but this was particularly tailored to a certain subset of the Haldane phase with a larger S_4 symmetry group.

A general solution was given in Refs. [19, 20]. Therein, it was shown that the junk and logical subsystems, once entangled, can be disentangled by measuring a large number of spins in the wire basis, and the overall evolution of the logical subspace is unitary as long as the angles θ describing deviations from the wire basis are kept small. This solution works for all SPT phases protected by abelian groups [149], but the resulting set of logical gates is only guaranteed to be universal in the maximally non-commutative case. Importantly, the protocol of Refs. [19, 20] does not require us to know the precise location of our system within the SPT phase. Rather, we are content with just knowing which phase it belongs to. The microscopic details of the states that are encoded in the junk matrices $B[k]$ are condensed into a handful of complex numbers that can be obtained during a calibration procedure that uses only local measurements. Finally, the initialization of the logical state $|\psi\rangle$ and its readout at the end of the computation can also be achieved with local measurements [20].

2.6.3 Higher dimensions and implications

There are also connections between MBQC and SPT phases in 2D. The 2D AKLT states, which have weak SPT order⁸, were shown to be universal on several different lattices [175–178]. This power was shown to persist for a certain path of Hamiltonian deformations, up until a phase transition into a symmetry-breaking phase of matter [179]. Similarly, fixed-point states for general SPT phases in 2D, which are essentially products of GHZ states, are universal for MBQC [21], and this universality persists under certain deformations [24]. In all of the above cases, the first step of the MBQC protocol is the use local measurements to reduce the resource state to a cluster state on some lattice. The universality then follows from the universality of the 2D cluster state, as long as certain percolation conditions are met [175].

In other works, resource states with genuine 2D SPT order were used to gain additional computational capability beyond that of the 2D cluster state. Namely, it was shown in Ref. [22] that the Union-Jack state (Eq. 2.18) is universal for MBQC using only Pauli measurements (that is, measurements of Pauli observables X, Y, Z). This is not possible for the 2D cluster state, which also needs measurements in, *e.g.*, the $X - Y$ plane⁹. This was later shown to also be true for other SPT states that

⁸It should be noted that the canonical resource for MQBC, the 2D cluster state, also has weak SPT order [22], although we will see later that it is better characterized by a different type of SPT order.

⁹The fact that such measurements are necessary can be seen as a consequence of the Gottesman-Knill theorem [180]: Pauli measurements on a stabilizer state like the cluster state are efficiently classically simulable, so they cannot lead to universal quantum computation. The Union-Jack state, on the other hand, is not a stabilizer state.

have a similar structure to the Union-Jack state [23, 181]. For these results, the intrinsic properties of 2D SPT orders (namely, their essential “non-stabilizerness” [48]) lead to computational advantages.

Notably, none of the above 2D investigations find a 2D SPT phase in which all ground states are universal for MBQC. Such a phase is presented in the next section, although we will find that it is necessary to go beyond the typical notion of SPT order to understand it.

Let us briefly explore the implications of the deep connections between SPT order and MBQC, starting with the practical. The initial motivation for studying SPT ordered states as resources for MBQC was to aid in state preparation [12, 173, 182]. If one encodes the MBQC resource state in the ground state of gapped Hamiltonian, it can be prepared by simulating this Hamiltonian in an experimental system and cooling the system to sufficiently low temperatures. If our resource state lies in an SPT phase which shares the same MBQC power, then our engineering of the Hamiltonian can endure unidentified errors: we do not need to prepare a specific Hamiltonian, rather we just need to make sure it belongs to the correct SPT phase of matter. This gives the state preparation step a certain kind of robustness to symmetry-preserving errors.

On the fundamental side, these results help us to understand the origin of quantum computational power. By now, it has been understood that quantum resources can be used to speed up certain computations. Yet, we do not fully understand which aspects of the quantum resources allow for this speed up. Candidates include superposition and interference [183], entanglement [4], and more contemporary ideas such as contextuality [184, 185], but none appear to tell the whole story. MBQC gives a unique viewpoint on this problem, since it pushes a majority of the potential “quantumness” onto the initial state¹⁰, thereby allowing us to approach the problem in terms of properties of many-body ground states. In the present case, we see that the structure of resource states that leads to universality seems to be closely related to the same structure that allows for SPT order to exist.

¹⁰The measurements do still contain some of this power, due to the fact that resource states like the Union-Jack can be universal with a smaller set of measurements bases compared to other resource states.

2.7 Subsystem symmetries

The discussion up to this point of the thesis lies within the universe of global symmetries, with topological phases being dual to systems with global symmetries via gauging. The remaining content of this thesis is concerned with a new universe: that of *subsystem symmetries*. In a system with D spatial dimensions, we define a subsystem symmetry to be generated by operators that have non-trivial action only on *rigid* k -dimensional subsystems, with $1 < k < D$. This can include 1D lines in a 2D system, 2D planes in 3D, or even fractals of non-integer dimension. We emphasize the word rigid to differentiate subsystem symmetries from the similar *higher-form symmetries* [91, 186, 187]. These symmetries also act on lower-dimensional subsystems, but they can be deformed and hence have no rigid geometrical structure. The rigid structure is a key element of subsystem symmetries, and is what leads to many of their unique properties that fall beyond the realm of topological quantum field theory [57].

In this section, we will first define the 2D cluster state and the 2D cluster phase, which is an example of a symmetry-protected topological order with subsystem symmetries. These constructions are very important to the rest of this thesis, so we will examine them in detail. Afterwards, we will show how they can naturally fit into the framework of MBQC with SPT phases, providing the first example of a computationally universal phase of matter. We will finish by briefly discussing the gauging of subsystem symmetries and fracton topological order.

2.7.1 The cluster state and SSPT order

The 2D cluster state (which we may simply refer to as “the cluster state” from now on), was originally envisioned for its entanglement properties: measuring one spin of the entangled many-body state in any basis leaves the rest of the spins entangled [188]. This means the entanglement is “persistent” as compared to, say, a GHZ (cat) state where measuring one spin can collapse the entire system into a product state. More importantly, it was shown that these measurements can be used to efficiently simulate the universal circuit model of quantum computation, thereby introducing the notion of measurement-based quantum computation with the cluster state as the original universal resource state [189]. Among its many other useful properties relating to entanglement and quantum computation, the cluster state is also interesting in terms of its properties as the ground state of a gapped Hamiltonian. As we have seen in Section 2.2.2, the 1D cluster state has SPT order. Now, we will show that the 2D cluster state is the simplest example of an SPT order with subsystem symmetries.

The 2D cluster state is defined similarly to the 1D cluster state (Eq. 2.11). We put qubits on the vertices of a square lattice, and define the state as,

$$|\mathcal{C}\rangle = \left(\prod_{\langle ij \rangle} CZ_{ij} \right) |++\cdots+\rangle, \quad (2.115)$$

where the product is over all nearest neighbours. More generally, we could define a cluster state on any lattice or graph by putting $|+\rangle$ states on the vertices and CZ

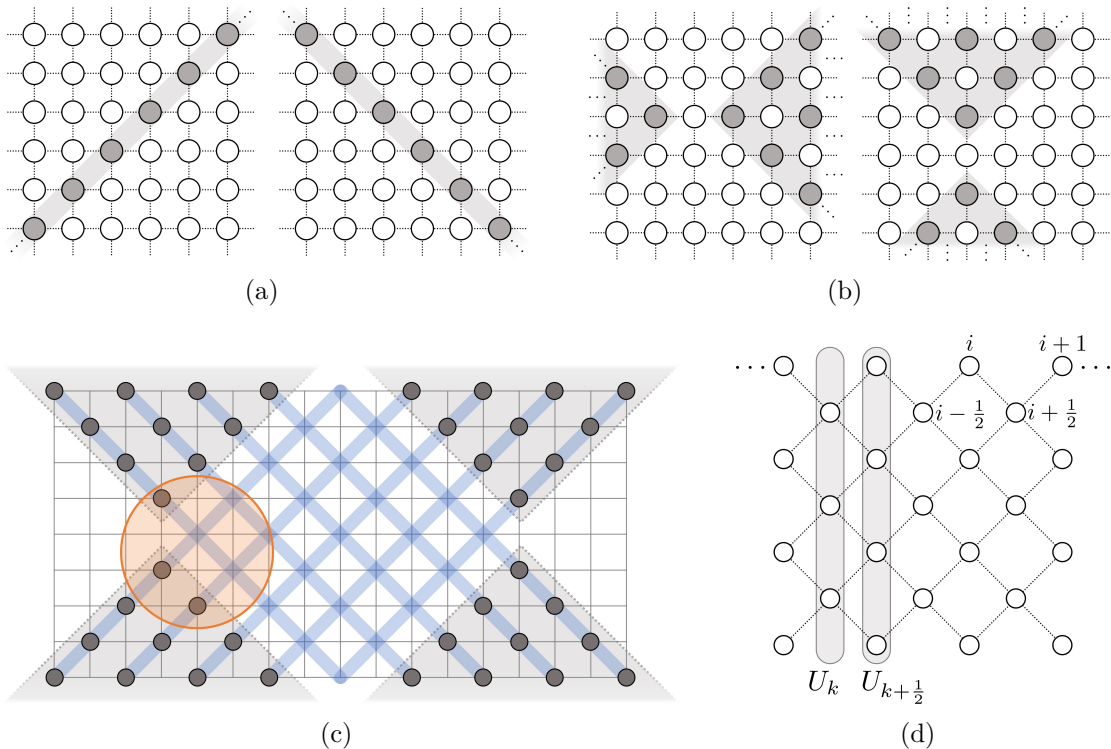


Figure 2.10: (a) and (b) show the line and cone symmetries of the 2D cluster state, respectively, where filled circles represent X operators. We show sections of an infinite lattice; the operators span the entire lattice. (c) The product of line symmetries along the thick diagonal lines cancels out in the middle region, leaving operators (indicated by small circles) only in cone-shaped regions. To an operator with local support, such as the large circular region, this product of line symmetries looks like a single cone symmetry. Therefore, if a local operator commutes with all line symmetries, it also commutes with the cone symmetries. (d) The cluster state on a rotated square lattice. Subsystem symmetries act on vertical (also horizontal) lines as indicated by highlighted regions.

gates on between all pairs of vertices sharing an edge. States constructed in this way are also sometimes called graph states. Note that we use similar notation for the 1D and 2D cluster states, as it will be clear from the context which one we refer to. A Hamiltonian for which the 2D cluster state is the unique ground state can be found in a similar manner as for the 1D cluster state, giving,

$$H_C = - \sum_{x,y} K_{x,y}, \quad (2.116)$$

where $K_{x,y} = X_{x,y} Z_{x+1,y} Z_{x-1,y} Z_{x,y+1} Z_{x,y-1}$ is the cluster state stabilizer and we label sites on the square lattice by a position $i = (x, y)$. The cluster state satisfies the relations,

$$K_{x,y} |\mathcal{C}\rangle = |\mathcal{C}\rangle, \quad (2.117)$$

for all x, y .

This Hamiltonian commutes with subsystem symmetries consisting of X acting on every site along any diagonal line on the lattice,

$$U_{c,\pm} = \prod_x X_{x,c\pm x}. \quad (2.118)$$

These symmetry operators can be derived by multiplying the Hamiltonian terms (stabilizers) in such a way that all Z operators cancel out, leaving only X operators behind, see Fig. 2.10(a). The line symmetries are actually a subgroup of a larger subsystem symmetry group generated by the cone symmetries pictured in Fig. 2.10(b). The line symmetries can be expressed as a product of cone symmetries¹¹, but the opposite is not true. Indeed, on an $N \times N$ torus, there are $2N$ independent cone symmetries but only $2N - 1$ independent line symmetries (since the product of all lines in both directions is the identity). In practice, this distinction is not important. This is because any *local* operator (such as a Hamiltonian term or a unitary gate) that commutes with the line symmetries also commutes with the cone symmetries, see Fig. 2.10(c). While it is sufficient to consider only the line symmetries, the cone symmetries will nonetheless be useful in some cases.

Let us now understand the nature of the SPT order of the cluster state by applying the Else-Nayak procedure. For this analysis, we choose our open system M to have the boundary conditions of a 45° -rotated square lattice, such that the line symmetries now move horizontally and vertically, see Fig. 2.10(d). As before, we remove all Hamiltonian terms associated to the boundary spins and then characterize the resulting degenerate ground space in terms of effective Pauli operators \bar{X}_i, \bar{Z}_i defined as follows,

$$\begin{aligned} \bar{X}_i &= U_{CZ,M} X_i U_{CZ,M}^\dagger = X_i Z_{i-\frac{1}{2}} Z_{i+\frac{1}{2}}, \\ \bar{Z}_i &= U_{CZ,M} Z_i U_{CZ,M}^\dagger = Z_i, \end{aligned} \quad (2.119)$$

where the index i labels the boundary spins as shown in Fig. 2.10(d), and $U_{CZ,M}$ is the truncated circuit of CZ gates applied to every edge in the truncated lattice M . Then, we can act on the effective Pauli operators with the vertical line symmetries to find,

$$\begin{aligned} U_i \bar{Z}_i U_i^\dagger &= -\bar{Z}_i, \\ U_{i\pm\frac{1}{2}} \bar{X}_i U_{i\pm\frac{1}{2}}^\dagger &= -\bar{X}_i, \end{aligned} \quad (2.120)$$

with all other actions being trivial, where U_i label line symmetries as in Fig. 2.10(d). We therefore find that the subsystem symmetries U_i act on the boundary as V_i defined as,

$$V_i = \bar{X}_i, V_{i+\frac{1}{2}} = \bar{Z}_i \bar{Z}_{i+1}. \quad (2.121)$$

It is clear that no local term can be added which commutes with all of these boundary symmetries. Therefore, the boundary of the cluster state has an extensive boundary degeneracy that is protected by the symmetry.

The SSPT order of the cluster state is characterized by the anti-commutation of neighbouring line symmetries on the boundary. This can be compared to a

¹¹For example, the product of the left cone symmetry in Fig. 2.10(b) with the same symmetry shifted by one site down and to the right yields the left line symmetry in Fig. 2.10(a).

stack of 1D cluster states, which also has line-like subsystem symmetries (in one direction) corresponding to the global symmetries of each of the 1D states. There is a pair of line symmetries for each line, and the pair anti-commute on the boundary. However, unlike the case of the 2D cluster state, these anti-commutations are restricted to a single line; symmetries on different lines always commute. This difference is what underlies the distinction between *strong* and *weak* SSPT order: an SSPT order is said to be weak if it is equivalent to a stack of 1D SPT orders, and otherwise it is strong [59, 190]. The 2D cluster state is an example of strong SSPT order [190].

It should be noted that cluster states on different lattices can have different forms of subsystem symmetry, including fractal symmetries [27, 191, 192]. In these cases, one can find similar forms of subsystem symmetry fractionalization on the boundaries.

2.7.2 Tensor network representation

Here we construct a tensor network representation of the 2D cluster state and investigate how the subsystem symmetries are realized in terms of symmetries of the local tensor. First, observe that the 1D cluster state tensor with a single-qubit unit-cell (Eq. 2.83) can be drawn pictorially as,

$$\begin{array}{c} | \\ \bullet \\ \text{---} \\ C_1 \end{array} = \begin{array}{c} | \\ \delta \\ \text{---} \\ H \end{array}, \quad (2.122)$$

where H is the Hadamard matrix and the small circle represents a δ -tensor which enforces that all incoming legs take the same value in the $\{|0\rangle, |1\rangle\}$ basis,

$$\begin{array}{c} i_2 \\ \dots \\ i_1 \text{---} \delta \text{---} i_N \end{array} = \delta_{i_1, i_2, \dots, i_N}. \quad (2.123)$$

With these definitions, we can depict a PEPS tensor for the 2D cluster state as follows,

$$\begin{array}{c} / \\ \bullet \\ \text{---} \\ C_1 \end{array} = \begin{array}{c} / \\ \delta \\ \text{---} \\ H \end{array}. \quad (2.124)$$

This tensor produces the correct sign structure of the 2D cluster state, in that it gives a factor of -1 to every pair of neighbouring 1's, just as in the MPS tensor for the 1D cluster state.

For visual clarity, we introduce an alternate tensor network notation,

$$A_{\alpha\beta\gamma\delta}^i = \alpha \begin{array}{c} i \gamma \\ / \\ \bullet \\ \text{---} \\ \delta \end{array} \beta = \alpha \begin{array}{c} \gamma \\ | \\ i \\ \text{---} \\ \delta \end{array} \beta, \quad (2.125)$$

where the physical index lives inside the circle. To derive the symmetries of the cluster tensor C_1 , note that the δ -tensor is invariant under applying X to all of its

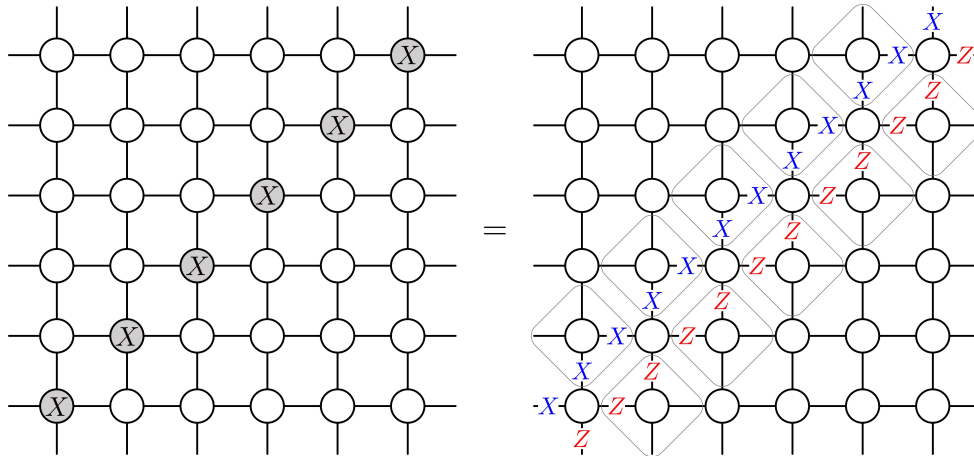


Figure 2.11: Tensor network realization of the line symmetries. The physical X operators in the circles push onto the virtual legs as products of Z and X operators. These operators are absorbed pairwise by the neighbouring tensors using the tensor symmetries, as indicated by diamond outlines.

legs, as well as applying Z to any pair of legs, and that H interchanges X and Z . With this, we can find the following symmetries,

$$\begin{array}{c} \circ \\ | \\ \circ \end{array} = \begin{array}{c} X \\ | \\ \circ \\ | \\ Z \end{array} = \begin{array}{c} Z \\ | \\ \circ \\ | \\ X \end{array} = \begin{array}{c} \circ \\ | \\ X \\ | \\ \circ \end{array} = \begin{array}{c} \circ \\ | \\ Z \\ | \\ \circ \end{array}. \quad (2.126)$$

The first symmetry shows how to push the action of a physical X operator onto the virtual legs of the tensor. The other three symmetries are purely virtual, in that there is no action of the physical index. The products of the above symmetries are also symmetries, but these four form a minimal generating set. These symmetries work together to realize the subsystem symmetries: the X operators push through onto the virtual legs and are subsequently annihilated pairwise using the purely virtual symmetries of neighbouring tensors, see Fig. 2.11. A similar picture holds for the lines symmetries in the other directions and for the cone symmetries.

2.7.3 The cluster phase

Having defined the cluster state and identified its symmetries, we move on to defining the cluster phase. The cluster phase is defined as the symmetry-protected topological phase of matter that contains the cluster state and respects its line symmetries. That is, the cluster phase consists of all states that can be connected to the cluster state with a finite depth quantum circuit whose gates commute with all of the line symmetries. This generalizes the notion of SPT phase to subsystem symmetries, so it is called a subsystem SPT (SSPT) phase [26, 59].

Our first step to characterizing the cluster phase is to understand the structure of PEPS representations of states within the phase. For this, we will establish an equivalent of Eq. 2.97 for the cluster phase [26]. That is, we will see that all states

in the cluster phase can be viewed as a cluster state with extra “junk” entanglement on top, as captured a decomposition of the PEPS tensor.

To warm up, we will re-derive Eq. 2.97 for the 1D cluster phase using an alternative approach. Let $|\Phi\rangle$ be a state in the same SPT phase as the 1D cluster state $|\mathcal{C}\rangle$ (recall that this phase is defined by a $G = \mathbb{Z}_2 \times \mathbb{Z}_2$ symmetry with $U(g_1, g_2) = X_{\text{even}}^{g_1} X_{\text{odd}}^{g_2}$). By definition, this means there is a finite depth quantum circuit $U_\Phi = \prod_i u_{\Phi,i}$ such that $|\Phi\rangle = U_\Phi|\mathcal{C}\rangle$, where each $u_{\Phi,i}$ acts on d qubits and $[u_{\Phi,i}, U(g)] = 0$ for all $g \in G$. Being a finite depth quantum circuit, U_Φ can be expressed as a finite bond-dimension MPO. We could simply combine the MPO tensor with the cluster state MPS tensor to get an MPS representation of $|\Phi\rangle$, giving the first part of Eq. 2.97, but we would be lacking the symmetry condition given by the second part of Eq. 2.97.

We will now transform U_Φ to another operator that acts equivalently on the cluster state such that the resulting MPO tensor satisfies the symmetry condition. Let us expand each gate $u_{\Phi,i}$ in the basis of d -qubit Pauli operators $P \in \mathcal{P}_d$ (which is always possible as they form a basis). We can write any Pauli operator (up to a phase) as a product $P = P^X P^Z$ where $P^{X/Z}$ is some string of X/Z operators (with $Y = iZX$). We then write,

$$u_{\Phi,i} = \sum_j c_j P_j^X P_j^Z, \quad (2.127)$$

for some complex numbers c_j . Since each Pauli operator either commutes or anticommutes with each symmetry $U(g)$, each Pauli operator in the expansion must be individually symmetric, $U(g)P_j^{X/Z}U(g) = P_j^{X/Z}$. Clearly P_j^X can be anything, while one can convince oneself that P_j^Z is only symmetric if it can be written as a product of operators $Z_i Z_{i+2}$.

Now, we observe that $Z_i Z_{i+2}|\mathcal{C}\rangle = X_{i+1}|\mathcal{C}\rangle$ by the form of the cluster state stabilizer. Therefore, when acting on the cluster state, any symmetric Z -string can be replaced by an X -string, such that every gate $u_{\Phi,i}$ in the first layer of the circuit can be re-written as sums of X -strings. For subsequent layers, we need to push the Z -strings down to the first layer where they can act on the cluster state and become X -strings. After all Z -strings in U_Φ have been replaced by X -strings, we will be left with a new operator T_Φ which acts in the same way as U_Φ on the cluster state. In general, T_Φ will no longer be unitary, and the required bond dimension of its MPO representation will be larger than that of U_Φ due to phase factors that were introduced by commuting Z -strings to the first layer, which creates correlations between overlapping gates. Importantly, this increase of bond dimension will only depend on the range and depth of the circuit, which are both finite, so the bond dimension remains finite in the thermodynamic limit. If we denote the MPO tensor that represents T_Φ as B_Φ , we can construct an MPS representation of $|\Phi\rangle$ using a tensor A_Φ defined as,

$$\begin{array}{c} | \\ \bullet \\ \text{---} \\ A_\Phi \end{array} = \begin{array}{c} | \\ \bullet \\ \text{---} \\ B_\Phi \\ \bullet \\ \text{---} \\ C_1 \end{array} \quad \text{where} \quad \begin{array}{c} X \\ | \\ \bullet \\ \text{---} \\ B_\Phi \end{array} = \begin{array}{c} | \\ \bullet \\ \text{---} \\ B_\Phi \\ | \\ X \end{array}. \quad (2.128)$$

which is precisely the statement of Eq. 2.97 for the cluster phase. The symmetry condition follows simply from the fact that T_Φ consists of X operators only.

Now we will repeat this process for the 2D cluster phase. As before, we have a symmetric circuit U_Φ connecting a state $|\Phi\rangle$ to the 2D cluster state. In this case, we take every gate in U_Φ to commute with the line symmetries of the cluster state. Expanding the gates in the Pauli basis, we again have constraints on which Z -strings can appear. Namely, they must be a product of the star operators $S_{x,y} = Z_{x-1,y}Z_{x+1,y}Z_{x,y-1}Z_{x,y+1}$ [26]. Using the 2D cluster state stabilizer, we can write $S_{x,y}|\mathcal{C}\rangle = X_{x,y}|\mathcal{C}\rangle$, so we can again replace U_Φ by a linear operator T_Φ which consists only of X -operators. Representing T_Φ as a tensor network defined by a 6-legged tensor B_Φ , we can construct a PEPS representation for $|\Phi\rangle$ by defining a PEPS tensor A_Φ as,

$$\begin{array}{c} | \\ \text{---} \\ \bullet \\ \text{---} \\ | \\ A_\Phi \end{array} = \begin{array}{c} | \\ \text{---} \\ \bullet \\ \text{---} \\ | \\ B_\Phi \\ \text{---} \\ \bullet \\ \text{---} \\ C_1 \end{array} \quad \text{where} \quad \begin{array}{c} X \\ | \\ \text{---} \\ \bullet \\ \text{---} \\ | \\ B_\Phi \end{array} = \begin{array}{c} | \\ \text{---} \\ \bullet \\ \text{---} \\ | \\ B_\Phi \\ \text{---} \\ X \end{array}. \quad (2.129)$$

This equation gives the fundamental characterization of the 2D cluster phase, and it will be very important for Chapters 3 and 4. One important implication of this equation is that the tensor symmetries of Eq. 2.126 hold throughout the entire cluster phase, where the operators acting on the virtual legs now in general act on a subsystem of the entire virtual space. We will now see how these symmetries allow us to further characterize the SPT order of the cluster phase, and to derive its universality for MBQC.

2.7.4 Quasi-1D SPT order

To analyze the cluster phase further, it will be very useful to adopt a quasi-1D picture. To move to quasi-1D, consider a long cylinder of circumference N and group sites of the lattice into $N \times N$ blocks. Then, the line symmetries act the same way on each block, such that the subsystem symmetries become standard global symmetries on the level of blocks, see Fig. 2.12. In this way, for each N , we can examine the 1D SPT order with respect to the line symmetries, which generate a \mathbb{Z}_2^{2N-1} global symmetry group. Likewise, the cone symmetries generate a \mathbb{Z}_2^{2N} global symmetry group. Let A_Φ denote the tensor obtained by contracting an $N \times N$ block of the local tensor A_Φ . As the subsystem symmetries are global symmetries of this blocked tensor, we can find the virtual representation $V(g)$ of the symmetry group as in Eq. 2.91. This can be done by using the tensor symmetries of Eq. 2.126, and the results are shown in Fig. 2.13. These symmetries hold throughout the entire cluster phase, where the virtual operators act on a subspace in general, by virtue of Eq. 2.129.

From these relations, we see that neighbouring line symmetries moving in the same direction anti-commute on the virtual boundary. This reproduces the result we saw using the Else-Nayak procedure. The advantage of the tensor network approach is that we can see this anti-commutation throughout the entire cluster phase. The virtual representation of the whole \mathbb{Z}_2^{2N} group of cone symmetries, on

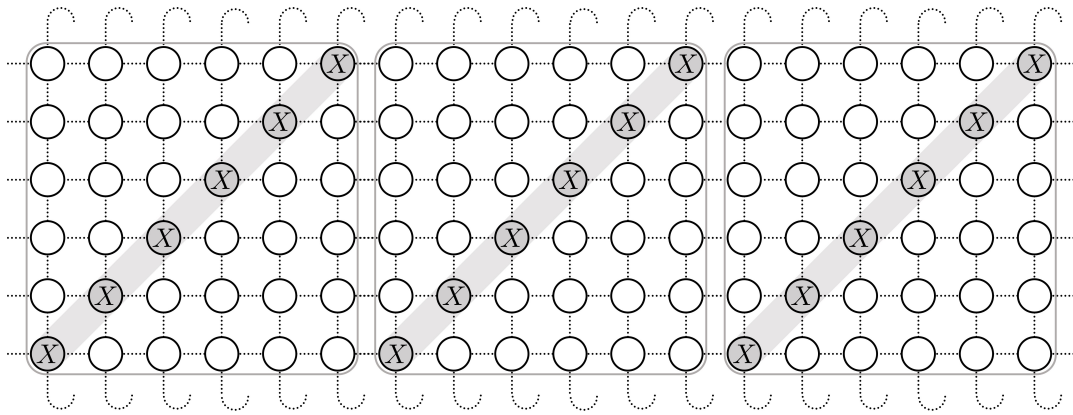


Figure 2.12: Line symmetries on a cylinder with periodic boundaries in the vertical direction. The lines become global symmetries on $N \times N$ blocks ($N = 6$ here), indicated by the square outlines.

the other hand, is given by the full set of N qubit Pauli operators. Importantly, this representation satisfies the condition of maximal non-commutativity defined in Section 2.5.2, since no Pauli operator commutes with all others. This means we can cast the tensor \mathbb{A}_Φ into the form of Eq. 2.95,

$$\mathbb{A}_\Phi[k] = \mathbb{B}_\Phi[k] \otimes \mathbb{C}[k], \quad (2.130)$$

where k labels states of the $N \times N$ block in the local X -bases. The matrices $\mathbb{C}[k]$ will be elements of the virtual symmetry representation, *i.e.* Pauli operators, and can be equivalently determined either by using Eq. 2.96, or by stitching together the cluster tensors C_1 into blocks.

2.7.5 Universal MBQC in the cluster phase

In this section we show that the cluster phase is a computationally universal phase of matter, in that every ground state in the phase can be used as a resource for universal MBQC. As we saw in Section 2.6, MBQC with SPT phases can be understood as an encoding of logical information into the protected edge modes. Since SSPT order has an extensive number of protected edge modes, it allows us to encode an extensive number of logical qubits, as is required to have a universal MBQC scheme. This simple observation helps to explain why SSPT order is the natural thing to consider for universal MBQC in 2D. Since the 2D cluster state fits into the framework of 1D SPT order after blocking, we can apply the techniques for MBQC with 1D SPT phases. We note that our use of blocking does not affect the notion of locality for MBQC, as we will still employ only single-qubit measurements. Indeed, this restriction to single-qubit measurements¹² is what stops us from trivially achieving universal MBQC by applying the 1D results to a 1D SPT phase with an exponentially large edge mode.

¹²More precisely, we would like that the dimension of the measured local degrees of freedom does not grow with the number of logical qubits.

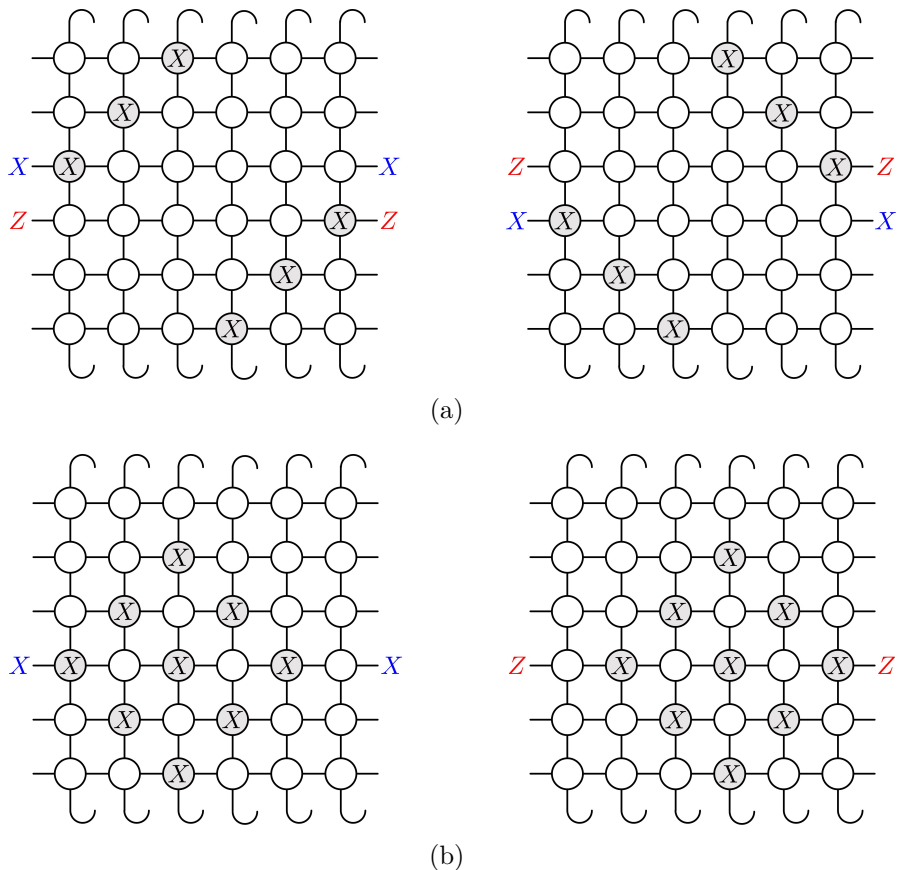


Figure 2.13: (a) Tensor network representation of line symmetries on the level of blocks, with the corresponding virtual symmetry representations shown on the edges. (b) Tensor network representation of cone symmetries.

To determine which gates can be performed, we need to identify (some of) the operators $\mathbb{C}[k]$ in Eq. 2.130. Let $|e_{i,j}\rangle$ denote the state of a block of $N \times N$ qubits where all qubits in the block are in the state $|+\rangle$ except for the qubit in column i and row j , which is in the state $|-\rangle$. Then, we can find,

$$\begin{aligned} \mathbb{C}[e_{1,j}] &= Z_j, \\ \mathbb{C}[e_{2,j}] &= Z_{j-1}X_jZ_{j+1}, \\ \mathbb{C}[e_{N,j}] &= X_j. \end{aligned} \tag{2.131}$$

Recall that non-trivial gates in the MBQC scheme are performed measuring in a rotated basis. The above equations tell us that measuring the j -th spin in the first (last) column in the basis $\{|\theta_+\rangle, |\theta_-\rangle\}$ [Eq. 2.110] results in a rotation of the j -th logical qubit about the Z -axis (X -axis) by θ , up to Pauli byproduct operators. These operations generate all single-qubit unitaries. Measuring the j -th qubit in the second column in the rotated basis results in an entangling gate between the j -th qubit and its two neighbours. Together with the single-qubit gates, this generates a full set of N -qubit gates [193]. Using the same techniques for 1D SPT phases, with some slight modifications, these gates can be implemented throughout the entire 2D cluster phase, making it the first example of a computationally

universal phase of matter [26].

2.7.6 Gauging subsystem symmetries and fracton topological order

In Section 2.3.4, we defined the gauging map that transforms trivial and SPT phases into topological phases. In this section, we briefly describe a generalized gauging procedure that can be done for subsystem symmetries [53, 110, 194]. In the case of global symmetries, we finished by expressing the gauging map as a duality transformation between the pure matter and pure gauge theories. For subsystem symmetries, we will jump straight to this expression of gauging, although we note that one can derive the following procedure using a more conventional minimal coupling procedure [53].

The generalized gauging procedure can be defined by the following three steps. For simplicity, will focus on gauging \mathbb{Z}_2 symmetries whose generators consist of products of X operators.

- The first step in the gauging procedure is to identify the minimal coupling terms. These are the minimal interactions that can be added to a Hamiltonian which respect all symmetries. For a global \mathbb{Z}_2 symmetry, the minimal coupling terms corresponds to nearest-neighbour ZZ interactions. We then add one gauge qubit associated to each minimal coupling term at the centre of the interaction, *e.g.* on the links of the lattice in the case of a global symmetry.
- The second step is to add the gauge constraint term. To identify this term, we look for relations among the minimal coupling terms, *i.e.* products of them that equal the identity. The gauge constraint is then a product of Z operators on every gauge qubit whose associated minimal coupling terms are involved in the relation. For example, the product of all nearest-neighbour ZZ interactions around a face of the lattice is the identity, so the gauge constraint for a global symmetry is a product of Z on all edges around each face.
- The final step is to map the original Hamiltonian terms of the matter theory onto modified terms acting on the gauge qubits. Every symmetric term can be expressed in terms of X operators and products of the minimal coupling terms. Each minimal coupling term is mapped onto a single Z acting on the associated gauge qubit. X operators are mapped onto a product of X operators on every gauge qubit whose associated minimal coupling terms anti-commutes with the original X operator.

It is straightforward to verify that applying this procedure to a global symmetry reproduces the procedure outlined in Section 2.3.4. In Chapter 5.2, we will apply this procedure to an example with subsystem symmetries. Importantly, only the final step depends on the Hamiltonian that is to be gauged, and the rest of the procedure depends only on the form of the subsystem symmetries.

While gauging global symmetries can result in topological order, gauging certain subsystem symmetries can result in a more exotic kind of order known as fracton topological order (or simply fracton order) [30, 50–55, 194–198]. This can only occur in 3D and higher [57]. Indeed, gauging, *e.g.*, line symmetries in 2D results in a model with symmetry breaking (or, in the case of the cluster state, simply maps it onto itself [110]). In 3D, gauging subsystem symmetries that act on planes or fractals can result in model of topological order in which the point-like topological excitations have restricted mobility [53, 110, 194]. That is, individual excitations may only be able to move (without creating additional excitations) in one or two directions, or they may be completely immobile. These mobility constraints, which arise from the geometry of the subsystem symmetries, are the defining characteristics of the umbrella term of fracton order.

Due to the rigid nature of the subsystem symmetries, models with fracton order are sensitive to the geometry of the space on which they are defined, as opposed to topological models which depend only on global topology. For example, the ground space degeneracy [30, 54] and topological entanglement entropy [199–201] of fracton models can depend both on topology and system size, and the nature of gapped boundaries changes drastically depending on the shape of the boundary [202]. These features mean that fracton order is beyond the realm of topological quantum field theory due to a mixing of infrared and ultraviolet scales [203], which makes it difficult to apply our usual tools for classifying phases of matter, although some promising frameworks are arising [57, 204]. Additionally, the mobility restrictions lead to slow dynamics [205] that can make certain fracton models suitable for robust storage of quantum information. More precisely, for some models, the energy barrier between two topological ground states grows with system size, meaning the lifetime of a qubit stored in the ground space grows with system size [44, 45]. For these reasons and more, fracton topological order is interesting to both the condensed matter and quantum information communities.

Chapter 3

Universal subsystem symmetry protected topological phases from quantum cellular automata

At the end of the previous chapter, we defined an SSPT phase of matter with line-like subsystem symmetries called the cluster phase. We then characterized it in terms of symmetries of PEPS tensors, and showed that it was an MBQC-universal phase of matter. In this chapter, we aim to generalize this result to encompass other SSPT phases with other types of subsystem symmetry. Our goal is twofold: we wish to characterize the symmetries and entanglement structure of these phases of matter, and we wish to understand their use for MBQC. It turns out that a single concept is sufficient to achieve both of these goals: quantum cellular automata (QCA) [132, 206–208]. QCA can be simply defined as a locality preserving unitary operators and, for the class of QCA we consider, they are equivalent to finite-depth quantum circuits.

To see why QCA are relevant to SSPT phases, consider a single column of the cluster state PEPS. Using the symmetries of a single tensor (Eq. 2.126), we can derive the following symmetries of the column,

$$\begin{array}{c} \text{---} \circ \text{---} \\ | \\ \text{---} \circ \text{---} \\ | \\ \text{---} \circ \text{---} \\ | \\ \text{---} \circ \text{---} \\ | \\ \text{---} \circ \text{---} \\ | \\ \text{---} \circ \text{---} \\ | \\ \text{---} \circ \text{---} \end{array} \begin{array}{c} \text{---} \circ \text{---} \\ | \\ \text{---} \circ \text{---} \\ | \\ \text{---} \circ \text{---} \\ | \\ \text{---} \circ \text{---} \\ | \\ \text{---} \circ \text{---} \\ | \\ \text{---} \circ \text{---} \\ | \\ \text{---} \circ \text{---} \end{array} = \begin{array}{c} \text{---} \circ \text{---} \\ | \\ \text{---} \circ \text{---} \\ | \\ \text{---} \circ \text{---} \\ | \\ \text{---} \circ \text{---} \\ | \\ \text{---} \circ \text{---} \\ | \\ \text{---} \circ \text{---} \\ | \\ \text{---} \circ \text{---} \end{array} \begin{array}{c} \text{---} \circ \text{---} \\ | \\ \text{---} \circ \text{---} \\ | \\ \text{---} \circ \text{---} \\ | \\ \text{---} \circ \text{---} \\ | \\ \text{---} \circ \text{---} \\ | \\ \text{---} \circ \text{---} \\ | \\ \text{---} \circ \text{---} \end{array}, \begin{array}{c} \text{---} \circ \text{---} \\ | \\ \text{---} \circ \text{---} \\ | \\ \text{---} \circ \text{---} \\ | \\ \text{---} \circ \text{---} \\ | \\ \text{---} \circ \text{---} \\ | \\ \text{---} \circ \text{---} \\ | \\ \text{---} \circ \text{---} \end{array} \begin{array}{c} \text{---} \circ \text{---} \\ | \\ \text{---} \circ \text{---} \\ | \\ \text{---} \circ \text{---} \\ | \\ \text{---} \circ \text{---} \\ | \\ \text{---} \circ \text{---} \\ | \\ \text{---} \circ \text{---} \\ | \\ \text{---} \circ \text{---} \end{array} \begin{array}{c} \text{---} \circ \text{---} \\ | \\ \text{---} \circ \text{---} \\ | \\ \text{---} \circ \text{---} \\ | \\ \text{---} \circ \text{---} \\ | \\ \text{---} \circ \text{---} \\ | \\ \text{---} \circ \text{---} \\ | \\ \text{---} \circ \text{---} \end{array} \tag{3.1}$$

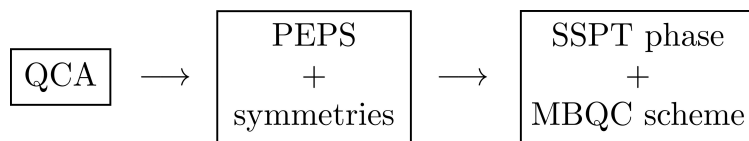
These equations show that the operator Z_i transforms into X_i when passing through the column tensor, while X_i transforms into $Z_{i-1}X_iZ_{i+1}$ (with the help of an X on the physical index). From these relations, it follows that contracting the physical

legs of the column tensor with states in the X -basis gives the following operator,

$$(3.2)$$

where $i_k = 0, 1$ represent the physical states $|+\rangle, |-\rangle$, respectively. We have drawn the resulting virtual operator using the notation of quantum circuits, where H is the Hadamard matrix, and the vertical lines represent CZ operators acting on the two connected legs. Contracting the physical legs in the $\{|+\rangle, |-\rangle\}$ basis results in a quantum circuit acting in the virtual space. As we will see in this chapter, this quantum circuit, which can be described using the language of QCA, determines the form of the subsystem symmetries, and plays an essential role in MBQC.

The construction in this chapter involves modifying this QCA to change the symmetries and MBQC power of the resulting SSPT phase of matter. In more detail, given a QCA, we define a fixed-point state via a local PEPS tensor such that the QCA lives in the virtual space of the tensor network, as in Eq. 3.2. This fixed-point state will have some subsystem symmetries determined by the QCA, so we can define an associated SSPT phase of matter as the set of all states connected to the fixed-point state while respecting the subsystem symmetries. This SSPT phase of matter will in turn have an associated MBQC scheme whose elementary gates are determined by the QCA. The whole process can be summarized via the following flowchart,



In this way, we show that QCA are the essential ingredient that unify SSPT phases and MBQC, see Fig. 3.1.

Our first main result in this construction shows that non-trivial SSPT order under the symmetries we consider is characterized by the presence of the QCA within the tensor network, which is persistent throughout the corresponding SSPT phase. This is akin to the behaviour that we have seen in the cluster phase in Section 2.7.1. This means the patterns of entanglement found in these phases are characterized in part by QCA, demonstrating the possible use of tensor networks in obtaining a classification of SSPT order. Interestingly, our framework treats line-like symmetries and fractal symmetries on the same footing, showing that different types of subsystem symmetries are more similar than one would think

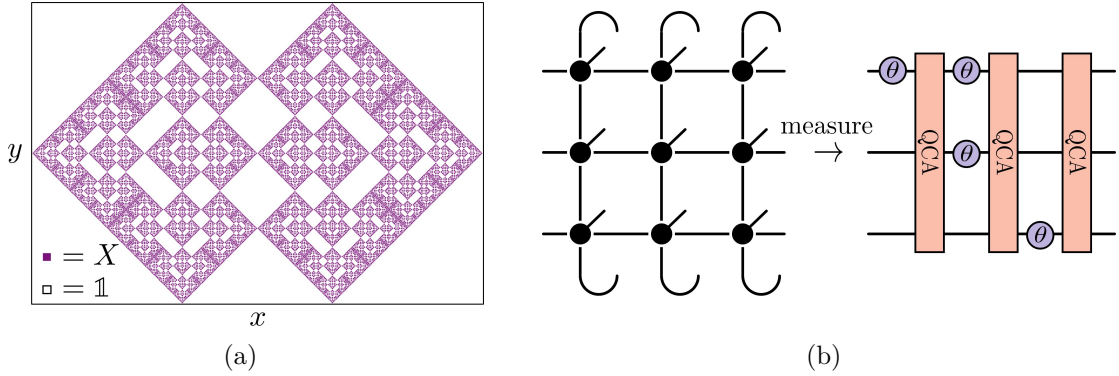


Figure 3.1: Two of the roles played by QCA in our results. a) Example of a fractal symmetry operator defined by QCA that emerges from our framework. The operator is a tensor product of local Pauli- X operators arranged on a square lattice in the pattern shown. b) We define tensor network states from QCA, such that measuring a block of spins results in a quantum circuit living in the virtual space of the tensor network. The circuit, which forms the backbone of our MBQC scheme, consists of global applications of the QCA interspersed by single qubit rotations determined by the bases in which spins are measured. This structure appears within every state in the corresponding SSPT phase, leading to uniform computational power across the phase.

based on their structure. Indeed, we find that the 2D cluster state has SSPT order under both types of symmetries.

We then turn to investigating the computational capability of the constructed phases. Using the above characterization, we show that every phase we construct is computationally universal in the same way as the cluster phase, except for those defined by non-entangling QCA. Hence, our framework gives a systematic way to identify computationally universal phases of matter which, up until now, have remained elusive outside a select few cases [26, 27]. The computational schemes we develop are strictly tied to the QCA that define the phases (see Fig. 3.1(b)), further strengthening the connection between quantum computation and SPT phases in 2D¹.

Our perspective on MBQC based on QCA has the additional feature that, by choosing different QCA, the set of gates executable in a single step can be tailored to suit the problem at hand. In particular, our framework allowed us to uncover a particular class of SSPT phases for which the corresponding computational schemes enjoy a quadratic reduction in the number of measurements per gate versus the number of logical qubits, as compared to previous schemes [26, 27]. One such phase is built around a modified cluster state with additional qubits placed on the horizontal edges. We briefly discuss the implications that this result and our general framework may have on related tasks such as blind quantum computation [209, 210], quantum computation with global control [193, 211, 212], and in experimental demonstrations of quantum computational advantage [213, 214].

¹Since the writing of this chapter, another work has furthered this line of work by identifying the QCA underlying cluster states on various regular lattices [192].

The rest of this chapter is organized as follows. In Section 3.1, we begin with a review the basic properties of QCA. In Section 3.2, we use QCA to define tensor network states and show that they have non-trivial SPT order under certain subsystem symmetries. Then, in Section 3.3, we investigate the properties of the corresponding SPT phases in a quasi-1D picture before moving to a genuine 2D picture in Section 3.4. In Section 3.5, we classify these phases by their computational power in measurement-based quantum computing. Finally, in Section 3.6, we discuss possible applications and extensions of our results.

3.1 Quantum cellular automata

In this section, we present a review of *quantum cellular automata (QCA)* for qubit systems, as described in Refs. [206–208], as they will be central to our description of SSPT order. A 1D QCA is a translationally-invariant locality-preserving unitary acting on a 1D chain of qubits [206]. That is, a QCA maps any locally supported operator to another locally supported operator, with the size of the support increased by an amount independent of the size of the original support. In Ref. [132], it was shown that QCA acting on 1D systems are equivalent to *matrix product unitaries (MPU)*, in that every QCA can be represented as an MPU with finite bond dimension, and every MPU is a QCA. An MPU is a matrix product operator defined by a local tensor \mathcal{T} , which generates a unitary T on a ring of arbitrary length N . Graphically, the MPU can be represented by the tensor network,

$$T = \text{---} \left(\begin{array}{c} | \\ \bullet \\ | \\ \mathcal{T} \end{array} \right) \text{---} \left(\begin{array}{c} | \\ \bullet \\ | \\ \mathcal{T} \end{array} \right) \text{---} \cdots \text{---} \left(\begin{array}{c} | \\ \bullet \\ | \\ \mathcal{T} \end{array} \right) \text{---} \cdot \quad (3.3)$$

We note that all QCA described in this chapter act on systems with periodic boundary conditions.

In what follows, we will focus on *Clifford quantum cellular automata (CQCA)* [207, 208], which are QCA that map products of Pauli operators to products of Pauli operators. For reasons of simplicity of notation, we focus on the Pauli Clifford group for qubits, even though the formalism laid out here could be applied larger dimensions as well [215, 216]. On a finite chain of N qubits, we can define the Pauli group \mathcal{P}_N as the group generated by all local Pauli operators X_i , Y_i , and Z_i acting on qubit i , where i is defined modulo N and can take negative values giving, for example, $X_{-1} = X_{N-1}$. A CQCA is a QCA that is also an automorphism of \mathcal{P}_N , defined by a unitary transition function T such that $P \mapsto T(P) := T^\dagger P T$ for any $P \in \mathcal{P}_N$.

CQCA have been studied extensively in Refs. [207, 208] which introduced a compact representation of CQCA. Firstly, a CQCA T is completely specified by the images $T(X_0)$ and $T(Z_0)$. To see this, note that the QCA is translationally invariant, and that X_i and Z_i generate the whole Pauli group up to phases, which contains a basis of the space of all $2^N \times 2^N$ matrices. We represent elements of \mathcal{P}_N , up to phases, by $2N$ -component binary strings $\boldsymbol{\xi} = (\boldsymbol{\xi}^X, \boldsymbol{\xi}^Z)$ such that,

$$V(\boldsymbol{\xi}) = \bigotimes_{i=1}^N X_i^{\xi_i^X} Z_i^{\xi_i^Z} \in \mathcal{P}_N. \quad (3.4)$$

These strings form the group $\mathbb{Z}_2^N \times \mathbb{Z}_2^N$, for which $\boldsymbol{\xi} \mapsto V(\boldsymbol{\xi})$ forms a faithful irreducible projective representation. Note that we ignore all complex phases in front of Pauli operators throughout, since they do not affect the symmetries or phases of matter we define. We further condense the notation using the language of Laurent polynomials [207]. We map $\boldsymbol{\xi}$ onto a vector of polynomials of a variable u as,

$$\begin{pmatrix} \boldsymbol{\xi}^X \\ \boldsymbol{\xi}^Z \end{pmatrix} \mapsto \begin{pmatrix} \sum_i (u^i)^{\xi_i^X} \\ \sum_i (u^i)^{\xi_i^Z} \end{pmatrix}. \quad (3.5)$$

The purpose of the variable u is to keep track of the moving and spreading of local Pauli operators under T . For example, the operator $X_1 Z_0 X_{-1}$ is represented as,

$$\boldsymbol{\xi} = \begin{pmatrix} u + u^{-1} \\ 1 \end{pmatrix}. \quad (3.6)$$

We use the symbol $\boldsymbol{\xi}$ to represent both the binary and polynomial representations of an element of \mathcal{P}_N interchangeably.

Finally, we can represent the CQCA T as a 2×2 matrix t of polynomials by arranging,

$$T(X_0) := t \begin{pmatrix} 1 \\ 0 \end{pmatrix}, \quad T(Z_0) := t \begin{pmatrix} 0 \\ 1 \end{pmatrix}, \quad (3.7)$$

into columns of a matrix. For a concrete example, consider the CQCA T_g defined by the relations,

$$T_g(X_i) = X_{i-1} Z_i X_{i+1}, \quad T_g(Z_i) = X_i. \quad (3.8)$$

This CQCA is the QCA of the 2D cluster state [11], which was derived in the introduction of this chapter and has appeared several times already in the context of quantum computation [193, 213, 217]. The subscript g refers to the term *glider* which we shall introduce shortly. In the polynomial representation, this CQCA becomes,

$$t_g = \begin{pmatrix} u + u^{-1} & 1 \\ 1 & 0 \end{pmatrix}. \quad (3.9)$$

Every CQCA T can be represented as a 2×2 matrix t whose entries are Laurent polynomials over \mathbb{Z}_2 , up to phase factors [207]. We further restrict to CQCA for which the images $T(X_i)$, $T(Z_i)$ are symmetric about site i , meaning there is no translation in the CQCA². As shown in Ref. [207], this corresponds to the matrix t having unit determinant. We make this restriction only because translation will not be particularly interesting for our purposes, as it would correspond to a simple lattice shear. With this restriction, we have that all entries in t are symmetric Laurent polynomials, meaning that u^{-k} appears whenever u^k does, for all k . Finally, we implement the periodic boundary conditions by taking all polynomials modulo the relation $u^N = 1$.

CQCA can be split into three classes depending on their trace [208].

- *Periodic CQCA*. When $\text{Tr}(t) = 0$ or 1 the CQCA has *periodic* behaviour.

²In Refs. [132, 218], QCA are assigned an index according to the amount of information flow to the left or right. Our restriction is to QCA with index 0

- *Glider CQCA*. When $\text{Tr}(t) = u^c + u^{-c}$ for some positive integer c , the CQCA supports *gliders*. These are operators on which the CQCA acts as translation by $\pm c$ sites.
- *Fractal CQCA*. If neither of these conditions hold, the CQCA will display self-similar *fractal* behaviour.

The CQCA in Eq. (3.8) is of glider type, with $\text{Tr}(t_g) = u + u^{-1}$. Indeed, we can check that $T_g(X_i Z_{i-1}) = X_{i+1} Z_i$, and $T_g(Z_{i+1} X_i) = Z_i X_{i-1}$.

The Laurent polynomial representation allows us to uncover an identity which will be useful at several points throughout this work. Namely, due to the Cayley-Hamilton theorem, we obtain [208],

$$t^2 = \text{Tr}(t)t + \mathbb{1}, \quad (3.10)$$

where we have used our assumption that $\det(t) = 1$, and the fact that the polynomials are defined over the field \mathbb{Z}_2 , so addition and subtraction are equivalent. This useful equation allows us to reduce any power of t to a linear combination of t and $\mathbb{1}$.

3.2 Defining PEPS from QCA

Now we use the correspondence between QCA and MPU to define fixed-point PEPS. Given a CQCA T , we first represent it as an MPU with local tensor \mathcal{T} , as described in Ref. [132]. We then define the PEPS in terms of \mathcal{T} by a local tensor A_T whose components are given by,

$$\begin{array}{c} |+\rangle \\ \downarrow \\ \text{---} \bullet \text{---} \\ /A_T \end{array} := \begin{array}{c} \text{---} \bullet \text{---} \\ / \mathcal{T} \end{array}, \quad \begin{array}{c} |-\rangle \\ \downarrow \\ \text{---} \bullet \text{---} \\ /A_T \end{array} := -Z \begin{array}{c} \text{---} \bullet \text{---} \\ / \mathcal{T} \end{array}. \quad (3.11)$$

Given \mathcal{T} , the PEPS tensors A_T for local qubit dimension can be uniquely defined in this way, the vectors $\{|+\rangle, |-\rangle\}$ constituting a basis. In this chapter we will mainly consider a quasi-1D geometry with the mapping to quasi-1D proceeding as in Section 2.7. That is, we put our PEPS on a long, skinny torus of dimensions $N \times M$ ($M \gg N$) and block tensors A_T into rings along the skinny direction of the torus,

$$\begin{array}{c} j_1 \\ \downarrow \\ \text{---} \bullet \text{---} \\ j_2 / A_T \\ \downarrow \\ \text{---} \bullet \text{---} \\ j_N / A_T \\ \downarrow \\ \text{---} \bullet \text{---} \\ j_N / A_T \end{array} := \begin{array}{c} j \\ \downarrow \\ \text{---} \bullet \text{---} \\ = A_T \end{array}, \quad (3.12)$$

where $j_i = 0$ (1) denotes the state $|+\rangle$ ($|-\rangle$). We denote the resulting blocked MPS tensor by \mathcal{A}_T . Notably, the virtual legs of A_T that are contracted to form

\mathcal{A}_T correspond to the virtual legs of the MPU defining T , such that the CQCA T appears in the virtual space of \mathcal{A}_T as seen in the introduction of this chapter.

The state vector of the fixed-point PEPS is then written as,

$$|\psi_T\rangle = \sum_{\mathbf{j}_1, \dots, \mathbf{j}_M} \text{Tr} \left(\mathcal{A}_T^{\mathbf{j}_1} \mathcal{A}_T^{\mathbf{j}_2} \dots \mathcal{A}_T^{\mathbf{j}_M} \right) |\mathbf{j}_1, \mathbf{j}_2, \dots, \mathbf{j}_M\rangle. \quad (3.13)$$

In general, $|\psi_T\rangle$ will not be rotationally invariant, and the dimension of the virtual indices along the horizontal and vertical directions may not even match. Since we will be mainly treating these PEPS as quasi-1D systems, we will not worry about this property of our construction here. We call the states $|\psi_T\rangle$ “fixed-point” PEPS because they will appear as special points within SPT phases, such as the cluster state within the cluster phase. However, they are not fixed-points of any renormalization transformation defined here. We stress that, although we use a quasi-1D approach, the SSPT phases that we construct can be distinct from stacks of 1D SPT chains, as will be discussed in Section 3.4.

We could have instead chosen to define our PEPS by replacing the Pauli Z in the $|-\rangle$ -component of A_T with an X or Y . It turns out that these cases are already included in the current definition. For example, replacing the Z with an X is equivalent to conjugating T by Hadamard gates on every leg, represented as $t \mapsto hth^{-1}$ where,

$$h = \begin{pmatrix} 0 & 1 \\ 1 & 0 \end{pmatrix}. \quad (3.14)$$

Similarly, exchanging Z with Y is equivalent to conjugation by phase gates, $t \mapsto sts^{-1}$, where,

$$s = \begin{pmatrix} 1 & 0 \\ 1 & 1 \end{pmatrix}. \quad (3.15)$$

Were we to also include a Pauli operator in the $|+\rangle$ -component of A_T , this would be equivalent to one of the three cases discussed above, up to rephasing of T , which is unimportant to us. Hence, we can use the definition of A_T given by Eq. (3.11) without loss of generality.

As follows straightforwardly from its definition (Eqs. (3.11,3.12)), the tensor \mathcal{A}_T has the symmetries,

$$\begin{aligned} X_i \text{---} \bullet \text{---} &= \text{---} \bullet \text{---} T(X_i), \\ \mathcal{A}_T & \mathcal{A}_T \\ Z_i \text{---} \bullet \text{---} &= \text{---} \bullet \text{---} T(Z_i). \\ \mathcal{A}_T & \mathcal{A}_T \end{aligned} \quad (3.16)$$

That is, a Pauli Z acting in the virtual space passes through each ring freely and is transformed by the QCA T , while a virtual X passes through with the help of a physical X operator. This is the generalization of Eq. 3.1. More generally, we can push any Pauli operator $V(\boldsymbol{\xi})$ through the ring in the following manner,

$$V(\boldsymbol{\xi}) \text{---} \bullet \text{---} = \text{---} \bullet \text{---} V(t\boldsymbol{\xi}), \quad (3.17)$$

where we have defined the physical symmetry operator,

$$u(\boldsymbol{\xi}) := \bigotimes_{i=1}^N X_i^{\xi_i^X}. \quad (3.18)$$

Since we impose periodic boundary conditions, the CQCA will have a finite period L such that $t^L = \mathbb{1}$. In general, L is a complicated function of the circumference N of the torus, a point which we return to in Section 3.5.1. If we push any Pauli operator in the virtual space through L rings of the PEPS, it will be mapped to itself, leading to the symmetry,

$$\begin{aligned} & \begin{array}{cccc} u(\boldsymbol{\xi}) & u(t\boldsymbol{\xi}) & u(t^2\boldsymbol{\xi}) & \dots & u(t^{L-1}\boldsymbol{\xi}) \\ \parallel & \parallel & \parallel & & \parallel \\ \text{---} \bullet \text{---} & \text{---} \bullet \text{---} & \text{---} \bullet \text{---} & \dots & \text{---} \bullet \text{---} \\ & \mathcal{A}_T & \mathcal{A}_T & & \mathcal{A}_T \end{array} \\ = & V(\boldsymbol{\xi}) \begin{array}{cccc} \parallel & \parallel & \parallel & \dots & \parallel \\ \text{---} \bullet \text{---} & \text{---} \bullet \text{---} & \text{---} \bullet \text{---} & \dots & \text{---} \bullet \text{---} \\ & \mathcal{A}_T & \mathcal{A}_T & & \mathcal{A}_T \end{array} V(\boldsymbol{\xi})^\dagger. \end{aligned} \quad (3.19)$$

Hence, if we set $M = kL$, $k \in \mathbb{N}$, our state satisfies,

$$U_T(\boldsymbol{\xi})^{\otimes k} |\psi_T\rangle = |\psi_T\rangle, \quad (3.20)$$

where the symmetry representation $\boldsymbol{\xi} \mapsto U_T(\boldsymbol{\xi})^{\otimes k}$ is defined as,

$$U_T(\boldsymbol{\xi}) := u(\boldsymbol{\xi}) \otimes u(t\boldsymbol{\xi}) \otimes \dots \otimes u(t^{L-1}\boldsymbol{\xi}). \quad (3.21)$$

The unitary $U_T(\boldsymbol{\xi})$ is more general than the usual global on-site symmetry operator. Rather than acting the same way on each site in the lattice, the representation “cycles” with a period L . Such symmetries have been called *L-cycle symmetries* in Ref. [219]. If we block our PEPS into large blocks of size $N \times L$, $U_T(\boldsymbol{\xi})^{\otimes k}$ becomes a standard global symmetry that acts in the same way on each block. In this way, we can look at the conventional 1D SPT order protected by $U_T(\boldsymbol{\xi})$. Since $\boldsymbol{\xi} \mapsto V(\boldsymbol{\xi})$ forms a projective representation of $\mathbb{Z}_2^N \times \mathbb{Z}_2^N$, the fixed-point PEPS have non-trivial quasi-1D SPT order with respect to this symmetry, and in fact satisfies the condition of maximal non-commutativity given in Section 2.5.2. As we discuss in Section 3.4, this means they also have non-trivial 2D SPT order with respect to the same symmetries.

Examples. Let us study some examples of the fixed-point PEPS we have constructed. First, consider the CQCA T_g from Eq. (3.8). In this case, the fixed-point PEPS defined by Eq. (3.11) represents the 2D cluster state. The corresponding L -cycle symmetry has the form of cone-like operators with $L = N$, as pictured in Fig. 2.10(b). The SPT phase defined by these symmetries is exactly the cluster phase defined in Section 2.7.1.

For an example using a CQCA with fractal behaviour, consider the CQCA T_f defined by the relations,

$$T_f(X_i) = X_{i-1}Y_iX_{i+1}, T_f(Z_i) = X_i. \quad (3.22)$$

The corresponding fixed-point PEPS will turn out to be the cluster state again, with the phase gate,

$$S = \begin{pmatrix} 1 & 0 \\ 0 & i \end{pmatrix}, \quad (3.23)$$

applied to each site. The L -cycle symmetries also have a fractal structure, see Fig. 3.1(a) for an example with $N = 512$, $L = \frac{3}{2}N = 768$. This shows that the cluster state also has SPT order under fractal symmetries that are tensor products of Pauli- Y operators (since $SXS^\dagger = Y$).

For a periodic CQCA, we choose T_p defined as,

$$T_p(X_i) = Z_i, T_p(Z_i) = X_i. \quad (3.24)$$

That is, $t_p = h$ where h is as defined in Eq. (3.14). This corresponds to a stack of decoupled 1D cluster states, and the L -cycle symmetries are simple horizontal lines which are the symmetries of each of the 1D states.

3.2.1 Stabilizer representations of fixed-point PEPS

The above examples are all states that can be defined by a local stabilizer group [89], which is a feature common for any fixed-point PEPS constructed by Eq. (3.11), as we now demonstrate.

To start, notice that the fixed-point PEPS defined by Eq. (3.11) have more symmetries than those shown in Eq. (3.16). They also have the following symmetries,

$$Z_i \underset{\mathcal{A}_T}{=} \bullet \underset{\mathcal{A}_T}{=} = \underset{\mathcal{A}_T}{=} \overset{Z_i}{\bullet} \underset{\mathcal{A}_T}{=} = \underset{\mathcal{A}_T}{=} \bullet \underset{\mathcal{A}_T}{=} T(Z_i). \quad (3.25)$$

Note that these symmetries exist only at the fixed-point, and they do not persist throughout the corresponding SPT phase. In addition to these symmetries, we also need the identity from Eq. (3.10). In general, we have $\text{Tr}(t) = \sum_{k=1}^m \alpha_k (u^k + u^{-k}) + \beta$ for $\alpha_k, \beta \in \{0, 1\}$. Stated in terms of operators, Eq. (3.10) tells us,

$$T^2(Z_i) = Z_i \bigotimes_{k=1}^m [T(Z_{i-k})T(Z_{i+k})]^{\alpha_k} T(Z_i)^\beta. \quad (3.26)$$

Using Eqs. (3.16), (3.25) and (3.26), we can now determine the form of the stabilizers

for our states,

$$\begin{aligned}
 \begin{array}{c} \parallel \\ \bullet \\ \parallel \\ \mathcal{A}_T \end{array} & \begin{array}{c} \parallel \\ \bullet \\ \parallel \\ \mathcal{A}_T \end{array} \begin{array}{c} \parallel \\ \bullet \\ \parallel \\ \mathcal{A}_T \end{array} = \begin{array}{c} Z_i \\ \parallel \\ \bullet \\ \parallel \\ \mathcal{A}_T \end{array} T(Z_i) \begin{array}{c} \parallel \\ \bullet \\ \parallel \\ \mathcal{A}_T \end{array} \begin{array}{c} \parallel \\ \bullet \\ \parallel \\ \mathcal{A}_T \end{array} \\
 & = \begin{array}{c} Z_i \\ \parallel \\ \bullet \\ \parallel \\ \mathcal{A}_T \end{array} \begin{array}{c} u(\tilde{\xi}) \\ \parallel \\ \bullet \\ \parallel \\ \mathcal{A}_T \end{array} T^2(Z_i) \begin{array}{c} \parallel \\ \bullet \\ \parallel \\ \mathcal{A}_T \end{array} \\
 & = \begin{array}{c} Z_i \\ \parallel \\ \bullet \\ \parallel \\ \mathcal{A}_T \end{array} \begin{array}{c} u(\tilde{\xi}) \cdot \tilde{Z} \\ \parallel \\ \bullet \\ \parallel \\ \mathcal{A}_T \end{array} \begin{array}{c} Z_i \\ \parallel \\ \bullet \\ \parallel \\ \mathcal{A}_T \end{array} . \quad (3.27)
 \end{aligned}$$

In the first equality, we have used Eq. (3.25). In the second, we used the symmetry relation of Eq. (3.16) and defined $\tilde{\xi} = (0, u^i)$ which represents the operator Z_i . In the third equality, we have used Eq. (3.26), and Eq. (3.25) to pull the Z_i and $\tilde{Z} := \otimes_{k=1}^m [Z_{i-k} Z_{i+k}]^{\alpha_k} Z_i^\beta$ onto the physical legs. Since $u(\tilde{\xi})$ is a localized product of X operators and \tilde{Z} is a localized product of Z operators, we have derived a local stabilizer operator. We can derive an independent stabilizer K_i for any site i in the lattice. One can easily check that, due to the reflection symmetry of the stabilizers, all stabilizers commute as needed. So the fixed-point PEPS is the unique ground state of the Hamiltonian,

$$H = - \sum_i K_i, \quad (3.28)$$

which is a local Hamiltonian with a uniform spectral gap.

We can now verify the claimed examples in Section 3.2. If we construct the stabilizers for the fixed-point PEPS defined by the CQCA T_g in Eq. (3.8), then we find that they have the following form,

$$\begin{array}{c} Z \\ K_i = Z X_i Z, \\ Z \end{array} \quad (3.29)$$

which is indeed the familiar form of the cluster stabilizer. If we use the CQCA T_f in Eq. (3.22), we find

$$\begin{array}{c} Z \\ K_i = Z Y_i Z, \\ Z \end{array} \quad (3.30)$$

which corresponds to the cluster state with the operator S (Eq. (3.23)) applied to every site. Finally, with the CQCA T_p of Eq. (3.24), we get stabilizers with the simple form,

$$K_i = ZX_iZ, \quad (3.31)$$

which does indeed correspond to a stack of uncoupled 1D cluster states.

3.2.2 Simple CQCA

For the time being, we will restrict our attention to *simple CQCA*, which we define to be CQCA that have the form,

$$t = \begin{pmatrix} \text{Tr}(t) & 1 \\ 1 & 0 \end{pmatrix}. \quad (3.32)$$

We make this restriction based on the fact that the MPS tensors \mathcal{A}_T that are normal for all N if and only if T is simple, as we will prove in this section. Recall that an MPS tensor A is said to be normal if its transfer matrix has a unique fixed point. This is also equivalent to the statement that, for sufficiently large l , the set of products $\{A^{i_1}A^{i_2}\dots A^{i_l}\}$ spans the space of all $D \times D$ matrices where D is the bond dimension [220]. An MPS tensor being normal means that it has finite correlation length. Therefore, restricting to simple CQCA ensures that the correlation length of the fixed-point PEPS has a well-defined thermodynamic limit. In Sec. 3.5 we will slightly alter the way in which we construct PEPS from CQCA, and in this construction we will no longer need to impose any restriction on the choice of CQCA.

Consider the N -qubit MPS tensor \mathcal{A}_T defined by Eqs. (3.11),(3.12). Note that \mathcal{A}_T is a different MPS tensor for each N . In particular, whether or not \mathcal{A}_T is normal can depend on N . In this section only, we make the N dependence explicit by using the notation $\mathcal{A}_{T,N}$ to indicate that \mathcal{A}_T is defined on a ring of circumference N . We now prove the following result.

Proposition 1. $\mathcal{A}_{T,N}$ is normal for all N if and only if T is a simple CQCA, as defined in Eq. 3.32.

The proof follows from the following two lemmas:

Lemma 1. $\mathcal{A}_{T,N}$ is normal if and only if the set of operators Z_i and $T(Z_i)$, $i = 1, \dots, N$, and their products forms a basis for all $2^N \times 2^N$ matrices.

Proof. In the present case, normal means that the set of products $\{\mathcal{A}_{T,N}^{\mathbf{j}_1} \dots \mathcal{A}_{T,N}^{\mathbf{j}_l}\}_{\mathbf{j}_1, \dots, \mathbf{j}_l}$ spans the space of all $2^N \times 2^N$ matrices. Since we have $\mathcal{A}_{T,N}^{\mathbf{j}} = C_N^{\mathbf{j}} T$ with $C_N^{\mathbf{j}} := \bigotimes_{i=1}^N (Z_i)^{j_i}$, we can rewrite this set as $\{C_N^{\mathbf{j}_1} T(C_N^{\mathbf{j}_2}) \dots T^{l-1}(C_N^{\mathbf{j}_l}) T^l\}_{\mathbf{j}_1, \dots, \mathbf{j}_l}$ where $T^k(C_N^{\mathbf{j}}) = T^k C_N^{\mathbf{j}} T^{\dagger k}$. When checking if the tensor is normal, the T^l at the end can be ignored, since it does not affect the rank of the span. Using Eq. (3.10), we can always reduce powers of T , such that $T^k(C_N^{\mathbf{j}})$ can always be expressed as a product of $C_N^{\mathbf{j}}$, $T(C_N^{\mathbf{j}})$ and their translations. Therefore, the tensor is normal if the operators Z_i , $T(Z_i)$ and their products form a basis. \square

In particular, Lemma 1 says that $\mathcal{A}_{T,N}$ is normal if and only if it is possible to obtain the operator X_0 as a product of Z_i and $T(Z_i)$, with X_i for $i \neq 0$ following from translation invariance.

To facilitate the rest of the proof, let us move to the Laurent polynomial notation. Recall that, when considering a ring of circumference N , we identify $u^N = 1$. We also work over the field \mathbb{Z}_2 , so all coefficients of the polynomials will

be taken modulo 2. In what follows, we use congruency (\equiv) to indicate equality subject to these identifications.

The condition that we can express X_0 as a product of Z_i and $T(Z_i)$ translates into the existence of Laurent polynomials ξ^Z and ζ^Z such that

$$\begin{pmatrix} 0 \\ \xi^Z \end{pmatrix} + t \begin{pmatrix} 0 \\ \zeta^Z \end{pmatrix} \equiv \begin{pmatrix} 1 \\ 0 \end{pmatrix}. \quad (3.33)$$

In particular, we have,

$$t_{12}\zeta^Z \equiv 1. \quad (3.34)$$

That is, t_{12} is invertible subject to the identification $u^N = 1$, which we call N -invertible. This can only be true for all N in the trivial case, as stated by the next Lemma,

Lemma 2. *A symmetric Laurent polynomial $p(u)$ with coefficients in \mathbb{Z}_2 is N -invertible for all N if and only if $p(u) = 1$.*

Proof. Clearly, $p(u) = 1$ is N -invertible for all N . For the converse we use Ref. [221], which shows that a polynomial $p(u)$ over \mathbb{Z}_2 is N -invertible if and only if no N -th root of unity ω is a root of $p(u)$, *i.e.* $p(\omega) \equiv 0$. To finish the proof, We will first show that $p(u)$ has such a root on the unit circle. Then, we will show that it must be an N -th root of unity for some N .

By assumption, $p(u)$ is a symmetric Laurent polynomial over \mathbb{Z}_2 , meaning it can be written in the following form,

$$p(u) = \beta + \sum_k \alpha_k (u^k + u^{-k}), \quad (3.35)$$

for some $\beta, \alpha_k \in \{0, 1\}$. If $\beta = 0$, then $p(1) \equiv 0$, and therefore 1 is trivially a root, so assume $\beta = 1$. If we write $u = e^{i\phi}$ for some angle ϕ , then we have,

$$p(e^{i\phi}) = 1 + 2 \sum_k \alpha_k \cos(k\phi). \quad (3.36)$$

Let K denote the number of non-zero α_k (which is finite), giving $p(1) = 2K + 1$. Let $\theta = \frac{\pi}{k}$ for some k with $\alpha_k \neq 0$, giving $p(e^{i\theta}) \leq 2K - 1$. Then, since $p(e^{i\phi})$ is continuous, there must exist some $\psi \in (0, \theta)$ such that $p(e^{i\psi}) = 2K \equiv 0$. Calling $\omega = e^{i\psi}$, we have a root on the unit circle.

Next, notice that $p(u^{2^n}) \equiv p(u)^{2^n}$ for any $n \in \mathbb{N}$. This holds because our coefficients are in \mathbb{Z}_2 , so the cross terms cancel out each time $p(u)$ is squared. Hence we have $p(\omega^{2^n}) = p(\omega)^{2^n} \equiv 0$, so ω^{2^n} is also a root for all $n \in \mathbb{N}$. But there are only a finite number of roots on the unit circle (since $p(u)$ is bounded on it), so we must have $\omega^{2^n} = \omega^{2^m}$ for some $m < n$. Thus ω is an N -th root of unity for $N = k(2^n - 2^m)$ for any $k \in \mathbb{N}$, and therefore $p(u)$ is not N -invertible. \square

Proof of Proposition 1. Applying this Lemma to t_{12} , which is by definition a symmetric Laurent polynomial, we see that if we want $\mathcal{A}_{T,N}$ to be normal for all N , we need to fix $t_{12} = 1$. By examining the stabilizer representation of our fixed-point

PEPS derived in Section 3.2.1, it is clear that the PEPS depends only on t_{12} and $\text{Tr}(t)$. Hence, if we set $t_{12} = 1$, the only meaningful degree of freedom left is $\text{Tr}(t)$, which we can obtain by setting $t_{11} = \text{Tr}(t)$ and $t_{22} = 0$. Finally, our condition that t has unit determinant enforces $t_{21} = 1$, and we are left with Eq. (3.32). \square

We finish this section by observing two nice properties of fixed-point PEPS defined by simple CQCA. First, $\boldsymbol{\xi} \mapsto U_T(\boldsymbol{\xi})$ is a faithful representation of $\mathbb{Z}_2^N \times \mathbb{Z}_2^N$ when T is simple. To see this, suppose that $U_T(\boldsymbol{\xi}) = \mathbb{1}$ for some $\boldsymbol{\xi} \in \mathbb{Z}_2^N \times \mathbb{Z}_2^N$. In particular, this implies that $u(\boldsymbol{\xi}) = u(t\boldsymbol{\xi}) = \mathbb{1}$. Since $u(\boldsymbol{\xi}) = \bigotimes_{i=1}^N X_i^{\xi_i^X}$, we see that $\xi_i^X = 0, \forall i$. Using this and Eq. (3.32), we have that $u(t\boldsymbol{\xi}) = \bigotimes_{i=1}^N X_i^{\xi_i^Z}$, which then implies $\xi_i^Z = 0, \forall i$. So $\boldsymbol{\xi} = 0$ and thus $\boldsymbol{\xi} \mapsto U_T(\boldsymbol{\xi})$ is a faithful representation. Finally, we observe, in general, the fixed-point PEPS defined by simple CQCA are graph states [222], up to a global application of the unitary S , as can be seen using their stabilizer representation.

3.3 SPT order with L -cycle symmetries

Above, we have used CQCA to define fixed-point PEPS with quasi-1D SPT order protected by L -cycle symmetries. We would now like to investigate the corresponding SPT phases that surround these fixed-points. It is important to note that these are indeed gapped phases of matter, since the fixed-point PEPS have gapped parent Hamiltonians, as shown in Section 3.2.1.

To begin, we first need a better understanding of L -cycle symmetries in 1D systems. In general, we consider a (quasi) 1D chain of d -level systems with length $M = kL$ which is invariant under L -cycle symmetries of the form $U(g)^{\otimes k}|\psi\rangle = |\psi\rangle$ where,

$$|\psi\rangle = \sum_{j_1, \dots, j_M=1}^d \text{Tr}(\mathcal{A}^{j_1} \dots \mathcal{A}^{j_M}) |j_1, \dots, j_M\rangle, \quad (3.37)$$

and,

$$U(g) := u(g) \otimes u(\phi(g)) \otimes \dots \otimes u(\phi^{L-1}(g)), \quad (3.38)$$

with $g \mapsto u(g)$ being a d -dimensional unitary representation of a group $G \ni g$, and ϕ an automorphism of G with $\phi^L = \mathbb{1}$. The representation $g \mapsto u(g)$ needs not be a faithful representation, but the whole cycle $U(g)$ should be faithful (otherwise G should be redefined such that $U(g)$ becomes faithful). The symmetries found in the previous section fall under this definition.

Again, we can block L consecutive sites into one larger site such that $U(g)^{\otimes k}$ acts in the same way on each block. If our state vector $|\psi\rangle$ is invariant under this

symmetry, then Eq. 3.43 holds,

$$\begin{aligned}
 & \begin{array}{ccccccc}
 & u(g) & & u(\phi(g)) & & u(\phi^2(g)) & & \dots & & u(\phi^{L-1}(g)) \\
 & | & & | & & | & & & & | \\
 \text{---} & \bullet & \text{---} & \bullet & \text{---} & \bullet & \text{---} & \dots & \text{---} & \bullet & \text{---} \\
 & \mathcal{A} & & \mathcal{A} & & \mathcal{A} & & & & \mathcal{A} &
 \end{array} \\
 = & V(g) \begin{array}{ccccccc}
 & | & & | & & | & & \dots & & | \\
 \text{---} & \bullet & \text{---} & \bullet & \text{---} & \bullet & \text{---} & \dots & \text{---} & \bullet & \text{---} \\
 & \mathcal{A} & & \mathcal{A} & & \mathcal{A} & & & & \mathcal{A} &
 \end{array} V(g)^\dagger. \tag{3.39}
 \end{aligned}$$

Therein, $g \mapsto V(g)$ is a projective representation of the group G , satisfying $V(g)V(h) = \omega(g, h)V(gh)$ for a cocycle ω [87]. We will focus here on maximally non-commutative cocycles, as defined in Section 2.5.2. Recall that these are defined to satisfy the property,

$$\{g|\omega(g, h) = \omega(h, g) \forall h \in G\} = \{e\}, \tag{3.40}$$

An important property is that, given a maximally non-commutative cocycle ω , there is only one irreducible representation $\tilde{V}(g)$ with cocycle ω , up to unitary equivalence [146]. Then, the decomposition of $V(g)$ into irreducible representations is made of up many copies of $\tilde{V}(g)$, such that we have the decomposition,

$$V(g) = \mathbb{1} \otimes \tilde{V}(g), \tag{3.41}$$

$\forall g \in G$. Our first main result is the following theorem.

Theorem 1 (Normal form of MPS in maximally non-commutative SPT phase). *Any state vector $|\psi\rangle$ on a ring of length kL that is in a maximally non-commutative SPT phase with respect to an L -cycle symmetry representation (Eq. (3.38)) of a finite Abelian group G admits an MPS representation of the form,*

$$\mathcal{A}_{[l]}^j = B_{[l]}^j \otimes (C^j \Phi), \tag{3.42}$$

for suitable tensors $B_{[l]}^j$. Therein, $[l]$ is a site index such that $[l] = [l + L]$, Φ is uniquely defined by the relation $\tilde{V}(g) = \Phi^\dagger \tilde{V}(\phi(g)) \Phi$, and $C^j = \tilde{V}(g_j)$ for some $g_j \in G$. Throughout the phase, C^j and Φ remain constant, while $B_{[l]}^j$ varies.

This result is the essentially analogous to that given in Section 2.5.2 when extended to L -cycle symmetries. Φ and C^j are hence protected by the symmetry $g \mapsto U(g)$, in that they are present in a subspace of the virtual space of the MPS representation of all states in the phase. C^j are completely defined by the on-site representation $g \mapsto u(g)$ of Eq. (3.38), while the transformation Φ contains the information about the structure of the L -cycle symmetry. Hence, the same patterns that define the L -cycle symmetry also appear in the entanglement structure.

Proof. We begin with a state whose MPS tensor is normal and satisfies Eq. (3.39), where $V(g)$ is a projective representation of a finite Abelian group G with maximally non-commutative cocycle ω . First, we use the result of Ref. [150], which shows

that, if a state is invariant under the L -cycle symmetry in Eq. (3.38), then the tensor \mathcal{A} satisfies the symmetry,

$$\begin{array}{c} u(\phi^l(g)) \\ | \\ \bullet \\ | \\ \mathcal{A} \end{array} = W_l(g) \begin{array}{c} | \\ \bullet \\ | \\ \mathcal{A} \end{array} W_{l+1}(g)^\dagger, \quad (3.43)$$

for some unitaries $W_l(g)$ ($l = 0, \dots, L$) with $W_0(g) = W_L(g)$. This equation, and all others that follow in this section, hold for all $g \in G$. From Eq. (3.43), we get,

$$\begin{array}{c} u(g) \quad u(\phi(g)) \quad u(\phi^2(g)) \quad \dots \quad u(\phi^{L-1}(g)) \\ | \quad | \quad | \quad \dots \quad | \\ \bullet \quad \bullet \quad \bullet \quad \dots \quad \bullet \\ | \quad | \quad | \quad \dots \quad | \\ \mathcal{A} \quad \mathcal{A} \quad \mathcal{A} \quad \dots \quad \mathcal{A} \end{array} \\ = W_0(g) \begin{array}{c} | \\ \bullet \\ | \\ \mathcal{A} \end{array} \begin{array}{c} | \\ \bullet \\ | \\ \mathcal{A} \end{array} \begin{array}{c} | \\ \bullet \\ | \\ \mathcal{A} \end{array} \dots \begin{array}{c} | \\ \bullet \\ | \\ \mathcal{A} \end{array} W_0(g)^\dagger. \quad (3.44)$$

If the tensor is normal, the only way this equation and Eq. (3.39) can both be true is if $W_0(g) \propto V(g)$. If we connect the relations in Eq. (3.43) in a different order, we find,

$$\begin{array}{c} u(\phi(g)) \quad u(\phi^2(g)) \quad u(\phi^3(g)) \quad \dots \quad u(g) \\ | \quad | \quad | \quad \dots \quad | \\ \bullet \quad \bullet \quad \bullet \quad \dots \quad \bullet \\ | \quad | \quad | \quad \dots \quad | \\ \mathcal{A} \quad \mathcal{A} \quad \mathcal{A} \quad \dots \quad \mathcal{A} \end{array} \\ = W_1(g) \begin{array}{c} | \\ \bullet \\ | \\ \mathcal{A} \end{array} \begin{array}{c} | \\ \bullet \\ | \\ \mathcal{A} \end{array} \begin{array}{c} | \\ \bullet \\ | \\ \mathcal{A} \end{array} \dots \begin{array}{c} | \\ \bullet \\ | \\ \mathcal{A} \end{array} W_1(g)^\dagger, \quad (3.45)$$

where we have used the fact that $\phi^L(g) = g$. Now compare this to Eq. (3.39) with g replaced by $\phi(g)$. Again, since the tensor is normal, we find that $W_1(g) \propto V(\phi(g))$. So, for some scalar $\lambda(g)$, we have,

$$\begin{array}{c} u(g) \\ | \\ \bullet \\ | \\ \mathcal{A} \end{array} = \lambda(g) V(g) \begin{array}{c} | \\ \bullet \\ | \\ \mathcal{A} \end{array} V(\phi(g))^\dagger. \quad (3.46)$$

Now, we would like to use Eq. (3.46) to prove Eq. (3.42). This proof is similar to that of Theorem 1 in Ref. [15], adapted to L -cycle symmetries. First, if $g \mapsto u(g)$ is a linear representation, and $\tilde{V}(g)$ (Eq. 3.41) is an irrep with cocycle ω , Eq. (3.46) tells us that the cocycle of $\tilde{V}(\phi(g))$ must be in the same cohomology class as ω . That is, there exist phases $\gamma(g)$ such that $\gamma(g)\tilde{V}(\phi(g))$ has cocycle ω . Since $\tilde{V}(g)$ is the unique irrep with cocycle ω , we must have $\gamma(g)\tilde{V}(\phi(g)) = \Phi^\dagger \tilde{V}(g) \Phi$ for some unitary Φ . Then it follows from Eq. (3.46) that $g \mapsto \lambda(g)\gamma(g)$ is a 1D representation of G . Then, according to Ref. [15], we can find a unitary Λ such that $\overline{\lambda(g)\gamma(g)}\tilde{V}(g) = \Lambda^\dagger \tilde{V}(g) \Lambda$.

With the above we can now rewrite Eq. (3.46) as,

$$\begin{array}{c} u(g) \\ | \\ \bullet \\ \hline \mathcal{A} \end{array} = \mathbb{1} \otimes \tilde{V}(g) \begin{array}{c} | \\ \bullet \\ \hline \mathcal{A} \end{array} \mathbb{1} \otimes \Phi^\dagger \Lambda^\dagger \tilde{V}(g) \Lambda \Phi. \quad (3.47)$$

If we multiply each side by $\mathbb{1} \otimes \Phi^\dagger \Lambda^\dagger$ on the right, then we get a relation for the composite tensor $\mathcal{A}^j(\mathbb{1} \otimes \Phi^\dagger \Lambda^\dagger)$. With this relation, we can use Schur's Lemma as in Theorem 1 of Ref. [15] to obtain,

$$\mathcal{A}^j(\mathbb{1} \otimes \Phi^\dagger \Lambda^\dagger) = B^j \otimes C^j, \quad (3.48)$$

hence,

$$\mathcal{A}^j = B^j \otimes (C^j \Lambda \Phi). \quad (3.49)$$

This expression holds with respect to the basis of physical spins $\{|j\rangle\}$ that diagonalizes $u(g)$, such that $u(g)|j\rangle = \chi_j(g)|j\rangle$ where $g \mapsto \chi_j(g)$ are 1D representations of G . We then have $C^j = \tilde{V}(g_j)$ where g_j are defined uniquely by the relation $\chi_j(g)\tilde{V}(g) = \tilde{V}(g_j)^\dagger \tilde{V}(g)\tilde{V}(g_j)$. B^j are unconstrained tensors and can vary throughout the SPT phase. Since λ is not uniformly defined throughout the SPT phase, Λ can also vary throughout the phase.

Finally, we would like to rewrite Eq. (3.49) in such a way that we separate the parts which are universal throughout the phase, namely Φ and C^j , from the rest. We can accomplish this in the following way. On each block of L sites, we push the matrix Λ through the tensors to the end of the block,

$$B^{j_1} \dots B^{j_L} \otimes C^{j_1} \Lambda \Phi \dots C^{j_L} \Lambda \Phi = B_{[1]}^{j_1} \dots B_{[L]}^{j_L} \otimes C^{j_1} \Phi \dots C^{j_L} \Phi \Lambda_*. \quad (3.50)$$

Λ commutes with all $\tilde{V}(g_j)$ up to a phase. So when Λ passes through the tensor \mathcal{A}^j , it leaves behind a phase, which is absorbed into the tensor B^j . The tensors $B_{[l]}^j$ are the original tensors B^j along with these phases, which are in general not translationally invariant within a block (We do, however, have $B_{[l]}^j = B_{[l+L]}^j$, so the representation is invariant under translation by L sites). The matrix $\Lambda_* := \Lambda \Phi^{L-1} \Lambda \Phi^{L-1} \dots \Phi^\dagger \Lambda \Phi$ is a scalar matrix and can thus be removed from the above expression. To see this, note that Eq. (3.39) says that $\lambda(g)$ must satisfy the constraint

$$\lambda_*(g) := \lambda(g)\lambda(\phi(g)) \dots \lambda(\phi^{L-1}(g)) = 1. \quad (3.51)$$

By definition, we have $\overline{\lambda_*(g)} \tilde{V}(g) = \Lambda_*^\dagger \tilde{V}(g) \Lambda_*$. Since $\lambda^*(g) = 1$, we have $\Lambda_* \propto \mathbb{1}$ by Schur's lemma. The proportionality constant can be absorbed into one of the tensors $B_{[l]}^j$ and therefore Λ_* can be removed from Eq. (3.50). Hence, we can represent our state by an MPS of the form

$$A_{[l]}^j = B_{[l]}^j \otimes (C^j \Phi), \quad (3.52)$$

as desired. \square

We can now apply Theorem 1 to the constructions found in the previous section. Given a CQCA T , we get a fixed-point PEPS which is in a non-trivial quasi-1D

SPT phase with respect to the L -cycle symmetry $\boldsymbol{\xi} \mapsto U_T(\boldsymbol{\xi})$ for $\boldsymbol{\xi} \in \mathbb{Z}_2^N \times \mathbb{Z}_2^N$. Since $V(\boldsymbol{\xi})$ are N -qubit Pauli operators, it follows that this SPT phase is maximally non-commutative. Hence, Theorem 1 applies, and if we consider an arbitrary state within this SPT phase, it admits a quasi-1D MPS representation of the form Eq. (3.42), which in this case reads

$$\mathcal{A}_{[l]}^{\mathbf{j}} = B_{[l]}^{\mathbf{j}} \otimes (C^{\mathbf{j}}T), \quad (3.53)$$

where $\mathbf{j} = (j_1, j_2, \dots, j_N)$ denotes the state of the N spins along a ring with $j = 0$ (1) corresponding to the vectors $|+\rangle$ ($|-\rangle$), and $C^{\mathbf{j}} = \bigotimes_{i=1}^N (Z_i)^{j_i}$. Notice that setting $B_{[l]}^{\mathbf{j}} = 1$ leaves us with $\mathcal{A}_{[l]}^{\mathbf{j}} = C^{\mathbf{j}}T$, which is the fixed-point PEPS defined in Eq. (3.11).

Thus, when CQCA are used to define subsystem symmetries, the presence of non-trivial SPT order under those symmetries is equivalent to the presence of the CQCA on the virtual level of the tensor network. This shows that the same structure appearing in the subsystem symmetry also appears in the entanglement structure found throughout the phase. This correspondence between QCA and SPT order protected by subsystem symmetries is the first major result of this work.

3.4 Relation to SSPT order

In this section, we re-cast our phases, which are so far only defined in the quasi-1D picture, as genuine 2D phases of matter protected by subsystem symmetries. We then show that, for phases defined by glider CQCA, the full L -cycle symmetry group is not necessary to protect the phase, and a subgroup of rigid line-like symmetries is sufficient.

3.4.1 From quasi-1D to 2D

Let us be clear about what is meant by quasi-1D SPT order and how it differs from a genuine 2D SPT order. The difference is in the notion of locality. SPT order can be defined as equivalence classes of states under finite depth quantum circuits which respect the symmetry [60]; two states are in the same SPT phase if they can be transformed into each other by such a circuit, which corresponds to a quasi-adiabatic evolution along a path of gapped, local Hamiltonians [5]. Here, ‘local’ depends on the dimensionality of the system. For our quasi-1D scenario, the evolution must be local between different rings of the torus (the long direction of the torus), but it may be non-local along the rings (the skinny direction around the torus). When we promote to a true 2D scenario, we enforce locality in both directions.

From each fixed-point PEPS, we define the corresponding quasi-1D (2D) SPT phase as all states that can be reached from the fixed-point PEPS via symmetric finite depth quantum circuits which are local in the quasi-1D (2D) sense. Note that, since any circuit that is local in the 2D sense is also local in the quasi-1D sense, the 2D SPT phases are contained within the quasi-1D SPT phases. Therefore, the results on quasi-1D phases derived in the previous section, Eq. (3.53) in particular,

also hold throughout the corresponding 2D phase defined by the same symmetries. One implication of this is the presence of zero-energy edge modes of dimension 2^N [223] throughout the phase. This exponentially growing edge degeneracy was noted in Refs. [59, 191] as a signature of SSPT phases. In Section 3.5, we encode logical information in these protected edge modes for the purposes of computation.

We note an important distinction between the quasi-1D and 2D scenarios. As mentioned in Sec. 3.3, 1D SPT phases are classified by a symmetry group G , a representation $g \mapsto U(g)$, and a cocycle ω . Often, the representation is not considered important to the classification of 1D SPT phases [87, 94, 138] because one can construct a path of Hamiltonians that smoothly interpolates between any two *local* symmetry representations without closing the gap. So 1D SPT phases that only differ by the symmetry representation defining them are often said to be equivalent. This is precisely the case for the SPT phases considered here: When regarded as quasi-1D SPT phases, they differ only by the L -cycle symmetry representation $\xi \mapsto U_T(\xi)$. Therefore, as quasi-1D phases, they may all be seen as equivalent. This argument breaks down in the 2D scenario, since the interpolation can act non-locally on blocks of size $N \times L$, violating the 2D notion of locality. So SPT phases defined by different CQCA can be distinct in the genuine 2D scenario. Indeed, as we saw above, defining the symmetry by the CQCA T_p (Eq. (3.24)) leads to an SPT phase built around a stack of decoupled 1D cluster states, while the phase defined by the CQCA T_g (Eq. (3.8)) is built around the 2D cluster state. These two phases are physically distinct, as discussed in the next subsection.

3.4.2 Line-like symmetries protect glider CQCA

In the case of glider CQCA, promoting to a 2D notion of locality allows us to equivalently define our phases in terms of rigid line-like symmetries acting on 1D subsystems. In Section 2.7.1, we argued that the 2D cluster phase can be equivalently defined by the line or cone symmetries. Here, we extend this argument to all phases defined by glider CQCA. The generating symmetries defined by a general glider CQCA are shaped like cones. This follows from Eq. (3.10) which, for glider CQCA, takes the form $t^2 = (u^c + u^{-c})t + 1$. Thus, if we apply T to any single-qubit Pauli P_i , we find,

$$T(T(P_i)) = T^2(P_i) = T(P_{i-c})P_iT(P_{i+c}). \quad (3.54)$$

We can continue in this fashion to see that powers of T can be expressed as cones which expand until they wrap all the way around the torus, after which they contract back to a point (see Fig. 3.2(a) for the case $P_i = Z_i$).

This picture also gives us an easy way to understand the existence of gliders, see Fig. 3.2(b). The gliders lead to line-like symmetries of the state, as pictured in Fig. 2.10(a) for the cluster phase. The line symmetries can be generated as products of the cone symmetries, but the converse is not true on a finite torus. Indeed, the line symmetries form a $\mathbb{Z}_2^{2(N-1)}$ subgroup of the full \mathbb{Z}_2^{2N} symmetry group of cones in the cluster phase. Despite this, we can prove the following result:

			$T(Z)$	Z		
		$T(Z)$	Z	$T(Z)$	Z	
Z	$T(Z)$	Z	$T(Z)$	Z	$T(Z)$	Z
		$T(Z)$	Z	$T(Z)$	Z	
			$T(Z)$	Z		

(a)

		$T(Z)$	Z			
	$T(Z)$	Z				
$T(Z)$	Z					$T(Z)$
Z					$T(Z)$	Z
				$T(Z)$	Z	
			$T(Z)$	Z		

(b)

Figure 3.2: Representation of the general appearance of cones (a) and lines (b) in glider CQCA, for $c = 1$. Each column represents a product of Pauli operators on $N = 6$ qubits with periodic boundaries, and advancing to the right is equivalent to one application of T . For example, the first three columns of (a) represents the operators Z_3 , $T(Z_3)$, and $T(Z_2)Z_3T(Z_4)$. After 6 steps, any operator returns to itself.

Proposition 2. *Consider a glider CQCA T and a 2D-local quantum circuit U_{circ} that commutes with all line symmetries $U_T(\xi)$, corresponding to ξ that are gliders. Then, U_{circ} in fact commutes with the whole subsystem symmetry group.*

This result tells us that, when a 2D notion of locality is enforced, the line symmetries defined by gliders are sufficient to protect the SPT order, *i.e.* the 2D phase defined by line symmetries is contained within the quasi-1D phase defined by the cone symmetries.

Proof. Fig. 3.2(b) shows that the operator $T(Z_i)Z_{i-1}$ defines a glider and hence a line symmetry. Likewise, $Z_iT(Z_{i-1})$ defines a glider moving in the opposite direction. Now, for any even integer k , we can write

$$Z_i \otimes Z_{i-k} = (Z_i T(Z_{i-1}))(T(Z_{i-1})Z_{i-2}) \dots (T(Z_{i-k+1})Z_{i-k}). \quad (3.55)$$

That is, we can write a product of non-neighbouring Z 's as a product of gliders. Since Z_i in the virtual space corresponds to a cone symmetry in the physical space, we see that we can create pairs of cone symmetries with products of line symmetries. The same argument can be repeated for X_i in place of Z_i .

If we separate these cones sufficiently far from each other, then each local gate in the finite depth quantum circuit will see only one of the cones. So a local gate that is symmetric under the line symmetries is also symmetric under the cone symmetries. Since we require in the definition of SPT order that each *local* gate of the finite depth quantum circuit commutes with the symmetry, this implies that a circuit which is symmetric under the line symmetries is also symmetric under the cone symmetries, which generate the entire subsystem symmetry group. \square

In Section 2.7, we made the distinction between weak and string SSPT phases with line symmetries, where a phase is called weak if it can be trivialized by adding 1D SPT chains along the direction of the symmetry operators, while strong SSPT phases are genuine 2D phases of matter that cannot be viewed as stacks of 1D SPT chains. For simple, periodic CQCA, the fixed-point states we construct are themselves stacks of 1D chains, so periodic CQCA correspond to weak SSPT phases. On the other hand, phases defined by simple, glider CQCA are strong. This has been shown in Ref. [190] for the 2D cluster phase. For phases defined by other simple glider CQCA, one can use the stabilizer representation of the fixed-point PEPS (Section 3.2.1) to see that they correspond to stacks of 2D cluster states. Since the subsystem symmetry group acts independently on each cluster state, the resulting system is still in a strong SSPT phase. Finally, for fractal CQCA, there are no line-like symmetries [208], and we must treat the fractal symmetries themselves as fundamental. This leads to a definition of 2D phases via fractal symmetry operators, as in Refs. [191, 224]. Whether there exists a notion of strong versus weak phases under fractal symmetry remains unknown [190].

3.5 Computational power of the QCA phases

Now that we have defined 2D SPT phases via CQCA, and we have understood some basic properties of these phases, we move on to characterizing their computational power in measurement-based quantum computing.

Before we can state our second main result, we need to define another class of CQCA, *entangling* CQCA. We call a CQCA T entangling if one or more of the entries of the matrix t is not 0 or 1. In other words, entangling CQCA are CQCA that spread information. All glider and fractal CQCA are entangling, but not all periodic CQCA are. In particular, non-entangling CQCA are those for which t can be expressed as a product of h, h^{-1} and s, s^{-1} as defined in Eq. (3.14) and Eq. (3.15), respectively. For this class of CQCA, we will prove our second main result:

Theorem 2 (Computational phases of matter). *For every entangling CQCA, there exists a 2D SPT phase in which every state is a resource for universal MBQC, except for a possible subset of zero measure. Furthermore, the universal circuit model is simulated with polynomial overhead.*

We begin with an outline of the main ideas that are needed to use an SPT phase as a resource for MBQC [19, 20, 26]. This is a more detailed account of the story that was presented in Section 2.7.5. There are three key features of the constructions which are relevant to the current work:

1. Logical qubits are encoded in the virtual space of the tensor network, as described in Section 2.6. Specifically, N qubits are encoded in the 2^N -dimensional logical subspace of Eq. (3.53) which is uniform throughout the corresponding SPT phase. One time-step of the computation is enacted by individually measuring every qubit in a *block* of size $N \times L$ consisting of L consecutive rings around the torus, where L is the period of the CQCA (to

be determined in Sec. 3.5.1). Information can be initialized into this space and subsequently read-out by appropriate measurement patterns on blocks.

2. Logical gates are performed by measuring a single qubit in a block in a perturbed basis,

$$\{|+\rangle + id\alpha|-\rangle, |-\rangle - id\alpha|+\rangle\}, \quad (3.56)$$

with $|d\alpha| \ll 1$, and measuring the rest of the qubits in a block in the basis $\{|+\rangle, |-\rangle\}$. According to Eq. (3.53), and the computational scheme of Ref. [20], if the qubit measured in the perturbed basis is located at site (i, l) in the block, the corresponding logical gate is, up to second order in $d\alpha$,

$$R_{(i,l)}(d\alpha) = \exp(2id\alpha\nu_{(i,l)}T^{L-l+1}(Z_i)), \quad (3.57)$$

where $\{\nu_{(i,l)}\}$ is a set of constants that characterize the part of the state that is not uniform within the SPT phase. That is, they are defined in terms of the $B_{[l]}^j$ from Eq. (3.53). These constants can be easily measured before computation, again using local measurements only. Therefore, they may be accounted for by adjusting $d\alpha$ accordingly. If one of $\nu_{(i,l)}$ is equal to 0, which only occurs for a subset of states of zero measure, the computation fails. The gate $R_{(i,l)}(d\alpha)$ represents an infinitesimal rotation generated by $T^{L-l+1}(Z_i)$. By composing these gates in the appropriate order, we can achieve any rotation generated by elements of the Lie algebra \mathcal{O}_T which is generated by the set $\{T^l(Z_i)|i = 1, \dots, N, l = 1, \dots, L\}$ with linear combinations and the matrix commutator. Thus our full set of gates is given by the Lie group $\mathcal{L}_T = \exp(i\mathcal{O}_T)$. \mathcal{L}_T is the same for every state in the SPT phase defined by the CQCA T (to be investigated in Section 3.5.2).

3. Every non-trivial gate must be followed up by measuring a large number of blocks of qubits in the $\{|+\rangle, |-\rangle\}$ basis. The number of blocks measured is on the order of the correlation length of the system (in the long direction), which is finite by the assumption of the tensors being normal. This serves to decouple the two virtual subspaces in Eq. (3.53), which become slightly entangled after each logical gate.

3.5.1 Period of the CQCA

We first determine the period L of our CQCA, which determines the length of a single step of computation. We recall the matrix representation t of the CQCA. The task is to determine the smallest L such that $t^L = \mathbb{1}$, which we do by invoking Eq. (3.10). We will prove the following result:

Proposition 3. *For every CQCA, there exists an unbounded sequence of increasing system sizes N such that the period grows at most linearly in N .*

This result is important, since it means that size of computational blocks, as described above, grows efficiently with the number of qubits.

N	L	N	L	N	L
2	3	18	84	34	510
4	6	20	60	36	168
6	12	22	186	38	1026
8	12	24	48	40	120
10	30	26	126	42	2340
12	24	28	36	44	372
14	18	30	1020	46	12282
16	24	32	48	48	96

Table 3.1: The period L as a function of the circumference N for the fractal CQCA T_f in Eq. (3.22). For $N = 2^k$, the relationship is linear. In general, L appears to grow with an exponential envelope.

Proof. Since the trace of the CQCA appears in t^2 , the analysis now splits into three parts, depending on whether the CQCA is of periodic, glider, or fractal type.

Periodic CQCA. For periodic CQCA, we have $\text{Tr}(t) = a$, where $a = 0, 1$. Using Eq. (3.10), it is easy to check that the period is then $L = a + 2$ [208]. Note that this period is independent of the circumference N . In particular, the CQCA is periodic even on an infinite chain, while the glider and fractal CQCA have a finite period only when periodic boundary conditions are enforced. This is the reason why only these CQCA are called “periodic”.

Glider CQCA. For CQCA that support gliders, the period can be determined from the cone structure in Fig. 3.2(a). For $c = 1$ and N even, this cycle takes N steps (for odd N , it takes $2N$ steps, but we only consider even N). For $c > 1$, the above is still true, but there may be a smaller number L also satisfying $t^L = \mathbb{1}$. We ignore this possibility for simplicity. Thus, the period of a glider CQCA on a ring of circumference $2N$ can always be taken to be $L = 2N$.

Fractal CQCA. The case is more complicated for CQCA with fractal behaviour. Indeed, due to their fractal nature, the period L of these CQCA can be a wildly fluctuating function of N . In fact, $L(N)$ can appear to have exponentially growing behaviour, see Table 3.1. This would pose a significant problem to computation. Since N is essentially the number of qubits, and L controls the duration of a single step of computation, an exponential relationship implies that computation time scales exponentially with the number of qubits. Thus, we could not call the resulting computational scheme universal, even if we have a full set of gates. Luckily, it turns out that this problem can be avoided. Indeed, although $L(N)$ may have an exponential envelope, it turns out that there is a subsequence of system sizes for which the relationship is linear. Specifically, for $N = 2^k$, the period L of a fractal CQCA is either $L = 2^k = N$ or $L = 2^k + 2^{k-1} = \frac{3}{2}N$, as we now show.

Throughout this calculation, we will be taking powers of polynomials like $\sum_k c_k u^k$. As in Section 3.2.2, we can write $(\sum_k c_k u^k)^{2^n} = \sum_k c_k (u^k)^{2^n} \forall n \in \mathbb{N}$. This

simplifies the following calculations significantly. Let,

$$\gamma := \text{Tr}(t) = \beta + \sum_i \alpha_i (u^i + u^{-i}), \quad (3.58)$$

for $\alpha_i, \beta \in \{0, 1\}$. With the periodic boundary conditions, we identify $u^{-2^{k-1}}$ and $u^{2^{k-1}}$. Then we have,

$$\gamma^{2^{k-1}} = \beta + \sum_i \alpha^i ((u^{2^{k-1}})^i + (u^{-2^{k-1}})^i) = \beta. \quad (3.59)$$

The proof now splits into two cases:

Case 1: $\beta = 0$. From Eq. (3.10), we have,

$$t^{2^k} = (t^2)^{2^{k-1}} = (\gamma t + \mathbb{1})^{2^{k-1}} = \gamma^{2^{k-1}} t^{2^{k-1}} + \mathbb{1}, \quad (3.60)$$

where cross terms again cancel out. Since $\gamma^{2^{k-1}} = \beta = 0$, we have $t^{2^k} = \mathbb{1}$, showing $L = 2^k = N$.

Case 2: $\beta = 1$. We need a formula for $t^{2^k+2^{k-1}}$. The result, which we will prove by induction, is,

$$t^{2^k+2^{k-1}} = (1 + \gamma^{2^k}) \gamma^{2^{k-1}-1} t + [(1 + \gamma^{2^k}) p_k(\gamma) + \gamma^{2^{k-1}}] \mathbb{1}. \quad (3.61)$$

Therein, $\gamma = \text{Tr}(t)$, and $p_k(\gamma)$ is some polynomial in γ . The expression is simple to confirm for $k = 1$ using Eq. (3.10), where $p_1(\gamma) = 0$. Now assume it is true for k . Then we have,

$$t^{2^{k+1}+2^k} = (t^{2^k+2^{k-1}})^2 = (1 + \gamma^{2^{k+1}}) \gamma^{2^k-2} t^2 + [(1 + \gamma^{2^k}) p_k(\gamma) + \gamma^{2^{k-1}}]^2 \mathbb{1}. \quad (3.62)$$

Now, we apply Eq. (3.10) to find,

$$t^{2^{k+1}+2^k} = (1 + \gamma^{2^{k+1}}) \gamma^{2^k-1} t + [(1 + \gamma^{2^{k+1}}) p_{k+1}(\gamma) + \gamma^{2^k}] \mathbb{1}, \quad (3.63)$$

which is the desired expression where $p_{k+1}(\gamma) = p_k^2(\gamma) + \gamma^{2^k-2}$. So the formula holds for all k . Now, since $\gamma^{2^{k-1}} = \beta = 1$, we get $t^{2^k+2^{k-1}} = \mathbb{1}$, so $L = 2^k + 2^{k-1} = \frac{3}{2}N$. \square

3.5.2 Determining gate set

We must now determine the Lie group of gates \mathcal{L}_T . We will show that we can construct a universal set of gates as long as T is simple and entangling, which implies that T is of glider or fractal type. We construct arbitrary single-qubit gates and a non-trivial two-qubit entangling gate, which together form a full gate set [225–227]. The single-qubit gates follow from the fact that T is a simple CQCA, which implies that $T(Z_i) = X_i$. Then, if we set $l = 1$ in Eq. (3.57), we get all Z -rotations on a single qubit, while setting $l = L$ gives all X -rotations. Together, these give a full set of single qubit gates.

To construct an entangling gate, we generalize the technique from Ref. [26], in which a two-qubit gate was constructed from a three-qubit gate by initializing one qubit into a particular eigenstate on which the three-qubit gate acts trivially. Consider $T^2(Z_i)$ for any i . If T is entangling, this operator must act non-trivially outside of site i . Then $T^2(Z_i)$ will be a product of Pauli operators supported on the interval $[i - n, i + n]$, for some minimal $n \neq 0$, which is symmetric about site i . The trick now is to make every $2n$ -th qubit a logical qubit, and initialize the qubits in between each logical qubit into the $+1$ eigenstate of the middle $2n - 1$ operators in $T^2(Z_i)$. This initialization can always be done since we have all single qubit gates at our disposal, as described in Ref. [26]. Then, $T^2(Z_i)$ will act as a two-qubit gate on logical qubits at positions $i - n$ and $i + n$ while leaving the qubits in between unchanged. Hence, by setting $l = L - 1$ in Eq. (3.57), we get a non-trivial two-qubit entangling gate on all neighbouring pairs of logical qubits which, together with the single-qubit gates, form a universal set.

For an explicit example, consider the CQCA from Eq. (3.8) with $T_g^2(Z_i) = X_{i-1}Z_iX_{i+1}$. We initialize every even numbered qubit in the $|0\rangle$ eigenstate and use only odd-numbered qubits as logical qubits. Then the gate $\exp(2id\alpha T_g^2(Z_{2i})) = \exp(2id\alpha X_{2i-1}Z_{2i}X_{2i+1})$ reduces to $\exp(2id\alpha X_{2i-1}X_{2i+1})$, which is an entangling gate on the logical qubits.

3.5.3 Proving computational universality

We have now all ingredients needed for the proof of Theorem 2 for simple, entangling CQCA. Next we show how to modify the above scheme such that we can drop the condition that our CQCA is simple and instead apply it to any entangling CQCA. One advantage of using simple QCA is that they allow us to easily construct a full set of single-qubit gates. For arbitrary CQCA that are not simple, this is not as straightforward. To address this issue, we modify the way in which we construct fixed-point PEPS from CQCA.

The new fixed-point PEPS are defined in terms of a two-qubit unit cell, labelling the two qubits within a unit cell by a and b . The local tensor A'_T has components given by,

$$\begin{array}{c}
 \begin{array}{c} | + + \rangle \\ \text{---} \bullet \text{---} \\ \text{---} / A'_T \end{array} := \begin{array}{c} / \\ \text{---} \bullet \text{---} \\ \text{---} \mathcal{T} \end{array} \quad , \quad \begin{array}{c} | + - \rangle \\ \text{---} \bullet \text{---} \\ \text{---} / A'_T \end{array} := \begin{array}{c} -Z- \\ \text{---} \bullet \text{---} \\ \text{---} \mathcal{T} \end{array}
 \end{array}
 \tag{3.64}$$

$$\begin{array}{c}
 \begin{array}{c} | - + \rangle \\ \text{---} \bullet \text{---} \\ \text{---} / A'_T \end{array} := \begin{array}{c} -X- \\ \text{---} \bullet \text{---} \\ \text{---} \mathcal{T} \end{array} \quad , \quad \begin{array}{c} | - - \rangle \\ \text{---} \bullet \text{---} \\ \text{---} / A'_T \end{array} := \begin{array}{c} -XZ- \\ \text{---} \bullet \text{---} \\ \text{---} \mathcal{T} \end{array}
 \end{array}$$

where \mathcal{T} is again the MPU representation of the CQCA. The choice of CQCA in this definition is completely free, as opposed to the previous sections where we required T to be simple CQCA.

The tensors A'_T can be used to define the ring tensor \mathcal{A}'_T as in Eq. (3.12). Proceeding from here in the same way as the qubit case, we can construct an

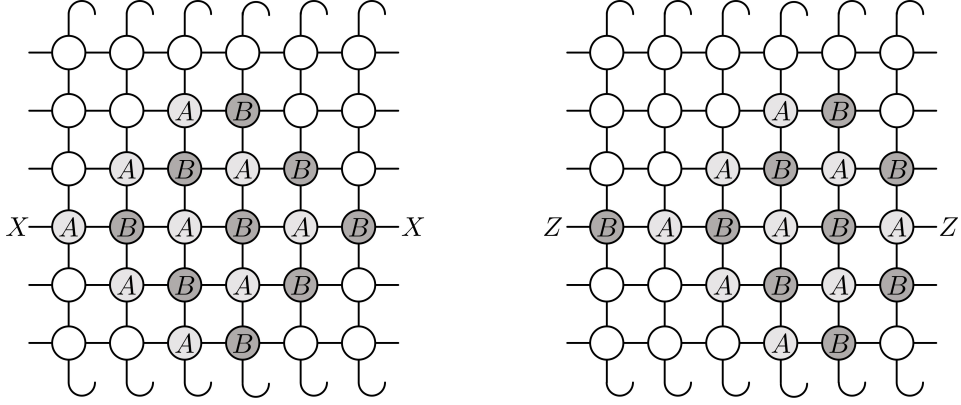


Figure 3.3: The modified cone symmetries arising from the cluster CQCA T_g of Eq. (3.8) when using the two qubit per-site construction. A (B) denotes the Pauli- X operator acting on qubit a (b) on a given site, while operators on the edges show the corresponding virtual representation. Modified line symmetries can similarly be constructed as products of the modified cone symmetries. Note that the analysis in Section 3.4 still holds in this case: the line symmetries are still sufficient to protect the phase.

L -cycle symmetry representation,

$$\boldsymbol{\xi} \mapsto U'_T(\boldsymbol{\xi}) = u'(\boldsymbol{\xi}) \otimes u'(t\boldsymbol{\xi}) \otimes \cdots \otimes u'(t^{L-1}\boldsymbol{\xi}), \quad (3.65)$$

of $\mathbb{Z}_2^N \times \mathbb{Z}_2^N$, where the on-site representation is defined by,

$$u'(\boldsymbol{\xi}) = \bigotimes_{i=1}^N X_i^{a\xi_i^X} X_i^{b\xi_i^Z}, \quad (3.66)$$

where X_i^a , X_i^b denotes the Pauli- X matrix acting on the qubit a and b at site i , respectively (see Fig. 3.3). It can be easily verified that $\boldsymbol{\xi} \mapsto U'_T(\boldsymbol{\xi})$ is a faithful representation of $\mathbb{Z}_2^N \times \mathbb{Z}_2^N$ as before. The virtual representation $\boldsymbol{\xi} \mapsto V(\boldsymbol{\xi})$ is again the Pauli representation, so the resulting state has non-trivial SPT order under this L -cycle symmetry. We can thus prove that Eq. (3.53) holds throughout the corresponding SPT phase, where $C^{\mathbf{j}}$ can now be any N -qubit Pauli, not just a product of Z 's.

We can briefly compare this two-qubit construction to the original one-qubit construction of Eq. (3.11). First, we show that every PEPS defined by Eq. (3.11) with a simple CQCA T is equivalent to the PEPS defined by Eq. (3.64) with CQCA T^2 . Therefore, this construction subsumes the original one, in that all fixed-point PEPS defined by Eq. (3.11) with a simple CQCA, along with the corresponding SSPT phases, can also be constructed by Eq. (3.64). To see this, note that the fixed-point PEPS defined by Eq. (3.11) can be written as an MPS as follows,

$$|\psi_T\rangle = \sum_{\mathbf{j}_1, \dots, \mathbf{j}_M} \text{Tr} \left(Z^{\mathbf{j}_1} T \dots Z^{\mathbf{j}_M} T \right) |\mathbf{j}_1, \dots, \mathbf{j}_M\rangle. \quad (3.67)$$

Where $P^{\mathbf{j}} = \bigotimes_{i=1}^N (P_i)^{j_i}$ for a Pauli operator $P = X, Y, Z$. If we commute half of the $Z^{\mathbf{j}}$ past the neighbouring CQCA T on the right, and we use the fact that

$T(Z^{\mathbf{j}}) = X^{\mathbf{j}}$ for simple CQCA, we get

$$|\psi_T\rangle = \sum_{\mathbf{j}_1 \dots \mathbf{j}_M} \text{Tr} \left(X^{\mathbf{j}_M} Z^{\mathbf{j}_1} T^2 \dots X^{\mathbf{j}_{M-2}} Z^{\mathbf{j}_{M-1}} T^2 \right) |\mathbf{j}_1, \dots, \mathbf{j}_M\rangle. \quad (3.68)$$

If we group the i -th qubits of columns $2k$ and $2k + 1$ together, this state is exactly the fixed-point PEPS defined by Eq. (3.64) with CQCA T^2 .

Since we no longer restrict to simple CQCA, we get new fixed-point states and phases in addition to those constructed by Eq. (3.11). In particular, all fixed-point states in the previous sections were graph states, while this is not generally the case for states defined by Eq. (3.64). It can also be shown, using the same technique as before, that they are nevertheless still stabilizer states, and so they are again unique ground states of gapped, local Hamiltonians.

The important distinction between the two constructions appears in their use for MBQC. Because of the different $C^{\mathbf{j}}$ appearing in Eq. (3.53), the set of logical gates that we can execute in one step is enlarged. The computational scheme is almost identical to that described above for the single-qubit unit cell, except that we now have a choice to measure either qubit a or b at a given site in a perturbed basis for a logical gate. The logical gates we can execute now have the form,

$$R'_{(i,l)}(d\alpha) = \exp(2id\alpha\nu_{(i,l)}T^{L-l+1}(P_i)), \quad (3.69)$$

where P_i is either Z_i or X_i , depending on whether qubit a or b is measured in the perturbed basis, respectively. Therefore, setting $l = 1$ in Eq. (3.69) already gives a full set of single-qubit rotations. We can then construct an entangling gate in a way exactly analogous to the previous case. Again, this construction can fail only if T is not entangling.

With this, we have constructed a full set of gates for all CQCA T which are entangling. So we can finally complete the proof of Theorem 2,

Proof of Theorem 2. Based on the above discussions, we see that a) N can always be scaled in such a way that the period L is linear in N or constant, and b) we can construct a universal set of gates on $q = \lfloor N/2n \rfloor$ qubits for a fixed n , *i.e.* $SU(2^q) \subset \mathcal{L}_T$. Finally, the computational scheme of Refs. [19, 20, 26] which we employ here has polynomial overhead for logical gates. Thus, overall, we can simulate the circuit model of quantum computation on q logical qubits in $poly(q)$ time, as stated in the theorem. \square

Within each phase, the computational power remains uniform and hence they truly constitute computational phases of matter. However, it is important to note that the measurement protocol needed for gates depends on certain details about the specific point within the phase, namely the constants $\nu_{(i,l)}$, as in similar schemes from previous works [19, 20, 26, 27]. This means that our schemes are not necessarily robust against unknown small deformations within the phase, as would be the case in fault-tolerant schemes for quantum computing. However, the constants $\nu_{(i,l)}$ can be readily obtained via local measurements, in a small pre-computation before the actual quantum computation [20], giving rise to uniform computational power across the phase. These constants are the same for each block of computation, as we have assumed translational invariance throughout.

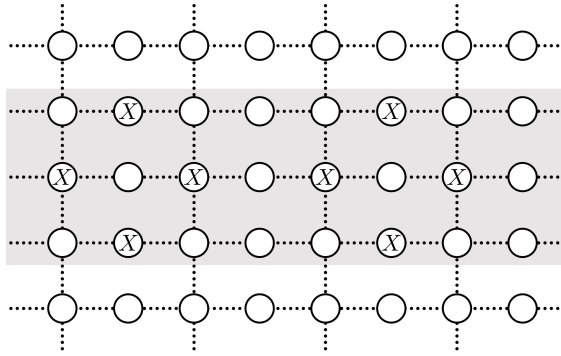


Figure 3.4: The dressed cluster state as defined by the CQCA t_e in Eq. (3.70). Each circle represents a qubit, and dotted lines represent graph state edges (not tensor network legs). One symmetry generator with period $L = 4$ is depicted. Since t_e is periodic, symmetries act along horizontal lines. However, because t_e is also entangling, the width of some horizontal lines is larger than one.

3.5.4 Periodic, entangling CQCA as universal resources for MBQC

Theorem 2 does not apply to every periodic CQCA, and there are examples of non-entangling periodic CQCA which do not lead to universal phases: consider again the CQCA T_p in Eq. (3.24), which is periodic and describes decoupled 1D chains. Such a system cannot be a universal resource for measurement-based quantum computation with our methods, since we cannot create entangling gates with local measurements. This shows that the presence of zero-energy edge modes of dimension 2^N is not sufficient for universal MBQC, and that some additional structure is needed to allow entangling gates. However, periodic CQCA can also be entangling and hence computationally universal as stated in Theorem 2. Surprisingly, in such cases being periodic is not a bug but rather a feature that we now investigate.

Periodic, entangling CQCA have a computational advantage over glider or fractal CQCA due to a quadratic reduction in the number of measurements per gate. This improvement stems from the constant period L of periodic CQCA in contrast to a period that scales linearly in N for glider or fractal CQCA (see Section 3.5.1). As an example, consider the following periodic, entangling CQCA,

$$t_e = ht_g = \begin{pmatrix} 1 & 0 \\ u + u^{-1} & 1 \end{pmatrix}. \quad (3.70)$$

The corresponding fixed-point state defined via Eq. (3.64) is a dressed cluster state which features additional qubits along horizontal lines (see Fig. 3.4). The CQCA has a period of 2 since $t_e^2 = 1$. Nevertheless, it is entangling since $T(X_i) = Z_{i-1}X_iZ_{i+1}$ spreads information. According to our computational scheme $T(X_i)$ can be used as an entangling gate on qubits $i - 1$ and $i + 1$ while single qubit gates come for free in the two-qubit construction. The advantage of the periodic CQCA comes from the fact that our scheme requires all the qubits within a block to be measured in order to perform a single gate. Since the block size is $N \times L$ with $L = 2$ for t_e , we

gain a computational advantage over glider and fractal CQCA which require at least $N \times N$ measurements per block.

3.6 Discussion & Conclusions

In this work, we have used quantum cellular automata to define subsystem symmetries and, subsequently, SSPT phases of matter. With this, we developed a new framework for identifying computationally universal phases of matter, and also for characterizing SSPT order. We have determined which of the resulting phases of matter are computationally universal from the perspective of measurement-based quantum computation. The relation we uncovered between QCA and SSPT order in tensor networks should aid in the understanding and classification of these novel phases of matter.

Our general framework of building MBQC schemes based on CQCA remains relatively unexplored. In particular, we can choose different CQCA in order to tailor the elementary logical gate set towards the problem at hand, a fact that we did not take advantage of in our general proof of universality. For example, when two-qubit nearest neighbour gates are sufficient, periodic CQCA can be employed for a computational speedup as shown in the previous section. On the other hand, altering the elementary gate set in MBQC to include higher order entangling gates is possible in our framework, and can lead to depth-savings in gate synthesis [181]. Also, as pointed out in Ref. [27], the self-similar nature of fractal CQCA can lead to the possibility of entangling far-separated qubits in a single step. It is therefore worthwhile to explore the different computational properties bestowed by different CQCA.

The flexibility of our framework could also have implications for other related protocols of quantum computation that are partially based around QCA. One example is that of secure delegated quantum computation: some protocols for universal blind quantum computation [209, 210] employ schemes for MBQC that only make use of measurements in a single plane. This requirement is naturally fulfilled by our scheme. The same requirement has also recently appeared in proposals to demonstrate superior quantum computational power in near-term devices [213, 214]. Also related is quantum computation restricted to translationally invariant operations [193, 211], which is particularly useful for quantum computing architectures that are restricted to global control [212]. There are examples of all of the above protocols that are based on the cluster state QCA T_g . It would be interesting to investigate whether our general framework can be adapted to these settings, and in particular whether the speedup identified in Section 3.5.4 carries over to advantages in any of the above protocols.

Finally, while we only considered QCA acting as Clifford circuits on chains of qubits, it is possible to generalize beyond this scenario. First, we could extend our analysis to systems of arbitrary local dimension d . In this case, we could realize systems with subsystem symmetry groups of the form $(G \times G)^N$ for an arbitrary finite Abelian group G with $|G| = d$, and our analysis would be in terms of generalized Pauli and Clifford operators [216]. Our general formalism in

Section 3.3 is already equipped to handle this extension, which would lead to new computationally universal phases, and may be useful for the classification of SSPT phases. Similarly, we can extend our results to higher dimensions using the same mapping to a quasi-1D system. In particular, moving to 3D opens up the study of fracton topological order [30, 52, 53] and fault-tolerant MBQC [228, 229]. Finally, with some modifications, our framework should also be able to handle non-Clifford QCA, although in this case the resulting subsystem symmetries would likely not be simple products of local operators.

Chapter 4

Detecting subsystem symmetry-protected topological order via entanglement entropy

By this point, we have characterized SSPT phases in terms of their tensor network representations, and shown how they may be used for universal MBQC. In this chapter, we turn to the physical properties of SSPT phases and show how they may be detected in numerical simulations. The starting point of our analysis is the observation of Ref. [107] that the topological entanglement entropy (TEE) of a ground state (see Section 2.3.3) may not always match the expected value based on the topological phase in which the state resides. In particular, the authors of Ref. [107] showed that the 2D cluster state has a non-zero TEE for certain bipartitions, despite the fact that it lies in a trivial topological phase. Further studies have found similar results, typically due to the presence of symmetry-protected topological (SPT) order localized around the boundary of the bipartition [107, 190, 230–233]. These observations are cause for concern since the existence of a non-zero TEE is often used as a smoking-gun signature of topological order in analytical, numerical, and potentially even experimental studies [106, 234–242].

The point of this chapter is to show that the “spurious” TEE of the 2D cluster state is not an accident, but rather an indication of non-trivial SSPT order. Before the writing of this chapter, SSPT order had been given as a sufficient condition for a non-zero TEE [190], but also an example of two states in the same SSPT phase with different non-zero values of the TEE had been given [232]. This suggests that SSPT phases of matter are not associated with a particular value of the TEE and therefore that its precise value is not useful for the characterization of SSPT order. In this chapter, we demonstrate the contrary by showing that the TEE takes the same value for all generic states in the cluster phase phase, with deviations only occurring at fine-tuned points. This value of the TEE, which we refer to as the *symmetry-protected entanglement entropy (SPEE)* in order to emphasize its origin, relates to the non-trivial symmetry fractionalization that occurs on the boundary of every state in the cluster phase. Therefore, the SPEE may be used to characterize SSPT phases of matter in the same way that the TEE characterizes topological phases of matter.

Going further, we turn the situation on its head by proposing to use the SPEE as the basis for a new numerical technique to detect SSPT order in ground states of gapped local Hamiltonians. Namely, we show how one can straightforwardly extract the SPEE from a PEPS representation of a ground state, and then apply this method to the ground states of various Hamiltonians obtained by perturbing the cluster state Hamiltonian. In accordance with our analytical arguments, we find that the SPEE can reliably and unambiguously detect SSPT order and SSPT phase transitions. Moreover, since the SPEE makes no reference to any particular symmetry of the system, it detects any and all SSPT order within a ground state, unlike usual SPT order parameters which must be defined with respect to a specific representation of the symmetry [14, 59, 135, 223, 243]. As a consequence of this, we discover a large region in which the SSPT order of the cluster state appears to persist despite the subsystem symmetries being explicitly broken. We make a preliminary analysis of this new phase of matter in terms of a new notion of subsystem time-reversal symmetry of the cluster state.

Together, our analytical and numerical results show that the SPEE is an effective tool to detect and characterize the SSPT order of the 2D cluster phase. Going beyond this, we also study 3D cluster states with different types of subsystem symmetries and calculate γ in each case, observing distinct behaviours depending on the structure of the symmetries. We believe that our uniformity arguments for the 2D cluster phase will hold equally well for these 3D phases, and also other types of SSPT order. In an outlook, we discuss the implications of our results for measurement-based quantum computation, detection of fracton order, and the possible experimental observation of SSPT order.

This chapter is organized as follows. In Section 4.1, we define the cluster state and cluster phase, and show their relation to corrections to the area law. In Section 4.2, we present an analytical argument that γ is the same for almost every state in the cluster phase. Then, in Section 4.3, we formulate our numerical method and use it to examine the SSPT order of the cluster state with various Hamiltonian fields and interactions added. In Section 4.4, we calculate the area law corrections for cluster states defined on various 3D lattices, and we finish in Section 4.5 by presenting our conclusions and future directions of work.

4.1 Cluster phase and corrections to the area law

We will begin by reviewing the definition of the cluster state and the cluster phase. We will then calculate the entanglement entropy for a continuous one-parameter family of states in the cluster phase, and find that all states in this family have the same correction to the area law, except for a singular point where the correction is larger. This singular point corresponds to the example given in Ref. [232]. We trace back this larger correction to extra symmetries of the state which do not generically hold in the cluster phase, thereby establishing the premise that all generic states in the cluster phase have the same correction to the area law.

Throughout this chapter, we consider the quasi-1D geometry of a 45° rotated 2D square lattice on an infinitely long cylinder with circumference N (although

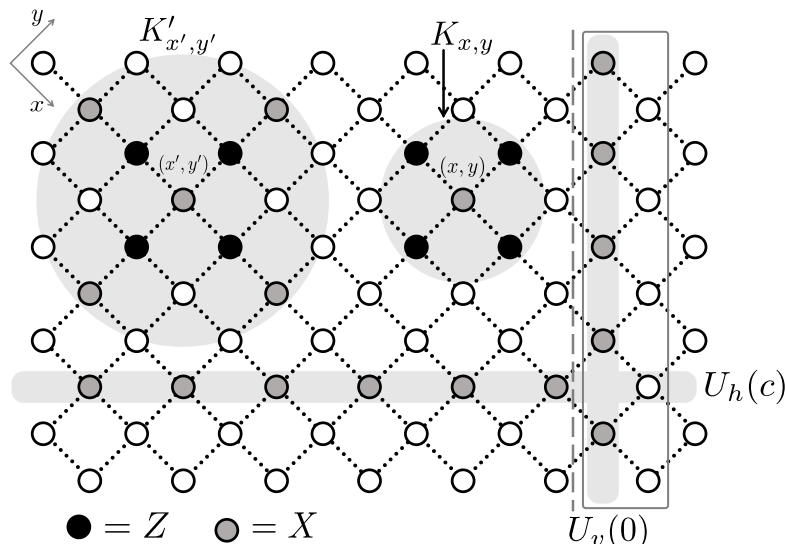


Figure 4.1: A section of the rotated square lattice considered in this chapter. The lattice lives on an infinite cylinder, extending infinitely to the left and right with periodic boundary conditions in the vertical direction. Here, the circumference is $N = 5$. The dashed line indicates the boundary between the A (right) and B (left) subsystems. The solid rectangle denotes the two columns of sites that make up one block in the quasi-1D system considered in Section 4.2. The subsystem symmetries $U_{h,v}(c)$ defining the cluster phase are pictured, as are the stabilizers $K_{x,y}$ and $K'_{x,y}$ that define the states $|C\rangle$ and $|C(\pi)\rangle$, respectively.

similar results hold also for a finite cylinder or torus with dimensions much larger than the correlation length). The cylinder is bipartitioned into two semi-infinite subsystems, denoted A and B . We denote the cluster state on this lattice as $|C\rangle$ and recall the Hamiltonian of the 2D cluster state,

$$H_C = - \sum_{x,y} K_{x,y}. \quad (4.1)$$

which is given in terms of the stabilizers $K_{x,y} = X_{x,y} Z_{x+1,y} Z_{x-1,y} Z_{x,y+1} Z_{x,y-1}$. Having rotated the square lattice, we denote the subsystem line symmetries, which move horizontally and vertically along the cylinder, as

$$\begin{aligned} U_v(c) &= \prod_{x=1}^N X_{x,c-x}, \\ U_h(c) &= \prod_{x=-\infty}^{\infty} X_{x,c+x}. \end{aligned} \quad (4.2)$$

We set our origin such that $U_v(0)$ corresponds to the symmetry lying parallel to the boundary of A , see Fig. 4.1.

This chapter deals with calculating the entropy of entanglement of the reduced density matrix ρ_A , where the A subsystem corresponds to the right half of the cylinder. For much of this chapter we will make statements about the structure of ρ_A directly, such that our claims hold for any α -Rényi entropy (Eq. 2.41) including

the Von Neumann entropy obtained in the limit $\alpha \rightarrow 1$. However, we will sometimes focus on $S_A^{(2)}$ as it is most amicable to our numerical methods. It is also the most convenient to measure experimentally [240–242]. Whenever we make a statement that holds for all α , we will simply use the notation S or $S_A \equiv S(\rho_A)$.

As the cluster state is a stabilizer state, S_A may be straightforwardly calculated using the method shown in Section 2.3.3. Namely, if G is the group generated by all stabilizers $K_{x,y}$, and $G_A \subset G$ is the group of all elements of G which act non-trivially only on region A , then we have the following equation from Section 2.3.3:

$$S_A = |A| - \log_2 |G_A|. \quad (4.3)$$

All stabilizers $K_{x,y}$ corresponding to lattice sites $(x, y) \in A - \partial A$ are contained in G_A . The product of all stabilizers along the boundary, which is precisely the line symmetry $U_v(0)$, is also in G_A , see Fig. 4.1. Hence we have $|G_A| = 2^{|A| - |\partial A| + 1}$, so $S_A = |\partial A| - 1 = N - 1$. We see that the SPEE takes the value $\gamma = 1$ ($= \log_2 2$) for the cluster state, due to the subsystem symmetries forming non-local constraints lying along the boundary of A [107, 232, 233].

As a first venture away from the cluster state, we consider a family of states $|C(\theta)\rangle = U(\theta)|C\rangle$, where the circuit $U(\theta)$ is defined by acting with the two-body unitary $(H \otimes H)C\theta(H \otimes H)$ on every pair of neighbouring sites, where H is the Hadamard matrix and $C\theta = \text{diag}(1, 1, 1, e^{i\theta})$. $U(\theta)$ is diagonal in the local X -basis, hence it commutes with the subsystem symmetries of the cluster state, so $|C(\theta)\rangle$ is in the cluster phase for all θ . We choose this family since it provides a smooth interpolation between the cluster state, $|C(0)\rangle$, and the state considered in Ref. [232], $|C(\pi)\rangle$, which was shown to display an enlarged value of γ .

For general θ , $|C(\theta)\rangle$ is not a stabilizer state, so we need a different method to calculate its entropy. In order to calculate $S_A^{(2)}(\theta)$, we use the method of Ref. [107]. Notice that $|C(\theta)\rangle$ may be created by a unitary circuit acting on a product state. Therefore, by applying unitaries on the A and B subsystems separately, which does not change the entropy, we may disentangle all qubits except those on a strip along the boundary. Thus the calculation of entropy for our 2D system is reduced to that of a 1D system with an extensive bipartitioning, and this may be easily computed using a transfer matrix method. Namely, we can construct a matrix $Q(\theta)$ that follows from the definition of $|C(\theta)\rangle$, such that $S_A^{(2)}(\theta) = -\log_2 \text{Tr}(Q(\theta)^N)$, see Ref. [107] for more details. Let $\{\lambda_k\}_k$ be the set of eigenvalues of $Q(\theta)$ with maximum magnitude and write $\lambda_k = r e^{i\phi_k}$. The entropy is then,

$$S_A^{(2)}(\theta) = N \log_2 r - \log_2 m + \dots, \quad (4.4)$$

where $m = \sum_k e^{iN\phi_k}$ and the terms contained in the dots decay exponentially in N . The prefactor of the area law is therefore given by $\log_2 r$, while the SPEE is given by $\log_2 m$. Thus, the SPEE can be determined by examining the eigenvalues of $Q(\theta)$ with largest magnitude. If there are no non-positive eigenvalues with magnitude r , then the constant m is simply the degeneracy of the largest eigenvalue. If such eigenvalues do exist, then m can exhibit periodic N dependence.

The spectrum of $Q(\theta)$ can be computed exactly¹, and the results are shown in

¹This is possible because $Q(\theta)$ is simply a 256×256 matrix, which can be exactly diagonalized

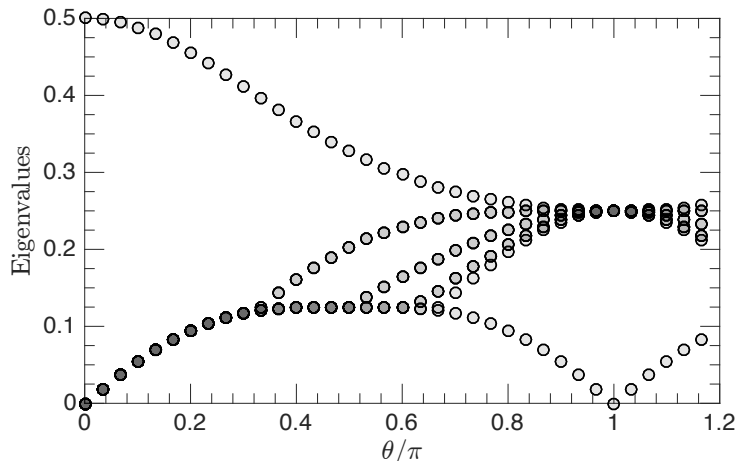


Figure 4.2: Spectrum of the transfer matrix $Q(\theta)$. For each value of θ , the moduli of the 18 largest eigenvalues of $Q(\theta)$ are depicted, where each dot indicates at least 2 degenerate eigenvalues. At each value of θ , the largest eigenvalue is two-fold degenerate, except for the point $\theta = \pi$ where it is 16-fold degenerate in magnitude.

Fig. 4.2. For $\theta \neq \pi$, there are two eigenvalues of largest magnitude, both of which are positive. Hence we have $m = 2$ and $\gamma = 1$. At $\theta = \pi$, there are 16 eigenvalues of largest magnitude. More precisely, we find that the non-zero eigenvalues of $Q(\pi)$ are $\frac{1}{4}$, $-\frac{1}{4}$, $\frac{i}{4}$, and $-\frac{i}{4}$ with degeneracies 8, 4, 2 and 2, respectively. In this case, we have $m = \left(8 + 4(-1)^N + 2i^N + 2(-i)^N\right)$, which gives,

$$S_A^{(2)}(\pi) = \begin{cases} 2N - 4 & \text{if } 4 \mid N \\ 2N - 3 & \text{if } 2 \mid N \text{ and } 4 \nmid N \\ 2N - 2 & \text{if } 2 \nmid N \end{cases} \quad (4.5)$$

Therefore, the states $|C(\theta)\rangle$ have a SPEE $\gamma = 1$ for all $\theta \neq \pi$, while $\gamma > 1$ for $\theta = \pi$.

The enlarged SPEE for $\theta = \pi$ can be attributed to the fact that $|C(\pi)\rangle$ has many extra symmetries, aside from those in Eq. (4.2), which are not satisfied for $\theta \neq \pi$. Namely, $|C(\pi)\rangle$ is a stabilizer state satisfying $K'_{x,y}|C(\pi)\rangle = |C(\pi)\rangle$ where the stabilizers $K'_{x,y}$ are as pictured in Fig. 4.1. One can alternatively compute $S_A^{(2)}(\pi)$ using Eq. (4.3), and the results agree with Eq. (4.5)². At the end of the next section, we will use the tensor network representation of $|C(\pi)\rangle$ to more clearly identify the mechanism through which these extra symmetries lead to a larger SPEE.

numerically

²The enlarged SPEE comes from extra subsystem symmetries which appear in G_A . It would be interesting to investigate whether or not the enlarged SPEE would persist if these extra symmetries were preserved.

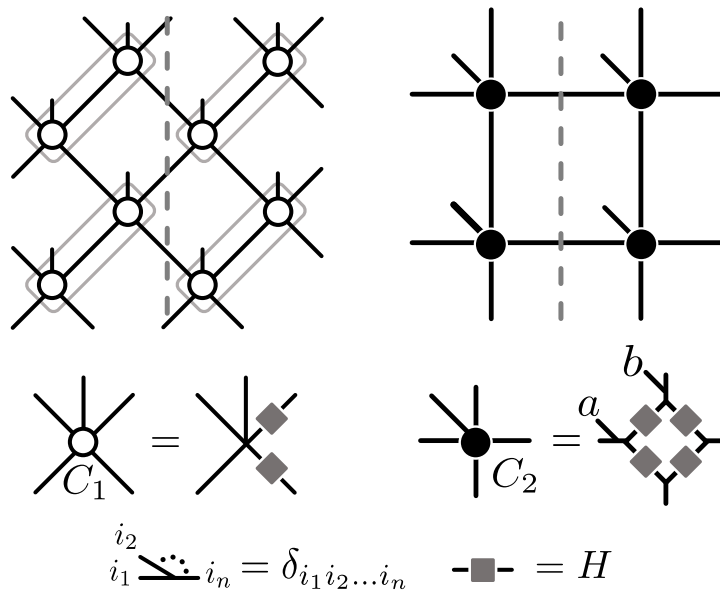


Figure 4.3: Two different tensor network representations of the 2D cluster state. On the left, we define the tensor C_1 which has the geometry of the rotated square lattice. On the right, we define the tensor C_2 which has two physical legs per tensor, labelled a and b . The corresponding tensor network has the geometry of a (non-rotated) square lattice. Both tensors are defined in terms of Kronecker- δ tensors and the Hadamard matrix H . The dashed lines indicate the boundary between the A and B subsystems.

4.2 Analytical argument for uniformity of the SPEE

The results of the previous section suggest that the SPEE γ is uniform throughout the cluster phase, except for certain fine-tuned states with enhanced symmetries. Now, we will use tensor networks to give an analytical argument that all generic states in the cluster phase do indeed have the same SPEE. The fact that $\gamma \geq 1$ was argued in Ref. [190] (using the result of Ref. [107]) under a similar set of assumptions as those used here³. The purpose of the more careful argument of this section is to argue that $\gamma = 1$ exactly. We begin by restating the tensor network characterization of the cluster phase given in Section 2.7.1 in a more suitable manner, and then we show how this can be used to constrain γ .

4.2.1 Tensor network description of the cluster phase

In Fig. 4.3, we define two PEPS representations of the cluster state. The first tensor, C_1 , is the usual PEPS representation of the cluster state (Eq. 2.124). In this section, we will find it more convenient to consider a different PEPS representation of the cluster state, denoted C_2 , which has two qubits per unit cell and is defined on a 45°-rotated square lattice, see Fig. 4.3. The two tensor networks in Fig. 4.3

³Namely, they assumed that, throughout the phase, we can disentangle the degrees of freedom far from the cut using unitary operators localized on either side of it. This is essentially the same as assuming a finite bond-dimension PEPS representation, as we do here.

can be related by merging and splitting δ -tensors appropriately. The equivalent tensor characterization of the cluster phase (Eq. 2.129) for this two qubit unit cell is,

The diagram shows two equations. The first equation is $A_2 = B_2 C_2$, where A_2 is a tensor with four legs (two horizontal, two diagonal), B_2 is a tensor with two horizontal legs and two diagonal legs, and C_2 is a tensor with two horizontal legs and two diagonal legs. The second equation is $B_2 X_{a/b} = B_2$, where $X_{a/b}$ is a tensor with two horizontal legs and two diagonal legs, and B_2 is a tensor with two horizontal legs and two diagonal legs.

$$A_2 = B_2 C_2 \quad \text{where} \quad B_2 X_{a/b} = B_2 \quad (4.6)$$

B_2 is some tensor describing a projected entangled pair operator which commutes locally with $X_{a/b}$ as indicated, where $X_{a/b}$ denotes X acting on one of the two qubits in a unit cell, labelled a/b as in Fig. 4.3. Throughout the cluster phase, C_2 stays the same, but B_2 varies.

If we contract the physical leg of any tensor A with some state $|i\rangle \in \{|+\rangle, |-\rangle, |-\rangle, |-\rangle\}$, we obtain a tensor with 4 virtual legs, denoted A^i . In terms of these components, Eq. (4.6) reads,

$$A_2^i = B_2^i \otimes C_2^i \quad (4.7)$$

Thus, the virtual space of the tensor network decomposes into two subspaces, which are again called the *junk* and *protected* subspaces, corresponding to the operators B_2^i and C_2^i , respectively. This decomposition is central to the following arguments.

We now map our system onto a quasi-1D system by combining $2N$ spins around the cylinder into one larger block as shown in Fig. 4.1. The associated tensor \mathcal{A} is obtained by combining N tensors A_2 in a ring around the cylinder, see Fig. 4.4. If we let $\mathbf{i} = (i_1, i_2, \dots, i_N)$ be an element of the index set I labelling all 2^{2N} states in a block, we can again define the tensor components $\mathcal{A}^{\mathbf{i}}$. Due to the subsystem symmetries $U_v(c)$, the wavefunction of our state consists only of terms with an even number of $|-\rangle$ states in both columns in each block. Denoting this even-parity subset of states $I_e \subset I$ and the corresponding odd-parity subspace as $I_o \subset I$, we can therefore modify the tensor \mathcal{A} by setting $\mathcal{A}^{\mathbf{i}} = 0, \forall \mathbf{i} \in I_o$, without changing the state described by \mathcal{A} . This modification simplifies our description later on.

For the remaining $\mathbf{i} \in I_e$, Eq. (4.7) implies the decomposition $\mathcal{A}^{\mathbf{i}} = \mathcal{B}^{\mathbf{i}} \otimes \mathcal{C}^{\mathbf{i}}$, where \mathcal{B} and \mathcal{C} denote the blocked tensors living in the junk and protected subspaces, respectively. We can straightforwardly determine $\mathcal{C}^{\mathbf{i}}$ using the definition of C_2 . We find that $\mathcal{C}^{\mathbf{i}} = \mathcal{P}^{\mathbf{i}} \Pi, \forall \mathbf{i} \in I_e$, where each $\mathcal{P}^{\mathbf{i}}$ is some tensor product of Pauli operators and,

$$\Pi = \frac{\mathbb{1} + X^{\otimes N}}{2}, \quad (4.8)$$

is a rank- 2^{N-1} projection matrix with $X^{\otimes N} \equiv \prod_{k=1}^N X_k$. Therein, X_k denotes X acting on the k -th component of the N -component protected subspace. Importantly, the operators $\mathcal{P}^{\mathbf{i}}$ also satisfy $\mathcal{P}^{\mathbf{i}} \Pi = \Pi \mathcal{P}^{\mathbf{i}}$, for all $\mathbf{i} \in I_e$.

4.2.2 Constraining the SPEE in the cluster phase

We will now use the above characterization of the cluster phase to show that the entanglement entropy S_A can be decomposed into two parts, $S_A = S_B + S_C$, where

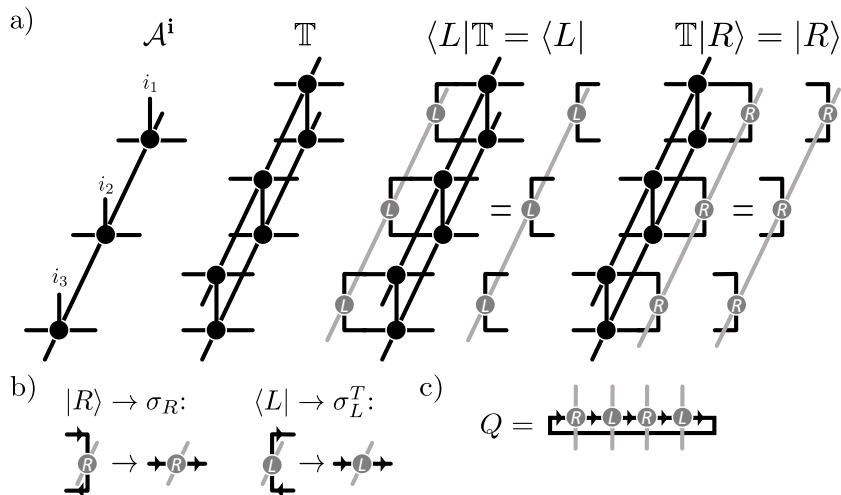


Figure 4.4: a) Illustration of the PEPS transfer matrix and its fixed points. b) Relation between the fixed points of \mathbb{T} and \mathcal{T} via reorientation of the legs of each tensor. c) The matrix Q whose spectrum encodes the entanglement entropy for all system sizes N .

S_C is the entropy of the cluster state, and S_B is essentially the entropy of the PEPS defined by the tensor B_2^i . Since we know $S_C = N - 1$, and we will argue S_B satisfies an area law with no correction for generic B_2^i , we will find that S_A has a correction of $\gamma = 1$ for generic states in the cluster phase.

As shown in Section 2.5, entanglement entropy can be straightforwardly calculated in tensor networks in terms of the fixed points of the transfer matrix. We define the transfer matrix as,

$$\mathbb{T} = \sum_{i \in I} \mathcal{A}^i \otimes \bar{\mathcal{A}}^i, \quad (4.9)$$

where the bar denotes complex conjugation. We can normalize our PEPS such that the largest eigenvalue of \mathbb{T} is 1, and denote by $|R\rangle$ and $\langle L|$ the left and right fixed-points of \mathbb{T} , such that $\mathbb{T}|R\rangle = |R\rangle$ and $\langle L|\mathbb{T} = \langle L|$. For the following proof, we will find it more convenient to work with the associated quantum channel,

$$\mathcal{T}(\rho) = \sum_{i \in I} \mathcal{A}^i \rho \mathcal{A}^{i\dagger}, \quad (4.10)$$

which is related to \mathbb{T} by redefining the input and output legs of the tensor. We will refer to both \mathbb{T} and \mathcal{T} as the transfer matrix. The fixed points $|R\rangle$ and $\langle L|$ of \mathbb{T} correspond to fixed points σ_R and σ_L of \mathcal{T} and its adjoint $\mathcal{T}^\dagger = \sum_i \mathcal{A}^{i\dagger} \rho \mathcal{A}^i$, respectively. See Fig. 4.4 for a graphical representation of these objects.

An important property of the cluster phase is that the fixed point of the transfer matrix is unique, with all other eigenvalues having magnitude less than unity. Specifically, a degenerate fixed point space of the transfer operator would manifest itself as long-range correlations along the cylinder axis – either for local operators, amounting to conventional long-range order [131], or for loop operators acting around the cylinder, amounting to topological order [244]. Since any such

order is absent in the cluster state (whose transfer operator has a unique fixed point), and thus by definition in the whole cluster phase, the fixed point of the transfer matrix must be unique in the whole cluster phase.

As shown in Section 2.5, we can express the reduced density matrix ρ_A as $\rho_A = \mathcal{V}^\dagger \sigma \mathcal{V}$ where \mathcal{V} is an isometry and $\sigma = \sqrt{\sigma_L^T} \sigma_R \sqrt{\sigma_L^T}$, with T denoting the transpose. Thus, $S_A = S(\sigma)$. The rest of this section is dedicated to constraining σ within the cluster phase.

To begin, note that, due to Eq. (4.7), \mathcal{T} satisfies many symmetries throughout the entire cluster phase. First, we have,

$$\begin{aligned} \mathcal{T}([\mathbb{1} \otimes X_k] \rho [\mathbb{1} \otimes X_k]) &= \sum_{\mathbf{i} \in I} \mathcal{A}^{\mathbf{i}} [\mathbb{1} \otimes X_k] \rho [\mathbb{1} \otimes X_k] \mathcal{A}^{\mathbf{i}\dagger} \\ &= \sum_{\mathbf{i} \in I_e} (\mathcal{B}^{\mathbf{i}} \otimes \mathcal{P}^{\mathbf{i}} \Pi X_k) \rho (\mathcal{B}^{\mathbf{i}} \otimes X_k \Pi \mathcal{P}^{\mathbf{i}}) \\ &= \sum_{\mathbf{i} \in I_e} (\mathcal{B}^{\mathbf{i}} \otimes X_k \mathcal{P}^{\mathbf{i}} \Pi) \rho (\mathcal{B}^{\mathbf{i}} \otimes \Pi \mathcal{P}^{\mathbf{i}} X_k) \\ &= [\mathbb{1} \otimes X_k] \mathcal{T}(\rho) [\mathbb{1} \otimes X_k]. \end{aligned} \quad (4.11)$$

Therein, X_k acts on the protected subspace, while $\mathbb{1}$ acts on the junk subspace. In the second equality, we substituted $\mathcal{A}^{\mathbf{i}} = \mathcal{B}^{\mathbf{i}} \otimes \mathcal{P}^{\mathbf{i}} \Pi$. In the third equality, we used the facts that $X_k \mathcal{P}^{\mathbf{i}} = \pm \mathcal{P}^{\mathbf{i}} X_k$ and $X_k \Pi = \Pi X_k$. In the same way, we can derive,

$$\mathcal{T}(Z_k Z_{k+1} \rho Z_k Z_{k+1}) = Z_k Z_{k+1} \mathcal{T}(\rho) Z_k Z_{k+1}. \quad (4.12)$$

Above, and in the rest of this section, we have omitted the identity operators acting on the junk subspace for notational simplicity. Finally, because $X^{\otimes N} \Pi = \Pi$, we also have the symmetries,

$$\mathcal{T}(\rho) = X^{\otimes N} \mathcal{T}(\rho) = \mathcal{T}(\rho) X^{\otimes N}. \quad (4.13)$$

All of the above symmetries hold also for \mathcal{T}^\dagger . These symmetries are a reflection of the symmetry fractionalization on the boundary that characterizes the cluster phase, as described in Section 2.7.1.

Since the fixed-points are unique, they inherit these symmetries. For example, if σ_R is the fixed-point of \mathcal{T} , Eq. (4.11) implies that $X_k \sigma_R X_k$ is as well. Since the fixed-point is unique up to a multiplicative constant, we have $X_k \sigma_R X_k \propto \sigma_R$. Since σ_R is positive, and conjugation by X_k preserves the trace, we must have $X_k \sigma_R X_k = \sigma_R$. Using similar arguments, we get all of the following symmetries:

$$\begin{aligned} [\sigma_{R/L}, X_k] &= [\sigma_{R/L}, Z_k Z_{k+1}] = 0, \\ X^{\otimes N} \sigma_{R/L} &= \sigma_{R/L} X^{\otimes N} = \sigma_{R/L}. \end{aligned} \quad (4.14)$$

These symmetries completely constrain $\sigma_{R/L}$ on the protected subspace, with Π being the unique solution to the constraints. Thus, the fixed points decompose across the junk and protected subspaces as $\sigma_{R/L} = \tilde{\sigma}_{R/L} \otimes \Pi$ for some unknown states $\tilde{\sigma}_{R/L}$. This gives $\sigma = \tilde{\sigma} \otimes \Pi$, where $\tilde{\sigma} = \sqrt{\tilde{\sigma}_L^T} \tilde{\sigma}_R \sqrt{\tilde{\sigma}_L^T}$.

Having constrained the fixed points in the protected subspace, what can we now say about the unconstrained part $\tilde{\sigma}$? It turns out that $\tilde{\sigma}_{R/L}$ are themselves fixed points of a certain transfer operator. Indeed, we have,

$$\begin{aligned} \mathcal{T}(\tilde{\sigma}_R \otimes \Pi) &= \sum_{\mathbf{i} \in I} \mathcal{A}^{\mathbf{i}}(\tilde{\sigma}_R \otimes \Pi) \mathcal{A}^{\mathbf{i}\dagger} \\ &= \sum_{\mathbf{i} \in I} \mathcal{B}^{\mathbf{i}} \tilde{\sigma}_R \mathcal{B}^{\mathbf{i}\dagger} \otimes \mathcal{C}^{\mathbf{i}} \Pi \mathcal{C}^{\mathbf{i}\dagger} \\ &= \sum_{\mathbf{i} \in I_e} \mathcal{B}^{\mathbf{i}} \tilde{\sigma}_R \mathcal{B}^{\mathbf{i}\dagger} \otimes \Pi, \end{aligned} \quad (4.15)$$

where we used the facts that $\mathcal{C}^{\mathbf{i}} = 0, \forall \mathbf{i} \in I_o$, and $[\mathcal{C}^{\mathbf{i}}, \Pi] = 0, \forall \mathbf{i} \in I_e$. Since $\mathcal{T}(\tilde{\sigma}_R \otimes \Pi) = \tilde{\sigma}_R \otimes \Pi$ by definition, this gives

$$\tilde{\mathcal{T}}(\tilde{\sigma}_R) := \sum_{\mathbf{i} \in I_e} \mathcal{B}^{\mathbf{i}} \tilde{\sigma}_R \mathcal{B}^{\mathbf{i}\dagger} = \tilde{\sigma}_R. \quad (4.16)$$

Furthermore, Eq. (4.15) implies that every eigenvector $\tilde{\rho}$ of $\tilde{\mathcal{T}}$ yields an eigenvector $\tilde{\rho} \otimes \Pi$ of \mathcal{T} with the same eigenvalue. Therefore, $\tilde{\sigma}_R$ is the unique fixed-point of $\tilde{\mathcal{T}}$, since the fixed-point of \mathcal{T} is unique. Similarly, $\tilde{\sigma}_L$ is the unique fixed-point of $\tilde{\mathcal{T}}^\dagger$.

Since $\sigma = \tilde{\sigma} \otimes \Pi$, the entanglement entropy decomposes into two components,

$$S_A = S(\sigma) = S(\tilde{\sigma}) + S(\Pi), \quad (4.17)$$

where $S(\Pi) = N - 1$ is the entropy of the cluster state. What remains is to understand the entropy contribution $S(\tilde{\sigma})$. We will argue that $S(\tilde{\sigma})$ generically satisfies an area law with no correction. To this end, consider a generic tensor $A_2^i = B_2^i \otimes C_2^i$ which is in the cluster phase. Since it belongs to the cluster phase, it can be connected to the cluster state via a smooth path $A_2^i(\theta) = B_2^i(\theta) \otimes C_2^i$ without closing the gap of the transfer operator \mathcal{T} . This implies that $B_2^i(\theta)$ smoothly connects B_2^i to a trivial tensor, where the corresponding transfer operator $\tilde{\mathcal{T}}$ must remain gapped along the path as well. Up to the restriction $\mathbf{i} \in I_e$, $\tilde{\mathcal{T}}$ is thus the transfer operator of a system in the trivial phase. However, we expect that such a global parity constraint will only affect the entropy if the system either has topological order – which we have ruled out – or physical symmetries in the basis of the constraint, which would require fine-tuning of the B_2^i . Thus, we expect the fixed point of $\tilde{\mathcal{T}}$ to have the structure of a generic fixed point in the trivial phase, which does not exhibit long-range correlations and thus no constant correction to the area law.

Overall, this reasoning implies that, for generic points in the cluster phase, the entropy $S(\tilde{\sigma})$ should scale as,

$$S(\tilde{\sigma}) \propto N, \quad (4.18)$$

with corrections vanishing as $N \rightarrow \infty$, whereas constant corrections are expected only at fine-tuned points with additional symmetries. This is confirmed by numerical study of generic tensors B_2^i up to bond dimension 4. We thus find that, for a generic point in the cluster phase, the entanglement entropy should scale like $S_A = aN - 1$ for some constant a .

In light of these arguments, let us now reconsider why $|C(\pi)\rangle$ from Section 4.1 has a correction $\gamma > 1$. For this state, one can write a PEPS in the form of Eq. (4.6), where B^i is the same tensor as C^i , up to applying H on each physical leg. Therefore, in addition to Eqs. (4.11-4.13), \mathcal{T} has just as many extra symmetries which act non-trivially on the junk subspace. These symmetries serve to constrain $\tilde{\sigma}_{R/L}$, leading to the increased value of γ . Such symmetries are generically not present in the cluster phase, and indeed disappear for all $\theta \neq \pi$, reflected by the generic correction $\gamma = 1$.

4.3 Numerical detection of SSPT order

Above, we have argued that $\gamma = 1$ within the entire cluster phase, except at certain fine-tuned points of enhanced symmetry. In this section, we perform numerical calculations of γ in ground states. The motivation of this is twofold. First, we would like to substantiate our analytical arguments. By considering known models, we will confirm that $\gamma = 1$ within the cluster phase, and $\gamma = 0$ in the trivial phase. Second, once we are confident that $\gamma = 1$ indicates the presence of SSPT order, we can use it as a probe for phase transitions. We will add various fields and interactions onto the cluster Hamiltonian, with phase transitions into the trivial phase indicated by γ suddenly dropping from 1 to 0. This study will lead us to the discovery of a new phase of matter beyond the cluster phase.

4.3.1 Description of the algorithm

We use the following method to calculate γ in ground states. Given a Hamiltonian H , we use variational infinite projected entangled pair state (iPEPS) techniques to obtain a PEPS approximation to the ground state [161]. We then use this PEPS to construct the transfer matrix as in Eq. (4.10), and use a TEBD-based infinite matrix product state (iMPS) algorithm to obtain matrix product operator (MPO) approximations for the fixed-points σ_R and σ_L . Using this, we can write

$$S_A^{(2)} = -\log_2 \text{Tr}(\sigma_R \sigma_L^T \sigma_R \sigma_L^T) = -\log_2 \text{Tr}(Q^N), \quad (4.19)$$

where Q is a matrix obtained from the MPO tensors describing σ_R and σ_L^T , see Fig. 4.4⁴. For all states encountered in this section, the leading eigenvalue of Q will either be unique or two-fold degenerate. Denote the two largest eigenvalues of Q (which may or may not be degenerate) as λ_0 and λ_1 . In analogy with Eq. (4.4), we have

$$S_A^{(2)} = N \log_2 \lambda_0 - \gamma + \dots, \quad (4.20)$$

where $\gamma = 1$ if $\lambda_0 = \lambda_1$, and $\gamma = 0$ otherwise. Therefore, we can determine γ from the ratio λ_1/λ_0 . We note that this ratio is closely related to the replica correlation length that was introduced in Ref. [107] to study spurious corrections to the area law. A similar method to compute entanglement entropy in PEPS was also proposed in Ref. [245].

⁴We remark that the matrix Q is not the same object as the matrix $Q(\theta)$ introduced in Section 4.1, although they are closely related

4.3.2 Stability of the cluster phase

Now we use the above method to investigate the fate of the SPEE under various local fields or interactions added to the cluster Hamiltonian, one at a time. The goal is to support our argument that the value $\gamma = 1$ characterizes the cluster phase, meaning that this value persists unless the subsystem symmetries are explicitly broken or a phase transition is crossed.

We consider a Hamiltonian of the form:

$$H' = H_C + \sum_{x,y} h'_{x,y}, \quad (4.21)$$

for several different choices of $h'_{x,y}$, each with different symmetries. In Fig. 4.5, we plot λ_1/λ_0 as a function of the strength of the perturbation $h'_{x,y}$. The important findings are the following:

(i) When a small symmetry respecting perturbation is added to the Hamiltonian, the SPEE keeps the value $\gamma = 1$.

(ii) When the strength of the symmetry respecting perturbations are increased, we encounter phase transitions indicated by a sudden drop to $\gamma = 0$. The location of the phase transitions agree with known results where available.

(iii) Adding a term which does not commute with the subsystem symmetries removes the SPEE for any finite coupling strength.

Overall, these results support our analytical results and confirm that the SPEE is a useful probe for detecting SSPT order and phase transitions. We will now discuss each choice of $h'_{x,y}$ in more detail.

Symmetry respecting terms

We first consider adding terms which commute with the subsystem symmetries. For such terms, we expect that the value of the SPEE will remain constant up until an SSPT phase transition is reached, at which point it should jump to 0. The first term we consider is a simple local X -field:

$$h'_{x,y} = -h_X X_{x,y}. \quad (4.22)$$

The model of a cluster Hamiltonian with added X -field been studied previously in Refs. [12, 49, 59, 246]. For $h_X \rightarrow \infty$, the model becomes a trivial paramagnet without SSPT order, so there must be a phase transition at some value of h_X . The model is self dual under the unitary circuit $U_{CZ} := U(\pi)$ (see Section 4.1), so this phase transition should occur at $h_X = 1$. Indeed, via a non-local duality transformation, this model can be mapped to the so-called Xu-Moore model with a transverse field, which is known to have a first order phase transition at $h_X = 1$ [12, 59, 247]. In agreement with these facts, we find that λ_1/λ_0 changes from 1 discontinuously at the transition point, such that γ jumps to 0 at this point, thereby correctly detecting the phase transition.

The next term we consider is a four-body interaction,

$$h'_{x,y} = -J_{ZZZZ}^{\diamond} Z_{x-1,y} Z_{x+1,y} Z_{x,y-1} Z_{x,y+1}. \quad (4.23)$$

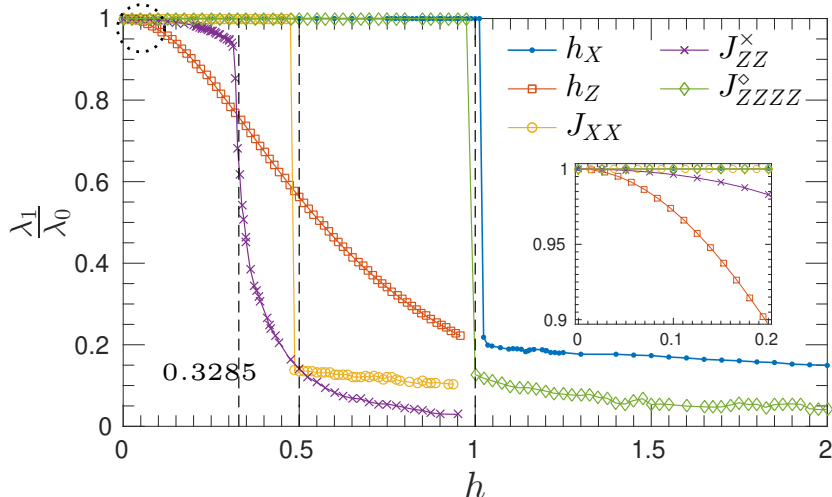


Figure 4.5: Entanglement entropy versus field or interaction strength of various terms added to the cluster Hamiltonian. h is a dummy variable, standing for the different variables indicated in the legend. The y-axis shows the ratio of the two largest eigenvalues of the transfer matrix Q defined in Fig. 4.4. There is a correction $\gamma = 1$ to the area law if $\lambda_1/\lambda_0 = 1$, and otherwise it is 0. The inset zooms in on the region indicated by the dotted circle, and shows that the symmetry-breaking terms destroy the correction for any finite value of h .

This is the minimal term that contains Z operators yet still commutes with all subsystem symmetries. Interestingly, this model behaves in the opposite way to first one, in that it is mapped to the Xu-Moore model under U_{CZ} , while it is self-dual under the same non-local duality transformation. These facts predict a phase transition at $J_{ZZZZ}^o = 1$, and this is again in agreement with the behaviour of λ_1/λ_0 .

The final symmetry-preserving term we consider is a nearest-neighbour Ising interaction,

$$h'_{x,y} = -J_{XX} (X_{x,y}X_{x+1,y} + X_{x,y}X_{x,y+1}). \quad (4.24)$$

To the best of our knowledge, this model has yet to be studied in the literature. Via the same non-local duality transformation mentioned earlier, it may be mapped onto two Xu-Moore models coupled by Ising interactions. The SPEE disappears at $J_{XX} = 0.5$, suggesting that there is an SSPT phase transition into the symmetry-breaking phase at this point.

We also verified that simultaneously adding all three symmetry respecting terms with random small couplings does not change the SPEE. This shows that the behaviour observed above is not a consequence of the specific Hamiltonians considered, and is instead generic behaviour.

Symmetry breaking terms

We now turn our attention to terms which anti-commute with the subsystem symmetries, and therefore explicitly break them. For these terms, the SSPT order

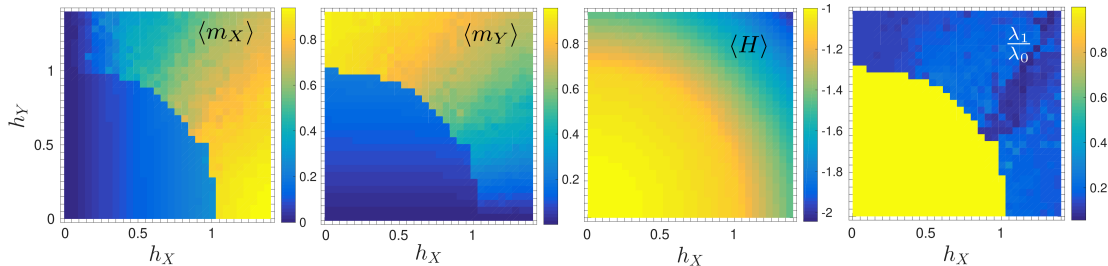


Figure 4.6: Phase diagram of the cluster model with added local Pauli X and Y fields with field strengths h_X and h_Y , respectively. The local magnetizations $\langle m_X \rangle$ and $\langle m_Y \rangle$ along the X and Y directions, and the ground state energy per site $\langle H \rangle$ are plotted alongside the ratio λ_1/λ_0 of the two largest eigenvalues of the matrix Q . There is a large region in which this ratio is very nearly 1, indicating that the SPEE takes the value $\gamma = 1$ in this region.

should be destroyed for any finite coupling strength, so λ_1/λ_0 should decrease from 1 immediately. The simplest symmetry-breaking term is a Z -field,

$$h'_{x,y} = -h_Z Z_{x,y}. \quad (4.25)$$

As predicted, we find $\lambda_1/\lambda_0 < 1$ for any value of h_Z . Furthermore, this model is mapped to a trivial Hamiltonian under the action of U_{CZ} . Therefore, there is no phase transition for any value of h_Z , and this is consistent with the smooth decay of λ_1/λ_0 that we observe.

The next term we consider is a next-nearest neighbour interaction,

$$h'_{x,y} = -J_{ZZ}^\times (Z_{x,y} Z_{x+1,y+1} + Z_{x,y} Z_{x-1,y+1}). \quad (4.26)$$

While this term anti-commutes with the subsystem symmetries, it commutes with the global “checkerboard” $\mathbb{Z}_2 \times \mathbb{Z}_2$ symmetry of the cluster state, which is generated by applying X to all even or all odd spins on the square lattice. The cluster state has “weak” 2D SPT order under this global symmetry group, which is defined by a 2D SPT order that is only non-trivial in the presence of translational invariance [22, 60]. Therefore, it is important to confirm that the non-zero value of the SPEE is due to the subsystem symmetries, and not the global symmetries alone. Indeed, we find $\lambda_1/\lambda_0 < 1$ for any finite value of J_{ZZ}^\times , indicating that the global symmetries are not sufficient to protect the SPEE. As opposed to the previous case, we observe some singular behaviour of λ_1/λ_0 as J_{ZZ}^\times is increased. This is explained by the fact that, under U_{CZ} , this model is mapped to two decoupled 2D quantum Ising models, which undergo a second order phase transition into a symmetry-breaking phase at $J_{ZZ}^\times \approx 0.3285$. Thus, the behaviour of λ_1/λ_0 also helps to detect non-SSPT phase transitions.

4.3.3 Beyond the cluster phase — Time reversal symmetry

We now consider adding the term,

$$h'_{x,y} = -h_Y Y_{x,y}. \quad (4.27)$$

This term anti-commutes with the subsystem symmetries, as with Eq. (4.25). Therefore, according to our findings in the previous subsection, we would expect any finite value of h_Y to remove the SPEE. This turns out not to be the case, as seen in Fig. 4.6, and this section is devoted to understanding this behaviour.

It was shown in Ref. [61] that the cluster state also has non-trivial SSPT order protected by fractal subsystem symmetries which are composed of tensor products of Y operators. Since the model is trivial when $h_Y \rightarrow \infty$, there should be a phase transition into the trivial phase for some h_Y . Since the model is self-dual under U_{CZ} followed by applying $S = \text{diag}(1, i)$ on every site, this transition should occur at $h_Y = 1$. Along the y -axes of Fig. 4.6, we see good evidence that this is the case. For example, the magnetization along the Y axis jumps discontinuously at this point.

What is surprising is that this transition is also detected by the SPEE, which remains equal to 1 up until $h_Y = 1$, even though the Y -field does not commute with the subsystem symmetries. It is tempting to attribute the SPEE to the fractal symmetries of the cluster state, which do commute with the Y -field, but this is not the case. Consider simultaneously adding X and Y magnetic fields to the cluster state,

$$h'_{x,y} = -h_X X_{x,y} - h_Y Y_{x,y}. \quad (4.28)$$

We see in Fig. 4.6 that the SPEE still persists in a large region. This cannot be due to the X line-like symmetries of Eq. (4.2), nor the Y fractal symmetries, since both are explicitly broken by the added fields. Therefore, it appears that we have discovered a new SSPT phase which contains at least part of cluster phase, and which is also accompanied by a non-zero SPEE.

A similar phenomenon occurs in 1D. The 1D cluster state has SPT order under a global $\mathbb{Z}_2 \times \mathbb{Z}_2$ symmetry, generated by applying X to all even or all odd spins on the chain. Similar to the current scenario, this SPT order is stable under adding a Y -field, despite the fact that this is a symmetry-breaking term. In this case, the resolution is that the 1D cluster state also has time-reversal symmetry [94]. This symmetry also protects the SPT order of the cluster state, and commutes with the Y -field.

Time-reversal turns out to be the solution here as well, although it takes an unusual form. In Ref. [59], the authors defined subsystem time-reversal symmetries as subsystem unitary symmetries, such as the line-like symmetries considered here, followed by *global* time-reversal. But it is easy to see that this also does not work, since the global time-reversal flips the sign of all Y -fields, not just those lying along a given line of subsystem symmetry. We therefore need a different notion of subsystem time-reversal, in which we enact time-reversal *locally* only on those sites of the lattice on which the subsystem symmetry acts non-trivially.

Ref. [248] suggested one way to implement time-reversal locally on a tensor network. Globally, time-reversal symmetry acts on a quantum state by the action of a unitary operator (here, the subsystem symmetries) combined with complex conjugation of the wavefunction. With tensor networks, the wavefunction is divided into local tensors. Thus, one can define local complex conjugation at a given site by conjugating only the tensor associated to that site. More precisely, we can define operators $\mathcal{K}_{x,y}$ which act on the PEPS by conjugating the tensor at site

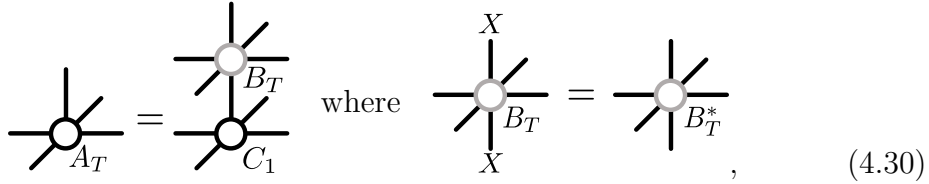
(x, y) only. Note that, to ensure that the proper notion of locality is used, we use the tensor network defined on a rotated square lattice with a single-qubit unit cell, shown in Fig. 4.3.

With this, we define our subsystem time-reversal as,

$$U_v^T(c) = \prod_{x=1}^N X_{x,c-x} \mathcal{K}_{x,c-x}, \quad (4.29)$$

$$U_h^T(c) = \prod_{x=-\infty}^{\infty} X_{x,c+x} \mathcal{K}_{x,c+x}.$$

Is this the correct symmetry to describe the phase of matter observed in Fig. 4.6? To answer this, we consider a state described by a tensor of the following form,



$$A_T = \begin{array}{c} \diagup \\ \bigcirc \\ \diagdown \\ \diagup \\ \bigcirc \\ \diagdown \end{array} = \begin{array}{c} \diagup \\ \bigcirc \\ \diagdown \\ \diagup \\ \bigcirc \\ \diagdown \\ \diagup \\ \bigcirc \\ \diagdown \end{array} \quad \text{where} \quad \begin{array}{c} X \\ \diagup \\ \bigcirc \\ \diagdown \\ X \end{array} = \begin{array}{c} \diagup \\ \bigcirc \\ \diagdown \\ \diagup \\ \bigcirc \\ \diagdown \end{array}, \quad (4.30)$$

where C_1 is the cluster tensor, and B_T^* is the complex conjugate of B_T . The state described by a tensor of this form is not generally symmetric under $U_{h,v}(c)$, but it is symmetric under $U_{h,v}^T(c)$ (note that the cluster state tensor C_1 is real, and hence unaffected by \mathcal{K}). Furthermore, if we pick a random A_T of the form given in Eq. (4.30) with bond dimension 4, then we can confirm numerically that the resulting PEPS does indeed have $\gamma = 1$.

We conjecture that ground states in the non-trivial phase in Fig. 4.6 can be captured by tensors of the form Eq. (4.30), in the same way that the cluster phase is captured by tensors of the form Eq. (4.7). To argue this, we use the framework of perturbation theory in PEPS. Consider a small perturbation away from the cluster state

$$H' = H_C + \sum_{x,y} h'_{x,y}, \quad (4.31)$$

where $h'_{x,y} = -h_X X_{x,y} - h_Y Y_{x,y}$ with $h_X, h_Y \ll 1$. Throughout this following, we will label sites by a single index $j = (x, y)$ to condense notation. Defining,

$$V(h_X, h_Y) = (H_C - E_C)^{-1} (\mathbb{1} - |C\rangle \langle C|) \sum_j h'_j, \quad (4.32)$$

the ground state, to first order in perturbation, is given by,

$$|\psi(h_X, h_Y)\rangle = [\mathbb{1} + V(h_X, h_Y)] |C\rangle \quad (4.33)$$

$$= \left[\mathbb{1} - \sum_j (H_C - E_C)^{-1} (\mathbb{1} - |C\rangle \langle C|) (h_X X_j + h_Y Y_j) \right] |C\rangle \quad (4.34)$$

$$= \left[\mathbb{1} - \sum_j (H_C - E_C)^{-1} (h_X X_j + h_Y Y_j) \right] |C\rangle \quad (4.35)$$

$$= \left[\mathbb{1} - \sum_j \left(\frac{h_X}{8} X_j + \frac{h_Y}{10} Y_j \right) \right] |C\rangle \quad (4.36)$$

$$= \Lambda(h_X, h_Y)^{\otimes N} |C\rangle + \mathcal{O}(h_X^2, h_Y^2, h_X h_Y), \quad (4.37)$$

where,

$$\Lambda(h_X, h_Y) = \mathbb{1} - \frac{h_X}{8}X - \frac{h_Y}{10}Y. \quad (4.38)$$

In going from Eq. (4.34) to (4.35), we have used that (adopting the notation of Section 4.4),

$$\langle C|X_k|C\rangle = \langle +|^{\otimes N} \left(\prod_{\langle ij \rangle} CZ_{ij} \right) X_k \left(\prod_{\langle ij \rangle} CZ_{ij} \right) |+\rangle^{\otimes N} \quad (4.39)$$

$$= \langle +|^{\otimes N} \left(\prod_{\langle ij \rangle} CZ_{ij} \right) \left(\prod_{\langle ij \rangle} CZ_{ij} \right) X_k \prod_{k' \in N(k)} Z_{k'} |+\rangle^{\otimes N} \quad (4.40)$$

$$= \langle +|+\rangle^{N-4} \langle +|-\rangle^4 \quad (4.41)$$

$$= 0, \quad (4.42)$$

where $N(k)$ denotes all nearest neighbours of the site k . Similarly, $\langle C|Y_j|C\rangle = 0 \quad \forall j$, since,

$$Y_k \left(\prod_{\langle ij \rangle} CZ_{ij} \right) = \left(\prod_{\langle ij \rangle} CZ_{ij} \right) Y_k \prod_{k' \in N(k)} Z_{k'}. \quad (4.43)$$

To go from Eq. (4.35) to (4.36), we exploited the fact that,

$$-H_C X_j |C\rangle = \sum_i K_i X_j |C\rangle \quad (4.44)$$

$$= \sum_{i \in N(j)} K_i X_j |C\rangle + \sum_{i \notin N(j)} K_i X_j |C\rangle \quad (4.45)$$

$$= - \sum_{i \in N(j)} X_j K_i |C\rangle + \sum_{i \notin N(j)} X_j K_i |C\rangle \quad (4.46)$$

$$= 4 \sum_{i \in N(j)} X_j |C\rangle + (4 - N) \sum_{i \notin N(j)} X_j |C\rangle, \quad (4.47)$$

which implies that for all j , $X_j |C\rangle$ is an eigenstate of $(H_C - E_C)^{-1}$ with inverse energy $1/8$ (note that $j \notin N(j)$). The same statement holds for $Y_j |C\rangle$ with inverse energy $1/10$.

Therefore, to first order in perturbation theory, we can approximate the ground states of the model described by Eqs. (4.21,4.28) with the following PEPS tensor,



$$\text{Diagram A} = \text{Diagram C}_1 \text{ with } \Lambda, \quad (4.48)$$

where $\Lambda = \Lambda(h_X, h_Y)$. Notice that Λ satisfies $X\Lambda X = \Lambda^*$, such that A is of the form given in Eq. (4.30). Furthermore, one can confirm that the fixed-point σ of the associated transfer matrix is exactly Π , independent of the values of h_X or h_Y , so we have $\gamma = 1$.

We will now argue that Eq. 4.30 holds to all orders in perturbation theory. To reach higher orders in perturbation theory, we use the exponential perturbation

theory developed in Ref. [249], which requires us to evaluate $\exp(V)|C\rangle$ where $V = V(h_X, h_Y)$. Therefore, we must evaluate terms like $V^2|C\rangle$, $V^3|C\rangle$, and so on. We can use the machinery of [249] to write down PEPOs enacting the perturbations with increasing bond dimension for any given order. The extra bond dimension is needed to account for the fact that higher powers of V will introduce products of X s and Y s with different prefactors, depending on the geometry of the operator.

As long as the action of $V^n|C\rangle$ on the cluster state can be expressed as sums of Pauli strings of X s and Y s with real coefficients, one can always find a tensor network representation of $\exp(V)$ in terms of a 6-legged tensor B which fulfills the right-hand-side of Eq. 4.30. In other words, we want to show that,

$$V^n|C\rangle = \sum_{\mathbf{ab}} c_{\mathbf{ab}} P_{\mathbf{ab}} |C\rangle, \quad (4.49)$$

for all n , where $P_{\mathbf{ab}} = \otimes_k X^{a_k} Y^{b_k}$, \mathbf{a} and \mathbf{b} are bit strings on the lattice and the $c_{\mathbf{ab}}$ are real coefficients. We have seen explicitly that Eq. (4.49) holds for $n = 1$. Now, assuming Eq. (4.49) holds for some n , we have,

$$\begin{aligned} V^{n+1}|C\rangle &= V \sum_{\mathbf{ab}} c_{\mathbf{ab}} P_{\mathbf{ab}} |C\rangle = (H_C - E_C)^{-1} (\mathbb{1} - |C\rangle\langle C|) \sum_{x,y} h'_{x,y} \sum_{\mathbf{ab}} c_{\mathbf{ab}} P_{\mathbf{ab}} |C\rangle \\ &= \sum_{\mathbf{ab}} c'_{\mathbf{ab}} P_{\mathbf{ab}} |C\rangle, \end{aligned} \quad (4.50)$$

where $c'_{\mathbf{ab}}$ are also real. Therein, we have used that the perturbation h' consists of Pauli- X s and Y s with real coefficients and the fact that each product of Pauli matrices either maps the cluster state to an exact excitation or to itself, making $(H_C - E_C)^{-1} (\mathbb{1} - |C\rangle\langle C|)$ act simply as a multiplication of each of the $c_{\mathbf{ab}}$ by a real number. So Eq. (4.49) holds for all n by induction.

Therefore, it is clear that, at any given order, the tensor B describing the perturbation will again act as a real linear combination of $\mathbb{1}$, X , Y and XY for any given virtual state, hence the resulting PEPS tensor has the form of Eq. (4.30). Therefore, at least up to the phase transition where perturbation theory breaks down, the ground states in the non-trivial phase of Fig. 4.6 can be captured by PEPS of the form Eq. (4.30), which we believe will generically have $\gamma = 1$. On the other hand, if we also add a Z field to the Hamiltonian, the tensor obtained from perturbation theory no longer has the form of Eq. (4.30) and, accordingly, the SPEE disappears.

To summarize, our understanding of the phase of matter in Fig. 4.6 comes from three steps: (1) The subsystem time reversal symmetries $U_{h,v}^T(c)$ are the relevant symmetries that protect the SSPT order and (2) states in the same phase as the cluster state under $U_{h,v}^T(c)$ can be captured by PEPS of the form Eq. (4.30), which (3) generically have a SPEE of $\gamma = 1$. We leave a more rigorous confirmation of steps (1)-(3) to future work.

4.3.4 Remarks on the numerical method

We finish this section by commenting on some relevant features of our numerical method. To begin, we briefly compare our method of computing γ to the more

common approach, which involves calculating ground states and their respective entropies S_A for several system sizes N , and then making a linear fit to extract γ [106]. This method is relatively costly, in that it requires the determination of several ground states, and it is also sensitive to finite size effects. On the other hand, our method can obtain γ from one PEPS tensor, and works directly in the thermodynamic limit, such that finite size effects are minimized.

Second, we see from Figs. 4.5 and 4.6 that the SPEE can serve as a very good probe for SSPT phase transitions, with the phase boundary marked by a clear discontinuity. In some cases, the phase transitions observed here may also be detected by discontinuities in local magnetizations. For example, the phase transition induced by an added X -field can be detected by $\langle m_X \rangle$, as seen in Fig. 4.6. However, Fig. 4.6 also shows that neither $\langle m_X \rangle$ nor $\langle m_Y \rangle$ can resolve the entire phase diagram alone. This is to be expected, as SPT phases cannot be completely detected by local order parameters. The SPEE, on the other hand, is inherently non-local, and can resolve the entire phase diagram. Nevertheless, the SPEE is still comparably simple to calculate given a PEPS ground state, so it is a genuinely useful tool to detect SSPT phase transitions.

Finally, we note a distinct property that the SPEE has as a tool to detect SSPT order. Usual quantities used to detect SPT order, such as string order parameters, are explicitly defined in terms of a certain symmetry [14, 59, 135, 223, 243]. Such quantities therefore can only determine whether a state has SPT order with respect to this symmetry. In contrast, the SPEE is “symmetry-agnostic”, meaning that it is not defined with respect to any particular symmetry of the state⁵. This is the reason that we were able to detect the phase of matter in Fig. 4.6 without a prior understanding of the relevant symmetry. The fact that a symmetry-agnostic quantity like the SPEE can characterize SSPT order reflects its fundamental differences from standard SPT order [233].

4.4 3D cluster states

We have now seen that the 2D cluster phase can be detected and characterized by a value $\gamma = 1$ of the SPEE. In this section, we move to investigating the SPEE in 3D systems. Going to 3D allows us to consider different types of subsystem symmetry, and also brings our discussion closer to fracton order, which exists only in dimension 3 and higher. We will consider cluster states defined on different 3D lattices, each with a different notion of subsystem symmetry, and each leading to a different type of area law correction. In light of our results for the 2D cluster phase, we expect the observed behaviour to hold throughout the corresponding SSPT phases.

We start by reviewing how to define cluster states on lattices other than the 2D square lattice, also known as graph states. Consider a graph $\mathcal{G} = (V, E)$ consisting of vertices $v \in V$ and edges $e \in E$. To define the corresponding graph state $|\mathcal{G}\rangle$,

⁵The geometry of the bipartition we use to calculate entropy is informed by the geometry of the subsystem symmetries, but this is the only way in which the symmetry enters the definition of the SPEE

Unit cell			
Symmetry	 Linear (●, ○)	 Linear(●)/Planar(○)	 1-form (●, ○)
2D boundary			
Entropy	$S = L^2 - (2L - 1)$	$S = L^2 - 1$	$S = L^2$

Figure 4.7: Summary of the results of Section 4.4. Light (dark) circles correspond to qubits on the A (B) sublattices.

we place a qubit in the $|+\rangle$ state on every vertex, and then act with CZ on every pair of vertices connected by an edge,

$$|\mathcal{G}\rangle = \prod_{e \in E} CZ_e \bigotimes_{v \in V} |+\rangle_v. \quad (4.51)$$

$|\mathcal{G}\rangle$ is the ground state the following Hamiltonian,

$$H_{\mathcal{G}} = - \sum_{v \in V} X_v \prod_{u \in N(v)} Z_u, \quad (4.52)$$

where $N(v) \subset V$ is the neighbourhood of v , and contains all vertices u where are connected to v by an edge.

To compute entanglement entropy, we need only consider an effective 2D system lying along the boundary of the partition, as discussed in Section 4.1. For these 2D boundary systems, we can use Eq. (4.3) to calculate S_A . In what follows, we will consider 3D cubic lattices with dimensions $L \times L \times L$ (such that $|\partial A| = L^2$) and periodic boundary conditions in all directions. Similar statements can be made for open boundary conditions after the addition of boundary terms in the Hamiltonians. We will consider a bipartition whose boundary is perpendicular to a coordinate axis, and all symmetries discussed will be tensor products of Pauli- X operators. We note that graph state symmetries made of Pauli- Y operators can also exist, but with drastically different, *e.g.* fractal, geometry as shown in Ref. [61].

Our results are summarized in Fig. 4.7. In each case, the boundary subsystem has dimensions $L \times L$. We will now discuss each model in turn.

(i) *bcc lattice*. This model has qubits on the vertices and centers of cubes. The subsystem symmetries take the form of lines moving in the x, y, z directions of the lattice. It was previously studied in Ref. [59], where it was also shown that it has non-trivial SSPT order under these line-like symmetries. The 2D system living on the boundary of the bipartition is exactly the 2D cluster state, where the A and B subsystems correspond to the A and B sublattices. Therefore, the $2L - 1$ line-like symmetries of the cluster state generate G_A in Eq. (4.3), and we get a lower dimensional “perimeter law” correction to the area law.

(ii) *fcc lattice*. The second model has qubits on the faces and vertices, and has line-like symmetries on the face qubits, but only planar symmetries on the vertex qubits. The 2D boundary system has only a single global symmetry in G_A , so there is a constant correction rather than a perimeter law correction. Thus, the planar symmetries seem to dictate the physics of this model, rather than the line-like symmetries. This example, along with the previous, suggest that SSPT phases in dimension D with k -dimensional subsystem symmetries are associated with a correction to the area law that scales like L^{D-k-1} .

(iii) *RBH lattice*. The third model, first introduced by Raussendorf, Bravyi, and Harrington (RBH) [193], was originally used in the context of fault-tolerant quantum computation [228, 229]. It is defined by qubits on the faces and edges of the lattice. It was later shown in Ref. [41] to have SPT order protected by so-called “1-form” symmetries [91]. Such symmetries are distinct from subsystem symmetries because they are *deformable*. While subsystem symmetries have rigid geometry like lines or planes, 1-form symmetries in a 3D system can live on *any* closed 2D surface. This follows from local symmetries generated by applying X to every face qubit in a single unit cell (or every edge qubit connected to a given vertex). In particular, this model also has planar symmetries as in the fcc lattice. Despite this, the boundary state is trivial, consisting of entangled pairs between the two subsystems, so there is no correction to the area law. The reason for this is as follows: For the previous two cases, as well as the 2D cluster state, the correction emerges because there is a non-local stabilizer that lives in one subsystem and is composed of local stabilizers that have support in both subsystems. For the case of 1-form symmetries, this is not the case: the non-local stabilizers can be decomposed into local stabilizers that are also contained in one subsystem. This behaviour was also noticed in a 2D example (which is actually the same state emerging on the boundary of the fcc lattice), in Ref. [232]. Therefore, 1-form symmetries are likely not associated with area law corrections in general.

4.5 Discussions & Conclusions

In this chapter, we have shown that the 2D cluster phase can be characterized by a uniform correction $\gamma = 1$ to the area law which we have called the symmetry-protected entanglement entropy (SPEE), and we used this to construct a new numerical technique to detect SSPT order. The SPEE is relatively easy to calculate

given a ground state PEPS tensor, hence it is an effective tool to detect SSPT order and SSPT phase transitions. A next step would be to check if the results presented in this chapter are unique to the 2D cluster phase, or are generally true for all non-trivial SSPT phases. For example, Ref. [190] showed that the SSPT phases protected by the line-like symmetries considered here can be sorted into 8 different equivalence classes, and constructed representative states for each class. It is also easy to generalize the cluster state to different symmetry groups as in Ref. [59] and Ref. [250], for example. Also, as shown here, there is rich behaviour of the correction for 3D cluster states. In all of these cases, it would be interesting to see whether there is a uniform value of the SPEE within the corresponding SSPT phases.

Using our method, we uncovered the surprising result that the SSPT order of the cluster state is preserved under the addition of local magnetic fields pointing anywhere in the X - Y plane, as indicated by the SPEE. This indicates that the cluster phase defined previously [26, 59, 190] is part of a larger, more robust SSPT phase of matter. We attributed this larger phase of matter to subsystem time-reversal symmetry, although an in-depth understanding is still missing. In particular, the physical meaning of our notion of subsystem time-reversal is unclear. Interestingly, the newly discovered phase ('T') contains at least part of both the cluster phase ('X') and the fractal SSPT phase ('Y') containing the cluster state [61]. This suggests that the phases 'X' and 'Y', whose symmetries differ drastically in geometry, can potentially be unified by considering the anti-unitary symmetries of the phase 'T'.

This newly discovered phase may also have implications in terms of quantum computation. It is known that phases 'X' and 'Y' are computationally universal [26, 61], meaning that every state within these phases may be used as a resource for universal measurement-based quantum computation. If the phase 'T' is also computationally universal, this would mean that the computational power of the cluster state is robust to a much larger class of perturbations than previously thought. In general, it would be worthwhile to understand whether there is a clear link between the SPEE and the usefulness of a state as a computational resource, and if so, how well the SPEE compares to other figures of merit used to determine the computational usefulness of, *e.g.*, perturbed cluster states [12, 49, 246].

In 3D, certain models with subsystem symmetries are dual to models with fracton order [53, 56, 110, 194, 224, 251]. This duality is realized by gauging the subsystem symmetries. In particular, if this gauging procedure is applied to a state with SSPT order, the resulting fracton model can be twisted [251], in the same way that gauging a 2D SPT leads to a twisted Toric Code, *i.e.* Double Semion model [90]. It is therefore plausible to think that a transition between different fracton orders could be dual to a transition between different SSPT orders, which could in turn be detected by the SPEE, or a 3D generalization thereof.

Finally, we briefly comment on the possibility to measure the SPEE experimentally. Measuring the topological entanglement entropy would be a direct way of observing the presence of topological order in a many-body state. However, this is experimentally daunting; a principle barrier being the difficulty of creating topological states in the first place. On the other hand, cluster states are relatively

easy to make in optical lattices with nearest-neighbour interactions [252]. Furthermore, the second Rényi entropy can be measured in optical lattices by interfering two identical copies of a ground state and performing local parity measurements [240, 241], and this has been done to observe area laws in 1D systems [242]. Thus, measuring the SPEE of the cluster phase seems feasible with current or near-term technologies. This would serve as a first route to verifying non-trivial quantum order via entanglement entropy.

Chapter 5

Subsystem symmetry-enriched topological order in three dimensions

In the previous two chapters, we have investigated SPT protected by subsystem symmetries. In this chapter, we turn to another role played by symmetries in quantum phases of matter: symmetry fractionalization. As a reminder, symmetry fractionalization occurs when the anyons carry a non-trivial symmetry charge, *i.e.* they transform under a non-trivial projective representation [111, 113, 253–256]. Symmetry fractionalization is possible in 2D due to the presence of conservation laws. For example, a conservation law in the toric code requires that there is always an even number of anyons in any excited state. In this way, each anyon can pick up, for example, an extra -1 phase factor under symmetry transformations, and the total phase factor coming from all anyons will always multiply to 1. Can such phenomena also occur in the presence of subsystem symmetries?

A simple argument suggests that subsystem symmetry fractionalization is not possible in 2D. It is commonly accepted that topological phases in 2D can be described by topological quantum field theories which have mobile, point-like anyonic excitations [77]. Suppose we act with a line-like subsystem symmetry on an excited state with some configuration of anyons. Because the anyons are mobile, we can move all except one away from the support of the line symmetry. Then, since the overall action of the symmetry must be linear (non-projective), and the symmetry only acts on a single anyon, the action of the symmetry on a single anyon must be linear, so there is no fractionalization. That is, because there are no conservation laws that restrict how many anyons exist on a given line, there can be no fractionalization. This same argument shows that subsystem symmetries of arbitrary geometry in any dimension cannot fractionalize on mobile, point-like anyons.

There are two ways around this argument¹. The first is to consider anyons with restricted mobility, such as those appearing in fracton topological orders in 3D and higher. The mobility constraints in fracton orders can be expressed in terms of conservation laws which, for example, say that the number of anyons in each

¹Recently, a third way has been discovered and is currently undergoing investigation. It is possible that mobile anyons can have their mobility restricted in the presence of subsystem symmetries, which may allow for subsystem symmetry fractionalization even in 2D.

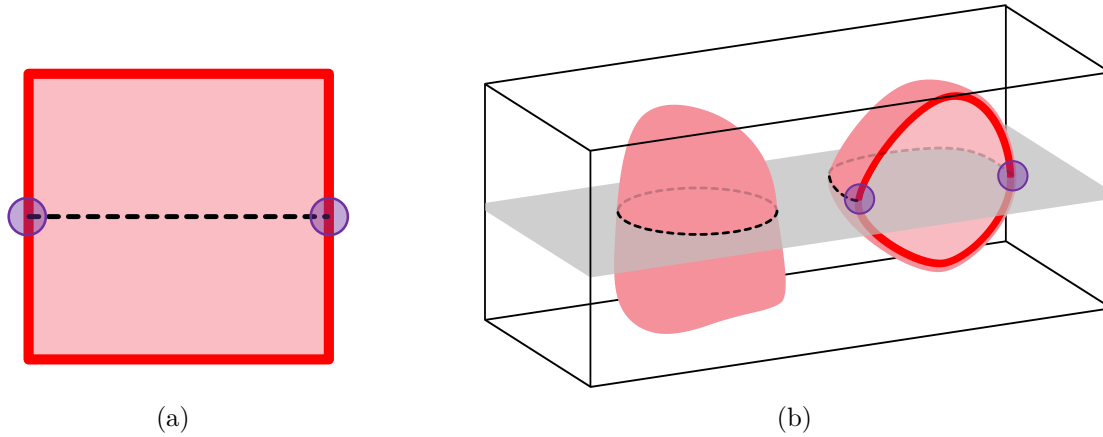


Figure 5.1: (a) Schematic diagram of a 2D SSPT order with line-like symmetries (dashed line) in the presence of a boundary (thick red line). Near a boundary, neighbouring line symmetries locally anti-commute (small circles), leading to an extensive degeneracy on the edge. (b) The ground state of the 3D SSET order has planar subsystem symmetries, and is a condensate of closed membranes of 2D SSPT orders. Left: a closed membrane of 2D SSPT order. Planar operators intersect the membrane along a loop, indicated by the dashed line, and reduce to the line symmetries of the membrane. Right: an open membrane carries a line-like excitation on its boundary, indicated by the thick red line, which transforms non-trivially under subsystem symmetries in the same way as the boundary of the 2D SSPT order.

plane must be even. In this case, fractionalization of a planar subsystem would be possible, leading to symmetry-enriched fracton order. This possibility was studied in Ref.[251].

As we will see in this chapter, another way around the argument is to consider higher-dimensional excitations. As we saw in Section 2.3.2, the 3D toric code model has 1D loop-like excitations in addition to point-like anyons². The main insight of this chapter is that there is a conservation law that says a closed loop must penetrate any plane an even number of times. Acting with a planar subsystem symmetry on the loop excitation reduces to a product of local actions at each intersection point, and these local actions can now be projective thanks to the conservation law. In this way, we can say that the loop-like excitations fractionalize the planar subsystem symmetries. A model exhibiting such behaviour can therefore be called an example of subsystem symmetry-enriched topological (SSET) order. The aim of this chapter is to construct such a model and analyze its properties.

Summary of results

Our SSET model can be understood as a decorated 3D toric code model (Section 2.3.2). Recall that the 3D toric code consists of qubits on the faces of a cubic

²For conventional SET order, these loop-like excitations complicate our understanding of symmetry fractionalization, but significant progress has nonetheless been made [257–263].

lattice, and the ground states can be visualized as equal-weight superpositions over all basis states where the faces in the state $|1\rangle$ form unions of closed 2D membranes. To enrich this model with subsystem symmetries, we introduce new qubits on the edges of the lattice and couple them to the faces in such a way that edge qubits lying on membranes form 2D cluster states, and those away from membranes remain in symmetric product states. Constructed in this way, the decorated model has planar subsystem symmetries acting on the edge qubits. This is due to the fact that, along the intersections of a given plane and the membranes, the symmetry action of the plane reduces to the line-like symmetries of the decorating cluster states, see Fig 5.1. Furthermore, the loop excitations of the toric code, which appear along the boundary of open membranes, now coincide with the boundary of cluster states. Due to the SSPT order of cluster states, these boundaries, and hence the loop excitations, fractionalize under the planar symmetries. The immediate consequence of this fractionalization is that the loop excitations are endowed with a degeneracy per unit length which is protected by the subsystem symmetry. The procedure of decorating topological orders with lower-dimensional SPT orders is a well-established way to create SET orders [96, 114, 264, 265], and our construction here can be seen as a generalization of this procedure to subsystem symmetries, with the notable feature that d -dimensional subsystem symmetries of the decorating SSPT translate into $(d + 1)$ -dimensional subsystem symmetries of the decorated model.

Another effect of the subsystem symmetry fractionalization that we discover is an increased value of the topological entanglement entropy (TEE). The 3D toric code, being an example of topological order, naturally has a non-zero topological entanglement entropy [102]. In addition, as discussed in the previous chapter, the cluster state has a non-zero value of the TEE, called the SPEE, for bipartitions aligned with the subsystem symmetries. Since the SSET model consists of a fluctuating “soup” of 2D cluster states, one might expect that the value of the TEE is increased as compared to the usual 3D toric code due to the additional presence of the SPEE, and we confirm that this is indeed the case.

Our SSET model stems from a unique interplay of global and subsystem symmetries. To better understand this interplay, we consider gauging and ungauging the symmetries of the SSET in various combinations, resulting in a network of eight different models, as pictured in Fig. 5.2. At the root of this network is a short range entangled model with SSPT order under a combination of global and subsystem symmetries. We calculate the cocycle that encodes the non-trivial action of the symmetries on the boundary of this model, revealing a mixed anomaly between global and subsystem symmetries. Using this cocycle, we calculate the effect of the symmetries on the extrinsic symmetry defects, which allows us to predict the outcome of gauging the symmetries in different combinations. We then discuss the nature of the topological order and the symmetry enrichment of each of the eight models, and in particular show that the model resulting from gauging all symmetries, *i.e.* the model resulting from gauging the subsystem symmetries of the SSET, displays the “panoptic” order that was recently discovered in Refs. [115, 266], and contains non-abelian fractons. Additionally, we find models containing both point-like excitations with restricted mobility, as well as loop-like excitations, and

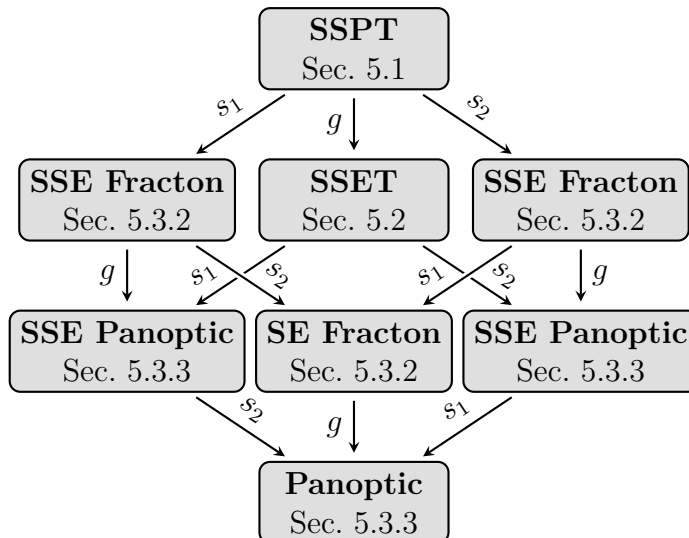


Figure 5.2: Flowchart describing the various models obtained by gauging and ungauging the symmetries of the SSET in different ways. The arrows are labelled by the symmetry which is gauged along the direction they point, where g , s_1 , and s_2 represent the global symmetry, lattice-plane subsystem symmetries, and dual-plane subsystem symmetries, respectively. A model is called “fracton” if all excitations display some mobility restrictions and “panoptic” if restricted-mobility excitations appear alongside fully mobile and loop-like excitations. “SE” (“SSE”) denotes models with symmetry enrichment due to global (subsystem) symmetries.

a non-trivial symmetry action that couples the two types, shedding further light on the roles that subsystem symmetries can play in 3D topological phases.

The rest of the chapter is structured as follows. In Section 5.1, we introduce a model with both global and subsystem symmetries, and show that it has non-trivial SPT order by analysing its boundary. Then, in Section 5.2, we gauge the global symmetries of this model to obtain our model of SSET order and study its properties. In Section 5.3, we consider gauging the subsystem symmetries and investigate the network of models in Fig. 5.2. Finally, in Section 5.4, we give our conclusions and discuss possible routes of future work.

5.1 SPT order with global and subsystem symmetries

To derive our model of SSET order, we begin with a short-ranged entangled model that has SPT order with respect to a combination of global and subsystem symmetries. The SSET model is obtained by gauging only the global symmetries of this model. The process of partially gauging symmetries of an SPT order to obtain SET order is well understood in the case of global symmetries [111, 142, 151, 263], as was discussed in a simpler 2D setting in Section 2.4.1.

We first define the short-range entangled model, and demonstrate its non-trivial SPT order by identifying the non-trivial action of the symmetries on the boundary, as encoded by a certain 3-cocycle. Notably, the non-trivial order arises from an

interplay between the global and subsystem symmetries, and the system becomes trivial if only the global symmetry or only the subsystem symmetry is preserved. We will refer to this type of order as SSPT order, despite the equal importance of both global and subsystem symmetries.

The SSPT model lives on a simple 3D cubic lattice, with qubits in the body centers (C) and on the edges (E). To begin, consider a trivial paramagnetic Hamiltonian acting on this system,

$$H_{triv} = - \sum_{c \in C} X_c - \sum_{e \in E} X_e, \quad (5.1)$$

whose unique ground state is a product state of $|+\rangle = \frac{1}{\sqrt{2}}(|0\rangle + |1\rangle)$ on every edge and body qubit. Our model can be defined by acting on this trivial system with a finite depth unitary circuit,

$$U_{CCZ} = \prod_{\Delta} CCZ_{\Delta}, \quad (5.2)$$

where the product runs over all triples of qubits Δ consisting of one body qubit and two of its nearest-neighbouring edge qubits, as pictured in Fig.5.3(a), and CCZ_{Δ} acts on the three qubits as $CCZ|i\rangle|j\rangle|k\rangle = (-1)^{ijk}|i\rangle|j\rangle|k\rangle$. Using the fact that $CCZ_{abc}X_aCCZ_{abc}^{\dagger} = X_aCZ_{bc}$, where $CZ|i\rangle|j\rangle = (-1)^{ij}|i\rangle|j\rangle$, we obtain the Hamiltonian,

$$H_{SSPT} = U_{CCZ}H_{triv}U_{CCZ}^{\dagger} = - \sum_{c \in C} \tilde{B}_c - \sum_{e \in E} \tilde{C}_e, \quad (5.3)$$

where $\tilde{C}_e \equiv U_{CCZ}X_eU_{CCZ}^{\dagger}$ is defined pictorially in Fig. 5.3(a) (bottom), and $\tilde{B}_c = X_cU_c$ with

$$U_c = \prod_{f \in c} U_f, \quad (5.4)$$

where $f \in c$ runs over the six faces of c , U_f is a product of four CZ operators in a diamond on face f , see Fig. 5.3(a).

H_{SSPT} has a unique ground state which we denote by $|SSPT\rangle$. We can get some intuition for this ground state using the viewpoint of decorated domain walls (DDW) [96], as shown in Fig. 5.3(b). Let $\mathcal{C} \subset C$ be a set of body centre qubits, and define the state $|\mathcal{C}\rangle$ of the body centre qubits such that each qubit in \mathcal{C} is in the $|1\rangle$ state, while the rest are in $|0\rangle$. Noting that $CCZ|i\rangle|j\rangle|k\rangle = |i\rangle \otimes CZ^i|j\rangle|k\rangle$, we can write the ground state in the following way,

$$|SSPT\rangle = \sum_{\mathcal{C} \subset C} |\mathcal{C}\rangle \otimes |\mathcal{G}_{\mathcal{C}}\rangle, \quad (5.5)$$

where the sum is over all subsets \mathcal{C} of C and we have defined the state $|\mathcal{G}_{\mathcal{C}}\rangle$ on the edge qubits as,

$$|\mathcal{G}_{\mathcal{C}}\rangle = \prod_{c \in C} U_c |+\rangle^{\otimes |E|}. \quad (5.6)$$

Since the CZ gates cancel out between neighbouring cubes in \mathcal{C} , $|\mathcal{G}_{\mathcal{C}}\rangle$ describes a state of 2D cluster states on the domain walls of \mathcal{C} , and $|+\rangle$ states away from

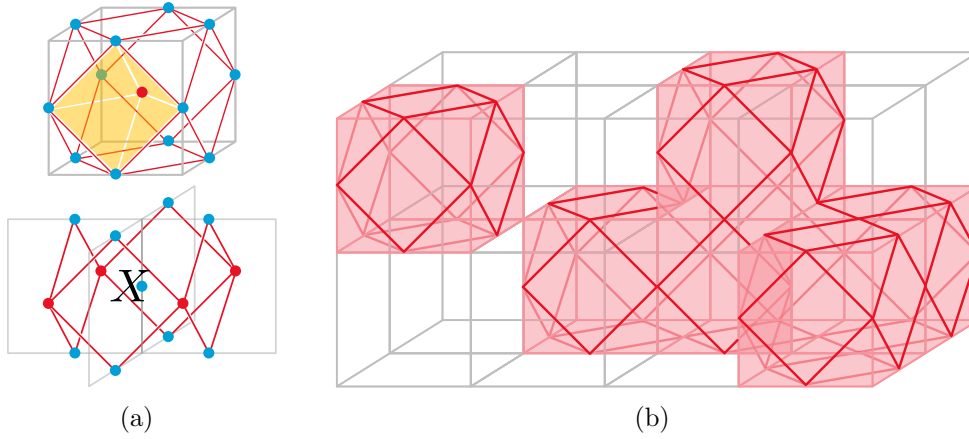


Figure 5.3: (a) Top: a unit cell of the 3D SSPT state. Four of the triangles Δ appearing in Eq. (5.2) are shown; there are four such triangles for each face within this cell. The red lines represent the CZ gates contained in U_c (Eq. (5.4)). Bottom: the Hamiltonian term \tilde{C}_e , where e is the central vertical edge. (b) Decoration by 2D cluster states. The shaded faces depict either domain walls, in the case of $|SSPT\rangle$, or membranes, in the case of $|SSET\rangle$.

them. As we saw in Section 2.7, the 2D cluster state is the paradigmatic example of a state with SSPT order under line-like symmetries. Therefore, $|SSPT\rangle$ can be described as an equal weight superposition over all body qubit configurations in which the domain walls of the body qubits are decorated with 2D SSPT states.

Let us turn to the symmetries of $|SSPT\rangle$. First, by nature of the DDW structure of $|SSPT\rangle$, we have a global \mathbb{Z}_2 symmetry acting on the body qubits $X_C = \prod_{c \in C} X_c$, which follows simply from the fact that the domain walls are invariant under flipping all body spins. The edge qubits have planar subsystem symmetries. For any plane moving parallel to one of the coordinate planes of the cubic lattice, we define the subset $\mathcal{P} \subset E$ as the set of edges that are intersected by this plane. We remark that these planes come in two distinct types, determined by whether they are parallel or perpendicular to the edges they intersect, and we refer to the two types as lattice-planes and dual-planes, respectively. We then define the subsystem symmetry for each plane as $X_{\mathcal{P}} = \prod_{e \in \mathcal{P}} X_e$. The fact that $X_{\mathcal{P}}$ is a symmetry of $|SSPT\rangle$ for all planes \mathcal{P} can be seen by first noticing that $[U_c, X_{\mathcal{P}}] = 0$ for all $c \in C$ and all \mathcal{P} . Then it follows that $X_{\mathcal{P}}$ is a symmetry of $|\mathcal{G}_C\rangle$ for all $C \subset C$, and therefore is also a symmetry of $|SSPT\rangle$ thanks to Eq. (5.5).

There is a more insightful way to understand the presence of the planar symmetries. Observe that the intersection of a plane \mathcal{P} with a domain wall configuration forms closed 1D loops, as pictured in Fig. 5.1(b). Since $X_{\mathcal{P}}$ acts trivially away from the domain walls, where the edge qubits are in the symmetric $|+\rangle$ state, we can restrict the action of $X_{\mathcal{P}}$ onto these closed loops. This is a symmetry, since the 2D cluster states living on the domain walls have line-like subsystem symmetries. Therefore, the planar symmetries of the 3D SSPT follow from the line-like symmetries of the 2D SSPT states which we use to decorate

domain walls³.

We can see explicitly that $|SSPT\rangle$ is in a trivial phase if only the global symmetry or only the subsystem symmetries are enforced by constructing disentangling circuits which respect one of the symmetries. Namely, if we group all of the CCZ gates from U_{CCZ} that live in a given cube, we obtain a local unitary that respects all of the subsystem symmetries. Applying this unitary to all cubes is therefore a subsystem symmetry-respecting circuit that disentangles $|SSPT\rangle$. A disentangling circuit which respects the global symmetries can be obtained by similarly grouping CCZ s into octahedrons, one for each face of the lattice. Importantly, neither disentangling circuit respects both types of symmetry, and we argue in the next section that such a symmetric disentangling circuit does not exist by virtue of the non-trivial SSPT order.

5.1.1 Boundary of the SSPT

We now demonstrate the non-trivial nature of our SSPT model by analyzing its boundary. Let us consider the geometry pictured in Fig. 5.4, where the boundary is a 2D square lattice with periodic boundary conditions and qubits on the edges. In the presence of this boundary, the whole 3D state may no longer be symmetric under the global or subsystem symmetries. In particular, it may be necessary to dress symmetry operators with additional action on the boundary qubits in order to leave the system invariant. For the planar symmetries, this turns out to be unnecessary, and the action of the planar symmetries on the boundary, for planes perpendicular to the boundary, is simply a line of X 's. The global symmetry, on the other hand, must be decorated with additional CZ 's acting between every nearest neighbouring pair of edges on the boundary. The action of the symmetries on the boundary is summarized in Fig. 5.4. This process to extract the boundary symmetry action is equivalent to that which was used throughout Chapter 2.

We see from the above analysis that neighbouring plane symmetries commute on the boundary. This is different from the 2D SSPT order of the 2D cluster state, where neighbouring line symmetries commute in the bulk but anti-commute on the boundary. However, we will see that, in the presence of a global symmetry flux threading the cylinder, which is introduced by adding the domain wall pictured in Fig. 5.4, neighbouring plane symmetries will anti-commute. This highlights the importance of both global and subsystem symmetries in our SSPT model.

To formalize this, we can use the language of group cohomology which classifies SPT order. Imagine “compactifying” our 3D system into a quasi-2D system [267]. This is achieved simply by fixing the length R in the y direction, as indicated in Fig. 5.4. We then get a different quasi-2D system for each compactification radius R . The subsystem symmetries perpendicular to the compactification direction, *i.e.* xz planes, become standard global symmetries of the compactified system. There are $2R$ of these symmetries, labelled by indices for $i = 1, \dots, 2R$ where even (odd) i corresponds to lattice-plane (dual-plane) symmetries, as pictured in Fig. 5.4.

³We note that this picture breaks down when \mathcal{P} is tangent to the domain walls, in which case $X_{\mathcal{P}}$ rather acts as a patch of global symmetry, which turns out to still be a symmetry

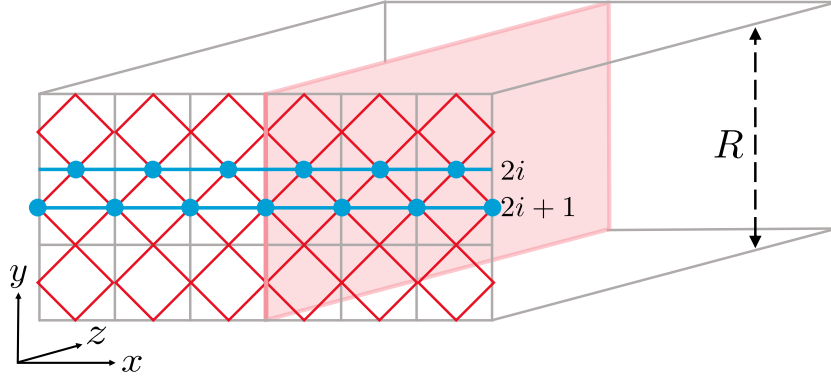


Figure 5.4: The 3D cylinder with periodic boundary conditions in the x and y directions, and open boundaries in the z direction. The effective action of the bulk symmetries on the boundary is shown. The red lines denote CZ gates coming from the global symmetry action, while blue lines indicate the action of xz planar symmetries, with blue dots denoting X operators. The plane in the yz direction represents a domain wall that is inserted to create a global symmetry flux through the cylinder.

Including the global symmetry as well, we can consider the symmetry group,

$$\begin{aligned} G_R &= \mathbb{Z}_2 \times \mathbb{Z}_2^{2R} \\ &= \{(g, \vec{s}) \mid \vec{s} = \{s_1, \dots, s_{2R}\}; g, s_i = 0, 1\}, \end{aligned} \quad (5.7)$$

where the generators g and s_i correspond to the global and subsystem symmetries, respectively.

For each R , we can study the 2D SPT order of the compactified system under the symmetry group G_R . This order is determined by a 3-cocycle $\omega : G_R \times G_R \times G_R \rightarrow U(1)$ corresponding to a cohomology class $[\omega] \in H^3(G, U(1))$ which characterizes the action of G_R on the boundary [74, 92]. We can straightforwardly calculate this cocycle using the Else-Nayak procedure (Section 2.2.1). Skipping over the details of the computation, which are very similar to Section 2.2.3, the result is,

$$\omega((g, \vec{s}), (g', \vec{s}'), (g'', \vec{s}'')) = (-1)^{g'' \sum_{i=1}^R s'_{2i}(s_{2i+1} + s_{2i-1})}. \quad (5.8)$$

We can determine the effect of inserting a global symmetry flux using the slant product, as described in Section 2.2.3. If we compute the slant product with $a = (1, \vec{0})$ corresponding to inserting a global symmetry flux via the domain wall added in Fig. 5.4, we find,

$$\chi_{(1, \vec{0})}((g, \vec{s}), (g', \vec{s}')) = (-1)^{\sum_{i=1}^R s'_{2i}(s_{2i+1} + s_{2i-1})}. \quad (5.9)$$

In particular, the commutation relation reads,

$$\frac{\chi_{(1, \vec{0})}((g, \vec{s}), (g', \vec{s}'))}{\chi_{(1, \vec{0})}((g', \vec{s}'), (g, \vec{s}))} = (-1)^{\sum_{i=1}^{2R} (s_i s'_{i+1} + s'_i s_{i+1})}. \quad (5.10)$$

This says precisely that neighbouring plane symmetries anti-commute on the boundary in the presence of a global symmetry flux. We can also compute the slant product for a subsystem symmetry flux, corresponding to $a = (0, \hat{i})$, where the vector \hat{i} contains 1 at position i , and 0 elsewhere. We find,

$$\chi_{(0, \hat{i})} \left((g, \vec{s}), (g', \vec{s}') \right) = (-1)^{g'(s_{i-1} + s_{i+1})}, \quad (5.11)$$

which tells us that, in the presence of a lattice-plane (dual-plane) subsystem symmetry flux, the global symmetry anti-commutes on the boundary with the two dual-plane (lattice-plane) subsystem symmetries neighbouring the flux.

One might wonder if we are missing out on any important information by only considering subsystem symmetries in one direction (the xz planar symmetries). Indeed, it could be the case that, *e.g.* perpendicular symmetry planes anti-commute in the presence of a certain symmetry flux. However, we have checked that this is not the case: the cases considered above capture all of the non-trivial fractionalization that occurs in our model.

From the non-trivial slant products computed above, we see that the 3-cocycle ω belongs to a non-trivial cohomology class for all compactification radii R . The general arguments of Ref. [74] then show that the boundary, when considered as a quasi-1D system, cannot be gapped and symmetric; either the symmetry will be spontaneously broken, resulting in a boundary degeneracy, or the boundary will be gapless. In addition to this, when we enforce a true 2D notion of locality, the boundary could potentially gain even more non-trivial features that we miss by employing compactification.

To probe these non-trivial features, we examine some possible Hamiltonians which respect the boundary symmetries. Recall that, on the boundary, the planar subsystem symmetries act like lines of X operators, while the global symmetry acts like CZ 's between neighbouring edges. The two simplest Hamiltonians that respect these symmetries are,

$$H_{cSSPT} = - \sum_{e \in \partial_E} X_e - \sum_{e \in \partial_E} X_e \prod_{e' \in n(e)} Z_{e'}, \quad (5.12)$$

$$H_{SSB} = - \sum_{e \in \partial_E} \prod_{e' \in n(e)} Z_{e'}, \quad (5.13)$$

where ∂_E denotes the set of edges on the boundary, and $n(e)$ contains the set of four edges that are nearest-neighbouring edges to e , as measured by distance to the centre-points of each edge. In H_{cSSPT} , the global symmetry interchanges the two sums. Note that the edge qubits lie on the vertices of the medial square lattice.

H_{cSSPT} is exactly a 2D cluster Hamiltonian in an external field, tuned to its critical point [12, 246]. This critical point corresponds to a first order phase transition between the 2D SSPT phase of the cluster state and the trivial phase [62]. Being first order, the phase transition is caused by a level crossing, such that H_{cSSPT} has two degenerate ground states with a gap above them. In fact, these two ground states are related by the boundary action of the global symmetry. H_{SSB} , on the other hand, corresponds to two decoupled plaquette Ising models [59], one on the vertical edges, one on the horizontal edges. The ground states of this model

spontaneously break the subsystem symmetries, such that there is an extensive number of degenerate ground states, with a gap above them.

We see that both of the above Hamiltonians have a degenerate ground space with a finite gap above. It is interesting to compare this to the analogous situation which arises on the boundary of a 2D SPT order, as discussed in Section 2.2.3. In that case, the boundary system is a 1D chain. The minimal Hamiltonian terms that commute with the boundary symmetry correspond to the 1D cluster Hamiltonian in a magnetic field tuned to its critical point, and two decoupled 1D Ising models. Thus the situation is similar to the current one. A crucial difference, however, lies in the fact that the ground state of the critical 1D cluster Hamiltonian respects the anomalous symmetry, and is therefore gapless [90]. Furthermore, adding the Ising interaction on top preserves the criticality in a finite region [95]. Therefore, the 2D SPT supports a boundary with symmetry-protected gaplessness. Conversely, it is not immediately clear how to engineer a gapless boundary for $|SSPT\rangle$. This is similar to the situation for 2D SSPT phases, which also only support degenerate boundaries [59]. We leave a more detailed analysis of the boundary of 3D SSPT phases to future work.

5.2 Subsystem symmetry enriched topological order

In this section, we gauge the global \mathbb{Z}_2 symmetry of $|SSPT\rangle$. The resulting model is a \mathbb{Z}_2 gauge theory in which the loop-like topological excitations fractionalize under the subsystem symmetries. We therefore call this model an example of SSET order. We show that this implies an extensive degeneracy of the loop excitations which is protected by the symmetry. We also show that the model has an enlarged value of the topological entanglement entropy, as compared to the underlying topological order, due to the subsystem symmetry enrichment.

The gauging procedure we employ is as described in Section 2.7.6. For the present case, procedure maps body qubits to qubits on the faces (F) of the lattice, in such a way that the face qubits $f \in F$ take the state $|1\rangle$ on the domain walls of the body qubits, and $|0\rangle$ elsewhere. That is, given a state $|\mathcal{C}\rangle$ on the body qubits, the effect of the gauging map Γ can be written as $\Gamma|\mathcal{C}\rangle = |\partial\mathcal{C}\rangle$, where $\partial\mathcal{C} \subset F$ is the set of faces on the boundary of \mathcal{C} , and $|\partial\mathcal{C}\rangle$ describes a state on the face qubits where all qubits in $\partial\mathcal{C}$ are in the state $|1\rangle$, and the rest are in $|0\rangle$. We note that the edge qubits are unaffected under the action of this map. We can then extend the map Γ to arbitrary states on the body qubits by linearity. Applying this procedure to $|SSPT\rangle$, we get,

$$\begin{aligned} |SSET\rangle &= \Gamma|SSPT\rangle \\ &= \sum_{\mathcal{C} \subset \mathcal{C}} \Gamma|\mathcal{C}\rangle \otimes |\mathcal{G}_{\mathcal{C}}\rangle \\ &= \sum_{\mathcal{C} \subset \mathcal{C}} |\partial\mathcal{C}\rangle \otimes |\mathcal{G}_{\mathcal{C}}\rangle. \end{aligned} \tag{5.14}$$

This state can again be visualized using Fig. 5.3(b), where now the shaded faces indicate elements of $\partial\mathcal{C}$, which can be viewed as a configuration of closed membranes

on the faces of the lattice. Therefore, $|SSET\rangle$ is a superposition over all closed membranes configurations on the face qubits, where the membranes are decorated with 2D cluster states on the edge qubits. It is clear from this structure that $|SSET\rangle$ has the same subsystem symmetries on the edge qubits as $|SSPT\rangle$.

If we were to remove $|\mathcal{G}_c\rangle$ from the above equation, the state described would be exactly the 3D toric code, $|TC\rangle = \sum_{\mathcal{C} \subset \mathcal{C}} |\partial\mathcal{C}\rangle$, which has topological order. In fact, we can disentangle the edge qubits from the face qubits using a unitary circuit \tilde{U}_{CCZ} which places four CCZ 's on each face as in Fig. 5.5(a). Applying this circuit to $|SSET\rangle$, we get,

$$\tilde{U}_{CCZ}|SSET\rangle = \sum_{\mathcal{C} \subset \mathcal{C}} \tilde{U}_{CCZ}(|\partial\mathcal{C}\rangle \otimes |\mathcal{G}_c\rangle) \quad (5.15)$$

$$= \sum_{\mathcal{C} \subset \mathcal{C}} |\partial\mathcal{C}\rangle \otimes \prod_{c \in \mathcal{C}} U_c |\mathcal{G}_c\rangle \quad (5.16)$$

$$= |TC\rangle \otimes |+\rangle^{\otimes |E|}. \quad (5.17)$$

Therefore, $|SSET\rangle$ is related to $|TC\rangle$ by a unitary circuit, up to trivial degrees of freedom, so the two states have the same topological order. However, this circuit does not respect the subsystem symmetries. In fact, we will show that, when these symmetries are enforced, $|SSET\rangle$ is in a distinct phase from $|TC\rangle$, as indicated by symmetry enrichment of the topological excitations. Therefore, we can say that $|SSET\rangle$ has subsystem symmetry enriched topological order.

5.2.1 Excitations and symmetry enrichment

The Hamiltonian for which $|SSET\rangle$ is a ground state can be obtained by gauging H_{SSPT} , and has the following form,

$$H_{SSET} = - \sum_{e \in E} A_e - \sum_{c \in \mathcal{C}} B_c - \sum_{e \in E} C_e \frac{1 + A_e}{2}, \quad (5.18)$$

where,

$$\begin{aligned} A_e &= \prod_{f \ni e} Z_f, \\ B_c &= U_c \prod_{f \in c} X_f, \end{aligned} \quad (5.19)$$

where $f \ni e$ denotes all faces incident on edge e . C_e is defined pictorially in Fig. 5.5(a). The new gauge term A_e enforces that the faces qubits form closed membranes in the ground state. The modified terms B_c and C_e are simply the original terms \tilde{B}_c and \tilde{C}_e rewritten as functions of the new face qubits, using the rules $X_c \mapsto \prod_{f \in c} X_f$ and $\prod_{c \ni f} Z_c \mapsto Z_f$ that follow from the gauging procedure. In addition, we project the C_e term onto the closed membrane subspace ($A_e = 1 \forall e \in E$) in order to ensure that the Hamiltonian respects the subsystem symmetries. We note that all terms in H_{SSET} commute. On a topologically non-trivial manifold like a three-dimensional torus, the ground space of H_{SSET} is degenerate. $|SSET\rangle$ is one of the degenerate ground states, and the others can be obtained by adding topologically non-trivial membranes into the superposition in Eq. (5.14).

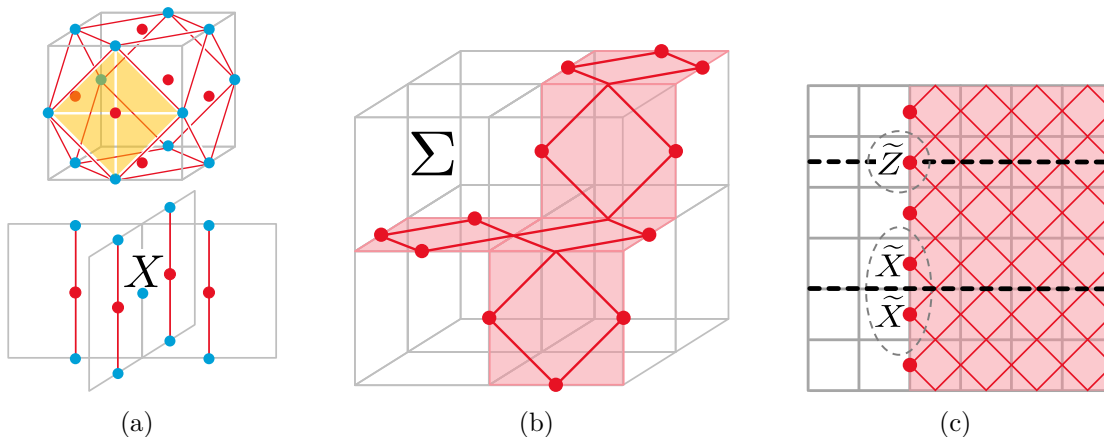


Figure 5.5: (a) Top: a unit cell of the 3D SSET state. Four of the triangles Δ appearing in \tilde{U}_{CCZ} are shown; there are four such triangles on each face of the lattice. Bottom: The Hamiltonian term C_e , where e is the central vertical edge. (b) A loop-like excitation appearing on the boundary of the surface Σ , indicated by shaded faces. Excitations appear on edges marked by points. (c) A 2D cut of our 3D lattice with a loop excitation corresponding to the half-infinite membrane Σ^∞ , as viewed from above. There is an effective qubit degree of freedom for each edge on the boundary of Σ^∞ , indicated by dots. The horizontal dashed lines represent the intersection of two symmetry planes \mathcal{P} with this 2D slice, and the action of $X_{\mathcal{P}}$ on the edge degrees of freedom, according to Eq. 5.24, is shown beside each line.

Let us now construct the excitations of H_{SSET} , which come in three types. Violations of C_e are topologically trivial particles that can be created locally by acting with Z_e , so we do not discuss them further. The other two types of excitation are topologically non-trivial, and must be created by extended non-local operators. Violations of B_e , called electric excitations, are point-like, and are created in pairs at the end points of string operators,

$$S_\Lambda^e = \prod_{f \in \Lambda} Z_f, \quad (5.20)$$

where $\Lambda \subset F$ is a curve on the dual lattice that penetrates faces. Violations of A_e , called magnetic excitations, are loop-like. They appear along the boundary of open membrane operators,

$$S_\Sigma^m = \prod_{f \in \Sigma} X_f U_f, \quad (5.21)$$

where $\Sigma \subset F$ is an open membrane of faces, as pictured in Fig. 5.5(b). If we were to braid an electric excitation through the loop of a magnetic excitation, we would pick up a minus sign due to the anti-commutation of X and Z . This is the same as in the toric code.

The difference from the toric code comes from the degeneracy of the excitations. In particular, since $A_e = -1$ when acting on the boundary of Σ , the projection $(1 + A_e)/2$ removes the corresponding terms C_e , so we can decorate the boundary of the membrane operator S_Σ^m with Z operators without changing the energy of

the resulting excitation:

$$S_{\Sigma}^{\text{m}}(\{a_e\}_{e \in \partial\Sigma}) = S_{\Sigma}^{\text{m}} \prod_{e \in \partial\Sigma} Z_e^{a_e}, \quad a_e = 0, 1, \quad (5.22)$$

where $\partial\Sigma$ denotes all edges on the boundary of the membrane Σ . Thus the loop-like excitation is two-fold degenerate per unit length. This degeneracy is protected by the subsystem symmetries. Intuitively, this is because the loop-like excitation coincides with the boundary of a 2D cluster state which has an exponential boundary degeneracy protected by the subsystem symmetries.

More precisely, consider a membrane Σ^{∞} which is a half-infinite plane, as shown in Fig. 5.5(c). This creates an excitation lying along $\partial\Sigma^{\infty}$ which is a line of N edges that we denote by e_i for $i = 1, \dots, N$. The degenerate subspace associated to this excitation is spanned by the states $|a_1, \dots, a_n\rangle$ defined as,

$$|a_1, \dots, a_n\rangle := S_{\Sigma^{\infty}}^{\text{m}} \prod_{i=1}^N Z_{e_i}^{a_i} |SSET\rangle, \quad a_i = 0, 1. \quad (5.23)$$

Let us now determine the action of the subsystem symmetries in this N -qubit space. Consider those symmetry planes that are perpendicular to Σ^{∞} and also cross $\partial\Sigma^{\infty}$, as pictured in Fig. 5.5(c). We can index these planes by \mathcal{P}_i and $\mathcal{P}_{i+1/2}$, corresponding to dual-planes intersecting edge e_i , or lattice-planes intersecting between edges e_i and e_{i+1} , respectively. Then we can calculate,

$$\begin{aligned} X_{\mathcal{P}_i} |a_1, \dots, a_n\rangle &= (-1)^{a_i} |a_1, \dots, a_n\rangle, \\ X_{\mathcal{P}_{i+1/2}} |a_1, \dots, a_n\rangle &= |a_1, \dots, a_i \oplus 1, a_{i+1} \oplus 1, \dots, a_n\rangle. \end{aligned} \quad (5.24)$$

Therefore, if we let $\widetilde{X}_i, \widetilde{Z}_i$ denote the logical Pauli operators in the degenerate edge subspace, we have $X_{\mathcal{P}_i} \cong \widetilde{Z}_i$ and $X_{\mathcal{P}_{i+1/2}} \cong \widetilde{X}_i \widetilde{X}_{i+1}$. We see that neighbouring plane symmetries anticommute on the edge of the excitation. This is the same pattern of symmetry fractionalization found on the boundary of the 2D cluster state [59]. In the case of the 2D cluster state, the line-like subsystem symmetry protects the exponential edge degeneracy of the 2D cluster state. In analogy, the planar subsystem symmetry here protects the exponential degeneracy of the line-like excitation. A similar discussion holds for an arbitrary membrane Σ , although there can be some finite size effects due to corners, as discussed in Ref. [59]. Therefore, the loop-like magnetic excitations of $|SSET\rangle$ carry a two-fold degeneracy per unit length that is protected by the planar subsystem symmetries.

5.2.2 Topological entanglement entropy

In this section, we show that the topological entanglement entropy (TEE) of our 3D SSET state is larger than that of the 3D toric code when the boundaries of bipartitions are aligned with the symmetry planes. This comes in analogy to the non-zero SPEE of the 2D cluster state that was examined in Chapter 4. In the present case, we say that the 3D SSET has a non-zero SPEE in addition to the TEE inherited from the topological order of the 3D toric code.

The origin of the SPEE can be imagined as follows. Consider one closed membrane in the membrane soup defining $|SSET\rangle$. If we bisect the membrane with a plane aligned with the subsystem symmetries, as in Fig. 5.1, we can calculate the entanglement between the two halves of the membrane. Since the membranes are decorated by 2D cluster states, and the cut is aligned with the line-like symmetries of the cluster state, we find a non-zero SPEE for this membrane. Since $|SSET\rangle$ is a fluctuating soup of such membranes, one can imagine that it also exhibits a non-zero SPEE. In the rest of this section, we show that this is indeed the case. The calculation is somewhat cumbersome, so we first present a high-level overview of it before giving the full details in the next section.

For simplicity we calculate the entropy of a finite section of a 3D torus, such that the boundary between subsystems A and B is two disconnected 2D tori. However, we expect the same results to hold for any geometry that is appropriately aligned with the subsystem symmetries, as in Ref. [232]. We will aim to determine the 2-Rényi entropy $S_A^{(2)} = -\ln \text{Tr}(\rho_A^2)$ where ρ_A is the reduced state of subsystem A ⁴. On a 3D torus, H_{SSET} has eight degenerate ground states. We choose $|SSET\rangle$ to be one of the minimal entropy states which have the largest TEE [70]. This is done by picking the ground state that is +1 eigenstate of the membrane operators $S_{\Sigma_z}^m$ where Σ_z is the non-contractible membrane, as well as the loop operators $S_{\Lambda_{x/y}}^e$ where $\Lambda_{x/y}$ are the non-contractible loops, as pictured in Fig. 5.6(a). In this way, the subsystem A has maximum knowledge of the whole state, and hence minimum entropy. We define G to be the abelian group generated by all Hamiltonian terms A_e, B_c, C_e as well as $S_{\Sigma_z}^m$ and $S_{\Lambda_{x/y}}^e$.

For simplicity, we assume that region A contains $L \times L \times L$ vertices, such that L^2 edges are cut on each boundary. In Appendix 5.2.3, we show that the entropy can be expressed in the following way for large L ,

$$S_A^{(2)} = (|A| + 2L^2) \ln 2 - \ln |G_A| - 2\mathcal{F}(\ln \sqrt{2}), \quad (5.25)$$

where $|A| = 6L^3 + 3L^2$ is the number of qubits in A , G_A is the subgroup of G containing those operators that act non-trivially on A only, and $\mathcal{F}(\beta)$ is the (extensive) free energy of a 2D square lattice Ising model at inverse temperature β . By counting independent generators in the same way as for the 3D toric code, [102], we can compute that $|G_A| = 2^{6L^3 - 2L^2 + 4}$. Compared to the toric code case, G_A here contains an additional non-local operator for each boundary, namely the product of C_e for all edges e on the boundary, which is equal to the subsystem symmetry on the corresponding dual plane.

To compute the free energy, we can use Onsager's result [268], which yields $\mathcal{F}(\ln \sqrt{2}) = \ln 2(\frac{1}{2} + \ln 2)L^2$ for large L (for more details, see Appendix 5.2.3). Crucially, the temperature $\beta = \ln \sqrt{2}$ lies in the disordered phase of the Ising model, such that the free energy is extensive with no constant term. Putting everything together, the entropy is,

$$S_A^{(2)} = 2cL^2 - 2\gamma_{\text{TEE}} - 2\gamma_{\text{SPEE}} + \dots, \quad (5.26)$$

⁴Ideally, we would calculate the Von-Neumann entropy, but this is more difficult since the entanglement spectrum will turn out to be non-flat

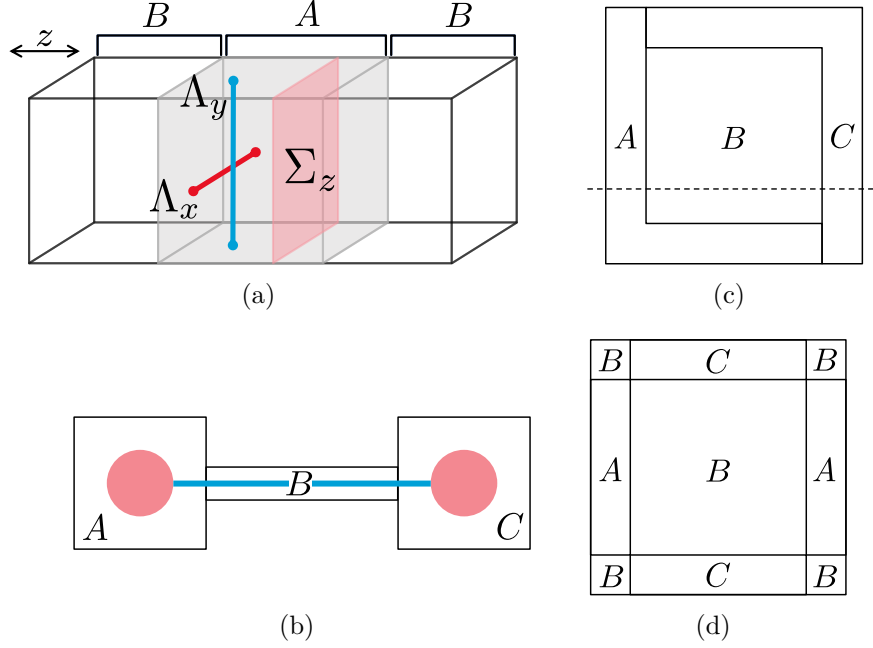


Figure 5.6: (a) The geometry considered throughout this section. Opposite sides are identified, resulting in a 3D torus. The A and B subsystems are shown, as well as the non-contractible loops $\Lambda_{x,y}$ and membrane Σ_z . (b) The dumbbell configuration for detecting the SPEE in 2D systems from Ref. [232]. (c) The picture frame configuration proposed to detect the SPEE that arises due to planar subsystem symmetries in 3D systems. Here we see a view from the top. A cross section along the dotted line reveals a shape identical to that of (b). (d) The alternate picture frame configuration that does not detect SPEE due to line-like symmetries.

where $c = (3 - \ln 2) \ln 2$, $\gamma_{\text{TEE}} = \gamma_{\text{SPEE}} = \ln 2$, and the dots represent terms that go to zero as L goes to infinity. We include the factors of 2 to emphasize the fact that A has two disconnected boundaries. γ_{TEE} comes simply from $|G_A|$ in the same way as for the 3D toric code, whereas γ_{SPEE} is due to the subsystem symmetries forming non-local constraints on the boundary of A .

While we have only shown the existence of a non-zero SPEE for this specific bipartition, we expect that it would also be present for other bipartitions whose geometry are aligned with the symmetry planes, as is the case for the SPEE of the 2D cluster state [232]. In Ref. [232], the authors also constructed a method to extract the SPEE due to line-like subsystem symmetries in a 2D system, such that it can be separated from the TEE. They show that the combination of entropies,

$$S_{\text{SPEE}} = S_B + S_{ABC} - S_{AB} - S_{BC}, \quad (5.27)$$

is equal to the SPEE, where subsystems A, B, C form a dumbbell shape as in Fig. 5.6(b). This is due to the fact that the line-like symmetries (blue line in Fig. 5.6(b)) can be terminated by applying local operators in the circled red regions, such that we get a constraint that reduces S_{ABC} . Crucially, the red regions have a larger radius than the width of B , such that the same truncated line cannot fit into

B , AB , or BC . On the other hand, the TEE is the same for each of the four terms in Eq. (5.27), and hence will cancel out, as will all extensive parts of the entropy.

Following the same logic, we propose a set of subsystems A, B, C such that S_{SPEE} will be equal to the SPEE due to planar symmetries, see Fig. 5.6(c). The subsystem B is a thin slab, while A and C are thickened, giving a geometry similar to that of a picture frame. As in the dumbbell, the planar subsystem symmetries can be truncated by applying operators along the boundary. Such an operator will fit into region ABC of the frame, but none of the other combinations. Therefore, we conjecture that S_{SPEE} should be equal to γ_{SPEE} for the picture frame geometry. If there is also a SPEE due to linear subsystem symmetries, then S_{SPEE} would grow as the perimeter of region B . If we take the alternate picture frame geometry in Fig. 5.6(d), we would only detect SPEE due to planar symmetries, since any truncated line operator that contributes to S_{ABC} will also contribute to one of S_{AB} or S_{BC} .

5.2.3 Calculation of topological entanglement entropy

Here we give the full calculation of the TEE. Observe that the subsystem A is defined by two planar cuts that run parallel to subsystem symmetry planes and intersect edges/faces of the lattice, such that the qubits on intersected edges and faces lie within subsystem A (*ie.* A has rough boundaries rather than smooth ones). The boundary between the two subsystems is therefore two disconnected tori. In a slight misuse of our notation, let $\partial A_E \subset E$ denote the edges intersected by the bipartitioning planes on each end of A . Likewise, let $\partial A_F \subset F$ denote the intersected faces, and let $\partial A = \partial A_E \cup \partial A_F$. Since the boundary is made of two disconnected pieces, we can break each set into left and right parts, *ie.* $\partial A_E = \partial A_E^L \cup \partial A_E^R$ and $\partial A_F = \partial A_F^L \cup \partial A_F^R$.

Let G be the abelian stabilizer group defined in the previous section. Then, since $|SSET\rangle$ is the unique state satisfying $g|\psi\rangle = |\psi\rangle \forall g \in G$, we can write [103, 107],

$$\rho = |\psi_{SSET}^{3D}\rangle\langle\psi_{SSET}^{3D}| = \frac{1}{2^{|A|+|B|}} \sum_{g \in G} g. \quad (5.28)$$

Where $|A|$ and $|B|$ are the number of qubits in subsystems A and B . When we trace out the B subsystem, all elements in G which have non-trivial support in B have zero partial trace, since the Pauli operators are traceless. The only exception are the operators C_e where $e \in \partial A_E$. In this case, the trace over B traces over one of the qubits involved in half of the CZ operators in C_e . This does not give 0, rather we have $\text{Tr}_a CZ_{ab} = 2P_b$ where $P = \frac{1+Z}{2}$. Using this, we find,

$$\rho_A = \frac{1}{2^{|A|}} \sum_{g \in G'_A} g \sum_{\mathcal{E} \subset \partial A_E} C'_\mathcal{E} P_\mathcal{E}, \quad (5.29)$$

where we have defined the projector $P_\mathcal{E}$ as,

$$P_\mathcal{E} = \prod_{f \in d\mathcal{E}} P_f, \quad (5.30)$$

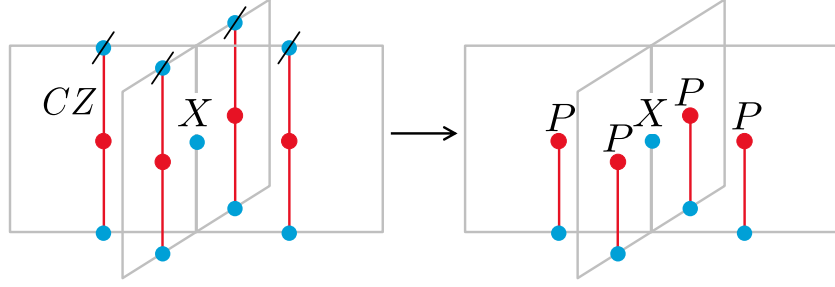


Figure 5.7: After tracing out qubits in the B subsystem, as, indicated by the slashes, the operator C_e (left) is transformed to $C'_e P_e$ up to a constant factor of $2^4 = 16$.

with,

$$C'_\mathcal{E} = \prod_{e \in \mathcal{E}} C'_e, \quad (5.31)$$

where C'_e is a unitary operator obtained from C_e by removing half of the CZ 's, see Fig. 5.7. The subgroup G'_A is defined to be generated by all elements of G which act non-trivially only on A , except for the two operators $\prod_{e \in \partial A_E^{L/R}} C_e$, which we exclude for notational convenience.

To compute ρ_A^2 , we observe that $[C'_\mathcal{E}, g] = [P_\mathcal{E}, g] = 0$ for all $g \in G'_A$ and $\mathcal{E} \subset \partial A_E$. Then we get,

$$\rho_A^2 = \frac{1}{2^{2|A|}} |G'_A| \sum_{g \in G'_A} g \sum_{\mathcal{E}, \mathcal{E}' \subset \partial A_E} C'_{\mathcal{E} \oplus \mathcal{E}'} P_\mathcal{E} P_{\mathcal{E}'}, \quad (5.32)$$

where we have used the facts $(\sum_{g \in G'_A} g)^2 = |G'_A| (\sum_{g \in G'_A} g)$ and $C'_\mathcal{E} C'_{\mathcal{E}'} = C'_{\mathcal{E} \oplus \mathcal{E}'}$. We observe that ρ_A^2 is not proportional to ρ_A because of the presence of the projectors $P_\mathcal{E}$. Therefore, ρ_A is not a projector, which shows that the entanglement spectrum of our model is not flat, as it would be for the 3D toric code.

Now we take the trace of ρ_A^2 in three steps, $\text{Tr}_A = \text{Tr}_{\partial A_F} \text{Tr}_{\partial A_E} \text{Tr}_{A-\partial A}$. When taking the first trace, all non-trivial elements of G'_A with support outside of ∂A are traceless, except again for C'_e for $e \in \partial A_E$. This gives,

$$\text{Tr}_{A-\partial A}(\rho_A^2) = \frac{2^{-|\partial A|}}{2^{|A|}} |G'_A| \sum_{g \in G'_{\partial A}} g \sum_{\mathcal{E}, \mathcal{E}' \subset \partial A_E} X_{\mathcal{E} \oplus \mathcal{E}'} P_\mathcal{E} P_{\mathcal{E}'}, \quad (5.33)$$

where,

$$X_\mathcal{E} = \prod_{e \in \mathcal{E}} X_e, \quad (5.34)$$

is obtained from $C'_\mathcal{E}$ after removing all CZ 's. $G'_{\partial A}$ contains all elements of G'_A which have act non-trivially only on ∂A , and is generated by the operators A_e for $e \in \partial A_E$. Now, the trace over ∂A_E is 0 unless $\mathcal{E} = \mathcal{E}'$, giving,

$$\text{Tr}_{\partial A_E} \text{Tr}_{A-\partial A}(\rho_A^2) = \frac{2^{-|\partial A_F|}}{2^{|A|}} |G'_A| \sum_{g \in G'_{\partial A}} g \sum_{\mathcal{E} \subset \partial A_E} P_\mathcal{E}, \quad (5.35)$$

where we used that $P_{\mathcal{E}}P_{\mathcal{E}} = P_{\mathcal{E}}$. At this point, it is useful to consider the two boundaries of A separately. We can write,

$$\mathrm{Tr}_{\partial A_E} \mathrm{Tr}_{A-\partial A}(\rho_A^2) = \frac{2^{-|\partial A_F|}}{2^{|A|}} |G'_A| \sum_{g \in G'_{\partial A_L}} g \sum_{\mathcal{E} \subset \partial A_E^L} P_{\mathcal{E}} \sum_{g' \in G'_{\partial A_R}} g' \sum_{\mathcal{E}' \subset \partial A_E^R} P_{\mathcal{E}'}. \quad (5.36)$$

Observing that the final trace over ∂A_F can further be factorized as $\mathrm{Tr}_{\partial A_F} = \mathrm{Tr}_{\partial A_F^L} \mathrm{Tr}_{\partial A_F^R}$, and the left and right boundaries are disjoint and equivalent so we can simply square the result for the left boundary, we get,

$$\mathrm{Tr}_A(\rho_A^2) = \frac{2^{-|\partial A_F|}}{2^{|A|}} |G'_A| \left(\sum_{\mathcal{E} \subset \partial A_E^L} \mathrm{Tr}_{\partial A_F^L} \left[P_{\mathcal{E}} \left(\sum_{g \in G'_{\partial A_L}} g \right) \right] \right)^2. \quad (5.37)$$

For each \mathcal{E} this remaining trace is 0 unless $g = e$, or $g = \prod_{e \in \mathcal{E}} A_e$. In the latter case, we have $P_{\mathcal{E}} \prod_{e \in \mathcal{E}} A_e = P_{\mathcal{E}}$. Therefore, every term in the sum over \mathcal{E} gets doubled, except when $\mathcal{E} = \emptyset$ or $\mathcal{E} = \partial A_E^L$. This gives,

$$\mathrm{Tr}_A(\rho_A^2) = \frac{2^{-|\partial A_F|}}{2^{|A|}} |G'_A| \left(2 \left[\sum_{\mathcal{E} \subset \partial A_E^L} \mathrm{Tr} P_{\mathcal{E}} \right] - \mathrm{Tr} P_{\emptyset} - \mathrm{Tr} P_{\partial A_E^L} \right)^2. \quad (5.38)$$

Noting that $\mathrm{Tr} P_{\emptyset} = \mathrm{Tr} P_{\partial A_E^L} = 2^{|\partial A_E^L|}$, we write,

$$\mathrm{Tr}_A(\rho_A^2) = \frac{4}{2^{|A|}} |G'_A| \left(2^{-|\partial A_E^L|} \sum_{\mathcal{E} \subset \partial A_E^L} \mathrm{Tr} P_{\mathcal{E}} - 1 \right)^2. \quad (5.39)$$

We now proceed by expressing the remaining sum in terms of the partition function of a 2D square lattice Ising model. To this end, we define an auxiliary square lattice system with degrees of freedom $\sigma_i = \pm 1$ on each vertex near the boundary. Each vertex i corresponds to an edge $e_i \in \partial A_E^L$. Given \mathcal{E} , we define a vector $\vec{\sigma}$ such that $\sigma_i = -1$ if $e_i \in \mathcal{E}$, and $\sigma_i = 1$ otherwise. With this notation, we can rewrite,

$$P_{\mathcal{E}} = \prod_{\langle i,j \rangle} \left(P_{l(e_i, e_j)} \right)^{\frac{1-\sigma_i \sigma_j}{2}}, \quad (5.40)$$

with the trace given by,

$$\mathrm{Tr} P_{\mathcal{E}} = \prod_{\langle i,j \rangle} 2 \left(\frac{1}{2} \right)^{\frac{1-\sigma_i \sigma_j}{2}} = \sqrt{2}^{|\partial A_E^L|} \prod_{\langle i,j \rangle} \sqrt{2}^{\sigma_i \sigma_j}, \quad (5.41)$$

such that,

$$\sum_{\mathcal{E} \subset \partial A_E^L} \mathrm{Tr} P_{\mathcal{E}} = \sqrt{2}^{|\partial A_E^L|} \sum_{\vec{\sigma}} e^{\ln \sqrt{2} \sum_{\langle i,j \rangle} \sigma_i \sigma_j}. \quad (5.42)$$

We have written the sum in such a way that it corresponds to the partition function $\mathcal{Z}(\ln \sqrt{2})$ of the 2D Ising model, where,

$$\mathcal{Z}(\beta) = \sum_{\vec{\sigma}} e^{\beta \sum_{\langle i,j \rangle} \sigma_i \sigma_j}. \quad (5.43)$$

With this, Eq. 5.39 becomes,

$$\mathrm{Tr}_A(\rho_A^2) = \frac{4}{2^{|A|}} |G'_A| \left(\sqrt{2}^{-|\partial A_E^L|} \mathcal{Z}(\ln \sqrt{2}) - 1 \right)^2. \quad (5.44)$$

For conceptual clarity, let us define the group G_A which is obtained by adding the two generators $\prod_{e \in \partial A_E^{L/R}} C_e$, which we omitted earlier, into G'_A . Then we have $|G_A| = 4|G'_A|$. By letting $N = |\partial A_E^L|$ be the number of spins in the Ising model, we get,

$$\begin{aligned} S_A^{(2)} &= -\ln \mathrm{Tr}_A(\rho_A^2) \\ &= |A| \ln 2 - \ln |G_A| - 2 \ln(2^{-N} \mathcal{Z}(\ln \sqrt{2}) - 1). \end{aligned} \quad (5.45)$$

This Ising model has a phase transition at inverse temperature $\beta_c = \frac{\ln(1+\sqrt{2})}{2}$ [268]. Since $\ln \sqrt{2} < \beta_c$, our partition function lies in the disordered phase. In this phase, the free energy is extensive, in the sense that $\mathcal{F}(\beta) := \ln Z(\beta) = \alpha N$ for large N . Importantly, there is no constant term in $\ln Z(\beta)$, as there would be in the ordered phase. The 2D Ising model has been solved exactly in the large- N limit by Onsager [268], and is given in Ref. [269] as,

$$\alpha = \ln(2 \cosh(2\beta)) + \frac{1}{2\pi} \int_0^\pi d\phi \ln \frac{1}{2} \left(1 + \sqrt{1 - k^2 \sin^2 \phi} \right), \quad (5.46)$$

where $k = 2 \sinh(2\beta) / \cosh^2(2\beta)$. Evaluating this integral numerically for $\beta = \ln \sqrt{2}$, we find that α is equal to $\ln 2(\ln 2 + \frac{1}{2})$ up to 6 decimal places. Thus for large values of N we get

$$\begin{aligned} S_A^{(2)} &= -\ln \mathrm{Tr}_A(\rho_A^2) \\ &= |A| \ln 2 - \ln |G_A| - 2 \ln \left(e^{\ln 2(\ln 2 - \frac{1}{2})N} - 1 \right). \end{aligned} \quad (5.47)$$

Note that $e^{\ln 2(\ln 2 - \frac{1}{2})} > 1$, such that we can approximate $\ln \left(e^{\ln 2(\ln 2 - \frac{1}{2})N} - 1 \right) \approx \ln \left(e^{\ln 2(\ln 2 - \frac{1}{2})N} \right)$ for large N , giving,

$$S_A^{(2)} = |A| \ln 2 - \ln |G_A| - 2 \ln 2 \left(\ln 2 - \frac{1}{2} \right) N. \quad (5.48)$$

The final step is to evaluate $|G_A|$. To do this, we need to count the number of independent generators of G_A . This is done using the usual counting arguments for the 3D toric code [102]. Suppose for simplicity that the region A contains $L \times L \times L$ vertices, such that $N = L^2$. We then have $3L^3 + L^2$ edges contained in A , and $3L^3 + 2L^2$ faces, giving $|A| = 6L^3 + 3L^2$. Starting with the body centre terms B_c , we have $L^3 - L^2$ terms contained in A , all of which are independent. We have $3L^3$ edge terms A_e , but they are not all independent. Namely, the product of all edge terms around a given vertex is the identity, and so is the product of all edge terms on a non-contractible plane (such as the plane Σ_z in Fig. 5.6(a), giving $L^3 + 1$ constraints, and hence $2L^3 - 1$ independent terms. Finally, we have one C_e term for each edge away from the boundary, all of which are independent, and

the two non-local terms $\prod_{e \in \partial A_E^{L/R}} C_e$, giving $3L^3 - L^2 + 2$ terms. Finally, we have the three non-local operators $S_{\Sigma_z}^m$ and $S_{\Lambda_{x,y}}^e$. Altogether, this gives $6L^3 - 2L^2 + 4$ terms, such that $|G_A| = 2^{6L^3 - 2L^2 + 4}$. The final result for the entropy is therefore,

$$S_A^{(2)}(L) = \ln 2(6 - 2 \ln 2)L^2 - 4 \ln 2, \quad (5.49)$$

plus corrections which go to zero as L goes to infinity.

5.3 Gauging the subsystem symmetries

In this section, we examine the variety of topological phases that arise from gauging some or all of the subsystem symmetries, starting either from $|SSPT\rangle$ or $|SSET\rangle$. More precisely, starting from $|SSPT\rangle$, we can independently choose to gauge the global symmetry, lattice-plane symmetry, and dual-plane symmetry, resulting in eight possible models (including $|SSPT\rangle$). We denote the global, lattice-plane, and dual-plane symmetries as \mathbb{Z}_2^{glob} , \mathbb{Z}_2^{sub1} , and \mathbb{Z}_2^{sub2} , respectively. We use this notation with the understanding that there are a sub-extensive number of subsystem symmetry generators, so $\mathbb{Z}_2^{sub1/2}$ describes the local action of the symmetry, not the total symmetry group. It is known that gauging subsystem symmetries can result in models with fracton topological order [53, 110, 194]. Here, by “fracton” topological order (or more succinctly fracton order), we mean any model in which *all* topological excitations have restricted mobility of some sort. In our definition, this includes systems like stacks of 2D toric codes, which are usually considered to be trivial as fracton orders. We use the usual terminology of fracton, lineon, and planon to describe point-like topological excitations which are fully immobile, constrained to a 1D line, or constrained to a 2D plane, respectively. Later, we consider models in which such excitations coexist with fully-mobile excitations, and we refer to the order in these models as “panoptic” [115].

Throughout this section, we do not explicitly perform the gauging as we did in the previous section (except in one case). Rather, we rely on our understanding of $|SSPT\rangle$ and its symmetries to determine both the mobility and type of symmetry enrichment of the resulting topological excitations. The key properties of the gauged models are summarized in Table 5.1.

5.3.1 Symmetry defects and gauging

To understand the effects of gauging, we need to understand the symmetry defects of $|SSPT\rangle$. We can define symmetry defects in terms of domain wall operators. We recall from Section 2.2 that domain wall operators $V_{\partial M}$ are obtained via U_M which applies some symmetry operator to a compact region M of the lattice. For a global symmetry, M is some 3D region, whereas for our subsystem symmetry, M would be a 2D region confined to a plane. Then, $V_{\partial M}$ is defined as the operator supported only on the boundary ∂M of M that acts equivalently to U_M on the ground space. $V_{\partial M}$ is a membrane of CZ 's for \mathbb{Z}_2^{glob} , while for the planar subsystem symmetries it is a 1D loop operator also consisting of CZ 's. Symmetry defects are defined

Table 5.1: Summary of gauged models. Gauge fluxes for the global symmetry are always loop-like, and gauge fluxes for subsystem symmetries are planons, but they may be composites of excitations with lower mobility.

Gauged symmetry	Mobility of gauge charges	Effect of ungauged symmetries
None	N.A.	Mixed glob./sub. boundary anomaly
Global	Unrestricted mobility	Fractionalization of loops
Lattice-plane	Lineon	Mixed glob./sub. fractionalization
Dual-plane	Planon	Mixed glob./sub. fractionalization
Global + Lattice-plane	Unrestricted + Lineon	Attaches charges to fluxes
Global + Dual-plane	Unrestricted + Planon	Attaches charges to fluxes
Lattice-plane + Dual-plane	Fracton	Fracton permutation
All	Unrestricted + Fracton	N.A.

to appear at the boundaries of open domain wall operators. The \mathbb{Z}_2^{glob} symmetry defects are closed 1D loops, while the $\mathbb{Z}_2^{sub_{1/2}}$ symmetry defects are point-like, see Fig. 5.8.

The symmetry defects carry important information about what happens after gauging the symmetry. After gauging, domain wall operators are proliferated, and the symmetry defects become deconfined topological excitations that we call gauge fluxes. As we saw in Section 5.2, \mathbb{Z}_2^{glob} gauge fluxes are mobile loop-like excitations. Gauge fluxes corresponding to generators of $\mathbb{Z}_2^{sub_{1/2}}$, on the other hand, are point-like and can only move within a single plane without creating additional excitations, *i.e.* they are planons. This is because the $\mathbb{Z}_2^{sub_{1/2}}$ symmetry defects are themselves point-like and mobile only within a given plane. However, we find that in some cases these planons can be decomposed into a pair of excitations of lower mobility, as in the X-cube model [53]. This is due to the symmetry domain walls decomposing further, such as a planar domain wall decomposing into a product of two cage-edge domain walls as in X-cube [55]. The properties of the symmetry defects before gauging, including the action of symmetry on them, determine the braiding and fusion statistics of the gauge fluxes, as well as possible symmetry fractionalization under any ungauged symmetries [111, 142, 151].

The other type of topological excitations that emerge from gauging are called the gauge charges. The gauge charges are gauged versions of symmetry charges, which are objects that locally anti-commute with the symmetry, corresponding in our case to a single Z operator on the lattice. As described in Ref. [110], the mobility of gauge charges can be determined directly from the spatial structure of the subsystem symmetries. Namely, if a symmetry charge is acted on by planar

symmetries in one, two, or three orthogonal directions, then the corresponding gauge charge will be a planon, lineon, or fracton, respectively.

The slant products calculated in Section 5.1 can be used to determine the relationship between the symmetry generators, symmetry charges, and symmetry defects. Indeed, although we initially performed these calculations in Section 5.1 to understand the action of the symmetry on the boundary in the presence of symmetry flux, a symmetry flux is in fact inserted using a domain wall operator, which terminates on the boundary via a symmetry defect. So we were actually calculating the action of the symmetries on the symmetry defects, regardless of whether or not these defects were pushed to the boundary. The action of the symmetry on the defects in $|SSPT\rangle$, as described by the slant products, allows us to determine the topological excitations that result from gauging a symmetry, along with the action of the ungauged symmetries on these excitations.

More precisely, for the SSPT model, if symmetries b and c anticommute on a a defect, *i.e.* $\chi_a(b, c)/\chi_a(c, b) = -1$, then acting with b (c) on an a defect creates a c (b) symmetry charge. This will manifest either as a fractionalization or permutation of the excitations in the gauged theory, depending on which symmetries are gauged. Specifically, if a is among the gauged symmetries, while b and c are not, the a gauge flux will carry a fractional charge under b and c . If a and b are gauged and c is not, then acting with c symmetry on an a (b) gauge flux attaches a b (a) gauge charge. The action of the symmetries on the symmetry defects of $|SSPT\rangle$ (and therefore on the corresponding gauge fluxes of the gauged models) can be determined by Eqs. (5.9) and (5.11), and is summarized in Fig. 5.8.

5.3.2 Gauging only subsystem symmetries: Fracton order

We now turn to gauging the subsystem symmetries of $|SSPT\rangle$. The resulting models all have fracton topological order, characterized by topological excitations with restricted mobility. The ungauged symmetries will either permute the excitations or fractionalize on them, depending on whether we gauge all or only some of the subsystem symmetries.

Gauging lattice-plane symmetries

Gauging \mathbb{Z}_2^{sub1} results in a non-trivial fracton model that is not obviously equivalent to any known models. Symmetry charges before gauging are acted on by two perpendicular subsystem symmetries, so the gauge charges are lineons. Interestingly, due to how the ungauged symmetries act on the gauge fluxes by creating symmetry charges (Figs. 5.8(b), 5.8(c)), the gauge fluxes transform as a non-trivial projective representation under \mathbb{Z}_2^{glob} and adjacent \mathbb{Z}_2^{sub2} symmetry generators. Therefore, this model represents a fracton model where excitations carry a fractional charge under the combination of global and subsystem symmetries.

Gauging dual-plane symmetries

Each edge qubit is acted on by only one generator of \mathbb{Z}_2^{sub2} . Therefore, the gauge charges are planons, and furthermore we can gauge the symmetry in each dual-plane

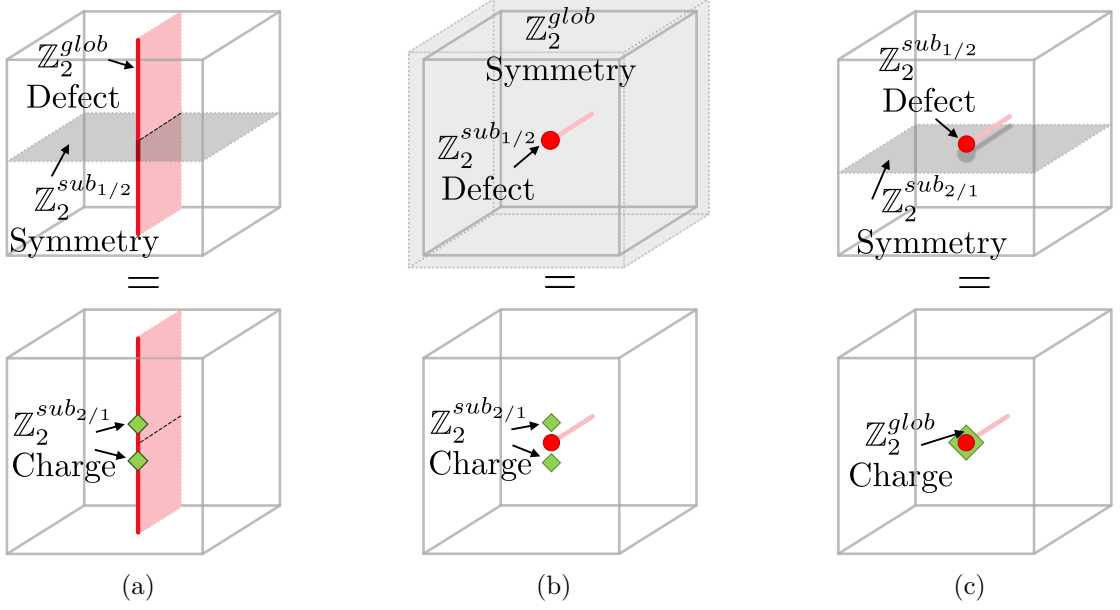


Figure 5.8: Interplay between symmetries, symmetry defects, and symmetry charges in $|SSPT\rangle$, as revealed by Eqs. (5.9) and (5.11). (a) Acting with a $\mathbb{Z}_2^{sub1/2}$ symmetry on the line-like \mathbb{Z}_2^{glob} flux creates $\mathbb{Z}_2^{sub2/1}$ charges on neighbouring planes. (b) \mathbb{Z}_2^{glob} symmetry on a point-like $\mathbb{Z}_2^{sub1/2}$ flux creates $\mathbb{Z}_2^{sub2/1}$ charges on neighbouring planes. (c) $\mathbb{Z}_2^{sub2/1}$ symmetry on a neighbouring $\mathbb{Z}_2^{sub1/2}$ flux attaches a \mathbb{Z}_2^{glob} charge to the flux.

separately, such that we arrive at a stack of decoupled 2D toric codes in all three directions, one for each dual plane, which can be viewed as a rather trivial fracton model. The layers are coupled via the body qubits in such a way that the \mathbb{Z}_2^{sub2} gauge fluxes in a given plane transform as a non-trivial projective representation under the adjacent \mathbb{Z}_2^{sub1} generators and \mathbb{Z}_2^{glob} (Figs. 5.8(b),5.8(c)).

Gauging all subsystem symmetries

Gauging all subsystem symmetries of $|SSPT\rangle$ results in a model with fracton excitations, where the global symmetry permutes the fractons. This permutation action can be understood by the fact that the global symmetry, when acting on a lattice-plane (dual-plane) symmetry defect, attaches a pair of symmetry charges to the neighbouring dual-planes (lattice-planes). Hence, in the gauged model, the global symmetry attaches gauge charges to gauge fluxes (Fig. 5.8(b)). As in the general case, the gauge flux is a planon. However, in this case, a planar domain wall can be decomposed into a pair of domain walls and thus the planon can be split into a pair of fractons. We can isolate these two fractons by considering the symmetry defect corresponding to a stack of dual-plane symmetries. Gauging this defect gives two fractons, one at the top of the stack and one at the bottom. The fact that these are fractons follows from relations between the gauge constraints, as we elaborate on in Fig. 5.9. Applying the global symmetry attaches a gauge charge to each fracton. Since the symmetry charges are acted on by planar symmetries

in all three directions, the gauge charges are fractons. In particular, there are relations between all subsystem symmetries in two orthogonal directions that imply the fractons are irreducible. Therefore, the global symmetry action causes fracton permutation.

This permutation action will be useful for understanding the model obtained by gauging all symmetries in Section 5.3.3, so here we will explicitly write down the gauged Hamiltonian. To perform this gauging, we follow the procedure for gauging subsystem symmetries outlined in Section 2.7.6. First, we identify the minimal coupling terms which commute with all subsystem symmetries, which in the present case takes the form of four-body interactions near an edge, pictured in Fig. 5.9. The gauge qubits are placed in the nexus of these interactions as shown in Fig. 5.9. We therefore have four qubits for each edge e , one for each cube c surrounding e . We may therefore label gauge qubits uniquely by a pair (c, e) . We can view the gauge qubits as living on the edges of a smaller cube within each cube of the lattice, and we use the labelling in Fig. 5.9 to reference each of the twelve gauge qubits in a given cube. Following Ref. [110], we now express existing Hamiltonian terms \tilde{B}_c and \tilde{C}_e in terms of the new gauge qubits, resulting in the terms \mathcal{B}_c and \mathcal{C}_e . Furthermore, we add additional flux terms which enforce a zero-flux constraint on the gauge qubits, as determined by relations between the minimal coupling terms [110]. There is one flux term \mathcal{A}_e for each edge, and nine flux terms $\mathcal{A}_c^{(k)}$ for each cube c . We define \mathcal{C}_e and the flux terms in Fig. 5.9. The precise form of \mathcal{B}_c is not required for our purposes here, as it is not associated with any topological excitations. Overall, the gauged Hamiltonian is,

$$H_{frac} = - \sum_{c \in C} \mathcal{B}_c - \sum_{e \in E} \mathcal{C}_e - \sum_{e \in E} \mathcal{A}_e - \sum_{c \in C} \sum_{k=1}^9 \mathcal{A}_c^{(k)}. \quad (5.50)$$

Now let us investigate the excitations of H_{frac} . Due to the sheer number of terms, and the fact that they are not all independent, the full spectrum of excitations is tedious to describe. Instead, let us focus on two types which allow us to see the non-trivial action of the global symmetry. Gauge charges, *i.e.* violations of \mathcal{C}_e , can be created at the corners of a membrane operator,

$$\mathcal{S}_{\mathcal{R}}^e = \prod_{c \in \mathcal{R}} Z_{(c,j)} Z_{(c,l)}, \quad (5.51)$$

where $\mathcal{R} \subset C$ is a rectangle of cubic cells in the xz plane, and excitations appear on the edges at the four corners of \mathcal{R} . Gauge fluxes corresponding to violations of \mathcal{A}_e can be created by the following membrane operator,

$$\mathcal{S}_{\mathcal{R}}^m = \prod_{c \in \mathcal{R}} X_{(c,m)} X_{(c,n)} X_{(c,o)} X_{(c,p)} C Z_{c,(c,j)} C Z_{c,(c,l)}, \quad (5.52)$$

where gauge fluxes again appear at the four corners of \mathcal{R} . The fact that these are fractons follows from the three orthogonal relations among flux terms described in Fig. 5.9. Now we observe that the global symmetry X_C permutes the membrane operators,

$$X_C \mathcal{S}_{\mathcal{R}}^m X_C^\dagger = \mathcal{S}_{\mathcal{R}}^m \mathcal{S}_{\mathcal{R}}^e. \quad (5.53)$$

This shows that acting with the global symmetry attaches gauge charges onto gauge fluxes, thereby permuting the fractons of the gauged theory.

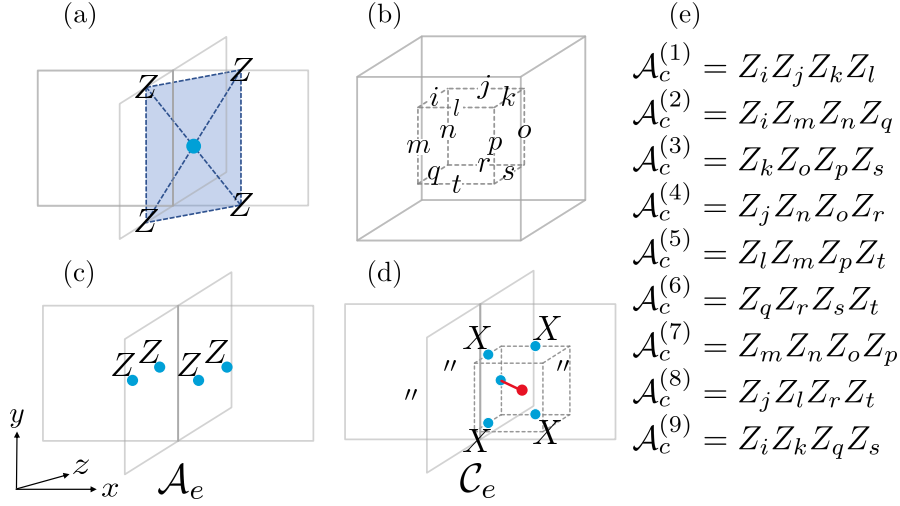


Figure 5.9: Hamiltonian terms of the fracton model obtained from gauging subsystem symmetries of $|SSPT\rangle$. (a) The minimal interaction term symmetric under all subsystem symmetries. The gauge qubit (blue dot) is placed at the nexus of the interaction. (b) Labelling of the 12 gauge qubits within a cube, which live on the edges of a smaller inscribed cube. (c) The flux term \mathcal{A}_e consists of four Z operators acting on the gauge qubits closest to e , where e is the central vertical edge. (d) The Hamiltonian term \mathcal{C}_e consists of sixteen X operators acting on gauge qubits and four CZ operators (denoted by a red line) that connect a gauge qubit to a body centre qubit. The interaction is only shown in one quadrant for clarity; it acts in an analogous (rotated) manner in all 4 cubes surrounding the edge e as indicated by the dashes. (e) The nine flux terms within a cube. $Z_{(c,\bullet)}$ is shorthand for $Z_{(c,\bullet)}$. The flux terms \mathcal{A}_e and $\mathcal{A}_c^{(i)}$ satisfy a number of relations which determine the mobility of gauge fluxes, such as the product of all \mathcal{A}_e and $\mathcal{A}_c^{(7)}$ in an xz dual-plane; \mathcal{A}_e , $\mathcal{A}_c^{(4)}$, $\mathcal{A}_c^{(5)}$ in a yx lattice-plane; and \mathcal{A}_e , $\mathcal{A}_c^{(2)}$, $\mathcal{A}_c^{(3)}$ in a yz lattice plane.

5.3.3 Gauging global and subsystem symmetries: Panoptic order

In this section, we consider gauging the global symmetry of $|SSPT\rangle$ along with some or all of the subsystem symmetries. Equivalently, we are gauging the subsystem symmetries of $|SSET\rangle$. In each case, we will find that fully mobile point-like and loop-like excitations, coming from the gauged global symmetry, coexist with the restricted-mobility excitations coming from the gauged subsystem symmetries. Such a system was dubbed to have “panoptic” order in Ref. [115].

Gauging lattice-plane and global symmetries

If we gauge \mathbb{Z}_2^{sub1} and \mathbb{Z}_2^{glob} , we end up with a model that is, in the absence of symmetry, equivalent to a stack of the 3D toric code and the fracton model from Section 5.3.2. The ungauged \mathbb{Z}_2^{sub2} symmetry couples the two models by permuting excitations between them. Specifically, a \mathbb{Z}_2^{sub2} generator creates \mathbb{Z}_2^{sub1} gauge charges on a pair of planes wherever it intersects the loop-like \mathbb{Z}_2^{glob} gauge

fluxes (Fig. 5.8(a)), and the same generator attaches a \mathbb{Z}_2^{glob} gauge charge to \mathbb{Z}_2^{sub1} gauge fluxes in adjacent planes (Fig. 5.8(c)). Thus, the symmetry enrichment manifests as an interesting permutation involving fully mobile excitations and those of restricted mobility.

Gauging dual-plane and global symmetries

Gauging \mathbb{Z}_2^{sub1} and \mathbb{Z}_2^{glob} gives a model in the same topological phase as a stack of the 3D toric code and layers of 2D toric codes in all three directions. Similar to the previous model, the remaining \mathbb{Z}_2^{sub1} symmetry generators permute excitations between the 2D and 3D toric codes by attaching \mathbb{Z}_2^{sub2} gauge charges to the loop-like \mathbb{Z}_2^{glob} gauge fluxes (Fig. 5.8(a)) and by attaching \mathbb{Z}_2^{glob} gauge charges to \mathbb{Z}_2^{sub1} gauge fluxes in adjacent planes (Fig. 5.8(c)).

Gauging all symmetries

To understand the model obtained by gauging all symmetries, it is easiest to start from H_{frac} in Eq. 5.50, where all subsystem symmetries have been gauged. Then, what remains is to gauge the global symmetry, which we saw enacts a non-trivial permutation on the fractons of the model. For this, we can use the general arguments of Ref. [115] (see also Ref. [266]). Therein, it is argued that gauging a fracton permuting symmetry results in a model with non-abelian fractons. Furthermore, gauge fluxes will be loop-like excitations that braid non-trivially with the excitations of reduced mobility. Since we expect the gauging of different symmetries to commute (as was indeed the case in Section 2.4.1), we can conclude that gauging the subsystem symmetries of the SSET will result in the same panoptic order with non-abelian fractons.

It is interesting to compare to the model obtained by gauging the layer-swap symmetry of the bilayer X-Cube model, as presented in Refs. [115, 266], which also has panoptic order with non-abelian fractons. A potential equivalence between this model and our own is suggested by the equivalence between the model obtained by gauging the layer-swap symmetry of the bilayer 2D toric code [115, 266], and the model obtained by gauging all symmetries of the non-trivial $\mathbb{Z}_2 \times \mathbb{Z}_2 \times \mathbb{Z}_2$ SPT (which is somewhat analogous to $|SSPT\rangle$), as discussed in Section 2.4.1. Therefore it is tempting to conjecture that the gauged bilayer X-Cube model and the model obtained by gauging all symmetries of $|SSPT\rangle$ are equivalent as gapped phases of matter.

5.4 Discussion & Conclusions

We investigated the phenomenon of subsystem symmetry enrichment in 3D systems. We began with a base model possessing SPT order under a mix of global and planar subsystem symmetries. By gauging the global symmetries of this model, we obtained a topological model with loop-like excitations that carry fractional charge of the subsystem symmetries, which we called an example of SSET order. We showed that this fractionalization leads to an extensive degeneracy of the excitations,

as well as an increased value of the topological entanglement entropy. We then considered also gauging the subsystem symmetries of the base model, resulting in a network of models all related by gauging and ungauging symmetries (Fig. 5.2). Using the algebra of the symmetry defects of the SPT model, we were able to understand the nature of each gauged model, uncovering several distinct types of subsystem symmetry enrichment. In particular, we found models supporting mixed global and subsystem symmetry fractionalization, permutation between mobile and restricted mobility excitations, and a model with non-abelian fractons.

The key feature that allows symmetry fractionalization in our model is the 1-form conservation law on loop excitations, which enforces that an excitation penetrates any closed 2D surface an even number of times. In particular, any loops penetrates a plane an even number of times, and this allows a planar subsystem symmetry to fractionalize. This suggests that a general theory of subsystem symmetry enrichment comes from studying the interplay between the conservation laws of the topological excitations and the geometry of the subsystem symmetries. This is particularly clear in the context of fracton order, where the geometry of the symmetries can be matched to the rigid mobility constraints of the excitations. As we have seen here, the same principles apply to extended excitations such as loop excitations, since the intersections of the excitations with the symmetry operators can be viewed as point-like excitations from the perspective of fractionalization.

Our SSET model can be obtained by decorating the 3D toric code with 2D cluster states. We can straightforwardly generalize our model by changing both the underlying 3D topological model, as well as the 2D SSPT model used to decorate. This raises the question of classification for SSET phases in 3D, and whether all phases can be captured by such decorated constructions. We remark that there should be some issues of compatibility, in that only certain combinations of topological model and SSPT are allowed. For example, in 2D SET models, the possible kinds of fractionalization that a point-like excitation can carry are restricted by its braiding statistics with other excitations [111]. In analogy, we suspect that there is a connection between subsystem symmetry fractionalization in loop-like excitations and their braiding with point-like excitations. As a further generalization, it is also plausible that, by decorating with a 2D SSPT possessing 2D fractal subsystem symmetries [61, 191, 194, 224], one could obtain a 3D SSET enriched by 3D fractal subsystem symmetries. These questions are closely related to the classification of SPTs with mixed global and subsystem symmetry, where the approach of Ref. [270] should be applicable.

Finally, we address the possible applications of our models to the storage and processing of quantum information. In general, it would be interesting to investigate whether the introduction of subsystem symmetries and subsystem symmetry defects into topological models can augment their computational capabilities, as is the case of global symmetry defects in 2D topological systems [39, 47, 271]. Regarding the SSET model from Section 5.2, the fact that it combines the universal (measurement-based) quantum computational power of the SSPT order [26, 27, 61, 192] together with the information storage capabilities of the topological order [6, 272, 273] suggests some potential applications. A relevant phenomenon that may be of use is the emergence of a symmetry protected degeneracy on the loop-like excitations.

Chapter 6

Conclusions

The motivation for this thesis began with a desire to understand the computational properties of subsystem symmetry-protected topological (SSPT) phases of matter. This led to a unified understand of SSPT order and measurement-based quantum computation (MBQC) using tensor networks and quantum cellular automata. This venture revealed that these phases of matter also had interesting physical properties, and so we moved on to investigating these properties through the lens of entanglement entropy, which led to a numerical algorithm that can be used to detect SSPT order. Finally, we explored further the various roles that subsystem symmetries can play in topological phases of matter by consider subsystem symmetry enrichment and fractionalization. Overall, the path taken during this thesis epitomizes the deep and fruitful relationship between quantum computation and quantum phases of matter.

On top of the open problems and further research directions proposed at the end of each chapter, there are two more big questions which are raised by this thesis, and we will conclude by briefly touching on them.

The results of Chapter 3 provide the most complete connection to date between MBQC and SPT order by constructing a very general class of phases that are all universal for MBQC. Yet, there remain some important open questions related to this connection. In particular, there have some examples of SPT ordered states that, when used as resources for MBQC, have nice properties beyond universality. The first example is the Union-Jack state, presented in Section 2.2.3, which was shown in Ref. [22] to be Pauli-universal, meaning that it is universal using only measurement in the Pauli bases. It would be very interesting if this property could be extended throughout an entire SPT phase of matter, since that would remove the impractical requirement of precise measurement angles that is a part of the usual scheme for MBQC with SPT phases. A potential route to find such a phase of matter would be 3D SSPT phases, since these would naturally combine the non-Clifford CCZ unitaries that are required for Pauli-universality with subsystem symmetries, which seem to required for a universal phase of matter. Another example of an SPT state that has interesting computational properties is the 3D RBH cluster state discussed in Section 4.4. As a resource for MBQC, this state has the advantage of fault-tolerance; the MBQC scheme is inherently robust to noise and error. The RBH cluster state has SPT order protected by higher-form

symmetries [41], which are similar to, yet distinct from, subsystem symmetries. Extending fault-tolerance throughout an SPT phase of matter would lead to an unprecedented robustness of the MBQC protocol.

Chapters 3 and 4 showed that tensor networks are useful to uncover the entanglement structure that characterizes 2D SSPT phases. As discussed throughout this thesis, fracton topological phases are dual to systems with subsystem symmetries. Despite the intense interest in fracton phases, there is almost no work regarding their representation by tensor networks [274]. Finding a general tensor network representation for fracton topological order, particularly for type II models such as Haah's code [30], should present an interesting avenue for understanding their general structure, finding generalizations, and developing numerical algorithms. More generally, it would be interesting to find tensor network representations that can incorporate aspects of both global and subsystem symmetries, as found in the model of Chapter 5. An interesting starting point is given by the hybrid fracton models of Ref. [275], which can produce both topological order and fracton order via condensation of certain excitations. Writing such a model as a tensor network might reveal the general structure required to capture global and subsystem symmetries.

Bibliography

- [1] Michael A Nielsen and Isaac Chuang. *Quantum computation and quantum information*. AAPT, 2002.
- [2] Bei Zeng, Xie Chen, Duan-Lu Zhou, and Xiao-Gang Wen. *Quantum information meets quantum matter: From Quantum Entanglement to Topological Phases of Many-Body Systems*. Springer, 2019.
- [3] Ignacio Cirac, David Perez-Garcia, Norbert Schuch, and Frank Verstraete. Matrix product states and projected entangled pair states: Concepts, symmetries, and theorems. 2020.
- [4] Guifré Vidal. Efficient classical simulation of slightly entangled quantum computations. *Phys. Rev. Lett.*, 91:147902, Oct 2003.
- [5] Xiao-Gang Wen. Colloquium: Zoo of quantum-topological phases of matter. *Rev. Mod. Phys.*, 89:041004, Dec 2017.
- [6] A.Yu. Kitaev. Fault-tolerant quantum computation by anyons. *Ann. Phys.*, 303(1):2 – 30, 2003.
- [7] Chetan Nayak, Steven H. Simon, Ady Stern, Michael Freedman, and Sankar Das Sarma. Non-abelian anyons and topological quantum computation. *Rev. Mod. Phys.*, 80:1083–1159, Sep 2008.
- [8] Barbara M. Terhal. Quantum error correction for quantum memories. *Rev. Mod. Phys.*, 87:307–346, Apr 2015.
- [9] Benjamin J. Brown, Katharina Laubscher, Markus S. Kesselring, and James R. Wootton. Poking holes and cutting corners to achieve clifford gates with the surface code. *Phys. Rev. X*, 7:021029, May 2017.
- [10] Jason Alicea, Yuval Oreg, Gil Refael, Felix von Oppen, and Matthew P. A. Fisher. Non-abelian statistics and topological quantum information processing in 1d wire networks. *Nature Physics*, 7:412–417, Feb 2011.
- [11] Robert Raussendorf, Daniel E. Browne, and Hans J. Briegel. Measurement-based quantum computation on cluster states. *Phys. Rev. A*, 68:022312, Aug 2003.
- [12] Andrew C. Doherty and Stephen D. Bartlett. Identifying phases of quantum many-body systems that are universal for quantum computation. *Phys. Rev. Lett.*, 103:020506, Jul 2009.
- [13] Akimasa Miyake. Quantum computation on the edge of a symmetry-protected topological order. *Phys. Rev. Lett.*, 105:040501, Jul 2010.
- [14] Stephen D. Bartlett, Gavin K. Brennen, Akimasa Miyake, and Joseph M. Renes. Quantum computational renormalization in the haldane phase. *Phys. Rev. Lett.*, 105:110502, Sep 2010.

- [15] Dominic V. Else, Ilai Schwarz, Stephen D. Bartlett, and Andrew C. Doherty. Symmetry-protected phases for measurement-based quantum computation. *Phys. Rev. Lett.*, 108:240505, Jun 2012.
- [16] Dominic V Else, Stephen D Bartlett, and Andrew C Doherty. Symmetry protection of measurement-based quantum computation in ground states. *New Journal of Physics*, 14(11):113016, Nov 2012.
- [17] Jacob Miller and Akimasa Miyake. Resource quality of a symmetry-protected topologically ordered phase for quantum computation. *Phys. Rev. Lett.*, 114:120506, Mar 2015.
- [18] Dong-Sheng Wang, David T. Stephen, and Robert Raussendorf. Qudit quantum computation on matrix product states with global symmetry. *Phys. Rev. A*, 95:032312, Mar 2017.
- [19] David T. Stephen, Dong-Sheng Wang, Abhishodh Prakash, Tzu-Chieh Wei, and Robert Raussendorf. Computational power of symmetry-protected topological phases. *Phys. Rev. Lett.*, 119:010504, Jul 2017.
- [20] Robert Raussendorf, Dong-Sheng Wang, Abhishodh Prakash, Tzu-Chieh Wei, and David T. Stephen. Symmetry-protected topological phases with uniform computational power in one dimension. *Phys. Rev. A*, 96:012302, Jul 2017.
- [21] Hendrik Poulsen Nautrup and Tzu-Chieh Wei. Symmetry-protected topologically ordered states for universal quantum computation. *Phys. Rev. A*, 92:052309, Nov 2015.
- [22] Jacob Miller and Akimasa Miyake. Hierarchy of universal entanglement in 2d measurement-based quantum computation. *npj Quantum Information*, 2:16036, 2016.
- [23] Jacob Miller and Akimasa Miyake. Latent computational complexity of symmetry-protected topological order with fractional symmetry. *Phys. Rev. Lett.*, 120:170503, Apr 2018.
- [24] Tzu-Chieh Wei and Ching-Yu Huang. Universal measurement-based quantum computation in two-dimensional symmetry-protected topological phases. *Phys. Rev. A*, 96:032317, Sep 2017.
- [25] Yanzhu Chen, Abhishodh Prakash, and Tzu-Chieh Wei. Universal quantum computing using $(\mathbb{Z}_d)^3$ symmetry-protected topologically ordered states. *Phys. Rev. A*, 97:022305, Feb 2018.
- [26] Robert Raussendorf, Cihan Okay, Dong-Sheng Wang, David T. Stephen, and Hendrik Poulsen Nautrup. Computationally universal phase of quantum matter. *Phys. Rev. Lett.*, 122:090501, Mar 2019.
- [27] Trithep Devakul and Dominic J. Williamson. Universal quantum computation using fractal symmetry-protected cluster phases. *Phys. Rev. A*, 98:022332, Aug 2018.

- [28] H. Bombin and M. A. Martin-Delgado. Topological quantum distillation. *Phys. Rev. Lett.*, 97:180501, Oct 2006.
- [29] D. Gross, J. Eisert, N. Schuch, and D. Perez-Garcia. Measurement-based quantum computation beyond the one-way model. *Phys. Rev. A*, 76:052315, Nov 2007.
- [30] Jeongwan Haah. Local stabilizer codes in three dimensions without string logical operators. *Phys. Rev. A*, 83:042330, Apr 2011.
- [31] Héctor Bombín. Gauge color codes: optimal transversal gates and gauge fixing in topological stabilizer codes. *New Journal of Physics*, 17(8):083002, aug 2015.
- [32] Guanru Feng, Guilu Long, and Raymond Laflamme. Experimental simulation of anyonic fractional statistics with an nmr quantum-information processor. *Phys. Rev. A*, 88:022305, Aug 2013.
- [33] Annie Ji Hyun Park, Emma McKay, Dawei Lu, and Raymond Laflamme. Simulation of anyonic statistics and its topological path independence using a seven-qubit quantum simulator. *New Journal of Physics*, 18(4):043043, apr 2016.
- [34] J K Pachos, W Wieczorek, C Schmid, N Kiesel, R Pohlner, and H Weinfurter. Revealing anyonic features in a toric code quantum simulation. *New Journal of Physics*, 11(8):083010, aug 2009.
- [35] Chao-Yang Lu, Wei-Bo Gao, Otfried Gühne, Xiao-Qi Zhou, Zeng-Bing Chen, and Jian-Wei Pan. Demonstrating anyonic fractional statistics with a six-qubit quantum simulator. *Phys. Rev. Lett.*, 102:030502, Jan 2009.
- [36] Chao Song, Da Xu, Pengfei Zhang, Jianwen Wang, Qiujiang Guo, Wuxin Liu, Kai Xu, Hui Deng, Keqiang Huang, Dongning Zheng, Shi-Biao Zheng, H. Wang, Xiaobo Zhu, Chao-Yang Lu, and Jian-Wei Pan. Demonstration of topological robustness of anyonic braiding statistics with a superconducting quantum circuit. *Phys. Rev. Lett.*, 121:030502, Jul 2018.
- [37] Christian Kraglund Andersen, Ants Remm, Stefania Lazar, Sebastian Krinner, Nathan Lacroix, Graham J. Norris, Mihai Gabureac, Christopher Eichler, and Andreas Wallraff. Repeated quantum error detection in a surface code. *Nature Physics*, 16(8):875–880, Aug 2020.
- [38] H. Bombin and M. A. Martin-Delgado. Family of non-abelian kitaev models on a lattice: Topological condensation and confinement. *Phys. Rev. B*, 78:115421, Sep 2008.
- [39] H. Bombin. Topological order with a twist: Ising anyons from an abelian model. *Phys. Rev. Lett.*, 105:030403, Jul 2010.

- [40] Beni Yoshida. Gapped boundaries, group cohomology and fault-tolerant logical gates. *Ann. Phys.*, 377:387 – 413, 2017.
- [41] Sam Roberts, Beni Yoshida, Aleksander Kubica, and Stephen D. Bartlett. Symmetry-protected topological order at nonzero temperature. *Phys. Rev. A*, 96:022306, Aug 2017.
- [42] Sam Roberts and Stephen D. Bartlett. Symmetry-protected self-correcting quantum memories. *Phys. Rev. X*, 10:031041, Aug 2020.
- [43] Markus S. Kesselring, Fernando Pastawski, Jens Eisert, and Benjamin J. Brown. The boundaries and twist defects of the color code and their applications to topological quantum computation. *Quantum*, 2:101, October 2018.
- [44] Sergey Bravyi and Jeongwan Haah. Energy landscape of 3d spin hamiltonians with topological order. *Phys. Rev. Lett.*, 107:150504, Oct 2011.
- [45] Sergey Bravyi and Jeongwan Haah. Quantum self-correction in the 3d cubic code model. *Phys. Rev. Lett.*, 111:200501, Nov 2013.
- [46] A. S. Darmawan and S. D. Bartlett. Graph states as ground states of two-body frustration-free hamiltonians. *New J. Phys.*, 16:073013, 2014.
- [47] Colleen Delaney and Zhenghan Wang. Symmetry defects and their application to topological quantum computing. *Contemporary Mathematics*, page 121–151, 2020.
- [48] Tyler D. Ellison, Kohtaro Kato, Zi-Wen Liu, and Timothy H. Hsieh. Symmetry-protected sign problem and magic in quantum phases of matter. 2020.
- [49] Román Orús, Henning Kalis, Marcel Bornemann, and Kai Phillip Schmidt. Bounds on universal quantum computation with perturbed two-dimensional cluster states. *Phys. Rev. A*, 87:062312, Jun 2013.
- [50] Rahul M. Nandkishore and Michael Hermele. Fractons. *Annual Review of Condensed Matter Physics*, 10(1):295–313, 2019.
- [51] Claudio Chamon. Quantum glassiness in strongly correlated clean systems: An example of topological overprotection. *Phys. Rev. Lett.*, 94:040402, Jan 2005.
- [52] Beni Yoshida. Exotic topological order in fractal spin liquids. *Phys. Rev. B*, 88:125122, Sep 2013.
- [53] Sagar Vijay, Jeongwan Haah, and Liang Fu. Fracton topological order, generalized lattice gauge theory, and duality. *Phys. Rev. B*, 94:235157, Dec 2016.

- [54] Wilbur Shirley, Kevin Slagle, Zhenghan Wang, and Xie Chen. Fracton models on general three-dimensional manifolds. *Phys. Rev. X*, 8:031051, Aug 2018.
- [55] Abhinav Prem, Sheng-Jie Huang, Hao Song, and Michael Hermele. Cage-net fracton models. *Phys. Rev. X*, 9:021010, Apr 2019.
- [56] Hao Song, Abhinav Prem, Sheng-Jie Huang, and M. A. Martin-Delgado. Twisted fracton models in three dimensions. *Phys. Rev. B*, 99:155118, Apr 2019.
- [57] David Aasen, Daniel Bulmash, Abhinav Prem, Kevin Slagle, and Dominic J. Williamson. Topological defect networks for fractons of all types. *Phys. Rev. Research*, 2:043165, Oct 2020.
- [58] Trithep Devakul, Wilbur Shirley, and Juven Wang. Strong planar subsystem symmetry-protected topological phases and their dual fracton orders. *Phys. Rev. Research*, 2:012059, Mar 2020.
- [59] Yizhi You, Trithep Devakul, F. J. Burnell, and S. L. Sondhi. Subsystem symmetry protected topological order. *Phys. Rev. B*, 98:035112, Jul 2018.
- [60] Xie Chen, Zheng-Cheng Gu, Zheng-Xin Liu, and Xiao-Gang Wen. Symmetry protected topological orders and the group cohomology of their symmetry group. *Phys. Rev. B*, 87:155114, Apr 2013.
- [61] David T. Stephen, Hendrik Poulsen Nautrup, Juani Bermejo-Vega, Jens Eisert, and Robert Raussendorf. Subsystem symmetries, quantum cellular automata, and computational phases of quantum matter. *Quantum*, 3:142, May 2019.
- [62] David T. Stephen, Henrik Dreyer, Mohsin Iqbal, and Norbert Schuch. Detecting subsystem symmetry protected topological order via entanglement entropy. *Phys. Rev. B*, 100:115112, Sep 2019.
- [63] David T. Stephen, José Garre-Rubio, Arpit Dua, and Dominic J. Williamson. Subsystem symmetry enriched topological order in three dimensions. *Phys. Rev. Research*, 2:033331, Aug 2020.
- [64] Caroline de Groot, David T Stephen, Andras Molnar, and Norbert Schuch. Inaccessible entanglement in symmetry protected topological phases. *Journal of Physics A: Mathematical and Theoretical*, 53(33):335302, Jul 2020.
- [65] José Garre-Rubio, Mohsin Iqbal, and David T. Stephen. String order parameters for symmetry fractionalization in an enriched toric code. *Phys. Rev. B*, 103:125104, Mar 2021.
- [66] Bei Zeng and Xiao-Gang Wen. Gapped quantum liquids and topological order, stochastic local transformations and emergence of unitarity. *Phys. Rev. B*, 91:125121, Mar 2015.

- [67] Don N. Page. Average entropy of a subsystem. *Phys. Rev. Lett.*, 71:1291–1294, Aug 1993.
- [68] J. Eisert, M. Cramer, and M. B. Plenio. Colloquium: Area laws for the entanglement entropy. *Rev. Mod. Phys.*, 82:277–306, Feb 2010.
- [69] Matthew B. Hastings and Tohru Koma. Spectral gap and exponential decay of correlations. *Communications in Mathematical Physics*, 265(3):781–804, Aug 2006.
- [70] Yi Zhang, Tarun Grover, Ari Turner, Masaki Oshikawa, and Ashvin Vishwanath. Quasiparticle statistics and braiding from ground-state entanglement. *Phys. Rev. B*, 85:235151, Jun 2012.
- [71] Jeongwan Haah. An invariant of topologically ordered states under local unitary transformations. *Communications in Mathematical Physics*, 342(3):771–801, Mar 2016.
- [72] Bowen Shi, Kohtaro Kato, and Isaac H. Kim. Fusion rules from entanglement. *Annals of Physics*, 418:168164, 2020.
- [73] Hui Li and F. D. M. Haldane. Entanglement spectrum as a generalization of entanglement entropy: Identification of topological order in non-abelian fractional quantum hall effect states. *Phys. Rev. Lett.*, 101:010504, Jul 2008.
- [74] Xie Chen, Zheng-Xin Liu, and Xiao-Gang Wen. Two-dimensional symmetry-protected topological orders and their protected gapless edge excitations. *Phys. Rev. B*, 84:235141, Dec 2011.
- [75] F. Verstraete, J. I. Cirac, J. I. Latorre, E. Rico, and M. M. Wolf. Renormalization-group transformations on quantum states. *Phys. Rev. Lett.*, 94:140601, Apr 2005.
- [76] Zheng-Cheng Gu and Xiao-Gang Wen. Tensor-entanglement-filtering renormalization approach and symmetry-protected topological order. *Phys. Rev. B*, 80:155131, Oct 2009.
- [77] Michael A. Levin and Xiao-Gang Wen. String-net condensation: A physical mechanism for topological phases. *Phys. Rev. B*, 71:045110, Jan 2005.
- [78] Thomas Scaffidi, Daniel E. Parker, and Romain Vasseur. Gapless symmetry-protected topological order. *Phys. Rev. X*, 7:041048, Nov 2017.
- [79] Daniel E. Parker, Thomas Scaffidi, and Romain Vasseur. Topological luttinger liquids from decorated domain walls. *Phys. Rev. B*, 97:165114, Apr 2018.
- [80] Ruben Verresen, Ryan Thorngren, Nick G. Jones, and Frank Pollmann. Gapless topological phases and symmetry-enriched quantum criticality. 2019.
- [81] Ryan Thorngren, Ashvin Vishwanath, and Ruben Verresen. Intrinsically gapless topological phases. 2020.

- [82] Xie Chen, Zheng-Cheng Gu, and Xiao-Gang Wen. Local unitary transformation, long-range quantum entanglement, wave function renormalization, and topological order. *Phys. Rev. B*, 82:155138, Oct 2010.
- [83] M. B. Hastings and Xiao-Gang Wen. Quasiadiabatic continuation of quantum states: The stability of topological ground-state degeneracy and emergent gauge invariance. *Phys. Rev. B*, 72:045141, Jul 2005.
- [84] Dominic V. Else and Chetan Nayak. Classifying symmetry-protected topological phases through the anomalous action of the symmetry on the edge. *Phys. Rev. B*, 90:235137, Dec 2014.
- [85] F. J. Burnell, Xie Chen, Lukasz Fidkowski, and Ashvin Vishwanath. Exactly soluble model of a three-dimensional symmetry-protected topological phase of bosons with surface topological order. *Phys. Rev. B*, 90:245122, Dec 2014.
- [86] Lukasz Fidkowski, Jeongwan Haah, and Matthew B. Hastings. Exactly solvable model for a 4 + 1D beyond-cohomology symmetry-protected topological phase. *Phys. Rev. B*, 101:155124, Apr 2020.
- [87] Norbert Schuch, David Pérez-García, and Ignacio Cirac. Classifying quantum phases using matrix product states and projected entangled pair states. *Phys. Rev. B*, 84:165139, Oct 2011.
- [88] W. Son, L. Amico, and V. Vedral. Topological order in 1d cluster state protected by symmetry. *Quantum Information Processing*, 11(6):1961–1968, Dec 2012.
- [89] Daniel Gottesman. Stabilizer codes and quantum error correction. 1997.
- [90] Michael Levin and Zheng-Cheng Gu. Braiding statistics approach to symmetry-protected topological phases. *Phys. Rev. B*, 86:115109, Sep 2012.
- [91] Beni Yoshida. Topological phases with generalized global symmetries. *Phys. Rev. B*, 93:155131, Apr 2016.
- [92] Michael P. Zaletel. Detecting two-dimensional symmetry-protected topological order in a ground-state wave function. *Phys. Rev. B*, 90:235113, Dec 2014.
- [93] Dominic J. Williamson, Nick Bultinck, Michael Mariën, Mehmet B. Şahinoğlu, Jutho Haegeman, and Frank Verstraete. Matrix product operators for symmetry-protected topological phases: Gauging and edge theories. *Phys. Rev. B*, 94:205150, Nov 2016.
- [94] Ruben Verresen, Roderich Moessner, and Frank Pollmann. One-dimensional symmetry protected topological phases and their transitions. *Phys. Rev. B*, 96:165124, Oct 2017.
- [95] Jacob C. Bridgeman and Dominic J. Williamson. Anomalies and entanglement renormalization. *Phys. Rev. B*, 96:125104, Sep 2017.

- [96] Xie Chen, Yuan-Ming Lu, and Ashvin Vishwanath. Symmetry-protected topological phases from decorated domain walls. *Nature Communications*, 5:3507, Mar 2014.
- [97] Alioscia Hamma, Paolo Zanardi, and Xiao-Gang Wen. String and membrane condensation on three-dimensional lattices. *Phys. Rev. B*, 72:035307, Jul 2005.
- [98] Chenjie Wang and Michael Levin. Braiding statistics of loop excitations in three dimensions. *Phys. Rev. Lett.*, 113:080403, Aug 2014.
- [99] Xiao-Gang Wen. A theory of 2+1d bosonic topological orders. *National Science Review*, 3(1):68–106, 2016.
- [100] Paul Webster and Stephen D. Bartlett. Fault-tolerant quantum gates with defects in topological stabilizer codes. *Phys. Rev. A*, 102:022403, Aug 2020.
- [101] Earl T. Campbell, Barbara M. Terhal, and Christophe Vuillot. Roads towards fault-tolerant universal quantum computation. *Nature*, 549(7671):172–179, Sep 2017.
- [102] Claudio Castelnovo and Claudio Chamon. Topological order in a three-dimensional toric code at finite temperature. *Phys. Rev. B*, 78:155120, Oct 2008.
- [103] Alioscia Hamma, Radu Ionicioiu, and Paolo Zanardi. Bipartite entanglement and entropic boundary law in lattice spin systems. *Phys. Rev. A*, 71:022315, Feb 2005.
- [104] Michael Levin and Xiao-Gang Wen. Detecting topological order in a ground state wave function. *Phys. Rev. Lett.*, 96:110405, Mar 2006.
- [105] Alexei Kitaev and John Preskill. Topological entanglement entropy. *Phys. Rev. Lett.*, 96:110404, Mar 2006.
- [106] Hong-Chen Jiang, Zhenghan Wang, and Leon Balents. Identifying topological order by entanglement entropy. *Nature Physics*, 8:902, Nov 2012.
- [107] Liujun Zou and Jeongwan Haah. Spurious long-range entanglement and replica correlation length. *Phys. Rev. B*, 94:075151, Aug 2016.
- [108] John Kogut and Leonard Susskind. Hamiltonian formulation of wilson’s lattice gauge theories. *Phys. Rev. D*, 11:395–408, Jan 1975.
- [109] Julien Vidal, Sébastien Dusuel, and Kai Phillip Schmidt. Low-energy effective theory of the toric code model in a parallel magnetic field. *Phys. Rev. B*, 79:033109, Jan 2009.
- [110] Wilbur Shirley, Kevin Slagle, and Xie Chen. Foliated fracton order from gauging subsystem symmetries. *SciPost Phys.*, 6:41, 2019.

- [111] Maissam Barkeshli, Parsa Bonderson, Meng Cheng, and Zhenghan Wang. Symmetry fractionalization, defects, and gauging of topological phases. *Phys. Rev. B*, 100:115147, Sep 2019.
- [112] Michael Hermele. String flux mechanism for fractionalization in topologically ordered phases. *Phys. Rev. B*, 90:184418, Nov 2014.
- [113] Nicolas Tarantino, Netanel H Lindner, and Lukasz Fidkowski. Symmetry fractionalization and twist defects. *New Journal of Physics*, 18(3):035006, mar 2016.
- [114] Daniel Ben-Zion, Diptarka Das, and John McGreevy. Exactly solvable models of spin liquids with spinons, and of three-dimensional topological paramagnets. *Phys. Rev. B*, 93:155147, Apr 2016.
- [115] Abhinav Prem and Dominic J. Williamson. Gauging permutation symmetries as a route to non-Abelian fractons. *SciPost Phys.*, 7(5):068, nov 2019.
- [116] José Garre-Rubio and Sofyan Iblisdir. Local order parameters for symmetry fractionalization. *New Journal of Physics*, 21(11):113016, nov 2019.
- [117] H. A. Kramers and G. H. Wannier. Statistics of the two-dimensional ferromagnet. part ii. *Phys. Rev.*, 60:263–276, Aug 1941.
- [118] Ian Affleck, Tom Kennedy, Elliott H. Lieb, and Hal Tasaki. Rigorous results on valence-bond ground states in antiferromagnets. *Phys. Rev. Lett.*, 59:799–802, Aug 1987.
- [119] M. Fannes, B. Nachtergaele, and R. F. Werner. Finitely correlated states on quantum spin chains. *Communications in Mathematical Physics*, 144(3):443–490, Mar 1992.
- [120] Steven R. White. Density matrix formulation for quantum renormalization groups. *Phys. Rev. Lett.*, 69:2863–2866, Nov 1992.
- [121] Stefan Rommer and Stellan Östlund. Class of ansatz wave functions for one-dimensional spin systems and their relation to the density matrix renormalization group. *Phys. Rev. B*, 55:2164–2181, Jan 1997.
- [122] F. Verstraete and J. I. Cirac. Valence-bond states for quantum computation. *Phys. Rev. A*, 70:060302, Dec 2004.
- [123] F. Verstraete and J. I. Cirac. Renormalization algorithms for quantum-many body systems in two and higher dimensions. 2004.
- [124] F. Verstraete, V. Murg, and J.I. Cirac. Matrix product states, projected entangled pair states, and variational renormalization group methods for quantum spin systems. *Adv. Phys.*, 57(2):143–224, 2008.

- [125] Jacob C Bridgeman and Christopher T Chubb. Hand-waving and interpretive dance: an introductory course on tensor networks. *J. Phys. A*, 50(22):223001, May 2017.
- [126] F. Verstraete and J. I. Cirac. Matrix product states represent ground states faithfully. *Phys. Rev. B*, 73:094423, Mar 2006.
- [127] Norbert Schuch, Michael M. Wolf, Frank Verstraete, and J. Ignacio Cirac. Entropy scaling and simulability by matrix product states. *Phys. Rev. Lett.*, 100:030504, Jan 2008.
- [128] D. Perez-Garcia, F. Verstraete, M. M. Wolf, and J. I. Cirac. Matrix product state representations. *Quantum Info. Comput.*, 7(5):401–430, Jul 2007.
- [129] J. Ignacio Cirac, Didier Poilblanc, Norbert Schuch, and Frank Verstraete. Entanglement spectrum and boundary theories with projected entangled-pair states. *Phys. Rev. B*, 83:245134, Jun 2011.
- [130] Frank Pollmann, Ari M. Turner, Erez Berg, and Masaki Oshikawa. Entanglement spectrum of a topological phase in one dimension. *Phys. Rev. B*, 81:064439, Feb 2010.
- [131] Manuel Risper, Kasper Duivenvoorden, and Norbert Schuch. Long-range order and symmetry breaking in projected entangled-pair state models. *Phys. Rev. B*, 92:155133, Oct 2015.
- [132] J Ignacio Cirac, David Perez-Garcia, Norbert Schuch, and Frank Verstraete. Matrix product unitaries: structure, symmetries, and topological invariants. *J. Stat. Mech.*, 2017(8):083105, Aug 2017.
- [133] J.I. Cirac, D. Pérez-García, N. Schuch, and F. Verstraete. Matrix product density operators: Renormalization fixed points and boundary theories. *Annals of Physics*, 378:100–149, 2017.
- [134] Norbert Schuch, Ignacio Cirac, and David Perez-Garcia. Peps as ground states: Degeneracy and topology. *Ann. Phys.*, 325(10):2153 – 2192, 2010.
- [135] Frank Pollmann and Ari M. Turner. Detection of symmetry-protected topological phases in one dimension. *Phys. Rev. B*, 86:125441, Sep 2012.
- [136] N. Bultinck, M. Mariën, D.J. Williamson, M.B. Şahinoğlu, J. Haegeman, and F. Verstraete. Anyons and matrix product operator algebras. *Ann. Phys.*, 378:183 – 233, 2017.
- [137] Kasper Duivenvoorden, Mohsin Iqbal, Jutho Haegeman, Frank Verstraete, and Norbert Schuch. Entanglement phases as holographic duals of anyon condensates. *Phys. Rev. B*, 95:235119, Jun 2017.
- [138] Xie Chen, Zheng-Cheng Gu, and Xiao-Gang Wen. Classification of gapped symmetric phases in one-dimensional spin systems. *Phys. Rev. B*, 83:035107, Jan 2011.

- [139] Shenghan Jiang and Ying Ran. Anyon condensation and a generic tensor-network construction for symmetry-protected topological phases. *Phys. Rev. B*, 95:125107, Mar 2017.
- [140] Andras Molnar, Yimin Ge, Norbert Schuch, and J. Ignacio Cirac. A generalization of the injectivity condition for projected entangled pair states. *J. Math. Phys.*, 59(2):021902, 2018.
- [141] Didier Poilblanc, J. Ignacio Cirac, and Norbert Schuch. Chiral topological spin liquids with projected entangled pair states. *Phys. Rev. B*, 91:224431, Jun 2015.
- [142] Dominic J. Williamson, Nick Bultinck, and Frank Verstraete. Symmetry-enriched topological order in tensor networks: Defects, gauging and anyon condensation. 2017.
- [143] Nick Bultinck, Dominic J Williamson, Jutho Haegeman, and Frank Verstraete. Fermionic projected entangled-pair states and topological phases. *J. Phys. A*, 51(2):025202, Dec 2017.
- [144] Henrik Dreyer, J. Ignacio Cirac, and Norbert Schuch. Projected entangled pair states with continuous virtual symmetries. *Phys. Rev. B*, 98:115120, Sep 2018.
- [145] D. Pérez-García, M. M. Wolf, M. Sanz, F. Verstraete, and J. I. Cirac. String order and symmetries in quantum spin lattices. *Phys. Rev. Lett.*, 100:167202, Apr 2008.
- [146] I_A G Berkovich and EM Zhmud. *Characters of finite groups*, volume 1. American Mathematical Soc., 1998.
- [147] Dominic V. Else, Stephen D. Bartlett, and Andrew C. Doherty. Hidden symmetry-breaking picture of symmetry-protected topological order. *Phys. Rev. B*, 88:085114, Aug 2013.
- [148] Abhishodh Prakash and Tzu-Chieh Wei. Ground states of one-dimensional symmetry-protected topological phases and their utility as resource states for quantum computation. *Phys. Rev. A*, 92:022310, Aug 2015.
- [149] David Thomas Stephen. *Computational power of one-dimensional symmetry-protected topological phases*. PhD thesis, University of British Columbia, 2017.
- [150] Andras Molnar, José Garre-Rubio, David Pérez-García, Norbert Schuch, and J Ignacio Cirac. Normal projected entangled pair states generating the same state. *New Journal of Physics*, 20(11):113017, Nov 2018.
- [151] José Garre-Rubio, Sofyan Iblisdir, and David Pérez-García. Symmetry reduction induced by anyon condensation: A tensor network approach. *Phys. Rev. B*, 96:155123, Oct 2017.

- [152] Oliver Buerschaper. Twisted injectivity in projected entangled pair states and the classification of quantum phases. *Annals of Physics*, 351:447–476, 2014.
- [153] Mehmet Burak Şahinoğlu, Dominic Williamson, Nick Bultinck, Michaël Mariën, Jutho Haegeman, Norbert Schuch, and Frank Verstraete. Characterizing topological order with matrix product operators. *Annales Henri Poincaré*, 22(2):563–592, Feb 2021.
- [154] Jutho Haegeman, J. Ignacio Cirac, Tobias J. Osborne, Iztok Pižorn, Henri Verschelde, and Frank Verstraete. Time-dependent variational principle for quantum lattices. *Phys. Rev. Lett.*, 107:070601, Aug 2011.
- [155] V. Zauner-Stauber, L. Vanderstraeten, M. T. Fishman, F. Verstraete, and J. Haegeman. Variational optimization algorithms for uniform matrix product states. *Phys. Rev. B*, 97:045145, Jan 2018.
- [156] Norbert Schuch, Michael M. Wolf, Frank Verstraete, and J. Ignacio Cirac. Computational complexity of projected entangled pair states. *Phys. Rev. Lett.*, 98:140506, Apr 2007.
- [157] V. Murg, F. Verstraete, and J. I. Cirac. Variational study of hard-core bosons in a two-dimensional optical lattice using projected entangled pair states. *Phys. Rev. A*, 75:033605, Mar 2007.
- [158] Román Orús and Guifré Vidal. Simulation of two-dimensional quantum systems on an infinite lattice revisited: Corner transfer matrix for tensor contraction. *Phys. Rev. B*, 80:094403, Sep 2009.
- [159] Zheng-Cheng Gu, Michael Levin, and Xiao-Gang Wen. Tensor-entanglement renormalization group approach as a unified method for symmetry breaking and topological phase transitions. *Phys. Rev. B*, 78:205116, Nov 2008.
- [160] G. Evenbly and G. Vidal. Tensor network renormalization. *Phys. Rev. Lett.*, 115:180405, Oct 2015.
- [161] Laurens Vanderstraeten, Jutho Haegeman, Philippe Corboz, and Frank Verstraete. Gradient methods for variational optimization of projected entangled-pair states. *Phys. Rev. B*, 94:155123, Oct 2016.
- [162] Hai-Jun Liao, Jin-Guo Liu, Lei Wang, and Tao Xiang. Differentiable programming tensor networks. *Phys. Rev. X*, 9:031041, Sep 2019.
- [163] J. Jordan, R. Orús, G. Vidal, F. Verstraete, and J. I. Cirac. Classical simulation of infinite-size quantum lattice systems in two spatial dimensions. *Phys. Rev. Lett.*, 101:250602, Dec 2008.
- [164] H. C. Jiang, Z. Y. Weng, and T. Xiang. Accurate determination of tensor network state of quantum lattice models in two dimensions. *Phys. Rev. Lett.*, 101:090603, Aug 2008.

- [165] R. Orús and G. Vidal. Infinite time-evolving block decimation algorithm beyond unitary evolution. *Phys. Rev. B*, 78:155117, Oct 2008.
- [166] Ho N. Phien, Johann A. Bengua, Hoang D. Tuan, Philippe Corboz, and Román Orús. Infinite projected entangled pair states algorithm improved: Fast full update and gauge fixing. *Phys. Rev. B*, 92:035142, Jul 2015.
- [167] Michael P. Zaletel and Frank Pollmann. Isometric tensor network states in two dimensions. *Phys. Rev. Lett.*, 124:037201, Jan 2020.
- [168] Frank Pollmann, Subroto Mukerjee, Ari M. Turner, and Joel E. Moore. Theory of finite-entanglement scaling at one-dimensional quantum critical points. *Phys. Rev. Lett.*, 102:255701, Jun 2009.
- [169] B. Pirvu, G. Vidal, F. Verstraete, and L. Tagliacozzo. Matrix product states for critical spin chains: Finite-size versus finite-entanglement scaling. *Phys. Rev. B*, 86:075117, Aug 2012.
- [170] Bram Vanhecke, Jutho Haegeman, Karel Van Acoleyen, Laurens Vanderstraeten, and Frank Verstraete. Scaling hypothesis for matrix product states. *Phys. Rev. Lett.*, 123:250604, Dec 2019.
- [171] Laurens Vanderstraeten, Jutho Haegeman, and Frank Verstraete. Tangent-space methods for uniform matrix product states. *SciPost Phys. Lect. Notes*, page 7, 2019.
- [172] Leong Chuan Kwek, Zhaohui Wei, and Bei Zeng. Measurement-based quantum computing with valence-bond-solids. *International Journal of Modern Physics B*, 26(02):1230002, 2012.
- [173] Gavin K. Brennen and Akimasa Miyake. Measurement-based quantum computer in the gapped ground state of a two-body hamiltonian. *Phys. Rev. Lett.*, 101:010502, Jul 2008.
- [174] D. Gross and J. Eisert. Novel schemes for measurement-based quantum computation. *Phys. Rev. Lett.*, 98:220503, May 2007.
- [175] Tzu-Chieh Wei, Ian Affleck, and Robert Raussendorf. Affleck-kennedy-lieb-tasaki state on a honeycomb lattice is a universal quantum computational resource. *Phys. Rev. Lett.*, 106:070501, Feb 2011.
- [176] Akimasa Miyake. Quantum computational capability of a 2d valence bond solid phase. *Annals of Physics*, 326(7):1656–1671, 2011. July 2011 Special Issue.
- [177] Tzu-Chieh Wei. Quantum computational universality of affleck-kennedy-lieb-tasaki states beyond the honeycomb lattice. *Phys. Rev. A*, 88:062307, Dec 2013.

- [178] Tzu-Chieh Wei and Robert Raussendorf. Universal measurement-based quantum computation with spin-2 affleck-kennedy-lieb-tasaki states. *Phys. Rev. A*, 92:012310, Jul 2015.
- [179] Andrew S Darmawan, Gavin K Brennen, and Stephen D Bartlett. Measurement-based quantum computation in a two-dimensional phase of matter. *New Journal of Physics*, 14(1):013023, jan 2012.
- [180] Scott Aaronson and Daniel Gottesman. Improved simulation of stabilizer circuits. *Phys. Rev. A*, 70:052328, Nov 2004.
- [181] Mariami Gachechiladze, Otfried Gühne, and Akimasa Miyake. Changing the circuit-depth complexity of measurement-based quantum computation with hypergraph states. *Phys. Rev. A*, 99:052304, May 2019.
- [182] Xie Chen, Bei Zeng, Zheng-Cheng Gu, Beni Yoshida, and Isaac L. Chuang. Gapped two-body hamiltonian whose unique ground state is universal for one-way quantum computation. *Phys. Rev. Lett.*, 102:220501, Jun 2009.
- [183] David Deutsch and Roger Penrose. Quantum theory, the church-turing principle and the universal quantum computer. *Proceedings of the Royal Society of London. A. Mathematical and Physical Sciences*, 400(1818):97–117, 1985.
- [184] Robert Raussendorf. Contextuality in measurement-based quantum computation. *Phys. Rev. A*, 88:022322, Aug 2013.
- [185] Mark Howard, Joel Wallman, Victor Veitch, and Joseph Emerson. Contextuality supplies the ‘magic’ for quantum computation. *Nature*, 510(7505):351–355, Jun 2014.
- [186] Davide Gaiotto, Anton Kapustin, Nathan Seiberg, and Brian Willett. Generalized global symmetries. *J. High En. Phys.*, 2015(2):172, Feb 2015.
- [187] Lokman Tsui and Xiao-Gang Wen. Lattice models that realize z_n -1 symmetry-protected topological states for even n . *Phys. Rev. B*, 101:035101, Jan 2020.
- [188] Hans J. Briegel and Robert Raussendorf. Persistent entanglement in arrays of interacting particles. *Phys. Rev. Lett.*, 86:910–913, Jan 2001.
- [189] Robert Raussendorf and Hans J. Briegel. A one-way quantum computer. *Phys. Rev. Lett.*, 86:5188–5191, May 2001.
- [190] Trithep Devakul, Dominic J. Williamson, and Yizhi You. Classification of subsystem symmetry-protected topological phases. *Phys. Rev. B*, 98:235121, Dec 2018.
- [191] Trithep Devakul, Yizhi You, F. J. Burnell, and S. L. Sondhi. Fractal Symmetric Phases of Matter. *SciPost Phys.*, 6:7, 2019.

- [192] Austin K. Daniel, Rafael N. Alexander, and Akimasa Miyake. Computational universality of symmetry-protected topologically ordered cluster phases on 2D Archimedean lattices. *Quantum*, 4:228, February 2020.
- [193] Robert Raussendorf. Quantum computation via translation-invariant operations on a chain of qubits. *Phys. Rev. A*, 72:052301, Nov 2005.
- [194] Dominic J. Williamson. Fractal symmetries: Ungauging the cubic code. *Phys. Rev. B*, 94:155128, Oct 2016.
- [195] Claudio Castelnovo and Claudio Chamon. Topological quantum glassiness. *Philosophical Magazine*, 92(1-3):304–323, 2012.
- [196] Isaac H. Kim. 3D local qubit quantum code without string logical operator. 2012.
- [197] Sagar Vijay, Jeongwan Haah, and Liang Fu. A new kind of topological quantum order: A dimensional hierarchy of quasiparticles built from stationary excitations. *Phys. Rev. B*, 92:235136, Dec 2015.
- [198] Michael Pretko, Xie Chen, and Yizhi You. Fracton phases of matter. *International Journal of Modern Physics A*, 35(06):2030003, 2020.
- [199] Han Ma, A. T. Schmitz, S. A. Parameswaran, Michael Hermele, and Rahul M. Nandkishore. Topological entanglement entropy of fracton stabilizer codes. *Phys. Rev. B*, 97:125101, Mar 2018.
- [200] Bowen Shi and Yuan-Ming Lu. Deciphering the nonlocal entanglement entropy of fracton topological orders. *Phys. Rev. B*, 97:144106, Apr 2018.
- [201] Wilbur Shirley, Kevin Slagle, and Xie Chen. Universal entanglement signatures of foliated fracton phases. *SciPost Phys.*, 6:15, 2019.
- [202] Daniel Bulmash and Thomas Iadecola. Braiding and gapped boundaries in fracton topological phases. *Phys. Rev. B*, 99:125132, Mar 2019.
- [203] Kevin Slagle, David Aasen, and Dominic Williamson. Foliated Field Theory and String-Membrane-Net Condensation Picture of Fracton Order. *SciPost Phys.*, 6:43, 2019.
- [204] Xiao-Gang Wen. Systematic construction of gapped nonliquid states. *Phys. Rev. Research*, 2:033300, Aug 2020.
- [205] Abhinav Prem, Jeongwan Haah, and Rahul Nandkishore. Glassy quantum dynamics in translation invariant fracton models. *Phys. Rev. B*, 95:155133, Apr 2017.
- [206] B. Schumacher and R. F. Werner. Reversible quantum cellular automata. 2004.

- [207] Dirk-M. Schlingemann, Holger Vogts, and Reinhard F. Werner. On the structure of clifford quantum cellular automata. *J. Math. Phys.*, 49(11):112104, 2008.
- [208] Johannes Gütschow, Sonja Uphoff, Reinhard F. Werner, and Zoltan Zimboras. Time asymptotics and entanglement generation of clifford quantum cellular automata. *J. Math. Phys.*, 51(1):015203, 2010.
- [209] Joseph F. Fitzsimons. Private quantum computation: an introduction to blind quantum computing and related protocols. *npj Quantum Information*, 3:23, 2017.
- [210] Atul Mantri, Tommaso F. Demarie, Nicolas C. Menicucci, and Joseph F. Fitzsimons. Flow ambiguity: A path towards classically driven blind quantum computation. *Phys. Rev. X*, 7:031004, Jul 2017.
- [211] Joseph Fitzsimons and Jason Twamley. Globally controlled quantum wires for perfect qubit transport, mirroring, and computing. *Phys. Rev. Lett.*, 97:090502, Sep 2006.
- [212] Joseph Fitzsimons, Li Xiao, Simon C. Benjamin, and Jonathan A. Jones. Quantum information processing with delocalized qubits under global control. *Phys. Rev. Lett.*, 99:030501, Jul 2007.
- [213] Juan Bermejo-Vega, Dominik Hangleiter, Martin Schwarz, Robert Raussendorf, and Jens Eisert. Architectures for quantum simulation showing a quantum speedup. *Phys. Rev. X*, 8:021010, Apr 2018.
- [214] Dominik Hangleiter, Juan Bermejo-Vega, Martin Schwarz, and Jens Eisert. Anticoncentration theorems for schemes showing a quantum speedup. *Quantum*, 2:65, May 2018.
- [215] Daniel Gottesman. Fault-tolerant quantum computation with higher-dimensional systems. In *Selected papers from the First NASA International Conference on Quantum Computing and Quantum Communications*. Springer, 1998.
- [216] Juan Bermejo-Vega and Maarten Van Den Nest. Classical simulations of abelian-group normalizer circuits with intermediate measurements. *Quant. Inf. Comp.*, 14(3-4):181–216, Mar 2014.
- [217] Atul Mantri, Tommaso F. Demarie, and Joseph F. Fitzsimons. Universality of quantum computation with cluster states and (x, y)-plane measurements. *Scientific Reports*, 7:42861, Feb 2017.
- [218] D. Gross, V. Nesme, H. Vogts, and R. F. Werner. Index theory of one dimensional quantum walks and cellular automata. *Commun. Math. Phys.*, 310(2):419–454, Mar 2012.

- [219] David Sauerwein, Andras Molnar, J. Ignacio Cirac, and Barbara Kraus. Matrix product states: Entanglement, symmetries, and state transformations. *Phys. Rev. Lett.*, 123:170504, Oct 2019.
- [220] M. Sanz, D. Perez-Garcia, M. M. Wolf, and J. I. Cirac. A quantum version of wielandt’s inequality. *IEEE Transactions on Information Theory*, 56(9):4668–4673, Sep. 2010.
- [221] Burton Voorhees. A note on injectivity of additive cellular automata. *Complex Systems*, 8(3):151–160, 1994.
- [222] M. Hein, J. Eisert, and H. J. Briegel. Multiparty entanglement in graph states. *Phys. Rev. A*, 69:062311, Jun 2004.
- [223] Iman Marvian. Symmetry-protected topological entanglement. *Phys. Rev. B*, 95:045111, Jan 2017.
- [224] Aleksander Kubica and Beni Yoshida. Ungauging quantum error-correcting codes. 2018.
- [225] Adriano Barenco, Charles H. Bennett, Richard Cleve, David P. DiVincenzo, Norman Margolus, Peter Shor, Tycho Sleator, John A. Smolin, and Harald Weinfurter. Elementary gates for quantum computation. *Phys. Rev. A*, 52:3457–3467, Nov 1995.
- [226] David Deutsch, Adriano Barenco, and Artur Ekert. Universality in quantum computation. *Proc. R. Soc. London A*, 449(1937):669–677, 1995.
- [227] Michael J. Bremner, Christopher M. Dawson, Jennifer L. Dodd, Alexei Gilchrist, Aram W. Harrow, Duncan Mortimer, Michael A. Nielsen, and Tobias J. Osborne. Practical scheme for quantum computation with any two-qubit entangling gate. *Phys. Rev. Lett.*, 89:247902, Nov 2002.
- [228] R. Raussendorf, J. Harrington, and K. Goyal. A fault-tolerant one-way quantum computer. *Annals of Physics*, 321(9):2242 – 2270, 2006.
- [229] R Raussendorf, J Harrington, and K Goyal. Topological fault-tolerance in cluster state quantum computation. *New Journal of Physics*, 9(6):199–199, Jun 2007.
- [230] Jennifer Cano, Taylor L. Hughes, and Michael Mulligan. Interactions along an entanglement cut in 2 + 1D abelian topological phases. *Phys. Rev. B*, 92:075104, Aug 2015.
- [231] Luiz H. Santos, Jennifer Cano, Michael Mulligan, and Taylor L. Hughes. Symmetry-protected topological interfaces and entanglement sequences. *Phys. Rev. B*, 98:075131, Aug 2018.
- [232] Dominic J. Williamson, Arpit Dua, and Meng Cheng. Spurious topological entanglement entropy from subsystem symmetries. *Phys. Rev. Lett.*, 122:140506, Apr 2019.

- [233] Albert T. Schmitz, Sheng-Jie Huang, and Abhinav Prem. Entanglement spectra of stabilizer codes: A window into gapped quantum phases of matter. *Phys. Rev. B*, 99:205109, May 2019.
- [234] Stefanos Papanikolaou, Kumar S. Raman, and Eduardo Fradkin. Topological phases and topological entropy of two-dimensional systems with finite correlation length. *Phys. Rev. B*, 76:224421, Dec 2007.
- [235] A. Hamma, W. Zhang, S. Haas, and D. A. Lidar. Entanglement, fidelity, and topological entropy in a quantum phase transition to topological order. *Phys. Rev. B*, 77:155111, Apr 2008.
- [236] Zohar Nussinov and Gerardo Ortiz. A symmetry principle for topological quantum order. *Ann. Phys.*, 324(5):977 – 1057, 2009.
- [237] Sergei V. Isakov, Matthew B. Hastings, and Roger G. Melko. Topological entanglement entropy of a bose-hubbard spin liquid. *Nature Physics*, 7:772–775, Jul 2011.
- [238] Steven T. Flammia, Alioscia Hamma, Taylor L. Hughes, and Xiao-Gang Wen. Topological entanglement rényi entropy and reduced density matrix structure. *Phys. Rev. Lett.*, 103:261601, Dec 2009.
- [239] Gábor B. Halász and Alioscia Hamma. Probing topological order with rényi entropy. *Phys. Rev. A*, 86:062330, Dec 2012.
- [240] Dmitry A. Abanin and Eugene Demler. Measuring entanglement entropy of a generic many-body system with a quantum switch. *Phys. Rev. Lett.*, 109:020504, Jul 2012.
- [241] A. J. Daley, H. Pichler, J. Schachenmayer, and P. Zoller. Measuring entanglement growth in quench dynamics of bosons in an optical lattice. *Phys. Rev. Lett.*, 109:020505, Jul 2012.
- [242] Rajibul Islam, Ruichao Ma, Philipp M. Preiss, M. Eric Tai, Alexander Lukin, Matthew Rispoli, and Markus Greiner. Measuring entanglement entropy in a quantum many-body system. *Nature*, 528:77 – 83, Dec 2015.
- [243] Jutho Haegeman, David Pérez-García, Ignacio Cirac, and Norbert Schuch. Order parameter for symmetry-protected phases in one dimension. *Phys. Rev. Lett.*, 109:050402, Jul 2012.
- [244] Norbert Schuch, Didier Poilblanc, J. Ignacio Cirac, and David Pérez-García. Topological order in the projected entangled-pair states formalism: Transfer operator and boundary hamiltonians. *Phys. Rev. Lett.*, 111:090501, Aug 2013.
- [245] Didier Poilblanc, Norbert Schuch, and Ian Affleck. $SU(2)_1$ chiral edge modes of a critical spin liquid. *Phys. Rev. B*, 93:174414, May 2016.

- [246] Henning Kalis, Daniel Klagges, Román Orús, and Kai Phillip Schmidt. Fate of the cluster state on the square lattice in a magnetic field. *Phys. Rev. A*, 86:022317, Aug 2012.
- [247] Cenke Xu and J. E. Moore. Strong-weak coupling self-duality in the two-dimensional quantum phase transition of $p + ip$ superconducting arrays. *Phys. Rev. Lett.*, 93:047003, Jul 2004.
- [248] Xie Chen and Ashvin Vishwanath. Towards gauging time-reversal symmetry: A tensor network approach. *Phys. Rev. X*, 5:041034, Nov 2015.
- [249] Laurens Vanderstraeten, Michaël Mariën, Jutho Haegeman, Norbert Schuch, Julien Vidal, and Frank Verstraete. Bridging perturbative expansions with tensor networks. *Phys. Rev. Lett.*, 119:070401, Aug 2017.
- [250] Courtney G Brell. Generalized cluster states based on finite groups. *New Journal of Physics*, 17(2):023029, feb 2015.
- [251] Yizhi You, Trithep Devakul, F.J. Burnell, and S.L. Sondhi. Symmetric fracton matter: Twisted and enriched. *Annals of Physics*, 416:168140, 2020.
- [252] Olaf Mandel, Markus Greiner, Artur Widera, Tim Rom, Theodor W. Hänsch, and Immanuel Bloch. Controlled collisions for multi-particle entanglement of optically trapped atoms. *Nature*, 425(6961):937–940, 2003.
- [253] Andrej Mesaros and Ying Ran. Classification of symmetry enriched topological phases with exactly solvable models. *Phys. Rev. B*, 87:155115, Apr 2013.
- [254] Maissam Barkeshli, Chao-Ming Jian, and Xiao-Liang Qi. Theory of defects in abelian topological states. *Phys. Rev. B*, 88:235103, Dec 2013.
- [255] Jeffrey C.Y. Teo, Taylor L. Hughes, and Eduardo Fradkin. Theory of twist liquids: Gauging an anyonic symmetry. *Annals of Physics*, 360:349 – 445, 2015.
- [256] Maissam Barkeshli, Parsa Bonderson, Meng Cheng, Chao-Ming Jian, and Kevin Walker. Reflection and time reversal symmetry enriched topological phases of matter: Path integrals, non-orientable manifolds, and anomalies. *Communications in Mathematical Physics*, 374(2):1021–1124, 2020.
- [257] Cenke Xu. Three-dimensional Z_2 topological phases enriched by time-reversal symmetry. *Phys. Rev. B*, 88:205137, Nov 2013.
- [258] Meng Cheng. Symmetry fractionalization in three-dimensional Z_2 topological order and fermionic symmetry-protected phases. 2015.
- [259] Xie Chen and Michael Hermele. Symmetry fractionalization and anomaly detection in three-dimensional topological phases. *Phys. Rev. B*, 94:195120, Nov 2016.

- [260] Shang-Qiang Ning, Zheng-Xin Liu, and Peng Ye. Symmetry enrichment in three-dimensional topological phases. *Phys. Rev. B*, 94:245120, Dec 2016.
- [261] Lukasz Fidkowski and Ashvin Vishwanath. Realizing anomalous anyonic symmetries at the surfaces of three-dimensional gauge theories. *Phys. Rev. B*, 96:045131, Jul 2017.
- [262] Tian Lan, Liang Kong, and Xiao-Gang Wen. Classification of $(3 + 1)$ D bosonic topological orders: The case when pointlike excitations are all bosons. *Phys. Rev. X*, 8:021074, Jun 2018.
- [263] Tian Lan and Xiao-Gang Wen. Classification of $3 + 1$ D bosonic topological orders (ii): The case when some pointlike excitations are fermions. *Phys. Rev. X*, 9:021005, Apr 2019.
- [264] Ching-Yu Huang, Xie Chen, and Frank Pollmann. Detection of symmetry-enriched topological phases. *Phys. Rev. B*, 90:045142, Jul 2014.
- [265] Wei Li, Shuo Yang, Meng Cheng, Zheng-Xin Liu, and Hong-Hao Tu. Topology and criticality in the resonating affleck-kennedy-lieb-tasaki loop spin liquid states. *Phys. Rev. B*, 89:174411, May 2014.
- [266] Daniel Bulmash and Maissam Barkeshli. Gauging fractons: Immobile non-abelian quasiparticles, fractals, and position-dependent degeneracies. *Phys. Rev. B*, 100:155146, Oct 2019.
- [267] Arpit Dua, Dominic J. Williamson, Jeongwan Haah, and Meng Cheng. Compactifying fracton stabilizer models. *Phys. Rev. B*, 99:245135, Jun 2019.
- [268] Lars Onsager. Crystal statistics. i. a two-dimensional model with an order-disorder transition. *Phys. Rev.*, 65:117–149, Feb 1944.
- [269] Somendra M. Bhattacharjee and Avinash Khare. Fifty years of the exact solution of the two-dimensional ising model by onsager. *Current Science*, 69(10):816–821, 1995.
- [270] Nathanan Tantivasadakarn and Sagar Vijay. Searching for fracton orders via symmetry defect condensation. *Phys. Rev. B*, 101:165143, Apr 2020.
- [271] Maissam Barkeshli, Chao-Ming Jian, and Xiao-Liang Qi. Twist defects and projective non-abelian braiding statistics. *Phys. Rev. B*, 87:045130, Jan 2013.
- [272] Eric Dennis, Alexei Kitaev, Andrew Landahl, and John Preskill. Topological quantum memory. *Journal of Mathematical Physics*, 43(9):4452–4505, 2002.
- [273] Aleksander Kubica, Michael E. Beverland, Fernando Brandão, John Preskill, and Krysta M. Svore. Three-dimensional color code thresholds via statistical-mechanical mapping. *Phys. Rev. Lett.*, 120:180501, May 2018.

- [274] Huan He, Yunqin Zheng, B. Andrei Bernevig, and Nicolas Regnault. Entanglement entropy from tensor network states for stabilizer codes. *Phys. Rev. B*, 97:125102, Mar 2018.
- [275] Nathanan Tantivasadakarn, Wenjie Ji, and Sagar Vijay. Hybrid fracton phases: Parent orders for liquid and non-liquid quantum phases. 2021.